FROM BOTTOM TO TOP: IDENTIFICATION TO PRECISION MEASUREMENT OF 3RD-GENERATION QUARKS WITH THE ATLAS DETECTOR

by

Kevin Sapp

B.S. in Physics, College of William and Mary, 2008

M.S. in Physics, University of Pittsburgh, 2012

Submitted to the Graduate Faculty of

the Kenneth P. Dietrich School of Arts and Sciences in partial fulfillment

of the requirements for the degree of

Doctor of Philosophy

University of Pittsburgh

2016

UNIVERSITY OF PITTSBURGH

DIETRICH SCHOOL OF ARTS AND SCIENCES

This dissertation was presented

by

Kevin Sapp

It was defended on

December 10th, 2015

and approved by

James Mueller, University of Pittsburgh

Joseph Boudreau, University of Pittsburgh

Adam Leibovich, University of Pittsburgh

Jeffrey Newman, University of Pittsburgh

Manfred Paulini, Carnegie Mellon University

Dissertation Director: James Mueller, University of Pittsburgh

FROM BOTTOM TO TOP: IDENTIFICATION TO PRECISION MEASUREMENT OF 3$^{\mathrm{RD}}$-GENERATION QUARKS WITH THE ATLAS DETECTOR

Kevin Sapp, PhD

University of Pittsburgh, 2016

The 3$^{\mathrm{rd}}$-generation quarks, bottom (b) and top (t), are recent additions to the Standard Model of particle physics, and precise characterization of their properties have important implications to searching for new physics phenomena. This thesis presents two analyses which use $4.6\,\mathrm{fb}^{-1}$ of pp collision data at $\sqrt{s} = 7$ TeV collected by the ATLAS detector at the Large Hadron Collider (LHC) to measure their properties. The first is an analysis which measures our ability to identify jets originating from b quarks with machine-learning algorithms applied to simulated and real data, so the result in simulation can be corrected to match that in data. This measurement has implications for our ability to identify processes with b quarks in their final state; t quarks decay to a b quark and a weak vector boson W more than 99% of the time. The second analysis presented measures properties of the $t \to Wb$ decay channel associated with phenomena not predicted by the Standard Model, through a set of effective couplings which preserve Lorentz covariance. The kinematic information of the final-state particles is used to construct an event-specific coordinate system, and probability density is estimated as a function of solid angle in these coordinates. A parameterization of the effective couplings is extracted via a novel unfolding method, finding their values consistent with the Standard Model expectation, contributing the first measurement of the correlation between the parameters, and improving on previous limits.

TABLE OF CONTENTS

LIST OF TABLES

LIST OF FIGURES

PREFACE

It takes a village to graduate a doctoral student, and I had an exceptional village of family, friends and colleagues as my support. First, I owe much of my growth as a physicist, a scientist, and a professional to my advisor, Dr. James Mueller. Our long discussions and your commitment to helping me understand not just the question at hand but the approaches to finding the answer and understanding the context have been critical to my success.

I would also like to thank our collaborator, Dr. Joseph Boudreau, for his mathematical and technical help with the analyses I've worked on throughout the thesis process, and his generosity with time, food and wine.

Many colleagues at CERN have played a role in completing the work presented in this thesis. I extend my gratitude particularly to Christian Weiser, Sara Strandberg, and Fabrizio Parodi for the work on b-tagging; and to Andi Wildauer, Oliver Maria Kind, S oren Stamm, Duc Bao Ta, Jose Enrique Garcia, Alison Lister, Mark Owen, Klaus Moenig and Kevin Kroninger for the single-top analysis.

I would also like to thank Dr. Adam Leibovich, Dr. Jeffrey Newman, and Dr. Manfred Paulini for serving on my committee, and for their assistance with this thesis.

I am grateful for the help, either direct or indirect, of colleagues at the University of Pittsburgh and at CERN. My collaborators Carlos Escobar, Jun Su, and Joseph Boudreau produced many things which helped me push the analysis towards completion. CERN colleagues Nicolas Bousson, Christian Jung, and Hendrik Esch made navigating my frequent shuttling to Geneva easier and more enjoyable. Pitt colleagues Mark Steger, Damon Hansen, Louis Lello, Kevin Wilk, Richard Ruiz, and Daniel Wiegand all deserve thanks for keeping me fascinated and sane at the same time.

I am indebted also to my undergraduate research advisors, Dr. Jeffrey Nelson and Dr.

Carl Carlson, for introducing me to so many different parts of the research experience that I found some I absolutely loved; and to my friends Ian Howley, Brian DeSalvo, and Andrew Leister, who have followed similar paths.

I could not have done this without the support of my family. To Marian and Gary Elder, to Tony and Jessica Elder, and to Beth Elder; to Jim Henry and to the extended Michaels, Sapp, and Henry families; thank you for all your support and love. To my mother: you've been the most supportive and wonderful mother I could imagine asking for. Thank you for everything you've given me.

Finally, the greatest debt of gratitude goes to my wife, Anna Elder. For the many times I've left her to work at CERN; for the many late nights and early mornings; for the difficult weeks and the exuberant ones; for all the unconditional love and support you've given, I'm eternally grateful. Here's to our future!

I. INTRODUCTION

Theories of fundamental, quantized constituents of matter and the study of the nature of their interactions have been around for millenia. They can be traced from historical atomist philosophies in ancient Greek and Indian societies, through the formulation of the scientific method and the formation of modern atomic and quantum theory, to the contemporary investigation of elementary particles and the forces which govern their interactions. The concept shed its speculative roots and became scientifically testable with the development of the kinetic theory of gases and statistical mechanics [1] and, shortly thereafter, quantum mechanics [2, 3][1]. The S-matrix and scattering theory were developed to explain the interactions between quantum-mechanical states in energetic, isolated collisions, and in this context, quantum field theories took shape. Their development made explicit the connection between statistical and quantum mechanics, and in the process created a framework with multiple distinct species of fundamental particles: force-carrying bosons, leptons, and fermions or quarks. These theoretical developments gave rise to, and were inspired by, scattering experiments built to test this framework. The first cyclotron, which accelerated charged particles in a tight spiraling path with a magnetic field, was developed in 1931 [4], and the parallel drivers of technological development and theoretical refinement have carried these basic techniques forward to the Large Hadron Collider [5] (LHC). Like many of its predecessors in their time, this machine is able to probe these theories at previously inaccessible and unprecedented energies and provides greater statistical precision for many of these measurements. This allow us to measure aspects of the current best theory of how

[1] The historical development of quantum mechanics is described in many books, articles, and other formats. Two references known to the author are provided for those interested; the first is accessible to a general audience, the second is intended for experts.

Table I.1: The fundamental constituents of matter contained in the Standard Model. Quarks are highlighted in red, leptons in green, vector bosons in blue, and the scalar boson in yellow. Spins and electromagnetic charges are denominated, and whether the field participates in strong (QCD) or electroweak (GWS) interactions is noted.

Fields	Spin	Charge	QCD?	GWS?
"Down"-type Quarks, d, s, b	1/2	-1/3	yes	yes
"Up"-type Quarks, u, c, t	1/2	+2/3	yes	yes
Charged Leptons, e, μ, τ	1/2	-1	no	yes
Neutrinos, ν_e, ν_μ, ν_τ	1/2	0	no	yes
Gluon, g	1	0	yes	no
Photon, γ	1	0	no	yes
Charged Weak Bosons, W	1	± 1	no	yes
Neutral Weak Boson, Z	1	0	no	yes
Higgs Boson, H	0	0	no	yes

the fundamental constituents of matter interact beyond previous limitations, in the hope of building on or reshaping this theory by discovering new and unexplained phenomena.

1. Paths to Discovery in Particle Physics

The Standard Model (SM) of particle physics is a quantum field theory containing interactions mediated by the strong nuclear force, called quantum chromodynamics (QCD), and a combined theory of the electromagnetic force and the weak nuclear force, called Glashow-Weinberg-Salam (GWS) electroweak theory. This framework describes interactions between a set of matter fields and a set of force-carrying fields which interact with each other (and

in the case of some bosonic fields, with themselves). These fields have associated particles, which are energy-dependent resonances localized to a point in space and time. Predictions of measurable properties of these particles extracted from the SM are limited in scope, as it does not provide a mechanism for exact calculations of such properties. Instead, it generates terms in a series expansion which at higher orders become relevant as energy increases, so calculations of observables depend on which terms are included in this series. As the order of the calculation is connected to the interaction energy at which it is a good approximation, the calculations can be limited to the terms necessary to attain enough precision for comparison with experiments. The SM has been very successful at predicting the outcomes of such experiments in the 50 years since its development, with few exceptions [6].

The SM describes the interactions between *fermions*, representing matter fields and their antimatter counterparts, mediated by *gauge bosons*, which carry the strong, electromangetic, and weak interactions. Fermions carry half-integer values of intrinsic angular momentum, or spin, while bosons carry integer values. The matter fields are *charged* under each interaction, where the charge determines the strength of that field's interaction with the gauge bosons. Fermions are further divided into leptons, which are only charged under the GWS interaction, and quarks, which are charged under both the GWS and strong interactions. Each configuration of charges and spins occurs in three fields of different mass, known as *generations*. The Higgs boson is unique, in that its interaction with the bosons $W^{\pm}$ and Z^0, as well as with the quarks and charged leptons, generates the mass of these fields. Table I.1 gives the spins and charges of these fundamental SM components. The LHC is able to study energies never previously observed in a collider experiment, and so a significant focus is placed on phenomena which are only observable at this or higher energy, often through other SM fields with large mass. The top (t) quark has the largest mass of any constituent; it is more than 100 times the mass of the proton, and more than 30 times the mass of the next heaviest fermion, the bottom quark (b). This makes it a natural choice for searching for new physics phenomena.

Evidence has been building, from areas of study outside particle physics, for the existence of physics phenomena not included in the SM. The tension is strongest with astrophysical measurements. Though they generally support the SM, they suggest that it must be extended

to include some unobserved particles, dubbed *dark matter*, which interact with other SM fields very rarely. Also notable is the SM's lack of a connection to the gravitational force; attempts to reconcile general relativity with the quantum field-theoretical framework of the SM results in a theory which does not make physical predictions in its simplest form, while more complex frameworks predict a variety of new particles. The SM itself is not guaranteed to be a reasonable approximation outside a well-tested range of energies, suggesting that there may be a more fundamental theory. These and other questions have inspired a continuous search for evidence of some deviation from SM predictions.

The ATLAS (A Toroidal LHC ApparatuS) experiment was designed with discovery of new physical phenomena in mind, as a general-purpose detector for measuring the results of energetic collisions produced in its center by crossing the paths of two circular beams of high energy protons accelerated by the LHC. By storing the location and timing information of activity in the detector after a collision, and using knowledge of the properties of the protons before the collision, properties like the momentum, direction, mass, and charge of a particle can be reconstructed. Quantities which can be measured from this reconstruction, like the amount of different species of particle, their energies and directions, what they decay into and the properties of the decay products, can all be compared to their SM predictions. New phenomena can be observed this way when they interact with known fields directly, or when they interfere with an interaction expected under the SM and change its behavior enough to deviate from the prediction.

2. Common Collider Observables

Observables measured by particle collider experiments are often dependent on counting the number of events measured with specific final-state properties. Two such quantities common in measurements involving particle X are its *production cross-section* σ_X, which describes how often it is produced in particle collisions (proton-proton collisions at the LHC), and its *decay rate* $\Gamma(X \to Y_1 \dots Y_n)$, quantifying how long particle X is expected to exist before decaying, and how likely that decay is to produce the particles $Y_1 \dots Y_n$. Particle collider experiments are designed so that, with the information known about the initial state, col-

lision events can be selected which are likely to contain particle X, or which contain all of the particles $Y_1 \dots Y_n$. By counting these and related events, these two quantities can be measured and more detailed properties of the processes can be studied.

The ATLAS and CMS (Compact Muon Solenoid) detectors are each situated on the beamline of the LHC, such that the two circular beams of protons can be crossed very close to the center of the detectors. Each crossing can initiate the interaction between two or more protons in the beam. The amount of data which could be collected corresponds to the typical frequency of such an interaction, described by the *luminosity* $\mathcal{L}$, integrated over the length of time that the beams were crossed to get the *integrated luminosity*, $\mathcal{L}_{\text{int}}$. The units of integrated luminosity are the total number of interactions in a 2-dimensional cross-section of the beam, often expressed as cm^{-2}. This quantity is closely related to production cross-sections, which are defined as the amount of the beam area in which simultaneous interactions would result in the production of some particle. In our example, the production cross-section of particle X is the fraction of all collisions in which particle X was produced, distributed over the beam cross-section, with units of cm^2. Thus the product of these two quantities give the total number of interactions in which an X particle was produced,

$$\mathcal{L}_{\text{int}}\sigma_X = \frac{N_{\text{total}}}{\sigma_{\text{total}}} \cdot \frac{N_X}{N_{\text{total}}} \cdot \sigma_{\text{total}} = N_X. \tag{I.1}$$

Most particles in the Standard Model, both elementary and composite, have a finite lifetime τ_X which can be described probabilistically. For a dataset of events in which particle X is produced, the probability per unit time that X will decay, or *decay rate*, $\Gamma_X \sim \frac{1}{\tau_X}$, can be measured, based on how far from the interaction point the particle traveled before decaying and how much energy it had. If the particle can decay into more than one final state, the relative probabilities of these decay channels, called the *branching ratios*, $BR(X \to Y_1 \dots Y_n)$, provide the fraction of the total number of X particles produced which can be identified by each final state. Particles with long lifetimes may decay outside the radius r of the sensitive regions of the detector, and thus cannot be identified by their decay products. However, for massive particles decaying close to the interaction vertex, only branching ratios are needed to identify a set of events containing X particles, and the decay rate and its properties can be measured from these events. To identify a particular initial state from an events containing

particles $Y_1 \dots Y_n$, selection criteria are designed to choose this initial state more frequently than background events. This results in a sample with a higher signal-to-background ratio, sometimes called *purity*, but with only a fraction of the total number of signal events, called the *selection efficiency*, ϵ. Together, the branching ratio and selection efficiency describe how many signal events are identified from the full dataset of events containing particle X,

$$\epsilon N_X \cdot BR(X \to Y_1 \dots Y_n) = \frac{N_X^{\text{sel}}}{N_X^{(Y_1 \dots Y_n)}} \cdot \frac{\Gamma_{X \to Y_1 \dots Y_n}}{\Gamma_X} \cdot N_X \overset{\tau_X \ll cr}{=} N_X^{\text{sel}}. \tag{I.2}$$

These considerations are used to define a dataset, selected to emphasize events containing particle X and decaying to $Y_1 \dots Y_n$, in terms of measurable quantities σ_X, $BR(X \to Y_1 \dots Y_n)$, and $\mathcal{L}_{\text{int}}$, and the number of signal and background events in the sample. Combining the production and decay channels describing the full process,

$$BR(X \to Y_1 \dots Y_n)\sigma_X = \frac{N_X^{\text{sel}} - N_{\text{bkg}}^{\text{sel}}}{\epsilon \mathcal{L}_{\text{int}}}. \tag{I.3}$$

Measurements of this quantity can be compared to the number of X particles produced which decay into $Y_1 \dots Y_n$ in the SM. In cases where the position of the production and decay can be resolved, the total and individual decay rates Γ_X and $\Gamma_{X \to Y_1 \dots Y_n}$ can be measured. For the high-mass particles discussed in the two analyses considered here, the particle lifetimes are very short and thus difficult to resolve, meaning that other experiments will make better predictions of the decay rates. However, normalized differential cross-sections and decay rates can be measured to describe the dependence of these quantities on the kinematics of the event.

3. Units and Conventions

To simplify calculations of these and other quantities, *natural units* are used, defined as $\hbar = c = 1$. This results in powers of units of energy replacing units of momentum, position, time, and derivative quantities. Standard versions of these units can be recovered by inserting combinations of $\hbar$ and c designed, through dimensional analysis, to produce the original units of the quantity. The energy units commonly used are called *electron-volts*, or eV, which is the amount of energy required to move an electron across a potential of one volt. To keep

most measured quantities within a few orders of magnitude of 1, energy units of MeV or GeV are chosen. Besides the standard units of $\text{cm}^{\pm 2}$, integrated luminosities and cross-sections are also measured in *barns*, defined as 1 barn = 10^{-24}cm^2. This unit was originally chosen in reference to atomic-scale experiments, and so is large compared to the scale of the quantities being measured at the LHC; cross-sections are commonly expressed in picobarns, 1 pb = 10^{-36} cm^2, and integrated luminosity in inverse femtobarns, 1 $\text{fb}^{-1} = 10^{39}\text{cm}^{-}2$.

The cylindrical shape of the ATLAS detector and the known properties of the initial state of collision events suggest a set of conventions for measuring particle momenta and positions. A cylindrical coordinate system is used with the z axis defined along the beamline. Less information about the momentum balance between the partons taking part in the interaction along the z-axis can be attained than in the perpendicular direction. Thus, rather than measuring the z component of momenta directly, the polar angle is measured in a form called the *pseudorapidity*,

$$\eta = -\ln\left(\tan\frac{\theta}{2}\right) = \frac{1}{2}\ln\left(\frac{|\vec{p}| + p_z}{|\vec{p}| - p_z}\right). \tag{I.4}$$

This quantity is useful in the limit $|p| \gg m$, where it approximates the Lorentz boost-invariant quantity *rapidity* y, given by

$$y = -\frac{1}{2}\left(\frac{E - p_Z}{E + p_Z}\right). \tag{I.5}$$

The interaction is generally agnostic about the azimuthal angles, ϕ, of the outgoing particles, and an angular distance measure is often defined using these two coordinates as $\Delta R = \sqrt{(\Delta\phi)^2 + (\Delta\eta)^2}$. However, the particle's momentum perpendicular to the beamline, called the *transverse momentum*, p_T, is approximately conserved for all particles measured in the event.

Measurements performed with the ATLAS detector are based on objects reconstructed from recorded activity in the detector. What is called a particle, measured in the detector, is the reconstruction of a path of energy deposition in isolated angular regions of the detector, following a radial trajectory with some curvature. Some particles, like muons μ, can be reconstructed with good resolution on their path, energy, and curvature. Muons can be identified from their intrinsic properties (mass and charge), and their energy and momentum

are well-measured. Many hadronic particles produced in the primary interaction produce a cascade of other particles, and little about them can be resolved in isolation. Understanding the properties of these particles requires the information from this cascade to be combined into an object called a *jet*, from which the energy and momentum of the initiating particle can be estimated and some intrinsic properties are accessible. Other objects, like neutrinos ν, may simply deposit no energy in the detector; this results in an imbalance in the sum of all transverse momenta in the event, and the *missing transverse momentum* vector is defined, with magnitude $E_{\mathrm{T}}^{\mathrm{miss}}$, to restore conservation of momentum to the event.

4. Organization

Chapter I has introduced the motivation behind studying the results of hadron collisions, and some of the basic properties which are measured. A brief description of the SM and its structure is given in Chapter II, along with discussions of specific processes related to the analysis presented in Chapter VI and how it will test SM properties. The data used to study these processes, produced by the LHC and recorded by the ATLAS detector, warrants some description of how these machines operate, given in Chapter III. The signals generated in the detector must then be processed via a number of specialized electronic components and algorithms to match them with physical particles or phenomena, called *reconstruction*. The reconstruction process for the objects of most interest to the analyses presented here are described in some detail in Chapter IV. One specific reconstruction task, b-jet tagging, involves the identification of b quarks (see Table I.1), and requires complex algorithms to determine probabilities for identification. Chapter V describes the algorithms used in ATLAS, and describes analysis which calibrates the results of these algorithms to ensure they perform similarly for simulated events and real data. Chapter VI describes an analysis of the decay of t quarks, testing the accuracy of its description in the SM. This analysis measures or constrains parameters which are not present in the SM, and can either constrain the possible forms of new physics phenomena or indicate how they might affect this SM process. In Chapter VII, a summary of the work presented in this thesis is offered, along with the prospects for future work with some of the techniques and processes discussed here.

II. PHENOMENOLOGY AT THE LARGE HADRON COLLIDER

The SM has been extraordinarily successful in describing the aftermath of high-energy collisions measured by the ATLAS experiment. The phenomenological descriptions it supplies for the interactions of two protons with $\sqrt{s} = 7$ TeV are sufficient to explain most measurements performed with this data. Additional parameterized information is measured in a regime in which the SM is not useful for predictive calculations, such as the initial state of the protons in the LHC beam. The production of the heavy bottom and top quarks from these collisions require both of the primary aspects of the SM theory: quantum chromodynamics, or QCD, and the Glashow-Weinberg-Salam electroweak theory. QCD describes the interactions of quarks and gluons, such as in the initial proton-proton collisions and the production of quarks and related particles in the aftermath of these collisions. Bottom quarks produced in QCD-driven interactions can be used to calibrate algorithms which identify them by the properties of their decay. GWS electroweak theory is a fusion of quantum electrodynamics, or QED, with the theory of weak interactions, and describes interactions among quarks, leptons, and the vector bosons $W^{\pm}$, Z^0, and γ. The Higgs boson h couples to this theory and, through the *spontaneous symmetry breaking* mechanism, gives mass to the vector bosons $W^{\pm}$ and Z^0, as well as all the massive fermions[1] like the top quark. Though top quarks can be produced in $t\bar{t}$ pairs via QCD, they can also be produced singly via the fusion of a W boson and a bottom quark. This production channel is the basis for a study of the coupling between the top and bottom quarks and the W boson.

[1] In the SM, the massive fermions includes all six quarks and the e, μ, and τ leptons. Neutrino masses, which are not included in the SM, may or may not be generated through this mechanism.

1. The Standard Model

The SM is a quantum field theory describing the interactions between all of the known fundamental fields and particles in Table I.1. It is often stated through an expression called the *Lagrangian density*, $\mathcal{L}(x)$, the difference between the kinetic and potential energy densities of a field at each point in spacetime x, which will be referred to as simply the Lagrangian. Its integral, the *action* $\mathcal{S}$, encapsulate all the dynamical information of the particles in the theory in their corresponding field values, $\phi_i(x)$, and their spacetime derivatives, $\partial\phi_i(x)$:

$$\mathcal{S}[\phi_i] = \int \mathcal{L}\left(\phi_i(x), \partial\phi_i(x), x\right) \; d^4x. \tag{II.1}$$

The action is defined for any configurations of the fields in the Lagrangian; for a stationary configuration, where the functional derivatives of S with respect to the fields ϕ_i are 0, the equations of motion for the fields are defined by the *Euler-Lagrange equations*, the equations of motion for fields ϕ_i,

$$\frac{\partial\mathcal{S}}{\partial\phi_i} = 0 \quad \Rightarrow \quad \frac{\partial\mathcal{L}}{\partial\phi_i} - \partial_\mu \frac{\partial\mathcal{L}}{\partial(\partial_\mu\phi_i)} = 0. \tag{II.2}$$

The internal *gauge symmetry* $\mathrm{SU(3)} \otimes (\mathrm{SU(2)_L} \otimes \mathrm{U(1)}_Y)$ describes the nature of the interactions between these fields. These symmetries are manifested by bosonic fields, called *gauge bosons*, which interact with fermionic fields representing quarks and leptons, given by ψ in the following. Each symmetry group is related to a list of properties governing an associated interaction, producing degrees of freedom in the Lagrangian which can be chosen or altered without affecting the equations of motion. Each symmetry's *charge* is assigned to fields, with relevant sign and magnitude, indicating which interactions they are involved in. In addition to these internal symmetries, the Lagrangian has a global *Poincaré symmetry*, meaning that its equations of motion are not affected by translations in space and time or *Lorentz transformations*, which include rotations and changes in the inertial reference frame of the system (also called *boosts*). The SM is then the most general definable Lagrangian containing these fields and their given properties.

a. The Dirac Equation The mathematical structures used to define the Lagrangian are determined by an internal property of the fields it contains called *spin*. This property acts as angular momentum in the rest frame of the particle, and thus contributes to its energy and interactions. A *fermion* has half-integer spin $\frac{n}{2}$, meaning it can take on possible values of $\pm\frac{1}{2}\times[1,\ldots,n]$; a *boson* has integer spin, with possible values of $\pm[0,\ldots,n]$. All fundamental SM fermions are spin $\frac{1}{2}$, and all gauge bosons are spin 1; the Higgs particle is a scalar, with spin 0.

Fermions which are not interacting with any other field have a Lagrangian defined by a kinetic term, describing the motion of the field, and a potential term, here just the particle's mass; this results in the *Dirac Lagrangian*,

$$\mathcal{L}_{\text{kin},\psi} = \overline{\psi}(i\partial\!\!\!/ - m)\psi = \overline{\psi}(i\gamma^\mu\partial_\mu - m)\psi \tag{II.3}$$

In this expression, the fermion fields are represented as a plane wave and a *Dirac spinor*, a four-component object describing the energy, momentum, and spin of particle and antiparticle states. The γ^μ are four 4×4 matrices called the *Dirac gamma matrices*, a representation of objects defined by the anticommutator

$$\{\gamma^\mu,\gamma^\nu\} = \gamma^\mu\gamma^\nu + \gamma^\nu\gamma^\mu = 2\eta^{\mu\nu}, \tag{II.4}$$

where $\eta^{\mu\nu}$, a diagonal matrix with signature $\eta = \text{diag}(1,-1,-1,-1)$, is the *metric* on Minkowski space. This equation is the only necessary property defining the γ^μ objects, so a variety of representations of this property can be defined. A useful matrix representation is defined by the basis matrices in Equation II.5, called the *Weyl basis*:

$$\gamma^0 = \begin{pmatrix} 0 & \mathbb{1} \\ \mathbb{1} & 0 \end{pmatrix}, \quad \vec{\gamma} = \begin{pmatrix} 0 & \vec{\tau} \\ -\vec{\tau} & 0 \end{pmatrix}, \quad \gamma^5 = i\gamma^0\gamma^1\gamma^2\gamma^3 = \begin{pmatrix} -\mathbb{1} & 0 \\ 0 & \mathbb{1} \end{pmatrix}. \tag{II.5}$$

These matrices are further defined in terms of the 2×2 identity matrix $\mathbb{1}$ and the three *Pauli matrices*, τ^i:

$$\mathbb{1} = \begin{pmatrix} 1 & 0 \\ 0 & 1 \end{pmatrix}, \quad \tau^1 = \begin{pmatrix} 0 & 1 \\ 1 & 0 \end{pmatrix}, \quad \tau^2 = \begin{pmatrix} 0 & -i \\ i & 0 \end{pmatrix}, \quad \tau^3 = \begin{pmatrix} 1 & 0 \\ 0 & -1 \end{pmatrix}. \tag{II.6}$$

The Dirac gamma matrices act as basis vectors in *Minkowski space*, a representation of both space and time coordinates on which the Poincaré transformations are defined. The quantities $\gamma^\mu a_\mu = \not{a}$ act like a vector under these transformations, so a product of the form $\overline{\psi}\not{a}\psi$ connects the properties of the particle to these types of transformations. The matrix γ^5 is also given, which is a combination of the other gamma matrices useful in describing certain types of interactions.

Using the Euler-Lagrange equations in Equation II.2 with the field $\overline{\psi}$, we find that the dirac spinors must satisfy the equation

$$(i\not{\partial} - m)\psi = 0. \tag{II.7}$$

The equivalent adjoint equation can be obtained by applying the equations using the field ψ. In the Weyl basis, this equation gives solutions representing a plane wave and a dirac spinor for both particles, $\psi = u(p)e^{-ip^\mu x_\mu}$, and antiparticles, $\psi = v(p)e^{-ip^\mu x_\mu}$. There is considerable freedom in choosing the structure of u and v; a specific case will be given in Section II..4.

b. Interactions The kinetic and mass terms given for free fermion fields in Equation II.3 do not include any strong, weak, or electromagnetic interactions. They arise when requiring that the Lagrangian be symmetric under certain transformations of its fields which are allowed to vary with x, called *local gauge symmetries*. These transformations do not necessarily preserve the form of the Lagrangian, particularly inside the differential. Therefore, to restore symmetry under local transformations requires the addition of new fields to the Lagrangian, defined by their transformation properties. This results in the gauge-covariant derivative D_μ,

$$\partial_\mu \Rightarrow D_\mu = \partial_\mu - ig\not{A}^a t^a. \tag{II.8}$$

These additional fields are the gauge bosons, A^a_μ, which each correspond one of the *generators* of the symmetry groups t^a introduced in Section II..1. The generators of a group are the set of basic group elements which define its behavior through the generic commutation relation

$$\left[t^a, t^b\right] = if^{abc}t^c, \tag{II.9}$$

where the constants f^{abc} are structure constants unique to the particular group. The t^a form the basis for the configuration of the A^a_μ fields, so that $A_\mu = A^a_\mu t^a$.

Interactions between fermionic fields and the gauge bosons are generated directly in the resulting Lagrangian,

$$\begin{aligned}\mathcal{L}_{\text{kin},\psi,\text{A}} &= \overline{\psi}\left(i\not{D} - m\right)\psi \\ &= \overline{\psi}\left(i\not{\partial} + g\not{A}^a t^a - m\right)\psi.\end{aligned} \tag{II.10}$$

The dynamics of the ψ field are now defined to include its original kinetic term, the potential arising from its mass, and the potential imparted by interactions with the gauge fields A^a. The gauge fields have some kinetic energy, which arises in the commutator of the gauge-covariant derivative,

$$[D_\mu, D_\nu] = -igt^a\left(\partial_\mu A^a_\nu - \partial_\nu A^a_\mu + gf^{abc}A^b_\mu A^c_\mu\right) \equiv -igt^a\mathcal{A}^a_{\mu\nu}. \tag{II.11}$$

The quantity $\mathcal{A}^a_{\mu\nu}$ is called the *field strength tensor*, and the sum over the inner products of its components defines the boson's kinetic term,

$$\mathcal{L}_{\text{kin,A}} = -\frac{1}{2}\,\text{Tr}\sum_a \mathcal{A}^a_{\mu\nu}\mathcal{A}^{\mu\nu}_a. \tag{II.12}$$

The mass terms $-m\overline{\psi}\psi$ are not necessarily gauge covariant by construction. A fermion mass term can be expressed as a coupling between the left- and right-handed components of the field,

$$\mathcal{L}_{\text{mass}} = -m(\overline{\psi}_L\psi_R + \overline{\psi}_R\psi_L), \tag{II.13}$$

and the ψ_L and ψ_R components do not need to be be defined to transform identically. However, if this term arises from a *Yukawa coupling* between ψ and the Higgs field h which is spontaneously broken, then the gauge covariance of the unbroken term will be preserved. Besides generating these masses, the Higgs also breaks the electroweak symmetry by generating masses for the $W^\pm$ and Z^0 bosons. These mechanisms are both explained in Section II..3.

c. Making Predictions Combining the above descriptions, the Lagrangians for each component of the SM can be written in the general form

$$\mathcal{L} = \overline{\psi}\left(i\not{D} - m\right)\psi - \frac{1}{2}\,\mathrm{Tr}\,\mathcal{A}^{a}_{\mu\nu}\mathcal{A}^{\mu\nu}_{a}, \tag{II.14}$$

where the fermion fields ψ with masses m are any fermions which interact with the boson field $\mathcal{A}$ and the gauge-covariant derivative and field strength tensor terms are defined as above. The full SM Lagrangian $\mathcal{L}_{SM}$ is constructed by extending D to include all gauge bosons which interact with each fermion and adding a self-interaction term for each gauge boson, and adding terms related to the Higgs field.

The SM is often interpreted in the context of *perturbation theory*, in which the interacting and non-interacting, or free field, components of the above equations are decoupled, and the interaction is treated as a perturbation of the free field. *Feynman diagrams* are often used to visualize the types of perturbative interactions allowed with lines describing propagating particles which meet in vertices describing interactions. The leading-order (LO) terms in the series are the simplest description of a measurable process, and exact calculations of observable properties can often be performed. However, next-to-leading-order (NLO) and higher-order corrections cause these quantities to diverge. This was solved by a technique called *renormalization*, which sets a characteristic energy scale at which measurable parameters of the theory are separated from the divergent regions in the integral, and these divergent quantities are canceled by the introduction of counterterms.

Not all quantum field theories can be renormalized; for example, introducing higher-dimensional effective operators [7] to the SM can render the resulting theory nonrenormalizable above some characteristic energy scale Λ. Also, not all divergences in the SM are eliminated by renormalization, particularly in unphysical low-energy regions of parameter space. Finally, perturbative descriptions are valid at high energies, where an interaction can be treated in isolation; low-energy interactions and bound state behavior must be modeled with other methods. These two caveats apply to particular cases arising in QCD which are important for calculating predictions for processes measured by the LHC: modeling the beam's protons in their initial state [8, 9, 10] and the behavior of quarks produced in the in the primary collision in the event, or the *hard interaction* [11, 12].

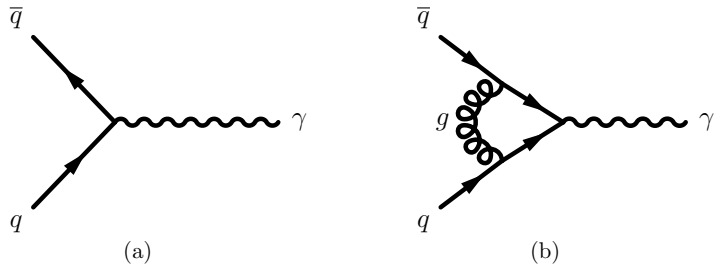

Figure II.1: Feynman diagrams describing quark-antiquark annihiliation into a photon. (a) At leading order, this proceeds via a single quark-photon coupling. (b) At next-to-leading order, the same final state can arise from multiple extra interactions; one example of a contributing loop diagram containing a gluon is given.

2. Quantum Chromodynamics

The theory of strong interactions affecting quarks and gluons is governed by the SU(3) symmetry. In Equation II.14, the fermion fields ψ can be identified with the quarks u, d, c, s, t, b, the field A^a_μ is the gluon field, and the generators $t^a = \frac{1}{2}\lambda^a$ are chosen to satisfy the expression Equation II.9 with the structure constants f^{abc} defined for this group. The λ^a are called the *Gell-Mann matrices*; they are a particular 3×3 representation of these generators commonly used in QCD.

The three quark charges indicated by the dimensions of λ^a are called *colors*, denoted red, green, and blue, while antiquark charges are called anti-red, anti-green, and anti-blue. Gluons, which mediate interactions between quarks and/or antiquarks, carry a superposition of color and anti-color, allowing them to self-interact. The form of the gluon's self-interaction prevents the strength of the interaction of two color-charged particles from diminishing with distance, resulting in the observation that color-charged particles are never observed alone; this is known as *color confinement*. The potential between two strongly-interacting particles increases as the distance between the particles increases. At lower energies this binds them into particles called *hadrons*, either as quark-antiquark pairs called *mesons* or three-quark particles called *baryons*. At higher energies, the increase in potential makes the conversion

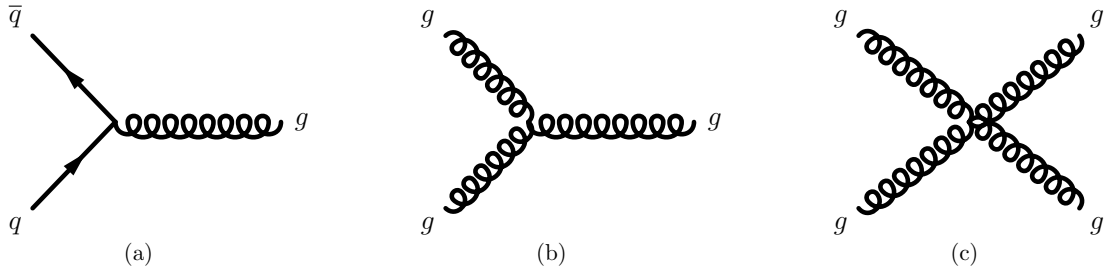

Figure II.2: Interactions allowed in QCD include (a) quark-gluon vertices, (b) three-gluon vertices, and (c) four-gluon vertices.

of this energy into many quark-antiquark pairs likely, a process called *fragmentation*. When groups of 2 or 3 particles produced in the fragmentation process particles have lost enough energy that they are no longer producing new $q\bar{q}$ pairs, they combine into bound states, a process called *hadronization*. Bound states at low energies are very difficult to describe perturbatively, as no free field component can be defined to isolate their interactions. At a hadron collider like the LHC, statistical models are developed to represent the initial states of these bound states, here two protons, called *parton distribution functions*, or PDFs [8, 9, 10]. The hard interaction between protons is modeled as PDF sets $f_{i/p}(x, Q^2)$, representing the probability that parton i, which can be any quark flavor or a gluon, can be found with fraction x of the total proton momentum at an overall energy scale Q^2. The data used to create these models is from deep inelastic scattering experiments such as HERA [13], in which a high-energy electron scatters off of constituents of the proton. From data taken at one energy scale, the behavior of the PDF at any other energy scale can then be predicted [14, 15, 16].

The production cross-section for a particular particle, as described in Section I..2, relies on both the properties of the proton beams and the initial states of the colliding protons described by PDFs. For hadron colliders, the PDF for each proton and the partonic cross sections $\hat{\sigma}_{i,j}$ for the production of the final state of interest are required [17],

$$\sigma(pp \to X + \cdots) = \sum_{i,j} \int_{x_{p_1}}^{1} dx_{p_1} \int_{x_{p_2}}^{1} dx_{p_2} f_{i/p_1}(\xi_{p_1}, \mu_F) \hat{\sigma}_{i,j}(pp \to X + \cdots) f_{j/p_2}(\xi_{p_1}, \mu_F), \quad \text{(II.15)}$$

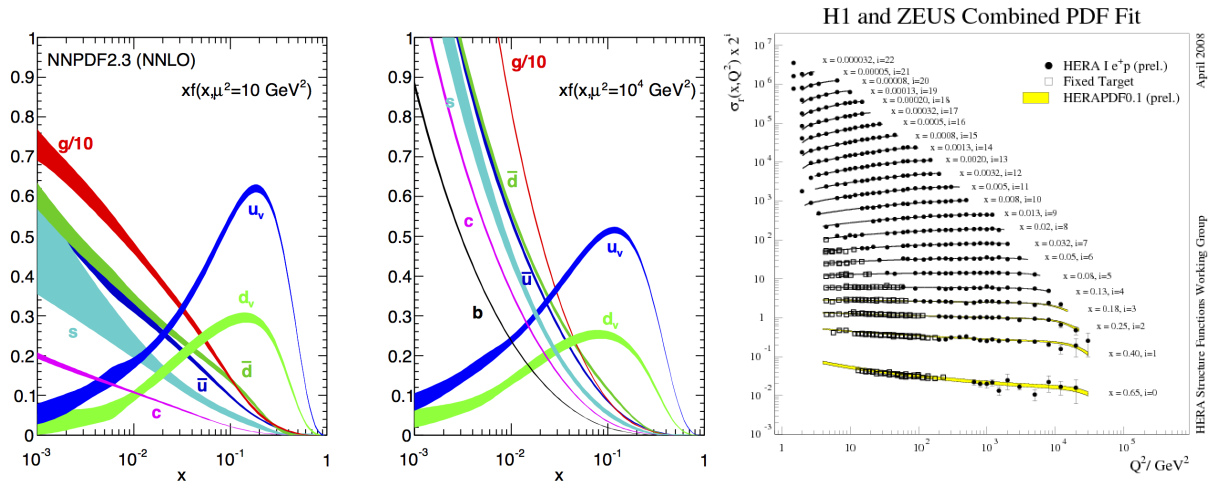

(a) (b)

Figure II.3: Parton distribution functions, (a) provided by the NNPDF collaboration [10], and (b) from fits to recent data collected by the H1 and ZEUS experiments [13]

where the sum is over the relevant parton species, and the integral is over the momentum fractions allowed by the energy requirements of the final state.

When the initial states described by PDFs collide, the large energy density of the hard interaction means that the theory can be described perturbatively, a property known as *asymptotic freedom*. In the final state of this interaction, the non-perturbative processes of fragmentation and hadronization turn the bare quarks back into hadronic bound states. A variety of models and techniques [12] exist for these processes, which for simulations of LHC data are done by dedicated algorithms [18, 19].

3. Electroweak theory

Electroweak theory began as a fusion of quantum electrodynamics, or QED, and the theory of the weak force. This fusion, with the introduction of electroweak symmetry breaking via the Higgs mechanism, produces the two interactions seen in nature: electromagnetics, mediated by the photon γ, and the weak interaction, mediated by the charged, $W^{\pm}$, and

neutral, Z^0, gauge bosons. The general theory will first be presented, then the mechanism for and result of this symmetry breaking will be shown.

a. The unbroken symmetry and the Higgs mechanism The $\mathrm{SU(2)_L} \otimes \mathrm{U(1)_Y}$ symmetries in the unbroken electroweak theory are described by gauge fields denoted W^a_μ, $a = [1, 2, 3]$, which carry *weak isospin* charge under $\mathrm{SU(2)_L}$ with generators $t^a = \frac{\tau^a}{2}$ where $\vec{\tau}$ are the 2×2 pauli matrices (Equation II.6), and B_μ, which carries *weak hypercharge* Y_W under $\mathrm{U(1)_Y}$, where the generator is a phase, $t = \frac{Y_W e^{i\phi}}{2}$. All quarks and leptons participate fully in the B_μ interactions; however, the W^a_μ fields only interact with their left-handed components. This is represented by the *projection* of the Dirac spinor of a particle into its left- or right-handed components via the projection operators,

$$P_{\mathrm{L,R}}\psi = \frac{1}{2}\left(1 \mp \gamma^5\right)\psi = \psi_{L,R}.$$

These fields mix the *flavors* of the left-handed particles, a property represented by grouping the quarks and leptons into doublets,

$$Q^i_L = \begin{pmatrix} u^i_L \\ d^{i\prime}_L \end{pmatrix} \quad \text{and} \quad L^i_L = \begin{pmatrix} \nu^i_\ell \\ \ell^i \end{pmatrix}$$

for three generations i. Though these suggest that the W^a_μ fields only mix between the two particles in each double, the quark sector contains additional mixing which arises between generations. It is parameterized by the experimentally-determined Cabbibo-Kobayashi-Maskawa (CKM) mixing matrix [20], with elements V_{ij} which relate each up-type quark i to the fraction of each down-type quark j present in its associated d' weak eigenstate,

$$d' = V_{ud}d + V_{us}s + V_{ub}b,$$

and similarly for the other two generations s' and b'. The right-handed states are not grouped into doublets, as they don't interact with the W^a_μ fields, and in the lepton sector, the right-handed neutrino is left out of the SM[2]. These two groups lead to a construction like in

[2] Evidence that neutrinos have mass [6] suggests, via Equation II.13 that some extension of the SM is needed to include a right-handed component. A common implementation of neutrino masses includes right-handed neutrinos through the *seesaw mechanism*, see Ref. [21].

Equation II.14 for two fields in the gauge-covariant derivative and two boson self-interaction terms, with the modifications mentioned:

$$\begin{aligned}\mathcal{L} = \overline{\psi}\gamma^{\mu}\left(i\partial_{\mu} + \frac{g_W}{2}W_{\mu}^{a}\tau^{a}V_{\mathrm{CKM}}P_L + \frac{g_B}{2}B_{\mu}Y_W - m\right)\psi \\ - \frac{1}{4}\mathcal{W}_{\mu\nu}\mathcal{W}^{\mu\nu} - \frac{1}{4}\mathcal{B}_{\mu\nu}\mathcal{B}^{\mu\nu}\end{aligned} \tag{II.16}$$

So far, no mass terms related to the gauge fields W_{μ}^{a} and B_{μ} have been introduced, but we know that these terms must exist to explain the short-range nautre of the interaction. The field ϕ, a doublet of complex scalar fields, was proposed to explain how these masses arise through a mechanism called *spontaneous symmetry breaking*. ϕ has the added ability to generate mass terms for the fermion fields ψ through a coupling to the left- and right-handed components of each field. The doublet $\phi = \binom{\phi^{+}}{\phi^{0}}$ has weak isospin and hypercharge, so the gauge covariant kinetic and self-interaction terms added are

$$\mathcal{L}_{kin,\phi} = (D_{\alpha}\phi)^{\dagger}(D^{\alpha}\phi) - \mu^2\phi^{\dagger}\phi - \lambda(\phi^{\dagger}\phi)^2. \tag{II.17}$$

The gauge-covariant derivative is $D_{\alpha} = \partial_{\alpha} - ig_W W_{\alpha}^{a}\frac{\tau^{a}}{2} - ig_B B_{\alpha}\frac{Y_W}{2}$, and the self-energy of the field contains a mass term μ^2 and a self-coupling term λ. The values of these parameters determine the behavior of this field; to break electroweak symmetry, the region $\mu^2 < 0$ and $\lambda > 0$ is chosen, inducing a local maximum at $|\phi^{+}|^2 + |\phi^{0}|^0 = 0$ and local minima at $|\phi^{+}|^2 + |\phi^{0}|^2 = \sqrt{-\mu^2/\lambda}$. Near the minimum, the four complex degrees of freedom are approximated by a single real one, which can be arbitrarily assigned. This is another expression of the SU(2) gauge symmetry of the Higgs doublet. As this doublet must be electrically charge-neutral after symmetry breaking, the gauge is chosen so that $v \equiv \mathrm{Re}[\phi^{0}] = \sqrt{-\mu^2/\lambda}$ is the *vacuum expectation value* of ϕ, so called because it is the minimum possible value of the field's self-energy. Small perturbations around this value produce the Higgs field h introduced in the SM,

$$\phi = \frac{1}{\sqrt{2}}\begin{pmatrix}0\\ v + h(x)\end{pmatrix}. \tag{II.18}$$

The non-zero vacuum expectation value is responsible for mass generation, and interactions mediated by h arise for massive particles.

b. Electroweak interactions in the SM Electroweak symmetry breaking happens when ϕ takes on the form in Equation II.18, which results in Equation II.17 producing mass terms and interactions with the Higgs field. In the kinetic term, this mechanism generates mass terms for the flavor-changing and flavor-conserving interactions, represented by mixtures of the W^a_μ and B_μ fields into the $W^\pm$ and Z^0 bosons with masses m_W and m_Z, and masslesss photon field A_μ,

$$W^\pm_\mu = \frac{1}{\sqrt{2}}\left(W^1_\mu \pm iW^2_\mu\right), \tag{II.19}$$

$$Z^0_\mu = -\sin\theta_W B_\mu + \cos\theta_W W^3_\mu, \text{ and} \tag{II.20}$$

$$A_\mu = \cos\theta_W B_\mu + \sin\theta_W W^3_\mu. \tag{II.21}$$

Masses arise through terms containing $(v + h(x))^2$; the v^2 generates a mass term, and the $2vh(x)$ and $h(x)^2$ generate couplings to the Higgs field. These masses and couplings are related through the *weak mixing angle* θ_W to the ratios of the couplings g_B and g_W,

$$\theta_W = \tan^{-1}\frac{g_B}{g_W} = \cos^{-1}\frac{m_W}{m_Z} \tag{II.22}$$

When the redefinition of the boson fields is propagated to the interaction terms, the electromagnetic interactions through the field A_μ appear with a massless photon γ and coupling e, which is now related to the weak mixing angle and the couplings as

$$e = g_W \sin\theta_W = g_B \cos\theta_W,$$

leaving an unbroken U(1) symmetry with the traditional electromagnetic charge. The remaining potential terms generate a mass for the Higgs boson and describe its self-coupling.

As mentioned, the Yukawa coupling between left- and right-handed components of the fermion fields through the Higgs field generates masses in a gauge-covariant way. A coupling to the Higgs double ϕ is split after spontaneous symmetry breaking into mass terms containg v and direct couplings to the Higgs field h. For the quark and lepton sectors, they are

$$\begin{aligned}
\mathcal{L}_{\text{Yukawa}} =& -y^d_{ij}\overline{Q}^i_L\phi d^j_R - y^u_{ij}\overline{D}^i_L\phi_c u^j_R - y^e_{ij}\overline{L}^i_L\phi e^i_R \\
\overset{\phi\to v+h(x)}{\Rightarrow}& -\frac{y^d_{ij}v}{\sqrt{2}}\overline{d}^i_L d^j_R - \frac{y^u_{ij}v}{\sqrt{2}}\overline{u}^i_L u^j_R - \frac{y^e_{ij}v}{\sqrt{2}}\overline{e}^i_L e^j_R \\
& -\frac{y^d_{ij}}{\sqrt{2}}h\overline{d}^i_L d^j_R - \frac{y^u_{ij}}{\sqrt{2}}h\overline{u}^i_L u^j_R - \frac{y^e_{ij}}{\sqrt{2}}h\overline{e}^i_L e^j_R
\end{aligned} \tag{II.23}$$

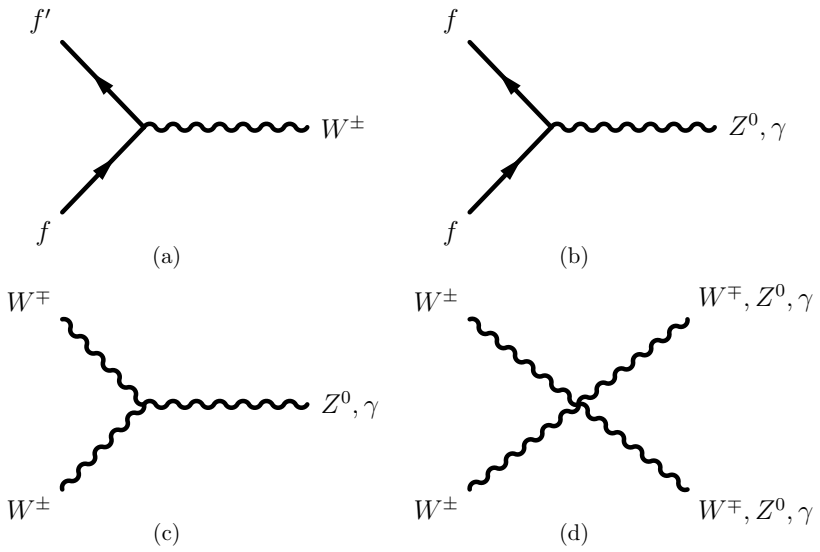

Figure II.4: Allowed Electroeak interactions include (a) charged (flavor-changing) vertices, (b) neutral (flavor-conserving) vertices, (c) three-boson couplings, and (e) four-boson couplings.

where ϕ_c is the charge-congjugate Higgs field which has the same transformation properties as ϕ, but which picks up its vacuum expectation value in the upper part of the doublet, required to give the up-type quarks mass. Off-diagonal terms in y^d_{ij} and y^u_{ij} arise which mix the weak eigenstates of the quark fields back into mass eigenstates, giving rise to the V_{CKM} matrix.

Symmetry breaking turns these Yukawa couplings into mass terms and direct couplings to the Higgs field for the quarks and charged leptons. In this form, and given the measured values of the higgs vacuum expectation value $v = 246$ GeV and top-quark mass $m_t = 173.21$ GeV [20], the top-quark coupling $y_t \equiv y^u_{tt} \approx 1$, while all other Yukawa couplings are very small. This fact was important in the recent observation of the Higgs boson [22, 23], as the coupling of the Higgs through a top-quark loop to two photons yielded one of the two decay channels used in the analysis. It also points out the top quark's unique position among the fermions; much heavier than the other quarks and leptons, it is the heaviest fundamental particle in the SM, and has a chance to provide insight into sources of new physics.

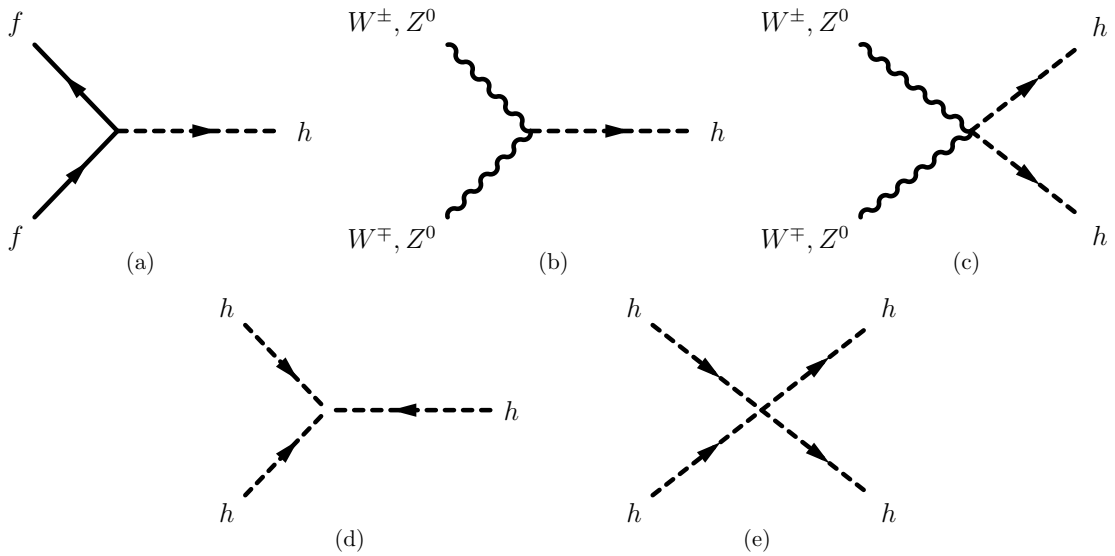

Figure II.5: Allowed Higgs interactions to massive particles include (a) fermion, (b,c) gauge boson, and (d,e) self couplings.

4. Third-Generation Quarks, t and b

The third generation of quark flavors, the up-type top quark, t, and down-type bottom quark, b, occupy a unique position in the SM. Their large masses make these particles rare, as any interaction which changes a t or b quark to a lower-mass particle is less likely to proceed in reverse if any energy is lost through radiation or other interactions. Thus, these quarks decay via weak interactions to lower-mass particles. Additionally, the CKM matrix elements V_{ub} and V_{cb} are very small, while $V_{tb} \sim 1$; as the top quark is much more massive than the b, this transition proceeds much more readily as $t \to W^+ b$ than $b^* \to W^- t$, where * indicates an off-shell particle. Their resulting lifetimes, very short for t and very long for b, give us more avenues for identification and property measurements.

With $m_b = 4.7$ GeV/c^2[3], the bottom quark's decay through a W^+ or Z^0 boson ($m_W = 80.4$ GeV/c^2, $m_Z = 91.2$ GeV/c^2) is energetically suppressed, and the weak transition to a top quark is kinematically disallowed for an on-shell b quark. Since its CKM matrix

[3] All values for masses quoted here can be found in Ref. [20].

couplings to the u and c quarks are small compared to V_{tb}, the b quark has limited options for decaying, and thus has a relatively long lifetime. In high-energy hadron collisions, it frequently hadronizes with particles in the jet it produces and travels some distance from the *primary vertex*, where the highest-energy collision in the event took place and where most particles in the jet originate, before decaying. The products of this B hadron decay often have a larger boost perpendicular to the jet direction, and can be traced to a displaced origin called a *secondary vertex*. We can use all of this information to construct an algorithm which performs *b-tagging*, typically calculating a weight for each jet in an event related to the probability that the jet contains a b quark. This can be useful for studying properties of such b-jets, but is also critical to identifying b quarks from the final state of another process, such as top-quark decay.

The decay of the top quark through the weak interaction to a bottom quark and W boson is, by contrast, very likely. In fact, the top-quark lifetime is $\mathcal{O}(10^{-25})$s, meaning that this transition takes place before the t can interact strongly and it does not have time to form jets or hadrons. As a quark which decays through the weak interaction before hadronizing, measurements of the top's properties provide a cleaner probe of these interactions for a particle with color charge than lighter quarks. Also, as it is the most massive particle in the SM, it is most likely to demonstrate deviations from SM values of its properties due to higher-mass fields and resonances, a possible window to new physics phenomena.

The top's large mass means that its production in the LHC is often close to threshhold, restricting its kinematics. When a top-antitop pair is produced from gluon splitting, $g \to t\bar{t}$, the spins of the top and antitop quarks are often correlated. When single top quarks are produced in the t-channel exchange of a W boson between a first- or second-generation u-type quark and a b quark, the large mass difference between the final state particles, a t and a d-type quark, results in a high degree of correlation between the top's spin direction and the momentum direction of the d-type *spectator quark*. This can be shown by calculating the squared matrix element for this process for individual top-quark helicity states. First, the matrix element for the interaction term is

$$\mathcal{M}(ub \to dt) = \frac{g_W^2}{2}(\overline{u}_t \gamma^\mu P_L V_{tb}^* u_b)\frac{g_{\mu\alpha} - q_\mu q_\alpha / m_W^2}{q^2 - m_W^2 + i m_W \Gamma_W}(\overline{u}_d \gamma^\alpha P_L V_{ud} u_u), \tag{II.24}$$

where $u_X \equiv u_X(p_X, \lambda_X)$ is a dirac spinor for particle X with momentum p_X and helicity λ_X, and $q = p_d - p_u = p_t - p_b$ is the momentum transfer carried by the W boson. The terms grouping the two fermion vertices are called *currents*, and the term connecting the two currents is known as the *propagator*. Note that in the relativistic limit $E_X \gg m_X$, we can effectively set $m_X = 0$. Setting $m_u = m_d = 0$, the second term in the propagator includes terms which vanish by the dirac equation, $\overline{u}_d \not{p}_d = 0$ and $\not{p}_u u_u = 0$, leaving only $g_{\mu\alpha}$. Squaring, summing over spins for u, d, and b, and using the expression $u_t(p_t, \lambda_t)\overline{u}_t(p_t, \lambda_t) = \frac{1}{2}(\not{p}_t - m_t)(1 + \gamma^5 \not{s}_t)$,

$$|\mathcal{M}(ub \to dt)|^2 = \frac{g_W^4}{8}|V_{tb}|^2|V_{ud}|^2 \frac{\mathrm{Tr}\left[(\not{p}_t - m_t)(1 + \gamma^5 \not{s}_t)\gamma^\mu \not{p}_b \gamma^\nu P_L\right] \mathrm{Tr}\left[\not{p}_d \gamma_\mu \not{p}_u \gamma_\nu P_L\right]}{\left(2p_u \cdot p_d - m_W^2\right)^2 + \left(m_W \Gamma_W\right)^2} \quad \text{(II.25)}$$

Simplifying the first trace in this expression leaves a momentum-like term for the top, $l_t = \frac{1}{2}(p_t - m_t s_t)$, in the same position as p_d in the second trace. The resulting expression shows the top and d-type quarks are linked through this momentum term:

$$|\mathcal{M}(ub \to dt)|^2 = 4g_W^4|V_{tb}|^2|V_{ud}|^2 \frac{(l_t \cdot p_d)(p_u \cdot p_b)}{\left(2p_u \cdot p_d - m_W^2\right)^2 + \left(m_W \Gamma_W\right)^2}. \quad \text{(II.26)}$$

In the top-quark rest frame, $p_t = (m_t, \vec{0})$ and $s_t = (0, \lambda_t \hat{p}_t)$. If we measure the top-quark spin λ_t in this frame along $\vec{p}_d$, then $l_t \cdot p_d \propto (1 + \lambda_t)$, and the expression vanishes if $\lambda_t = -1$. This means that only $\lambda_t = 1$ is realized, and the t is produced 100% polarized along this direction.

A subdominant process which mixes with the above production process is $\overline{d}b \to \overline{u}t$. It proceeds as described in Equation II.24, but with the charge-conjugate spinors for the light quarks, d^c and u^c. These fields can be written as a transformation of the original spinors, and the resulting square of the matrix element can be shown to have exactly the same form as Equation II.25, and thus leads to the same expression as in Equation II.26. In this case, the fact that λ_t is along $\vec{p}_{\overline{d}}$ means that the preferred direction of the top-quark spin will be along the proton beam from which this antiquark originates. Similar results can be shown for $d\overline{b} \to u\overline{t}$ and $\overline{u}\overline{b} \to \overline{d}\overline{t}$, where antitop quarks are produced with $\lambda_{\overline{t}} = -1$ along $\vec{p}_d$. When the combination of these four processes is measured, the amount of top quarks with $\lambda_t = 1$ and antitop quarks with $\lambda_{\overline{t}} = -1$ along the direction of the outgoing quark is quantified by

the *degree of polarization*, which is found to be $P \approx 0.9$ in this case. Further details can be found in Refs. [24, 25].

When such a polarized particle decays, the momentum and spin of the particles in the final state have strongly restricted kinematics as well. In this case, it is useful to describe this decay in the helicity formalism [26], which applies the angular momentum formalism used in nonrelativistic quantum mechanics, to produce a detailed description of the angular distributions of the decay of these polarized top quarks. This formalism makes use of the total angular momentum of the initial state, described by quantum numbers J and M, to predict the probabilities of producing two particles with helicities λ_1 and λ_2 which result in a final state characterized by the direction (θ, ϕ). The resulting form of the amplitude described in this formalism is

$$\mathcal{M}\left(i \to f_1 f_2\right) = \sqrt{\frac{2J+1}{4\pi}} D^{J*}_{M,\lambda}(\varphi, \theta, -\varphi) A_{\lambda_1,\lambda_2}, \tag{II.27}$$

where J and M are the spin and helicity of the decaying particle i, λ_1 and λ_2 are the helicities of the outgoing particles f_1 and f_2, $\lambda - \lambda_1 - \lambda_2$, and A_{λ_1,λ_2} is the amplitude for a decay to the specified helicity states. The Wigner D-matrix $D^J_{M,\lambda}$ is a representation of spatial rotations for spin-$\frac{1}{2}$ particles:

$$\begin{aligned} D^{J*}_{M,\lambda}(\varphi, \theta, -\varphi) &= < J\lambda | e^{-i\varphi J_z} e^{i\theta J_y} e^{i\varphi J_z} | JM > = d^{J*}_{M,\lambda}(\theta) e^{-i(\lambda - M)\varphi}, \quad \text{for} \\ d^{J*}_{M,\lambda}(\varphi, \theta, -\varphi) &= < J\lambda | e^{i\theta J_y} | JM > . \end{aligned} \tag{II.28}$$

The decay of the polarized tops produced in the t-channel, $t \to W^+ b$, has fixed initial-state quantum numbers for the top spin, $J_t = \frac{1}{2}$ and $M_t = \frac{1}{2}$, resulting in the helicity amplitude in Equation II.29. If we then observe the decay of the W^+ into a lepton and a neutrino, $W^+ \to \ell^+ \nu_\ell$, the restriction that the neutrino always be left-handed limits the degrees of freedom available in the final state, so $J = 1$, $M = \lambda_W$, $\lambda_\ell = \frac{1}{2}$, and $\lambda_\nu = -\frac{1}{2}$, producing the helicity amplitude in Equation II.30.

$$\mathcal{M}\left(t \to W^+ b\right) = \sqrt{\frac{1}{2\pi}} D^{\frac{1}{2}*}_{\frac{1}{2},\lambda_W - \lambda_b}(\varphi, \theta, -\varphi) A_{\lambda_W,\lambda_b} \tag{II.29}$$

$$\mathcal{M}\left(W^+ \to \ell^+ \nu_\ell\right) = \sqrt{\frac{3}{4\pi}} D^{1*}_{\lambda_W,1}(\varphi^*, \theta^*, -\varphi^*) A_{\frac{1}{2},-\frac{1}{2}} \tag{II.30}$$

The total decay distribution can be calculated from the magnitude squared of the product of these amplitudes summed over the intermediate helicity λ_W, for each value of λ_b:

$$\begin{aligned}
&\left|\mathcal{M}\left(t \to W^+ b \to \ell^+ \nu_\ell b\right)\right|^2 \equiv \frac{dN}{d\Omega d\Omega^*} \\
&= \sum_{\lambda_b} \left| \sum_{\lambda_W} \frac{\sqrt{6}}{4\pi} D^{\frac{1}{2}*}_{\frac{1}{2},\lambda_W-\lambda_b}(\varphi,\theta,-\varphi) A_{\lambda_W,\lambda_b} D^{1*}_{\lambda_W,1}(\varphi^*,\theta^*,-\varphi^*) A_{\frac{1}{2},-\frac{1}{2}} \right|^2 ,
\end{aligned}$$

where the solid angles $d\Omega = \sin\theta d\theta d\varphi$ and $d\Omega^* = \sin\theta^* d\theta^* d\varphi^*$ represent the top and W^+ decays respectively. This expression produces no interference between different b helicity states, but allows interference between each of the two W helicity states possible for each value of λ_b. As the phases allowed in these interference terms are the only source of φ and φ^* dependence, and for each interference term we get a combined phase of $\exp \pm i(\varphi^* - \varphi)$, the dependence on the two azimuthal angles is degenerate, through $\phi^* = \varphi^* - \varphi$. When this degeneracy is removed, the simplified expression for the angular distribution of top-quark decay can be expressed in terms of spherical harmonics for the angles θ^* and ϕ^*, and associated legendre polynomials for the angle θ:

$$\begin{aligned}
\frac{1}{N}\frac{dN}{d\Omega d\Omega^*} = \frac{1}{(4\pi)^{\frac{3}{2}}} \Bigg[& \left(\left(|A_{-1,-\frac{1}{2}}|^2 + |A_{1,\frac{1}{2}}|^2 + |A_{0,-\frac{1}{2}}|^2 + |A_{0,\frac{1}{2}}|^2 \right) P_0^0(\cos\theta) \right. \\
& \left. + P\left(|A_{-1,-\frac{1}{2}}|^2 - |A_{1,\frac{1}{2}}|^2 + |A_{0,-\frac{1}{2}}|^2 - |A_{0,\frac{1}{2}}|^2 \right) P_1^0(\cos\theta) \right) Y_0^0(\theta^*,\phi^*) \\
& + \frac{\sqrt{3}}{2} \left(\left(|A_{-1,-\frac{1}{2}}|^2 - |A_{1,\frac{1}{2}}|^2 \right) P_0^0(\cos\theta) \right. \\
& \left. + P\left(|A_{-1,-\frac{1}{2}}|^2 + |A_{1,\frac{1}{2}}|^2 \right) P_1^0(\cos\theta) \right) Y_1^0(\theta^*,\phi^*) \\
& + \frac{1}{\sqrt{5}} \left(\frac{1}{2} \left(\left(|A_{-1,-\frac{1}{2}}|^2 + |A_{1,\frac{1}{2}}|^2 \right) P_0^0(\cos\theta) + P\left(|A_{-1,-\frac{1}{2}}|^2 - |A_{1,\frac{1}{2}}|^2 \right) P_1^0(\cos\theta) \right) \right. \\
& \left. - \left(\left(|A_{0,-\frac{1}{2}}|^2 + |A_{0,\frac{1}{2}}|^2 \right) P_0^0(\cos\theta) + P\left(|A_{0,-\frac{1}{2}}|^2 - |A_{0,\frac{1}{2}}|^2 \right) P_1^0(\cos\theta) \right) \right) Y_2^0(\theta^*,\phi^*) \\
& - P \left(\frac{\sqrt{3}}{2} \left(A_{-1,-\frac{1}{2}} A^*_{0,-\frac{1}{2}} + A^*_{1,\frac{1}{2}} A_{0,\frac{1}{2}} \right) P_1^1(\cos\theta) Y_1^1(\theta^*,\phi^*) \right. \\
& + \sqrt{3} \left(A^*_{-1,-\frac{1}{2}} A_{0,-\frac{1}{2}} + A_{1,\frac{1}{2}} A^*_{0,\frac{1}{2}} \right) P_1^{-1}(\cos\theta) Y_1^{-1}(\theta^*,\phi^*) \\
& + \frac{\sqrt{3}}{2\sqrt{5}} \left(A_{-1,-\frac{1}{2}} A^*_{0,-\frac{1}{2}} - A^*_{1,\frac{1}{2}} A_{0,\frac{1}{2}} \right) P_1^1(\cos\theta) Y_2^1(\theta^*,\phi^*) \\
& \left. + \frac{\sqrt{3}}{\sqrt{5}} \left(A^*_{-1,-\frac{1}{2}} A_{0,-\frac{1}{2}} + A_{1,\frac{1}{2}} A^*_{0,\frac{1}{2}} \right) P_1^{-1}(\cos\theta) Y_2^{-1}(\theta^*,\phi^*) \right) \Bigg] .
\end{aligned} \tag{II.31}$$

The normalization $\frac{1}{N}$ is chosen to enforce $\sum_{\lambda_W,\lambda_b} |A_{\lambda_W,\lambda_b}|^2 = 1$. Through the amplitudes $A_{-1,-\frac{1}{2}}$, $A_{0,-\frac{1}{2}}$, $A_{0,\frac{1}{2}}$, and $A_{1,\frac{1}{2}}$, this expression provides a relationship between the individual helicity amplitudes allowed in this decay, and different ratios of these amplitudes control the resulting angular distribution in θ^* and ϕ^*. As these amplitudes control properties of the Wtb vertex, it also provides a connection to how these properties affect the production of the top quark through the same vertex through the angle θ. The degree of polarization P of the top quarks is the only parameter affected by the production, and is affected by the mixing between the single top-quark production modes described previoiusly as well as properties of the protons and their partonic initial states.

5. Effective Field Theories

Thus far, in setting up the different field theories which constitute the SM and the details of single top-quark production and decay, we have constructed Lagrangians which account for the kinetic and potential energies of a field and follow some tranformation properties called gauge symmetries. From this construction, individual interactions between particles arise, and we have explored such interactions for the top quark in the previous section. This set of interactions can be extended to add couplings between fields which are not defined in the SM, representing some unknown interaction which is measurable through the implied final state configuration. The search for or measurement of these interactions becomes a way to investigate the sources and couplings of new physics phenomena, by measuring the form and magnitude of a coupling with an SM prediction for its final state that is accessible through a property of the final state, to find out if modifications are required to explain the result. These phenomena are modeled by adding interaction terms to the SM Lagrangian which parameterize the possible new or modified couplings, called an *effective field theory* (EFT) approach [27].

Effective interactions added to the SM Lagrangian should involve only fields in the SM and should obey all applicable properties and symmetries. They should be calculable at any perturbative order, and should become negligible in an appropriate limit, such as below an energy where the SM is known to be accurate. With these properties, EFT terms can be

treated as perturbations on the SM Lagrangian relevant at higher energies, and measured values of the effective coupling constants will indicate how the new physics they represent should behave. The SM contains all interactions which satisfy the conditions it imposes which are *mass dimension* 4, which is needed to make its integral, the action, dimensionless. This means that effective terms will have higher mass dimension, and their coupling constants have inverse mass dimension. We will focus on the lowest-order terms affecting all SM particles, which have mass dimension 6; the Lagrangian containing these terms is typically given in the form

$$\mathcal{L}_{\text{EFT}} = \mathcal{L}_{\text{SM}} + \sum_i \frac{C_i}{\Lambda^2}\mathcal{O}_i, \tag{II.32}$$

where the interaction is encapsulated in the operators $\mathcal{O}_i$, which has coupling C_i. The factor Λ^2 is in units of energy; it is often chosen to represent the energy scale at which the interaction may become significant.

The top quark's large mass means that the energy scale at which effective interactions are measurable could be higher than other particles, making it a good candidate for probing higher energies for deviations from the SM. The full list of dimension-6 operators in Ref. [7] can be reduced for top-quark interactions to that given in Ref. [28]. We restrict our interest to the top charged-current weak vertex, Wtb, which contains only four such operators. The resulting Lagrangian containing both SM and effective operators becomes

$$\begin{aligned}\mathcal{L}_{Wtb}^{\text{EFT}} = &\frac{g_W}{\sqrt{2}}\bar{q}_{L,3}\gamma^\mu V_{tb} q_{L,3} W_\mu^- \\ &+ \frac{C_{\phi q}^{(3,3+3)*}}{\Lambda^2}\mathcal{O}_{\phi q}^{(3,3+3)*} + \frac{1}{2}\frac{C_{\phi\phi}^{33*}}{\Lambda^2}\mathcal{O}_{\phi\phi}^{33*} \\ &+ \sqrt{2}\frac{C_{dW}^{33*}}{\Lambda^2}\mathcal{O}_{dW}^{33*} + \sqrt{2}\frac{C_{uW}^{33}}{\Lambda^2}\mathcal{O}_{uW}^{33} + \text{ h.c.},\end{aligned} \tag{II.33}$$

where Λ is a common energy scale to all effective operators. The dimension-6 interactions represented by the operators $\mathcal{O}_i$ are:

- $\mathcal{O}_{\phi q}^{(3,3+3)*} = \frac{i}{2}\left[\phi^\dagger(\tau^a \overrightarrow{D}_\mu - \overleftarrow{D}_\mu \tau^a)\phi\right](\bar{q}_{L,3}\gamma^\mu\tau^a q_{L,3})$, which reduces via electroweak symmetry breaking to $g\frac{v^2}{\sqrt{2}}(\bar{b}_L\gamma^\mu t_L)W_\mu^-$ and contributes an additional left-handed vector coupling term to the SM Wtb vertex;
- $\mathcal{O}_{\phi\phi}^{33*} = i(\phi_c^\dagger D_\mu\phi)(\bar{t}_R\gamma^\mu b_R)$, which reduces similarly to $ig\frac{v^2}{2\sqrt{2}}(\bar{b}_R\gamma^\mu t_R)W_\mu^-$ and contributes a new right-handed vector coupling;

- $\mathcal{O}_{dW}^{33*} = (\overline{q}_{L,3}\sigma^{\mu\nu}\tau^a b_R)\phi W^a_{\mu\nu}$, which reduces similarly to $iv(\overline{b}_R\sigma^{\mu\nu}t_L)W^-_{\mu\nu}$ and contributes a new left-handed tensor coupling; and
- $\mathcal{O}_{uW}^{33} = (\overline{q}_{L,3}\sigma^{\mu\nu}\tau^a t_R)\phi_c W^a_{\mu\nu}$, which reduces similarly to $iv(\overline{b}_L\sigma^{\mu\nu}t_R)W^+_{\mu\nu}$ and contributes a new right-handed tensor coupling.

In these expressions, ϕ is the Higgs field, $q_{L,i}$ is the left-handed quark doublet of generation $i \in [1,2,3]$, the q_R are the right-handed quark singlets, v is the Higgs vacuum expectation value, and the tensor $\sigma^{\mu\nu} = \frac{i}{2}[\gamma^\mu, \gamma^\nu]$. Taking these operators in their form after electroweak symmetry breaking, we can simplify the notation from Equation II.33 into coupling constants representing the left- and right-handed vector couplings with coefficients $V_{\mathrm{L,R}}$ and the corresponding tensor couplings with coefficients $g_{\mathrm{L,R}}$. This parameterization makes the substitutions

$$V_L = V_{tb} + C_{\phi q}^{(3,3+3)*}\frac{v^2}{\Lambda^2} \qquad V_R = \frac{1}{2}C_{\phi\phi}^{33*}\frac{v^2}{\Lambda^2} \tag{II.34}$$

$$g_L = \sqrt{2}C_{dW}^{33*}\frac{v^2}{\Lambda^2} \qquad g_R = \sqrt{2}C_{uW}^{33*}\frac{v^2}{\Lambda^2} \tag{II.35}$$

to produce another form of the interaction Lagrangian between the W boson, t quark, and b quark,

$$\mathcal{L}_{Wtb}^{\mathrm{EFT}} = -\frac{g_W}{\sqrt{2}}\overline{b}\left[\gamma^\mu(V_{\mathrm{L}}P_{\mathrm{L}} + V_{\mathrm{R}}P_{\mathrm{R}}) + \frac{i\sigma^{\mu\nu}q_\nu}{m_W}(g_{\mathrm{L}}P_{\mathrm{L}} + g_{\mathrm{R}}P_{\mathrm{R}})\right]tW^-_\mu + h.c. \tag{II.36}$$

In this expression, q_ν is the momentum of the W boson. These four terms are sufficient to describe all possible lorentz-covariant terms in the structure of the Wtb vertex.

In the SM, the couplings V_{R} and $g_{\mathrm{L,R}}$ are 0 and $V_{\mathrm{L}} = V_{tb}$, where the CKM matrix element $V_{tb} \approx 1$. As the top quark's short lifetime prevents it from hadronizing, the $t \to W^+b$ decay channel is dominant. Top quarks can be produced in $t\bar{t}$ pairs via strong interactions, or singly through the Wtb vertex. Single top production proceeds through three primary channels: with a down-type or anti-up-type quark in the s- and t-channels, or by associated production with a W boson. This production mode results in a top which is produced and decays through this weak vertex, providing a method for detailed studies of the couplings $V_{\mathrm{L,R}}, g_{\mathrm{L,R}}$ inside the general vertices depicted in Figure II.6.

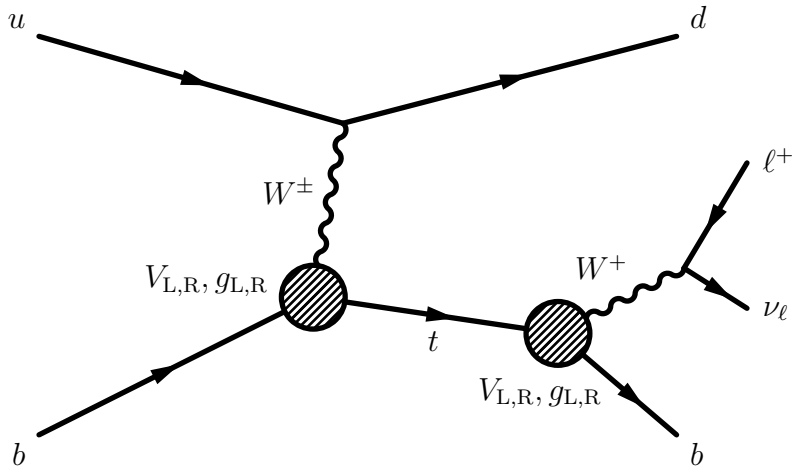

Figure II.6: The single top-quark production and decay process, with blobs representing the possible non-SM-like structure of the Wtb vertex, parameterized by the coefficients $V_{\mathrm{L,R}}$ and $g_{\mathrm{L,R}}$, used in the analysis presented in Chapter VI.

In the context of the angular distribution of the decay of the top quark described in Equation II.31, the coupling constants $V_{\mathrm{L,R}}$ and $g_{\mathrm{L,R}}$ are parameterized by the four helicity amplitudes $A_{-1,-\frac{1}{2}}$, $A_{0,-\frac{1}{2}}$, $A_{0,\frac{1}{2}}$, and $A_{1,\frac{1}{2}}$. The detailed form of this parameterization is given to $\mathcal{O}(m_b)$ and to squared order in the couplings $V_{\mathrm{L,R}}$ and $g_{\mathrm{L,R}}$ in Refs. [29, 30]. This parameterization is reformulated in terms of helicity amplitudes and the relative phases between interfering final states; this reformulation is given in Equations II.37 - II.42 up to $\mathcal{O}(m_b^2)$. The squared amplitudes (normalized by $\frac{1}{N}$ as in Equation II.31) and the phase differences between interfering amplitudes can be expressed in terms of $V_{\mathrm{L,R}}$ and $g_{\mathrm{L,R}}$, $x_W = \frac{m_W}{m_t}$, $x_b = \frac{m_b}{m_t}$, m_t, the momentum of the W boson, $q = \frac{m_t}{2}\sqrt{(1-(x_W-x_b)^2)(1-(x_W+x_b)^2)}$. A set of numeric constants u_i are defined to simplify the expression,

$$u_1 = 1 - x_W^2 - 2x_b^2 - x_W^2 x_b^2 + x_b^4 \qquad u_2 = 1 - x_W^2 + x_b^2 \qquad u_3 = 1 - x_W^2 - x_b^2$$
$$u_4 = 1 - 2x_W^2 - 2x_b^2 + x_W^4 - 2x_W^2 x_b^2 + x_b^4 \qquad u_5 = 1 + x_W^2 - x_b^2 \qquad u_6 = 1 - x_b^2$$
$$u_7 = 1 - 2x_b^2 - x_W^4 + x_b^4.$$

This yields the definitions

$$
\begin{aligned}
|A_{1,\frac{1}{2}}|^2 = \frac{1}{N}\Bigg(& u_2(|V_{\rm L}|^2+|V_{\rm R}|^2) - 4x_b{\rm Re}[V_{\rm L}V_{\rm R}^* + g_{\rm L}g_{\rm R}^*] + \frac{u_1}{x_W^2}(|g_{\rm L}|^2+|g_{\rm R}|^2) \\
& -\frac{2u_3}{x_W}{\rm Re}[V_{\rm L}g_{\rm R}^* + V_{\rm R}g_{\rm L}^*] + \frac{2u_5}{x_W}x_b{\rm Re}[V_{\rm L}g_{\rm L}^* + V_{\rm R}g_{\rm R}^*]\Bigg) \\
& + \frac{2q}{m_t}\Bigg(-(|V_{\rm L}|^2-|V_{\rm R}|^2) + \frac{u_6}{x_W^2}(|g_{\rm L}|^2-|g_{\rm R}|^2) \\
& + \frac{2}{x_W}{\rm Re}[V_{\rm L}g_{\rm R}^* - V_{\rm R}g_{\rm L}^*] + \frac{2}{x_W}x_b{\rm Re}[V_{\rm L}g_{\rm L}^* - V_{\rm R}g_{\rm R}^*]\Bigg),
\end{aligned}
\tag{II.37}
$$

$$
\begin{aligned}
|A_{0,\frac{1}{2}}|^2 = \frac{1}{2N}\Bigg(& \frac{u_1}{x_W^2}(|V_{\rm L}|^2+|V_{\rm R}|^2) - 4x_b{\rm Re}[V_{\rm L}V_{\rm R}^* + g_{\rm L}g_{\rm R}^*] + u_2(|g_{\rm L}|^2+|g_{\rm R}|^2) \\
& -\frac{2u_3}{x_W}{\rm Re}[V_{\rm L}g_{\rm R}^* + V_{\rm R}g_{\rm L}^*] + \frac{2u_5}{x_W}x_b{\rm Re}[V_{\rm L}g_{\rm L}^* + V_{\rm R}g_{\rm R}^*]\Bigg) \\
& - \frac{2q}{m_t}\Bigg(\frac{u_6}{x_W^2}(|V_{\rm L}|^2-|V_{\rm R}|^2) - \frac{1}{x_W^2}(|g_{\rm L}|^2-|g_{\rm R}|^2) \\
& -\frac{2}{x_W}{\rm Re}[V_{\rm L}g_{\rm R}^* - V_{\rm R}g_{\rm L}^*] + \frac{2}{x_W}x_b{\rm Re}[V_{\rm L}g_{\rm L}^* - V_{\rm R}g_{\rm R}^*]\Bigg),
\end{aligned}
\tag{II.38}
$$

$$
\begin{aligned}
|A_{0,-\frac{1}{2}}|^2 = \frac{1}{2N}\Bigg(& \frac{u_1}{x_W^2}(|V_{\rm L}|^2+|V_{\rm R}|^2) - 4x_b{\rm Re}[V_{\rm L}V_{\rm R}^* + g_{\rm L}g_{\rm R}^*] + u_2(|g_{\rm L}|^2+|g_{\rm R}|^2) \\
& -\frac{2u_3}{x_W}{\rm Re}[V_{\rm L}g_{\rm R}^* + V_{\rm R}g_{\rm L}^*] + \frac{2u_5}{x_W}x_b{\rm Re}[V_{\rm L}g_{\rm L}^* + V_{\rm R}g_{\rm R}^*]\Bigg) \\
& + \frac{2q}{m_t}\Bigg(\frac{u_6}{x_W^2}(|V_{\rm L}|^2-|V_{\rm R}|^2) - \frac{1}{x_W^2}(|g_{\rm L}|^2-|g_{\rm R}|^2) \\
& -\frac{2}{x_W}{\rm Re}[V_{\rm L}g_{\rm R}^* - V_{\rm R}g_{\rm L}^*] + \frac{2}{x_W}x_b{\rm Re}[V_{\rm L}g_{\rm L}^* - V_{\rm R}g_{\rm R}^*]\Bigg),
\end{aligned}
\tag{II.39}
$$

$$
\begin{aligned}
|A_{-1,-\frac{1}{2}}|^2 = \frac{1}{N}\Bigg(& u_2(|V_{\rm L}|^2+|V_{\rm R}|^2) - 4x_b{\rm Re}[V_{\rm L}V_{\rm R}^* + g_{\rm L}g_{\rm R}^*] + \frac{u_1}{x_W^2}(|g_{\rm L}|^2+|g_{\rm R}|^2) \\
& -\frac{2u_3}{x_W}{\rm Re}[V_{\rm L}g_{\rm R}^* + V_{\rm R}g_{\rm L}^*] + \frac{2u_5}{x_W}x_b{\rm Re}[V_{\rm L}g_{\rm L}^* + V_{\rm R}g_{\rm R}^*]\Bigg) \\
& - \frac{2q}{m_t}\Bigg(-(|V_{\rm L}|^2-|V_{\rm R}|^2) + \frac{u_6}{x_W^2}(|g_{\rm L}|^2-|g_{\rm R}|^2) \\
& + \frac{2}{x_W}{\rm Re}[V_{\rm L}g_{\rm R}^* - V_{\rm R}g_{\rm L}^*] + \frac{2}{x_W}x_b{\rm Re}[V_{\rm L}g_{\rm L}^* - V_{\rm R}g_{\rm R}^*]\Bigg),
\end{aligned}
\tag{II.40}
$$

$$
\begin{aligned}
\arg\left(A_{1,\frac{1}{2}}A^*_{0,\frac{1}{2}}\right) &= \arctan\frac{\mathrm{Im}[A_{1,\frac{1}{2}}A^*_{0,\frac{1}{2}}]}{\mathrm{Re}[A_{1,\frac{1}{2}}A^*_{0,\frac{1}{2}}]},\\
\mathrm{Im}[A_{1,\frac{1}{2}}A^*_{0,\frac{1}{2}}] &= \left(\frac{u_4}{x_W}\mathrm{Im}[V_\mathrm{L}g^*_\mathrm{R}+V_\mathrm{R}g^*_\mathrm{L}]\right)\\
&\quad+\frac{q}{m_t}\left(-4x_b\mathrm{Im}[V_\mathrm{L}V^*_\mathrm{R}+g_\mathrm{L}g^*_\mathrm{R}]-\frac{2u_3}{x_W}\mathrm{Im}[V_\mathrm{L}g^*_\mathrm{R}-V_\mathrm{R}g^*_\mathrm{L}]\right)\\
\mathrm{Re}[A_{1,\frac{1}{2}}A^*_{0,\frac{1}{2}}] &= \left(u_3(|V_\mathrm{L}|^2+|V_\mathrm{R}|^2+|g_\mathrm{L}|^2+|g_\mathrm{R}|^2)-2u_5x_b\mathrm{Re}[V_\mathrm{L}V^*_\mathrm{R}+g_\mathrm{L}g^*_\mathrm{R}]\right.\\
&\quad\left.-\frac{u_7}{x_W}\mathrm{Re}[V_\mathrm{L}g^*_\mathrm{R}+V_\mathrm{R}g^*_\mathrm{L}]+\frac{4}{x_W}x_b\mathrm{Re}[V_\mathrm{L}g^*_\mathrm{L}+V_\mathrm{R}g^*_\mathrm{R}]\right)\\
&\quad+\frac{q}{m_t}\left(-2(|V_\mathrm{L}|^2-|V_\mathrm{R}|^2-|g_\mathrm{L}|^2+|g_\mathrm{R}|^2)+\frac{2u_5}{x_W}\mathrm{Re}[V_\mathrm{L}g^*_\mathrm{R}-V_\mathrm{R}g^*_\mathrm{L}]\right),
\end{aligned}
$$

$$
\begin{aligned}
\arg\left(A^*_{-1,-\frac{1}{2}}A_{0,-\frac{1}{2}}\right) &= \arctan\frac{\mathrm{Im}[A^*_{-1,-\frac{1}{2}}A_{0,-\frac{1}{2}}]}{\mathrm{Re}[A^*_{-1,-\frac{1}{2}}A_{0,-\frac{1}{2}}]},\\
\mathrm{Im}[A^*_{-1,-\frac{1}{2}}A_{0,-\frac{1}{2}}] &= -\left(\frac{u_4}{x_W}\mathrm{Im}[V_\mathrm{L}g^*_\mathrm{R}+V_\mathrm{R}g^*_\mathrm{L}]\right)\\
&\quad-\frac{q}{m_t}\left(-4x_b\mathrm{Im}[V_\mathrm{L}V^*_\mathrm{R}+g_\mathrm{L}g^*_\mathrm{R}]-\frac{2u_3}{x_W}\mathrm{Im}[V_\mathrm{L}g^*_\mathrm{R}-V_\mathrm{R}g^*_\mathrm{L}]\right)\\
\mathrm{Re}[A^*_{-1,-\frac{1}{2}}A_{0,-\frac{1}{2}}] &= \left(u_3(|V_\mathrm{L}|^2+|V_\mathrm{R}|^2+|g_\mathrm{L}|^2+|g_\mathrm{R}|^2)-2u_5x_b\mathrm{Re}[V_\mathrm{L}V^*_\mathrm{R}+g_\mathrm{L}g^*_\mathrm{R}]\right.\\
&\quad\left.-\frac{u_7}{x_W}\mathrm{Re}[V_\mathrm{L}g^*_\mathrm{R}+V_\mathrm{R}g^*_\mathrm{L}]+\frac{4}{x_W}x_b\mathrm{Re}[V_\mathrm{L}g^*_\mathrm{L}+V_\mathrm{R}g^*_\mathrm{R}]\right)\\
&\quad-\frac{q}{m_t}\left(-2(|V_\mathrm{L}|^2-|V_\mathrm{R}|^2-|g_\mathrm{L}|^2+|g_\mathrm{R}|^2)+\frac{2u_5}{x_W}\mathrm{Re}[V_\mathrm{L}g^*_\mathrm{R}-V_\mathrm{R}g^*_\mathrm{L}]\right).
\end{aligned}
\tag{II.41, II.42}
$$

With the expressions shown in Equations II.37 - II.42, the dependence of the angular distribution of the top-quark decay products on the new physics effects introduced by the dimension-6 operators introduced in Equation II.33 is made explicit. It can be adjusted to predict the effects on the angular distribution of simulated events with new physics phenomena which generate non-zero values of V_R, g_L, or g_R, or deviations from $V_\mathrm{L} = V_{tb}$. Similarly, the expressions can be used to measure directly the values of the coupling constants in measured data.

III. THE LHC AND THE ATLAS EXPERIMENT

This chapter briefly details the design and operation of the apparatuses which deliver and collect the data used in the LHC, a particle accelerator and collider located at CERN, the European Organization for Nuclear Research (formerly Conseil Européen pour la Recherche Nucléaire, from which the name is derived), on the Franco-Swiss border near Geneva, Switzerland. The LHC accelerates protons to higher energies and in greater number than any previous similar experiment. More detail on the design, construction, and operation of the LHC can be found in its conceptual design report [31], an overview [32], and its commissioning report [33]. The ATLAS detector is described in detail in its technical design report [34, 35] and an overview [36].

1. The Large Hadron Collider

The LHC is comprised of a ring of superconducting magnets designed to direct and accelerate a beam of protons in a circular path. It is installed in a tunnel built for the former LEP (Large Electron-Positron) collider [37], 26.7km in circumference. The ring consists of 8 arcs and 8 straight sections, with superconducting magnets operating at 1.9 K and with a field of up to 8.33 T controlling the direction and energy of the beam. In the arcs, the beams are bent with a quadrupole magnetic field to direct them along the next straight section. In each straight section, two radio-frequency (RF) cavities supply an electromagnetic field generated by voltages of up to 2 MV, accelerating protons up to a maximum design energy: 7 TeV for data taken during 2010 and 2011, 8 TeV for data taken during 2012, and 13 TeV in 2015. The RF-varying electromagnetic field is tuned to 400 MHz to accelerate protons grouped into distinct *bunches*, each beginning with 1.1×10^{11} protons. The number of bunches circulating

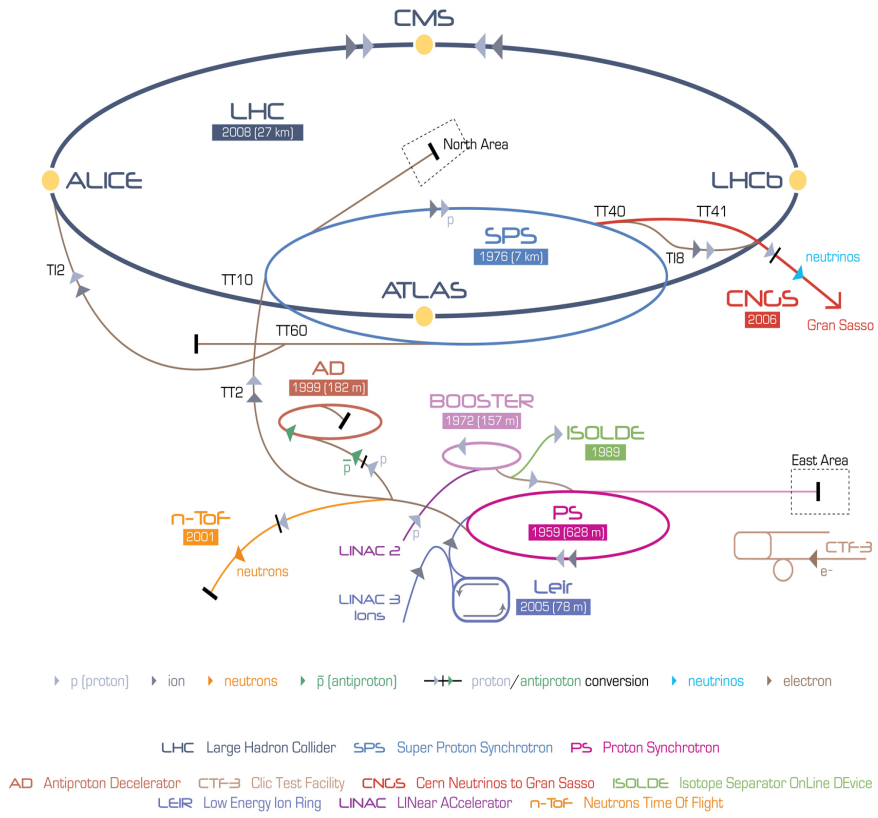

Figure III.1: Accelerator facilities at CERN and associated experiments. Courtesy of CERN.

B, the number of particles per bunch n, the bunch shape and normalized density profile $\rho(\vec{x})$, the angle φ between the beams in the $x-z$ plane, the bunch velocity βc, and the frequency of revolution f together provide a way to express the instantaneous luminosity from individual bunch crossings [38],

$$\mathcal{L}_{\text{inst}} = 2\beta c B f \cos^2\frac{\varphi}{2}\int_{t_i}^{t_f}\left(n^2\int_V \rho(\vec{x}_+)\rho(\vec{x}_-)d\vec{x}\right)dt, \quad \text{for} \quad \vec{x}_\pm = (x, y, z \pm \beta c(t-t_i)). \tag{III.1}$$

This expression can be integrated under the assumption of gaussian beam profiles in all three directions, with width parameters σ_x, σ_y, and σ_z, to yield [39]

$$\mathcal{L}_{\text{inst}} = \frac{\beta f B n^2}{4\pi\sigma_x\sigma_y}S, \tag{III.2}$$

where S is a factor which can depend on φ, σ_z, and other factors related to the magnetic field or the geometry of the beam.

The acceleration process for the proton beams begins with the production of the protons from ionized Hydrogen atoms, accelerated in the linear particle accelerator LINAC 2 to an energy of 50 MeV. These protons are fed into the Proton Synchrotron Booster (PSB), where they are accelerated to 1.4 GeV, then into the Proton Synchrotron (PS), where they reach energies of 26 GeV. They are then injected into the Super Proton Syncrhotron (SPS) and accelerated up to 450 GeV, before being injected into the LHC where they will reach its design energy. Lead ions are produced in another linear accelerator, LINAC 3, and accelerated by the Low Energy Ion Ring (LEIR), before entering the PSB and following a similar acceleration procedure as the protons.

Once circulating in the LHC, the beams can be used to produce data for any of the experiments situated along the beamline. There are four major experiments which investigate the aftermath of particle collisions, each having a detector installed at one of the interaction points. The ATLAS detector at Point 1 and the CMS detector [40] at Point 5 are large, general purpose detectors designed to be able to detect a wide variety of potential new physics phenomena at high energy scales, especially from proton-proton (pp) collisions. The ALICE (A Large Ion Collider Experiment) detector [41] at Point 2 is aimed at studying lead-ion collisions (PbPb) to investigate the conditions of the early universe by creating extremely high matter densities, also providing insight into QCD. The LHCb (LHC beauty) detector [42] at Point 8 is designed to investigate topics relating to the heavy quark flavors c and b, with a focus on the asymmetry of matter and antimatter present in the universe, often referred to as $\mathcal{CP}$ *violation*. Three smaller experiments, installed at the same interaction points, are designed to measure or search for specific phenomena outside the reach of the larger experiments. The TOTEM [43] (Total, Elastic and diffractive cross-section Measurement) and LHCf [44] (LHC forward) experiments study particles produced in the forward regions of the CMS and ATLAS detectors, respectively, which are too close to the beampipe to be seen by the larger detectors. The MoEDAL (Monopole and Exotics Detector At the LHC) experiment [45] shares Point 8 with LHCb, and searches for magnetic monopoles or particles with similar properties.

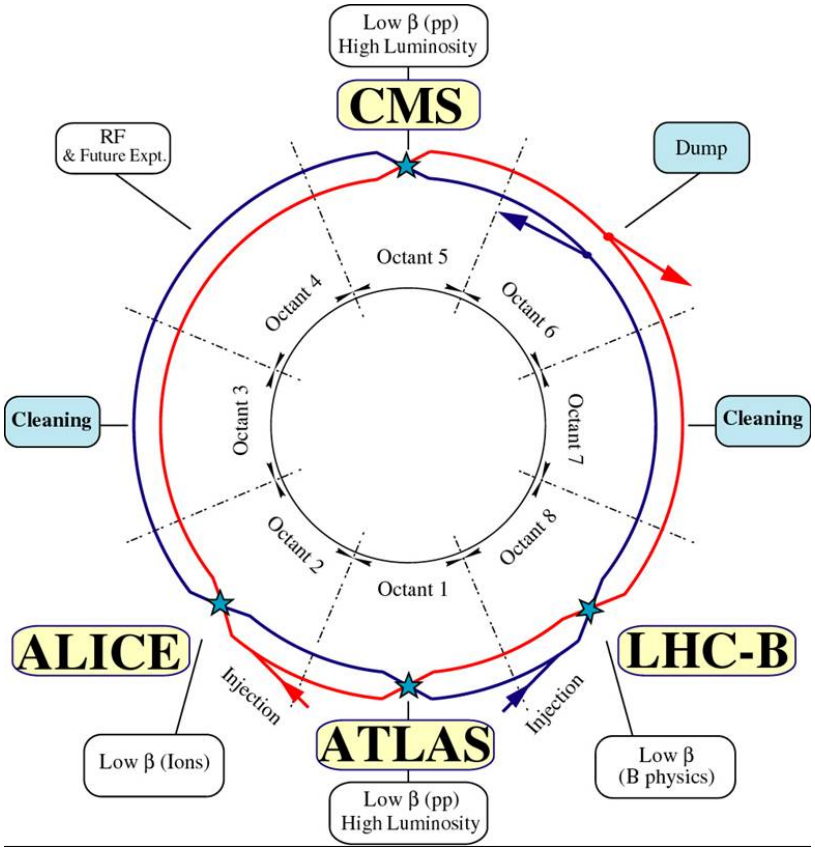

Figure III.2: Octants representing the access points on linear segments, where acceleration and beam crossings take place. Courtesy of CERN.

Construction of the LHC and associated detectors was completed in 2008, and on the 10^{th} of September it was first turned on. Unfortunately, during testing of superconducting magnets 9 days later, an electrical fault resulted in a rapid rise in temperature and release of helium from the magnet cooling system, causing mechanical damage to a number of magnets. Repairs after this incident took another year, and by the 20^{th} of November, 2009, beams were circulating in the machine again. *pp* collision data at 7 TeV began in 2010, when an integrated luminosity of 45 pb^{-1} was recorded with a spacing between proton bunches of 150 ns. These numbers were quickly surpassed in 2011 [48], with 5.46 fb^{-1} delivered to the ATLAS detector and 6.10 fb^{-1} delivered to the CMS detector (see Figure III.3), at a peak instantaneous luminosity of $3.6 \times 10^{33}\text{cm}^{-1}\text{s}^{-1}$ and a bunch spacing of 50 ns. In 2012,

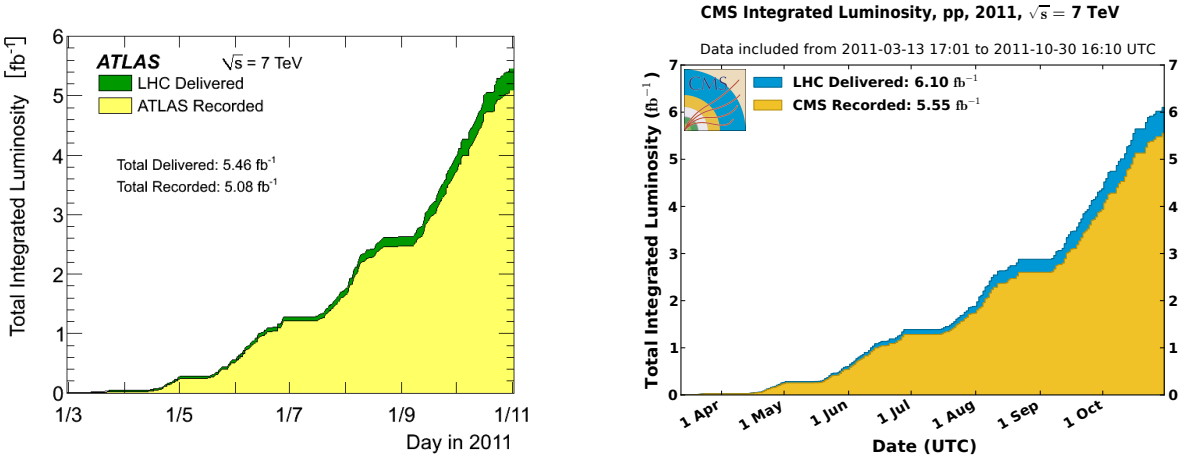

(a) (b)

Figure III.3: Total proton beam luminosity delivered to, and recorded by, the ATLAS (left) and CMS (right) detectors during *pp* collisions with a 7 TeV center-of-mass energy in 2011. Details of the luminosity measurements for each detector can be found in Ref. [46] for ATLAS and Ref. [47] for CMS. Courtesy of ATLAS and CMS collaborations.

individual beams were raised from energies of 3.5 TeV to 4 TeV, resulting in a center-of-mass energy of $\sqrt{s} = 8$ TeV. At this energy, a peak instantaneous luminosity of $7 \times 10^{33}\text{cm}^{-1}\text{s}^{-1}$ was reached, approaching the design luminosity of $10^{34}\text{cm}^{-1}\text{s}^{-1}$.

2. The ATLAS Detector

The interactions of protons delivered by the LHC result in a shower of particles, freed from the proton or pulled from the vacuum in the high-energy interaction between two of its partons. The ATLAS detector is designed to measure energies and trajectories from interactions of these particles with sensitive regions of the detector, and to reconstruct the basic kinematic quantities of particles, or physics objects like jets, in each event. From these quantities, specific particles can often be identified by their properties such as charge, mass, and spin, which provide hints to the form of the initiating interaction. To assist in identifying intrinsic properties, the detector is divided into multiple subdetectors positioned in layers, listed from

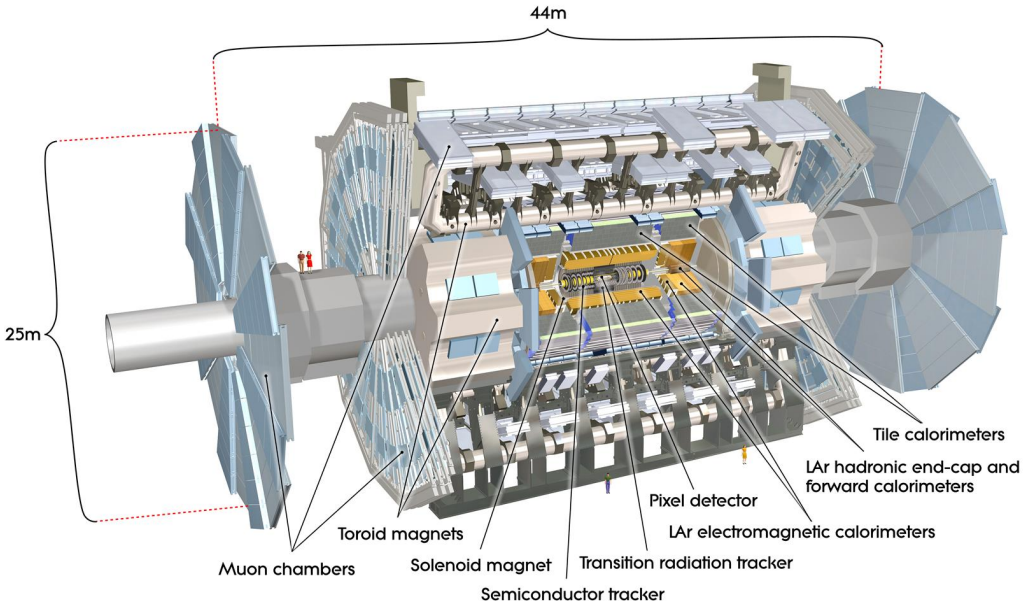

Figure III.4: An illustration of the ATLAS detector, indicating its overall dimensions and the major detector systems. Courtesy of ATLAS Collaboration.

closest to the beam crossing point to farthest from it:

- tracking detectors, described in Section III..2.c, measure the paths of charged particles with high precision;
- calorimeters described in Section III..2.d, measure energies and help separate particle species with varied density and detecting materials; and
- muon spectrometers, described in Section III..2.e, record track information of muons which are likely to pass through the calorimeters without stopping.

A system of toroidal and solenoidal magnets, described in Section III..2.b are positioned throughout the detector, which bend the paths of the particles in proportion to their momentum and charge-to-mass ratio. This improves the momentum resolution of charged particles in tracking detectors, as the radius of curvature will decrease for higher-momentum particles, and can help to distinguish particles with the same charge but different masses which may otherwise leave similar signals in the detector. Given the incredibly high rate of collisions

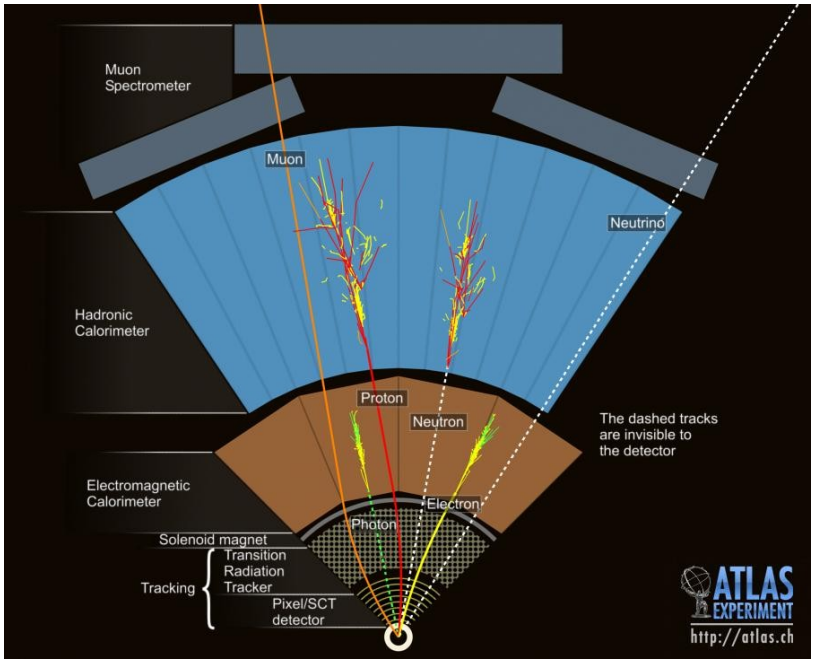

Figure III.5: Patterns of interaction for different particle species in each subdetector. Charged particles leave tracking hits in the inner detectors; light electromagnetic particles (i.e. electrons and photons) leave showers in the electromagnetic calorimeter; hadronic particles which interact through QCD leave showers in the hadronic calorimeter; and particles with long decay lengths (i.e. muons) or which escape the hadronic calorimeter may leave tracking hits in the muon spectrometers. Courtesy of CERN.

occurring in the ATLAS detector, not all events can be effectively measured and recorded. A trigger system, described in Section III..2.f is implemented to manage how frequently events are recorded. Separate triggers are defined based on indications of objects of interest in the raw signals from the detector, and trigger rates are chosen based on the frequency of such events up to limitations imposed by the hardware. The detector and its data acquisition abilities are modeled by a detailed simulation of the geometry and material composition of the detector, described in Section III..3, to predict the detector response to particular events. This simulation must be both fast and accurate to be useful in comparisons with real data, and a few different approaches to this challenge are used.

a. Detector dimensions and coordinate system The ATLAS detector [36, 49] is a cylindrical, hermetic detector encircling the LHC at the first of its eight interaction points. Its subdetector systems are installed in layers separated into *barrel* and *endcap* components. The detector weights about 7000 tons, and is about 44 m long and 25 m in diameter; its shape and dimensions, and those of its subsystems individually, are chosen to efficiently enclose the full interactions of nearly all particles produced in collisions, which ensures that the properties of the particles can be fully characterized. The coordinate system used to describe the detector's components and interaction events inside it is based on a standard cylindrical coordinate system. The expected interaction point is defined as the origin of the coordinate system, and the beam direction defines the $\hat{z}$-axis, with the $+z$ direction being towards Point 8 as depicted in Figure III.2. The azimuthal angle ϕ is measured around the beamline, with $\phi = 0$ at the x-axis defined to point toward the center of the LHC ring. The polar angle θ is measured from the $+z$ axis. When discussing the momentum of detected objects, the transverse momentum p_{T} and pseudorapidity η are often used (see Section I..3), in conjunction with either the mass or energy of the object to complete its kinematic characterization. These variables simplify the manipulation of highly-boosted objects, where $|\vec{p}| \gg m$ and η reduces to the rapidity, y, as shown in Equations I.4 - I.5. This maintains constant relative differences under Lorentz transformations, and p_{T} does not vary under boosts along the beam.

b. Magnet systems Magnetic fields are induced inside the ATLAS detector, particularly in the inner detector and muon spectrometers, to bend the trajectories of charged particles to improve the resolution on their momentum measurement. A solenoid [50] with an inner diameter of 2.46 m, a thickness of 0.1 m, and a length of 5.8 m generates a 2 T axial magnetic field within the tracking-focused inner detectors, from a 7730 A current running through the 1154 turns of wire. The solenoid was designed to minimize the impact of its material on particles' energy loss before entering the calorimeters, and it contributes only 0.66 radiation lengths at $\eta = 0$. Three toroidal magnets generate a magnetic field for the muon spectrometers: a barrel toroid [51] and two endcap toroids [52]. The barrel toroid is a system of eight coils ringing the detector, 25.3 m long and with an inner diameter of 9.4 m

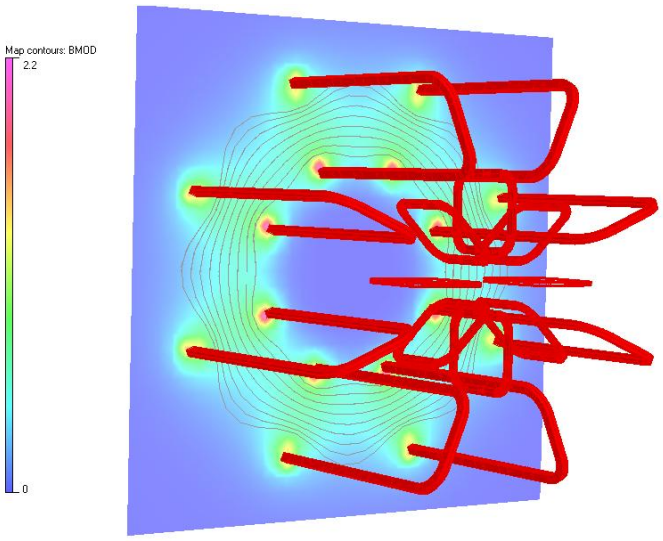

Figure III.6: An illustration of the field generated by the barrel toroid system with a cross-sectional slice. The irregularities in the field are precisely modeled to make accurate muon momentum measurements. Courtesy of ATLAS Collaboration.

and an outer diameter of 20.1 m producing a 1 T field, and the two endcap toroids also have eight coils, extending out 5 m, with an inner diameter of 1.65 m and outer diameter of 10.7 m to produce 0.5 T fields. The barrel and endcap toroid coils have around 120 and 116 turns of wire each, respectively. The toroid systems do not produce a field as uniform as the solenoid, so detailed maps of the magnetic field in the muon spectrometers are used to predict the precise paths of particles moving through them.

c. Inner detectors The inner detector [53, 54] components of the ATLAS detector are designed to provide momentum measurements of charged tracks produced near the interaction point of protons in the two beams, called the *primary vertex*, with a resolution of 0.05%. The high density of tracks near the vertex requires the Pixel and silicon microstrip (SCT) detectors to have very high spatial resolution, so that pattern-matching algorithms can reconstruct tracks from 'hits' in these detectors. A third layer, the transition radiation tracker (TRT), measures only azimuthal information to further enhance the accuracy of track

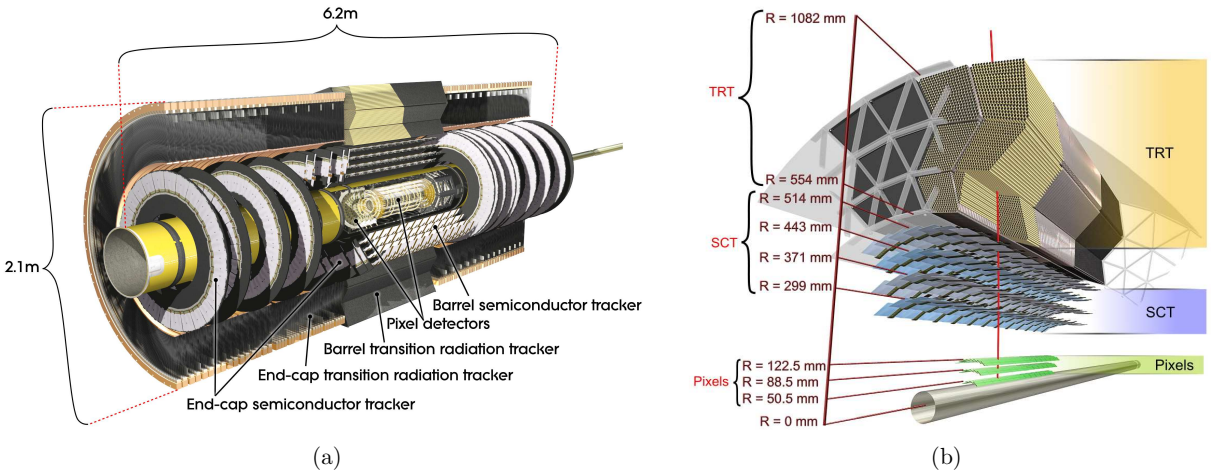

(a) (b)

Figure III.7: Assembled (a) and exploded (b) illustrations of the structure of the Pixel, SCT, and TRC components of the inner detector. Courtesy of ATLAS Collaboration.

reconstruction and identification.

The Pixel detector [55] is closest to the interaction point, covering the region $|\eta| < 2.5$ with sensitive layers extending radially from 5 cm to 12 cm in the barrel and from 9 cm to 15 cm in the endcaps. It has the highest granularity of any ATLAS subdetector; its 1744 modules are arranged in three layers, and correspond to about 80.4×10^6 readout channels with a granularity of $50 \times 400 \mu\text{m}^2$. The intrinsic accuracies of the modules are 10 μm in the ϕ direction in the barrel and endcaps, and 115 μm in the z direction in the barrel or the radial direction in the endcaps. The inner Pixel layer experiences an ionizing radiation dose of up to 158 kGy/yr[1], and must be replaced after 3 years of operation at the LHC design luminosity. The remaining two layers are designed to last for the expected length of the data-taking program.

The SCT detectors [56, 57] surround the pixel detectors, also covering $|\eta| < 2.5$ with sensitive layers from 30 cm to 51 cm in the barrel and from 27.5 cm to 56 cm in the endcaps, radially from the beamline. They consist of four double layers of strips, with extents of 40 mrad in ϕ and θ, axially and radially arranged in the barrels and endcaps respectively.

[1] One *Gray*, abbreviated 1 Gy, is defined as the absorption of 1 J of radiation energy per 1 kg of matter.

These strips are grouped into 4088 modules, corresponding to 6.3 million readout channels. Each 40 mrad strip is set at a slight pitch of 80 μm relative to the cylinder. The axial and radial positioning results in a high intrinsic accuracy along ϕ of 17 μm in the barrel and endcaps, while the resolution along z in the barrel, or the radial direction in the endcaps, is 580 μm. The innermost layer of the SCT will experience a much lower radiation dose than the pixel detector, up to 7.6 kGy/yr. Both the pixel and SCT detectors must be operated at -5° C to -10° C [58] to minimize electronic noise.

The TRT detectors [59, 60, 61] surround the SCT detectors, only covering $|\eta| \leq 2.0$, and are sensitive between radii of 56 cm and 107 cm in the barrel and 64 cm to 100 cm in the endcaps. The TRT detectors only measure azimuthal information with an intrinsic resolution of 130 μm in ϕ. They are composed of from 4 mm-diameter straw tubes, 144 cm axial tubes in the barrel and 37 cm radial tubes in the endcap, for a total of about 351,000 readout channels. The tubes have a conducting anodic wire in their center and cathodic walls, and are filled with a gas mixture containing 70% Xe, 27% CO_2, and 32% O_2. This gas is chosen to produce larger signals for transition-radition photons than for minimum-ionizing charged particles, assisting in discrimination.

d. Calorimeters The ATLAS calorimeters are designed to measure the energy of long-lived particles by inducing and containing showers of particles, the total energy of which are interpreted as the initial energy. A high-density absorber medium, which induces interactions, is interspersed with a sampling medium, which transmits information about the energy of the shower. Two different calorimeter designs are nested such that they can distinguish low-mass particles interacting electromagnetically, usually electrons and photons, and higher-mass particles dominated by the strong interaction, like protons, neutrons, pions, and other hadronic particles.

The electromagnetic (EM) calorimeters [62] consist of two barrel segments and two endcaps, depicted in Figure III.8a. A liquid Argon (LAr) sampling medium fills the space around the lead absorbers, which are arranged in an accordion shape depicted in Figure III.8b. This increases their stopping power for electromagnetic showers, with > 22 radiation lengths in the barrel and > 24 in the endcaps, and ensures complete azimuthal coverage. The barrel,

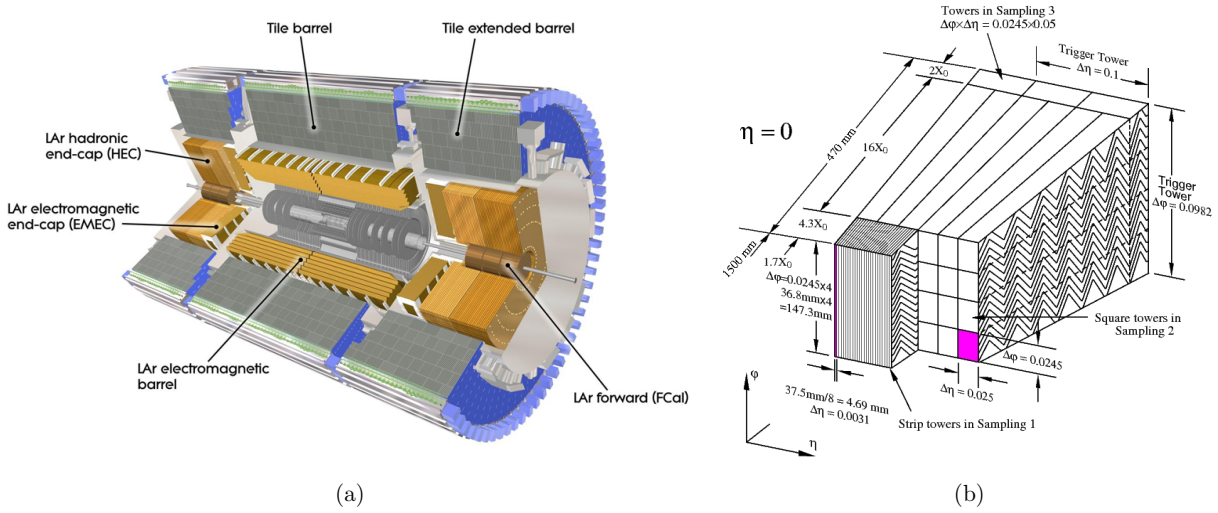

(a) (b)

Figure III.8: (a) An assembled illustration of the electromagnetic and hadronic calorimeters. (b) A detailed view of the accordion structure of the electromagnetic calorimeter. Both courtesy of ATLAS Collaboration.

covering $|\eta| < 1.475$, is segmented into five layers with a minimum granularity in $\Delta\eta$ of 0.003125 and in $\Delta\phi$ of 0.025, mapping to 101,760 readout channels. The endcaps, divided into two wheels covering $1.375 < |\eta| < 2.5$ and $2.5 < |\eta| < 3.2$, are segmented into 2 to 3 layers with minimum granularity in $\Delta\eta$ of 0.003125 and in $\Delta\phi$ of 0.1, mapping to 62,208 readout channels. A LAr-filled presampler layer is located inside the EM calorimeter, in the region $|\eta| < 1.8$, and measures energy lost upstream from the calorimeter. The EM calorimeters are designed to have an overall energy resolution of $\sigma_E/E = 10\%/\sqrt{E} \pm 0.2\%$, where the first term represents stochastic variation and the second reflects local non-uniformities in calorimeter response, falling within the the desired accuracy for energy measurement resolution.

The hadronic calorimeters [63] consist of a tile calorimeter barrel composed of steel absorbers and plastic scintillators as the sampling medium, two liquid argon endcaps, and a LAr forward calorimeter which extends the reach in $|\eta|$ to improve hadronic shower energy measurements in the high-$|\eta|$ region. The tile calorimeter covers $|\eta| < 1.0$ in a central barrel

and $0.8 < |\eta| < 1.7$ in two extensions, organized in 3 layers with a granularity in $\Delta\eta \times \Delta\phi$ of 0.1×0.1 in the inner two layers and 0.2×0.1 in the third layer, resulting in 9852 readout channels. The endcaps are again separated into two wheels, covering $1.5 < |\eta| < 2.5$ and $2.5 < |\eta| < 3.2$ with granularities in $\Delta\eta \times \Delta\phi$ of 0.1×0.1 and 0.2×0.2, respectively. The energy resolution for the hadronic calorimeter systems varies with each component and particle species, but all are within the desired resolution of $\sigma_E/E = 50\%/\sqrt{E} \pm 3\%$.

The forward calorimeters [64] (FCal) extend the range of both electromagnetic and hadronic calorimetry with coverage in the region $3.1 < |\eta| < 4.9$, overlapping slightly with the endcaps to minimize gaps in coverage. They are divided into three modules; the first is electromagnetic, and contains copper absorbers, while the remaining hadronic modules contain tungsten absorbers. The FCal granularities are described in $\Delta x \times \Delta y$; they measure 3.0cm × 2.6cm in the electromagnetic layer, 3.3cm × 4.2cm in the first hadronic layer, and 5.4cm × 4.7cm in the second hadronic layer. This segmentation yields 3524 total readout channels. The energy resolution of the FCals also fall within desired values, here $\sigma_E/E = 100\%/\sqrt{E} \pm 10\%$.

e. Muon spectrometers Muons are unique among the common particles produced by high-energy interactions; their large mass makes them unlikely to shower in the calorimeters, and their long lifetime means that, at higher energies, they will frequently decay outside the detector. The muon spectrometer [65] adds additional tracking capabilities in the region outside the hadronic calorimeter, so muons can be distinguished primarily by tracks in this and the inner detector. The muon spectrometers have momentum resolution of around 10% for high-p_{T} tracks, boosted by the toroid magnet systems, independent of information from the inner detectors. The system is made up of chambers with complementary purposes: tracking chambers which measure the component of the muon track in the bending direction induced by the magnetic field to high precision, and trigger chambers which measure the perpendicular coordinate and provide timing resolution, allowing a muon to be matched to a particular bunch crossing.

The high-precision tracking is performed by monitored drift tubes (MDTs) in the region $|\eta| < 2.7$, where the ionization of argon gas produces a signal in a central wire. The tubes are

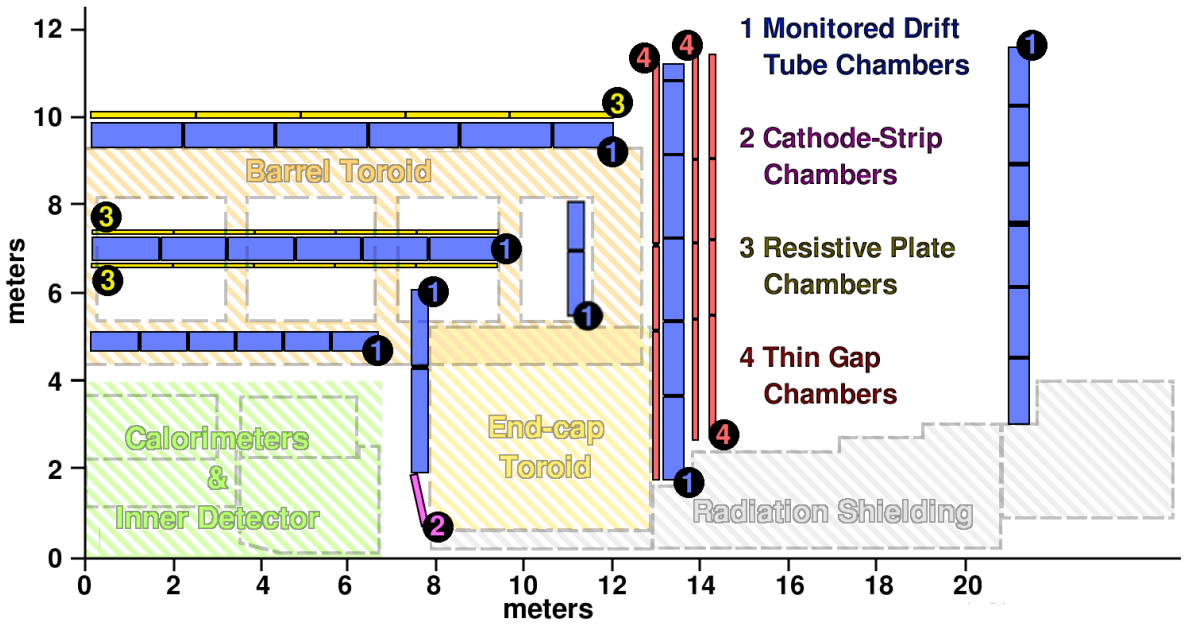

Figure III.9: A partial detector cross-section with details on the layout of muon detector components [66].

oriented parallel to the magnetic field direction and divided into three layers in the barrel or two wheels in the endcap. In the region $2.0 < |\eta| < 2.7$, the first layer's MDTs are replaced by cathode strip chambers (CSCs), which provide better timing resolution and measure both tracking coordinates simultaneously. These chambers are filled with argon gas, which when ionized induce a signal on multiple anode wires and perpendicular cathode strips. The MDTs have 354,000 readout channels, while the CSCs have 31,000.

Timing resolution in the muon chambers is critical to associating the muon to the correct interaction; this and the perpendicular tracking coordinate are provided by trigger chambers. Resistive plate chambers (RPCs) are used in the barrel region, $|\eta| < 1.05$; they are parallel plates with a resistive gap, fed into 373,000 readout channels. Thin gap chambers (TGCs) are used in the endcap region, $|\eta| < 2.4$; they have a similar design to the CSCs, but optimized to measure the track coordinate perpendicular to the bending direction, and are fed into 318,000 readout channels. These chambers provide timing resolution of around 1.5–4 ns,

assigning $> 99\%$ of triggered muons to the correct bunch crossing.

f. Trigger systems The signals collected in the tracking and calorimetric subdetectors from collisions happening at 40 MHz can only be sampled from the readouts of the detector at about 450 Hz due to the capabilities of the electronic components which receive signals from the detector. The triggering system optimizes the types of events sampled into multiple categories expected to have a particular physics object of interest above a p_{T} threshold, such as a muon or a photon.

The Level-1 (L1) trigger [67] is a hardware-only trigger, using reduced-granularity calorimeter information ($\Delta\eta \times \Delta\phi$ of 0.1×0.1 in most regions) to select high transverse-energy[2] (E_T) electrons, photons, jets, and hadronically-decaying τ leptons, as well as events with high $E_{\mathrm{T}}^{\mathrm{miss}}$, and use the muon trigger chambers (the RPCs and TGCs) to select muons. E_T information from the enlarged calorimeter regions and p_{T} information from the muon RPCs and TGCs is sent to the central trigger processor (CTP), which makes decisions based on the combined information and for up to 256 trigger items. This level reduces the overall rate to at most 75 kHz.

Information from the L1 selection is passed to the high level trigger [68] (HLT) system, which are hardware- and software-based systems consisting of the Level-2 (L2) and event filter (EF) triggers. The L2 trigger assembles the full detector information from regions of interest (RoIs) identified as having an L1-triggered object and performs an event selection. Algorithms like calorimeter clustering, tracking, and cluster-track matching can be used in the L2 event selection process. This level reduces the overall rate to 3.5 kHz. Finally, the event filter (EF) trigger performs a selection based on properties of an offline event reconstruction. It is seeded by the decisions of the L2 event selection, and categorizes events by selected objects into data streams: electron, muon, jet, photon, tau and $E_{\mathrm{T}}^{\mathrm{miss}}$, and b physics. This level reduces the final rate to 200 Hz, and provides seed events for offline analysis.

[2] Transverse energy is defined as $E_T = \sqrt{m^2 + p_{\mathrm{T}}^2}$; it is commonly used to describe calorimetric energy measurements, which are performed in $\Delta\eta \times \Delta\phi$ regions with their axis perpendicular to the beam axis.

3. Detector simulation

The complexity of the hardware systems described for measuring event data makes straightforward, high-precision calculations of how real events are likely to appear in the detector difficult. A software simulation of the ATLAS detector [69, 70] automates these predictions by simulating the propagation of particles through the detector components and their interactions with sensitive regions and signal transmission. The simulation takes as input collision events generated by other programs and propagated to the state expected before entering the detector, and produces an estimate of the signals generated by the resulting particles. Events are generated via *Monte Carlo* (MC) methods, based on calculated differential cross-sections for the processes of interest. Then, the simulation emulates the material composition and distribution in the detector, including all service material (e.g. support structures, physical electronic components), and simulates particle propagation and decay through this material, storing interactions inside sensitive components into hits with location, energy deposition, and time recorded. Then, these hits are digitized by simulating the actions of the electronics in producing the signal which is read out, and simulating the effect of trigger decisions. The primary pp collision in which the interaction of interest takes place, called the *hard* interaction, is combined with additional interactions which add low-energy signals to the readout in real data, called *pile-up*, and with electronic detector noise.

The MC method for event generation begins with a calculation of the matrix element and differential cross-sections for a particular process. These distributions are used as probability distributions in one or more variables which dictate how often the interaction takes place, and with what kinematic properties. These distributions are then randomly sampled to simulate events arising from this process. The parton-level interaction is related to the two-proton initial state by the PDFs of each proton, as described in Equation II.15, and the resulting distributions referring to the hard interaction are fed into a parton shower (PS) simulation which fragments free quarks and adds initial-state and final-state gluon radiation. Finally, the result of the parton shower is sent to a hadronization routine which collects all free partons into hadrons to complete the event description. These process can be carried out with a variety of existing programs; the routines used in the analyses described in Chapter V

and Chapter VI will be discussed explicitly.

The detector simulation is built with the GeoModel toolkit [71], a shape library, and translated into a full description of the detector shapes and materials in GEANT4 [72]. A library of detector conditions which could change frequently during a run, such as calibration constants, dead channels, or detector misalignments, is applied to each simulation run. The GEANT4 program propagates particles through the detector with short distance steps between potential interactions, and uses a list of applicable physics processes to decide whether or not any of a list of possible interactions should take place at each step. If an interaction is chosen to happen, the resulting final state is recorded as the starting point for the next step. A trajectory is terminated when the particle decays, traverses its full "range" defined by the energy loss or absorption length in the detector, or when it escapes the detector region. Any time an interaction results in energy loss in a sensitive detector region, this is recorded as a hit for which the position, energy deposition, and time are stored.

The hits in sensitive regions stored during the simulation are then sent to the digitization software, which simulates the operation of the electronic components specific to each subdetector in producing digital signals. The specific properties of the electronics installed in the detector are emulated, and run conditions such as dead channels are read from the detector conditions database. Up to this point, the simulation has followed a single elastic pp interaction; during digitization, the effects of pile-up interactions, like inelastic pp interactions and detector activity from neighboring bunch crossings, are overlaid on the primary event. L1 trigger decisions are also simulated at this step; no events are removed, and the decision is stored. The information output from this procedure is equivalent to the signals recorded from real events, and the same processing can be performed on both types of events from this point onward.

a. Optimization A number of optimizations are used in the GEANT4 simulation to reduce the simulation time needed for each event. One such optimization replaces some species of particles below a defined energy threshold at the inner edge of a calorimeter with one of a pre-simulated library of *frozen showers* [73], rotated and scaled to match the energy and direction of the original particle. Frozen shower libraries are implemented for electrons and

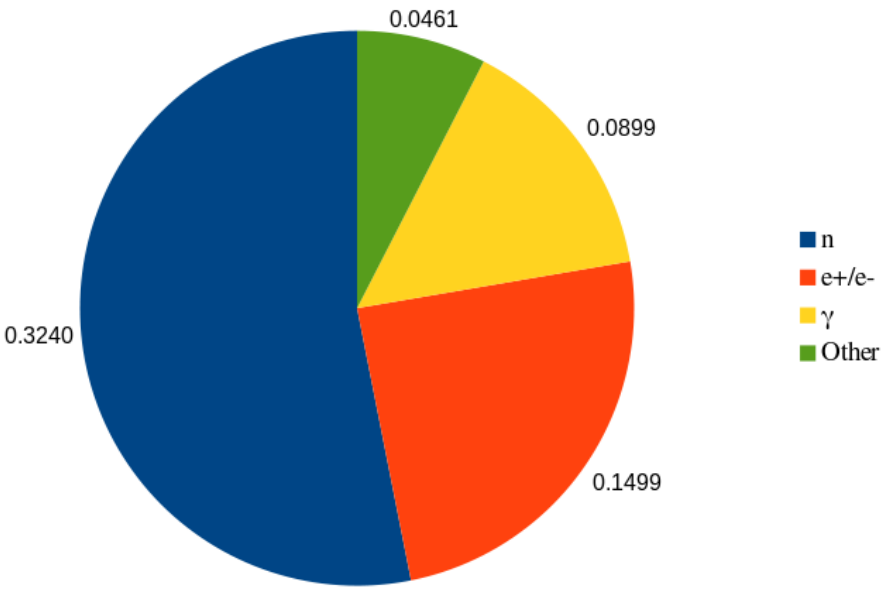

Figure III.10: Timing information for particle propagation in the ATLAS detector simulation. The fraction of the total simulation time spent transporting each particle species is indicated.

positrons with 10MeV $< E_e <$ 1000MeV, and for photons with $E_\gamma <$ 10MeV, energy regimes in which the full detail of the shower is generally not needed for understanding high-energy processes. To investigate whether there were additional particles or detector components that made good candidates for similar optimizations, I developed a tool to check the simulation time for individual particles and detector volumes. Timing of neutron propagation in the LAr calorimeters, a detector which is rarely important for neutron reconstruction, was found to take up more than 50% of the simulation time (see Figure III.10). I was able to reduce neutron simulation times by placing a cut on neutrons in the calorimeter at $E_n >$ 100MeV, as shown in Table III.1. These findings resulted in the creation and addition of neutron frozen-shower libraries to the detector simulation, implemented in a similar energy regime.

I also had the opportunity to work on the geometry implementation of the detector simulation. The actual construction of the detector is sometimes different from the planned design, and in many such cases the simulation was constructed to match the former. In many cases, the difference does not affect the performance of the simulation in comparison to the

Table III.1: Integrated CPU time t^{CPU} spent transporting electrons and neutrons in some calorimeter volumes, before and after imposing the requirements $E_e > 100\mathrm{MeV}$ and $E_n > 100\mathrm{MeV}$, and the time reduction factor achieved by each cut.

Volume	t^{CPU} [s]	t_e^{CPU}	R_e	$t_{e,n}^{\mathrm{CPU}}$	$R_{e,n}$
Atlas::Atlas	58000.10	28290.89	2.05	18653.03	3.11
BeamPipe::BeamPipe	2564.67	—	—	3146.49	0.82
IDET::IDET	2873.28	—	—	3551.46	0.81
MUONQ02::MUONQ02	1710.76	—	—	2198.25	0.78
CALO::CALO	50453.61	18285.72	2.76	9232.11	5.47
LArMgr::LArMgr	49425.20	17121.42	2.89	8469.35	5.84
LArBarrel	6528.77	2115.68	3.09	1572.37	4.15
Total LAR Volume	5824.49	1573.36	3.70	54.67	5.52
LAr::Barrel::Cryostat::HalfLAr::PosPhysical	2914.44	744.75	3.91	547.51	5.32
LArEndcapPos	21108.76	6995.00	3.02	3319.20	6.36
LAr::Endcap::Cryostat::EmecHecLAr	8367.67	3135.87	2.67	1204.75	6.95
LArMgr::LAr::EMEC::Mother	7469.67	2165.56	3.45	574.29	13.01
LArMgr::LAr::FCAL::LiquidArgonC	10906.52	2701.64	4.04	792.10	13.77
LArMgr::LAr::FCAL::Module1::Absorber	6630.70	831.91	7.97	201.96	32.83
LArMgr::LAr::FCAL::Module2::Absorber	2827.05	1257.28	2.25	255.51	11.06
LArMgr::LAr::FCAL::Module3::Absorber	1110.16	409.34	2.71	108.36	10.25

real detector, but when it does, the difference can be checked to first order by comparing the the fraction of readout channels registering activity in each event, or *occupancy*, of the real detector to that of the simulation. The state of the occupancy comparison in the summer of 2010 is given in Figure III.11, which shows a significant deficit in the occupancy of the simulated liquid-argon calorimeter in channels near $\phi = 0$ and $\phi = \pi$. After inspecting this region, it was seen that the rails on which the inner detector rests inside the calorimeter had been implemented with a different design than that used in the simulation, as shown in Figure III.12. This component of the rails was redesigned to match the final implementation, and these changes to the geometry are now standard in the ATLAS simulation.

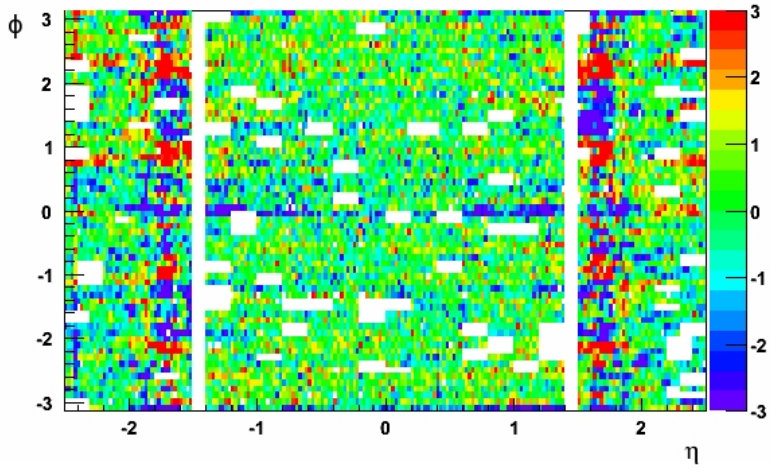

Figure III.11: Occupancy difference significance of liquid-argon calorimeter sensitive regions in η vs. ϕ.

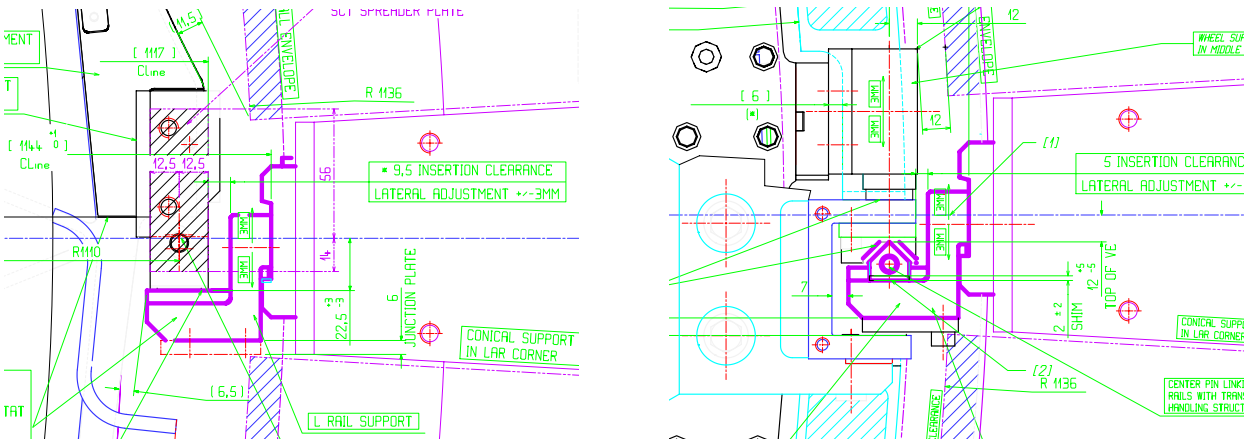

(a) (b)

Figure III.12: Schematic of the inner detector rails, (a) as originally designed, and (b) as implemented.

IV. PHYSICS OBJECT IDENTIFICATION & RECONSTRUCTION

Data collected by the ATLAS detector starts out as electronic signals generated in its subdetectors. These signals are converted into a bytestream and read out from the detector electronics for real pp collisions, and this process is emulated for MC simulation events passed through the detector simulation in the digitization step. The bytestream represents information about the quantity, location, and time of energy deposits in the inner detector, calorimeters, or muon spectrometer. To begin relating this information to descriptions of the underlying physics of the event, algorithms are applied to group these energy depositions in patterns associated with different physics phenomena. Tracks left by charged particles in the inner detector and muon spectrometer are reconstructed from hits in these high-granularity detectors, and individual calorimeter cell energy depositions are clustered to represent showers from individual particles. Tracks and calorimeter clusters, and their relationships to one another, are used to reconstruct particles or more general final state objects based on their charge, mass, decay length, and other properties. Electrons, muons, jets, and $E_{\mathrm{T}}^{\mathrm{miss}}$ can all be reconstructed in this way, and higher-order relationships between these objects can be used to identify the signatures of short-lived SM particles, like the b and t quarks, and identify events most likely to contain these particles.

A. TRACKS AND PRIMARY VERTICIES

In the inner detectors, an event contains a set of spatially-constrained signals representing hits in the various subdetectors, with some extent in η and ϕ dependent on the segmentation of the detector. These signals can be grouped into tracks which follow a physical,

typically curved, path through the detector [74]. Reconstruction methods used in the inner detectors are an *inside-out* reconstruction, where tracks in the Pixel and SCT detectors are supplemented by hits in the TRT, and a subsequent *outside-in* method, where the opposite is done to resolve ambiguous hits or tracks arising from secondary vertices. These two routines also produce an estimate for the location of primary and secondary interaction vertices, or tracks with kinks resulting from *bremsstrahlung* radiation of photons. Tracking in ATLAS is designed to be available to both offline analyses and at the event filter (EF) trigger. The necessary speed is achieved by seeding tracks with ROI information from the L2 trigger, then applying the same track-finding procedures described.

Inside-out track reconstruction begins with the construction of 3-dimensional objects, representing the physical elements activated by each hit in the Pixel and SCT detectors. These volumes are grouped into track seeds; two detector elements and a z-vertex constraint are first used to predict vertex positions, then groups of three further constrain tracks originating near these vertices. Beginning with these track seeds, a *Kalman filter* [75] reconstructs track candidates by following each possible track's trajectory from one tracking detector layer to the next, adding the information from nearby hits at each layer as it is reached, and updating the trajectory before extending it to the next layer. After the remaining ambiguities between tracks are resolved through a scoring system based on numbers of hits in each layer, the tracks are extended into the TRT where hit associations are registered without altering the tracks. Finally, a refit of the track is performed using the Pixel, SCT, and TRT extension together, and the scoring is recalculated. The track associated with the higher score between this combined fit and the silicon-only fit is retained.

After reconstructing tracks with the inside-out method, an outside-in track reconstruction [76] beginning in the TRT is performed. This procedure is meant to identify tracks which fall into the ambiguous cases mentioned, but cannot be resolved when the silicon detector track is given primacy; only hits not associated with inside-out tracks are considered. Outside-in reconstruction begins by finding track candidates from hits in the TRT straw-tube tracking detector. These hits are resolved only in the plane perpendicular to the direction of the straw tubes, $r - \phi$ for the barrel and $r - z$ for the endcaps. Segments are constructed from these hits for tracks above 500 MeV by searching in the parameter space

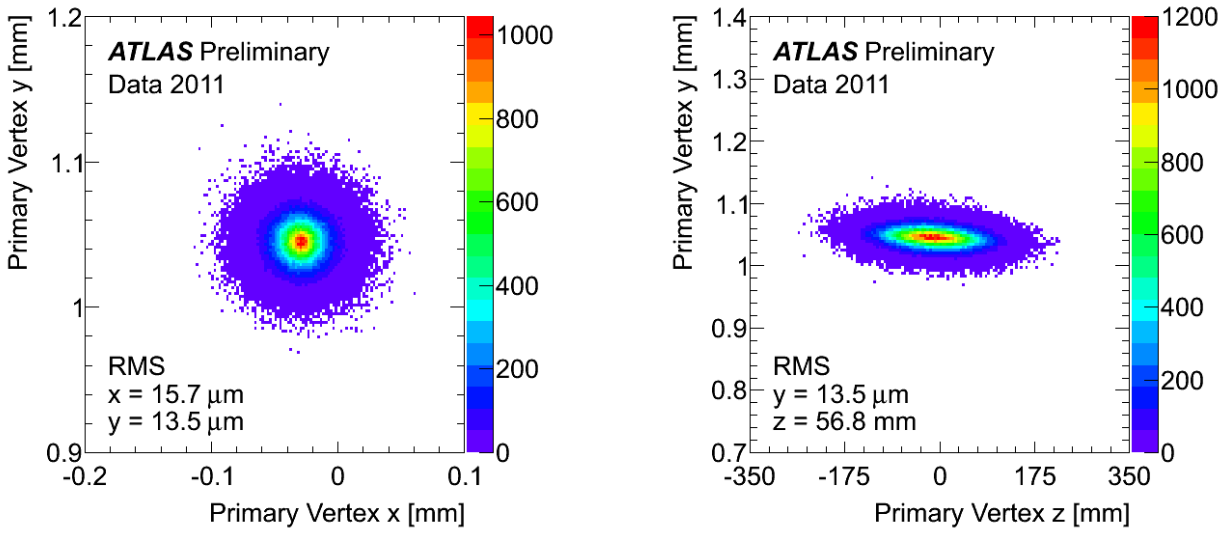

(a) (b)

Figure IV.1: Reconstructed primary vertex position distribution in 2011 data at $\sqrt{s} = 7$ TeV, projected into the (a) $x - y$ and (b) $y - z$ planes. See Ref. [77].

describing possible lines in this plane for the greatest number of hits which can be associated to this line, called a Hough transform. This is done independently for multiple slices in η, to reduce the overlap in potential track segments. The segments are further resolved by choosing those which cross the most straw tubes, and setting a minimum on the number of tubes crossed, then smoothing them with a Kalman filter. The TRT track candidates are checked for extensions into the silicon detectors, first by searching for track seeds in the SCT in $r - \phi$ bins which meet some requirements on the track direction and curvature. These seeds are converted into candidates, and any remaining ambiguities are resolved to produce final tracks via the same methods described for inside-out tracking.

Reconstructed tracks are used to identify which interaction vertices are candidates for the primary vertex, and to reconstruct their position and assign an associated uncertainty. An iterative algorithm is used to identify a primary vertex. First, a vertex seed is created from the maximum of the distribution of track z_0, the longitudinal impact parameter of a track relative to the center of the coordinate system, for tracks with 4 hits in the SCT, 6 hits

combined between the Pixel and SCT detectors, $p_{\mathrm{T}} > 150$ MeV, $|d_0| > 4$ mm, $\sigma(d_0) < 5$ mm, and $\sigma(z_0) < 10$ mm. The position of this vertex is then fit based on the seed location and the nearby tracks, using an adaptive vertex fitter [78]. Any track inconsistent with the vertex found by this procedure at $> 7\sigma$ is then associated to a new vertex, and the procedure is repeated for each vertex until no tracks are incompatible at this level with their associated vertices. After the primary vertices are determined, the associated tracks are refit with the reconstructed vertex set as their point of origination.

B. CALORIMETER CLUSTERING

The calorimeters are segmented into independent cells, defined by their extent in $\Delta\eta \times \Delta\phi$, where energy deposition can be resolved. Often, multiple nearby cells contain the total energy deposited by a particle shower. Calorimeter clustering [79] groups cells into objects representing this total energy deposit, to be used in reconstruction algorithms for identifying specific types of particles. Two such algorithms are used by the ATLAS experiment, each suited to reconstructing different physics objects. A "sliding window" algorithm sums the energy depsoited in all cells in a rectangular window. A topological algorithm starts with a seed cell and iteratively adds nearby cells above some noise threshold.

Clusters constructed with the sliding window algorithm are used in ATLAS to define electromagnetic showers and combined clusters containing information from both the EM and hadronic calorimeter for τ-lepton identification. First, towers are built from cells in $\Delta\eta \times \Delta\phi$ regions of dimension 0.025×0.025 for EM calorimeter towers and 0.1×0.1 for combined towers, from all available calorimeter layers. Cells which fall within several towers have their energy divided amongst the towers according to the fractional area associated with each. Next, a window 5 towers to a side is moved across the grid of towers, and window positions with total energy at a local maximum and above a threshold of 3 GeV for EM towers and 15 GeV for combined towers are identified as preclustering seeds. Their location is set at the center-of-mass determined from a sliding 3×3 window within the precluster region. Combined clusters are constructed directly from these seeds by combining the energy

measurements of all cells contained in the window. Electromagnetic clusters are then filled on a layer-dependent basis, with different window definitions specified. In the barrel, a 3×7 window is used to create clusters for electrons or photons converted to electron-positron pairs, and a 3×5 window is used for photons. In the endcaps, a 5×5 windown is used for all possibilities, with small variations depending on the radial distance of the layer. The seed location is determined similarly to the precluster location, and the locations determined in each layer are used as the seeds for the adjacent layer. The cells in the windows determined at each layer are then combined into the final cluster.

The topological algorithm is used in ATLAS particularly for jet and $E_{\mathrm{T}}^{\mathrm{miss}}$ reconstruction. It is divided into a cluster building algorithm and a splitting algorithm which separates adjacent and overlapping clusters. Here, individual cells serve as both the seeds and additive components for cluster construction. First, seeds are identified as cells with a signal-to-noise ratio t above some high threshhold, t_{seed}. Then, for seeds ordered in t from greatest to least, the neighboring cells above a medium threshold $t_{\mathrm{neighbor}} < t_{\mathrm{seed}}$ are added to a list of neighbor seeds for that cluster. If the neighboring cell is below t_{neighbor} but above a low threshold $t_{\mathrm{cell}} < t_{\mathrm{neighbor}}$, it is added to the cluster, but not stored in the list of neighbor seeds. Once all the seeds have been processed in this way, the lists of neighbor seeds are each processed, iterating until no more seeds are found. The values of the thresholds assigned for electromagnetic clustering are $t_{\mathrm{seed}} = 6$, $t_{\mathrm{neighbor}} = 3$, and $t_{\mathrm{cell}} = 3$, while for combined clustering, $t_{\mathrm{seed}} = 4$, $t_{\mathrm{neighbor}} = 2$, and $t_{\mathrm{cell}} = 0$.

This clustering procedure is adequate for signals which are well-separated in the calorimeter, but in real collision data, the energy deposition patterns left by high-energy particles producing a shower in the calorimeters are often nearby or overlapping. A cluster splitting procedure follows to split clusters likely to arise from multiple separate physics objects. First, local maxima are identified within clusters as having greater energy than any neighboring cell. If more than one local maximum is found, $N_{\mathrm{local}} > 1$, it is split into N_{local} separate clusters. The clustering procedure is then reapplied to only the cells contained in each cluster, but using the absolute cell energies rather than signal-to-noise ratios t. When cells are found adjacent to two or more clusters, they are assigned to be split between the two with the greatest total energy. The list of shared cells is expanded by adding any neighbors in

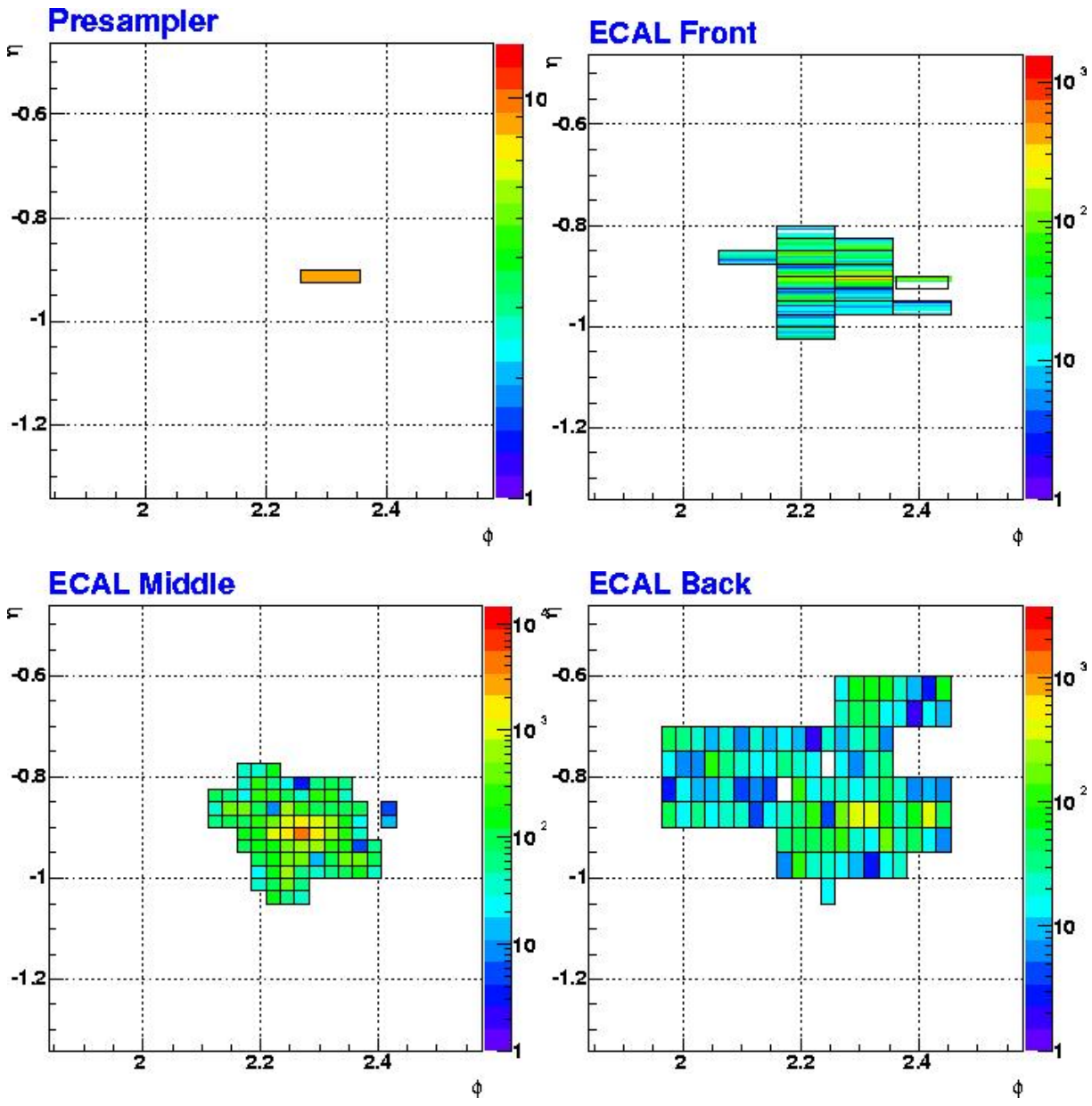

Figure IV.2: A combined (electromagnetic and hadronic calorimeter) topological cluster for a simulated jet with $p_{\mathrm{T}} > 70$ GeV and $|\eta| < 5$. Only components in the electromagnetic calorimeter are shown, separated by layer. The z-axis colors indicate cell energy in MeV. Courtesy of the ATLAS Collaboration.

the original list of clustered cells that have not yet been reclustered, and the shared cells are finally divided between the two clusters according to their relative energies and the relative distance of the cell from their centers. These procedures are performed iteratively until no previously clustered cells remain unassigned.

C. ELECTRONS

Electrons produced near the primary vertex can be reconstructed from one or more tracks in the inner detectors and showers in the electromagnetic calorimeter. The reconstruction procedure [80, 81, 82] begins by identifying electron candidates from sliding-window calorimeter clusters with a 3×5 window, keeping clusters with $E > 2.5$ GeV. In the region $|\eta| < 2.5$ covered by the inner detectors, an electron must have one or more reconstructed tracks matched to a cluster, seeded by the candidates constructed in the previous step. The track-cluster matching is performed by extending the track to the second layer of the electromagnetic calorimeter and comparing the η and ϕ coordinates of the impact point to those of the cluster. A match must satisfy $\Delta\eta < 0.05$; to account for bremsstrahlung losses, $\Delta\phi < 0.1$ is required on the side the extrapolated track bends towards, and $\Delta\phi < 0.05$ is required on the opposite side. If multiple tracks satisfy these conditions for one cluster, the associated track is preferred to have hits in the silicon detectors, and among those remaining, the track-cluster pairing with the smallest $\Delta R = \sqrt{\Delta\eta^2 + \Delta\phi^2}$ is chosen.

Once the track-cluster matching is performed, the cells are reclustered with the sliding windows defined for electrons in Section IV.B. The energy of the resulting cluster is computed from the total energy deposit in the cells, with estimated corrections applied for energy deposits in the calorimeter but outside the cluster, and in the material before and beyond the calorimeter. These corrections are determined from comparisons of detailed simulations and real data for the $Z \to e^+e^-$ decay process. Assigning this energy as the total energy of the electron, its momentum is determined from the matched track, with η and ϕ taking the values determined at the vertex. In the region $2.5 < |\eta| < 4.9$, only the calorimeter has coverage and the electron must be defined from calorimeter cell and cluster information.

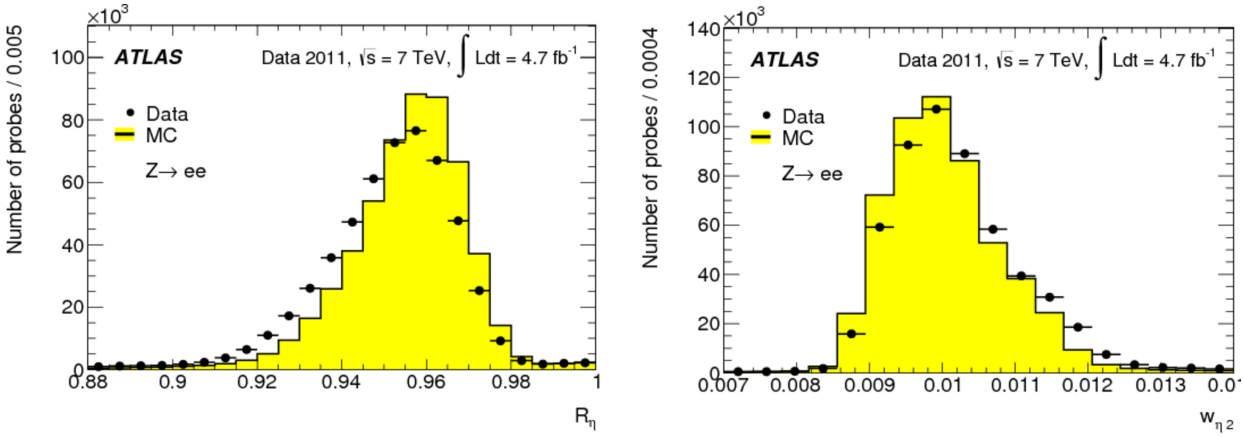

(a) (b)

Figure IV.3: Comparisons of two shower shape variables for $Z \to e^+e^-$ events between MC simulation and data, for electrons with 40 GeV$< E_T <$45 GeV: (a) R_η, the ratio of energies in 3×7 cell clusters to that in 7×7 cell clusters, and (b) $w_{\eta 2} = \sqrt{< \eta_i^2 > - < \eta_i >^2}$, the shower width in η. See Ref. [81].

Here, topological clustering is used to estimate the energy of the electron, and its direction is defined by the center of the cluster. In this region, only electrons with transverse energy $E_T > 5$ GeV and with a small hadronic energy deposition are reconstructed.

The cluster energies measured for electron candidates are calibrated for a $\sqrt{s} = 7$ TeV center-of-mass [83] to bring energy measurments in MC simulation and data into agreement. First, simulated electron cluster shapes and their relationship to the true and measured energies of electrons are used to train a multivariate machine-learning algorithm [84]. The resulting mappings are applied to MC simulation samples and real data with the relative energy scales between calorimeter layers corrected to match that in the MC training samples, to determine an overall energy scale correction. Next, collision data is corrected for variations in the signal response measured in particular regions of the calorimeter. Then, $Z \to e^+e^-$ events are compared between the simulation and data. Scale factors are determined which bring distributions of electron kinematics in the data into agreement with those in the simulation, and the resolution in simulation is broadened to match that in data.

Finally, the calibrated electron energy scale is validated with $J/\psi \to ee$ events in data. The same calibration procedure is used for photons, including the same $Z \to e^+e^-$ scale factors, and is validated with $Z \to \ell^+\ell^-\gamma$ events.

Electrons are selected from reconstructed and calibrated candidates passing requirements on the variables associated with each candidate, called *cuts*. These cuts distinguish electrons originating at the primary vertex from electrons resulting from photon conversion, secondary decays of other particles, or hadronic jets producing an electron-like signal. Three sets of cuts are used for identification, each of which is a subset of the next most stringet requirements. The values at which the cuts are made are optimized in 10 η bins and 11 E_T bins from 5 GeV to 80 GeV. Electrons selected by each set are labeled *loose*, *medium*, or *tight*. Electrons labeled *medium* and *tight* are both used in the analysis presented in Chapter VI. Real electrons coming from the hard interaction, called *prompt*, are identified with *tight* requirements, while non-prompt electrons or those from certain background events which mimic the signal are identified with *medium* requirements. The *medium* requirements used in this analysis, denoted `medium++` to distinguish it from earlier versions, improves background rejection by a factor of about 50 with cuts on the leakage of the shower into the hadronic calorimeter, the width of the shower, and the quality of the matched track. The corresponding `tight++` cuts further improve rejection by a factor of 2 over the `medium++` criteria, with additional cuts on track quality, track-cluster matching, and removal of reconstructed photon conversions. In the forward region, no tracking information is available, and requirements on track quality and matching are replaced with with extra shower shape variables using *cluster moments*, $\langle x_i^n \rangle$, defined as energy-weighted averages of variables like the distance of a cell to the shower center. Further details on the selection criteria are given in Ref. [81].

D. MUONS

Muons [85, 86] are reconstructed from tracks in the muon spectrometer, described in Section III..2.e, which are matched to a track in the inner detector. Hits in the MDT and CSC components of the muon spectrometer (MS) give precise measurements of the muons'

deflection by the magnetic field, which improve energy and momentum measurement, while the RPC and TGC components provide the rest of the directional information. Hits in both types of detectors are necessary to define a muon track. Muons can be reconstructed with information from the MS, inner detectors, and calorimeters in different combinations, resulting in four "types" of reconstructed muons. Stand-alone (SA) muons use only the hits in the MS to reconstruct the track and determine the muon's four-momentump; SA muons are often used for reconstruction in the region $2.5 < |\eta| < 2.7$ covered by the MS and not the inner detectors. Combined (CB) muons match tracks reconstructed in the MS and in the inner detector, which make up the majority of reconstructed muons and are the only type used in the analyses presented in Chapters V - VI. Segment-tagged (ST) muons match reconstructed tracks in the inner detector to hits or track segments in the MS, useful for low-p_{T} muons or those in a low-acceptance region of the MS. Finally, calorimeter-tagged (CaloTag) muons match a track reconstructed in the inner detector to a calorimeter deposit matching that of a minimum-ionizing particle, which are useful in gaps in the sensitive regions of the MS at $|\eta| < 0.1$.

The three reconstruction algorithms using muon-spectrometer tracks are performed by two chains in tandem [87], which reconstruct muons of each types with different strategies, known as Staco and Muid. Both chains begin by building track segments in the MS and combining them into full tracks. The Staco algorithm finds straight-line connections in the bending plane of the magnetic field and additional associated information in the other directions when available, while Muid uses Hough transforms in the bending and non-bending planes. The resulting tracks are then extrapolated back to their point of closest approach to the beamline. To combine MS tracks with inner detector tracks for CB muon reconstruction, Staco forms a statistical combination of the two tracks weighted by their covariance matrices, and Muid performs a new fit of the information used to reconstruct the MS track, starting with the inner detector track. Finally, two separate approaches are used for extending inner detector tracks and attempting to match nearby MS track segments to produce ST muons. The Staco-related algorithm uses a chi^2 fit and only considers tracks not used in the previous step, while the Muid-related algorithm uses an artificial neural network over all tracks to select these muons.

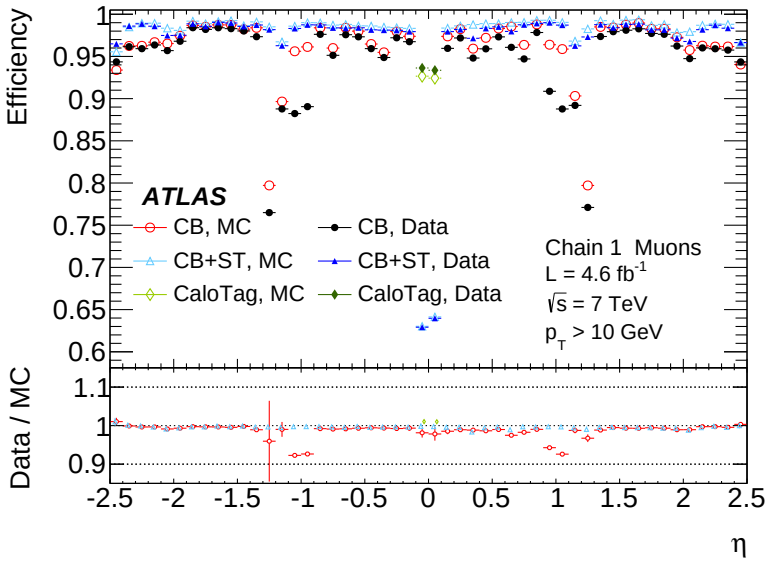

Figure IV.4: Muon reconstruction efficiency measured in $Z \to \mu\mu$ events for different reconstruction algorithms in $\sqrt{s} = 7$ TeV MC simulation and 2011 data. See Ref. [86].

All inner detector tracks used for matching with MS tracks, or in CaloTag muons, are chosen to have 1 hit in the Pixel detector, 5 hits in the SCT, at most 2 layers with no hits in these two detectors combined, and 9 hits in the regions of the TRT where full acceptance is expected. Muon energy measurements are corrected for extrapolated depositions in the calorimeter, with a minimum of 3 GeV lost in traversal. The resulting efficiencies for reconstructing muons with $p_{\mathrm{T}} > 10$ GeV are close to 1 for the majority of the region within $|\eta| < 2.5$, as shown in Figure IV.4. The drop in efficiency in the region $|\eta| < 0.1$ is where only CaloTag muons can be used, and the dip around $1.1 < |\eta| < 1.3$ is in a region where in 2011 some muon spectrometer components were not yet installed. Further details on muon validation can be found in Ref. [86].

E. JETS

Jets originate from high-energy quarks or gluons in the final state of the hard interaction, which fragment into multiple new quarks and gluons that then hadronize, or combine into colorless mesons and baryons. They are defined primarily by the energy deposits left in the electromagnetic and hadronic calorimeters from these hadrons, which are largely contained by showering in these detectors. They are defined by grouping energy deposition in individual calorimeter cells according to a topological clustering algorithm. The most common in ATLAS is the anti-k_T algorithm [88], which is used for all the jets discussed in the analyses presented in Chapters V - VI. The basic principle of this algorithm is the sequential grouping of *proto-jet* objects with defined four-momentum p_i^μ, like individual or grouped calorimeter cells, according to a requirement placed on a distance measure between two proto-jets, d_{ij}, and a decision measure for each proto-jet d_i. Given a combined list of d_{ij} and d_i, if the smallest value is a d_{ij}, the two proto-jets it compares are combined, and if the smallest is a d_i, clustering is terminated and the object is classified as a jet. For the anti-k_T algorithm, these measures are

$$\begin{aligned} d_{ij} &= \min\left(\frac{1}{k_{Ti}^2}, \frac{1}{k_{Tj}^2}\right) \frac{(y_i - y_j)^2 + (\phi_i - \phi_j)^2}{R^2}, \text{ and} \\ d_i &= \frac{1}{k_{Ti}^2}. \end{aligned} \tag{IV.1}$$

Here, k_T is the transverse energy of the proto-jet, y is the jet rapidity, and the parameter R represents a cutoff cone size in y and ϕ. This produces jets initiated by proto-jets forming around the largest energy deposits, then adds nearby cells with smaller deposits until reaching the cone radius R, and generally divides proto-jets among overlapping jets based on their overall transverse momenta. For the ATLAS experiment, jets are constructed with the FastJet [89] implementation of the anti-k_T algorithm with maximum allowed sizes in ΔR of either 0.4 or 0.6. Either calorimeter clusters or tracks can be used as proto-jets, and the resulting jets are named *calorimeter jets* or *track jets*, respectively. Track jets are often used when the structure of the jet is of primary importance to the analysis, such as in boosted final states; only calorimeter jets are discussed here.

A set of calibrations [90] are applied to both clusters used to find jets, then the jets themselves, to account for inefficiencies in the calorimeters' energy measurements. Clusters used to find calorimeter jets are initially reconstructed at the electromagnetic (EM) scale, by measuring energy deposits from particles produced in electromagnetic showers. A second calibration step, called local cluster weighting (LCW), classifies clusters as electromagnetic or hadronic, then uses single-pion MC simulations to derive corrections to the clusters. A series of calibrations are applied to jets found in real data with either cluster type to restore their energy scale to that measured in jets constructed from the true kinematics of particles in MC simulation events, called *truth jets*. First, a correction is applied to remove excess contributions to cell energies from particles arising from pileup interactions, as a function of the number of primary vertices and the expected number of interactions and in bins of η and p_{T}. Next, the jet direction is corrected by shifting its origin from the coordinate system origin to the location of the primary event vertex. Then, corrections are applied to jets measured in data based on comparisons of events containing two isolated jets, called *dijet* events, between MC simulation and data. Finally, *in situ* corrections are applied which harmonize momentum balances between central and forward jets, a jet and a photon or Z^0 boson, a photon and the full hadronic recoil, and a high-p_{T} jet with a collection of low-p_{T} jets. Jets formed with EM (LCW) clusters, and with these correction applied, are referred to as being calibrated with the EM+JES (EM+LCW) scheme.

Quality cuts [91] are also applied to jet collections, especially to remove jet candidates not originating from the hard-scatter primary vertex of interest in the event. These may include protons interacting with the residual beam gas or in the beam halo, cosmic rays overlapping in time with collision events, and electronic noise in the calorimeter. Noise bursts are characterized by a large fraction of jet energy arising in a particular calorimeter component, including cells with poor signal quality, and the appearance of a negative energy in neghboring cells. These quantities are all required to be below a threshold. Other non-collision backgrounds can produce signals out-of-time with the collision, so a cut on the jet time, defined as the cluster moment of the reconstructed cell times $< t_i^{\mathrm{cell}} >$, is applied. A real jet is expected to produce tracks and deposit some energy in the electromagnetic calorimeter. Signals which have no such depositions are removed with cuts on the fraction

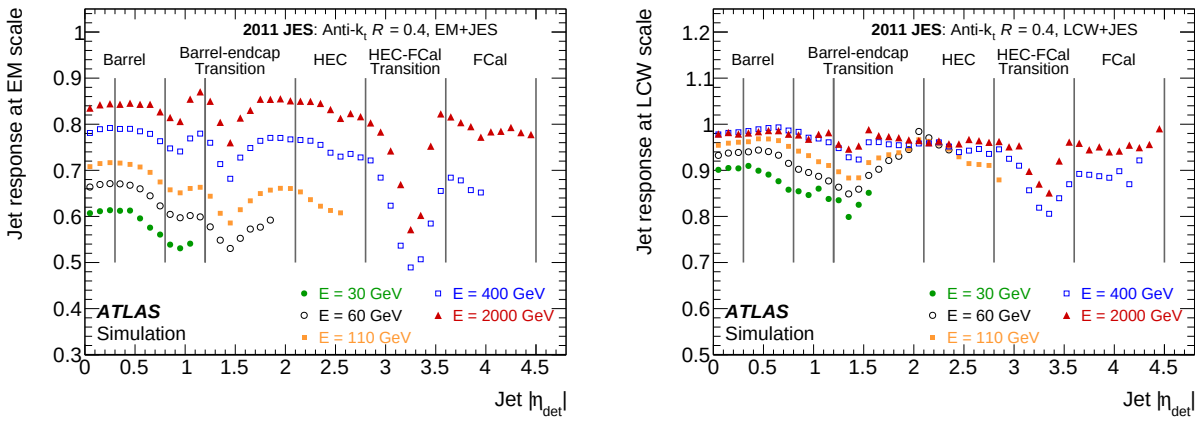

(a) (b)

Figure IV.5: Response function $\mathcal{R}^{\text{calib}} = E_{\text{jet}}^{\text{calib}}/E_{\text{jet}}^{\text{truth}}$ of simulated jets at the (a) EM scale and (b) LCW scale, for different energies and as a function of jet $|\eta|$. The inverse of $\mathcal{R}^{\text{calib}}$ is applied as the JES correction for that calibration type. See Ref. [90].

of the jet energy coming from the electromagnetic calorimeter, f_{EM}, and the ratio of the scalar sum of the p_{T} of tracks associated to the jet to the p_{T} of the jet, called the jet charged fraction, f_{ch}. Finally, if the jet's energy is entirely deposited in one layer of the calorimeter, it likely originates from a non-collision background. Cuts on the fractions of the energy appearing in each layer, f_{layer}, removes these candidates. These variables are used to define multiple levels of selection with increasing purity; the loosest selection has an efficiency of over 99%.

F. MISSING TRANSVERSE ENERGY

Observable objects in the ATLAS detector, like those described in Sections IV.C - IV.E, are characterized by energy depositions in either the tracking detectors or the calorimeters. However, given that at least one class of known particles (neutrinos) and a number of hypothetical particles interact very rarely, some energy produced in the initial collision

will not be accounted for by energy depositions in any part of the detector. This energy is quantified [92] by calculating the momentum imbalance in the transverse direction for all calorimeter depositions and reconstructed momenta in the muon spectrometer, and defining a vector called missing transverse momentum, $\vec{E}_{\mathrm{T}}^{\mathrm{miss}}$, to restore its conservation. The missing transverse energy, $E_{\mathrm{T}}^{\mathrm{miss}}$, is its magnitude, and its direction is given by ϕ^{miss}.

The magnitude and direction of $\vec{E}_{\mathrm{T}}^{\mathrm{miss}}$ are defined from x and y components, $E_{x,y}^{\mathrm{miss}}$, which each are the sum of components determined from the calorimeters and the muon spectrometer. The calorimeter terms are derived from the sum of the x and y components arising from each object identified with calorimeter clusters. The transverse momenta from each such object are projected the x and y components of each cell's positions and summed, and the $E_{x,y}^{\mathrm{miss}}$ components are defined to make the sum 0. Electrons, photons, jets from hadronically-decaying taus, and jets from other sources are all separately included. A final term is introduced to include clusters not associated to any reconstructed objects, called the CellOut term, which is important to the $\vec{E}_{\mathrm{T}}^{\mathrm{miss}}$ resolution. Calibration of the calorimeter terms is performed separately for each cell included in the calculation, following the procedures used for each object. Electron and photon cells are only considered if $p_{\mathrm{T}} > 10$ GeV, and are taken only from calibrated electrons and uncalibrated photons. Tau leptons are also required to have $p_{\mathrm{T}} > 10$ GeV, and cells are taken from LCW-calibrated jets identified as hadronically decaying tau leptons. Jets between $7\mathrm{GeV} < p_{\mathrm{T}} < 20\mathrm{GeV}$ are also calibrated with the LCW scheme, and have a width parameter of $R = 0.6$, while jets with $p_{\mathrm{T}} > 20$ GeV use the full LCW+JES scheme. Finally, unaffiliated clusters in the CellOut term are calibrated with LCW and have contributions from low-p_{T} tracks which have momenta reconstructed in the inner detector but which do not reach the calorimeter. These are of particular importance in low-particle-multiplicity W/Z events.

Following the calorimeter's contribution, the the x and y momentum components of combined muons are summed to determine the momentum balance of the tracks in the muon spectrometer, and its contribution is also defined as the x and y components which would make this sum 0. If a muon is isolated from all jets by at least $\Delta R > 0.3$, or is in the region $2.5 < |\eta| < 2.7$ where track-matching can't be used, then the muon p_{T} measurement includes its energy deposition in the calorimeters and the muon contribution to the calorimeter term

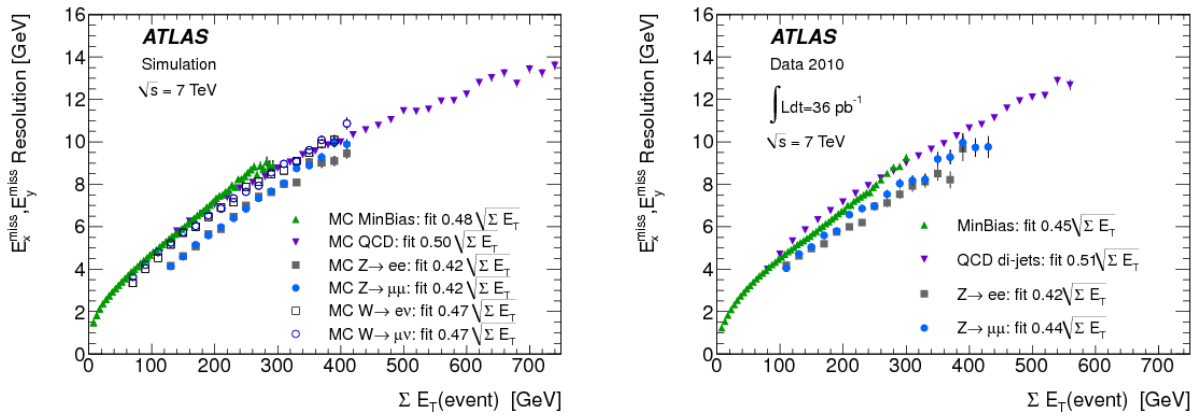

(a) (b)

Figure IV.6: Resolution of the 2-dimensional $E_{\mathrm{T}}^{\mathrm{miss}}$ distribution (combined E_x^{miss} and E_y^{miss} distribution) as a function of the sum of the transverse energy of all other objects in the event, $\sum E_{\mathrm{T}}$, for (a) MC simulated events from QCD, $Z \to \ell^+\ell^-$, and $W \to \ell\nu$ decays, and (b) data taken with $\sqrt{s} = 7$ TeV for QCD and $Z \to \ell^+\ell^-$ events. The resolution is generally stochastic, and can be described by a function of the form $\sigma = k\sqrt{\sum E_{\mathrm{t}}}$. See Ref. [92].

must be removed. Otherwise, the muon p_{T} is only measured from the muon spectrometer track, after energy loss in the calorimeter, and the calorimeter muon term remains.

G. RECONSTRUCTING STANDARD MODEL PARTICLES

The objects described here represent the primary observables in the ATLAS detector, from which all final states must be reconstructed. A number of additional SM particles can be important to the final states of many analyses, and can be reconstructed from the observable particles discussed previously before being used as a primary final-state object in an analysis. One example is tau leptons ($\tau^{\pm}$). Taus can decay to electrons or muons with two neutrinos through the process $\tau \to \ell\nu_\tau\overline{\nu}_\ell$. Electrons and muons are defined observables, and neutrinos will appear as $\vec{E}_{\mathrm{T}}^{\mathrm{miss}}$. Due to their mass, $m_\tau = 1.777$ GeV, they are the only leptons which

can also decay hadronically, typically to a small number of pions and kaons. These produce tracks that allow them to be distinguished from other hadronic activity like jets. Hadronic τ decay modes are described in Ref. [93], but only leptonically-decaying τ leptons are used in the analyses presented in Chapters V - VI. $W^{\pm}$ and Z^0 bosons can be identified through any of their numerous decay modes. Properties of the Z boson are very well-measured, so particles produced through particular decay channels can be calibrated in the detector on the basis of its properties and the expected parameters of this decay channel. In Chapter V, the identification of jets containing a b quark is the primary goal of a number of multivariate algorithms, which are sensitive to the shapes of jets and their associated tracks. Though these algorithms are based on properties which in principle may allow the reconstruction of B hadrons in the jet, not all of them actually perform this reconstruction. The calibration of these algorithms' identification efficiencies is studied, to ensure that b-quark identification performs similarly in MC simulation and real data. In Chapter VI, reconstructing the t quark is of primary importance, requiring jets, b-tagging, leptons including the τ, and $E_{\mathrm{T}}^{\mathrm{miss}}$ to be reconstructed accurately, in service to the investigation of the form of the t-quark coupling.

V. IDENTIFYING BOTTOM QUARKS IN JETS

Jets originating from final-state quarks are not generally distinguishable by the flavor of the quark which initiated the jet. In cases when the initiating quark is very energetic and is unlikely to be produced in the fragmentation process, it can be distinguishable from the other hadronic particles constituting the jet and provide indications of the flavor of this initiating quark. Jets initiated by a bottom (b) or charm (c) quark can often be identified by their structure, or by the properties of tracks within the jet arising from the decay of the charmed or b hadrons. Bottom quarks hold particular interest for their use in identifying and characterizing top quarks, for which they were originally developed [94, 95]; Higgs bosons, which for $m_H = 125$ GeV decay to $b\bar{b}$ pairs most often [96, 97, 98]; and new physics phenomena like heavy vector bosons and other tb resonances [99, 100], or supersymmetric particles [101, 102]. Given its importance to identifying final states for these and other physics phenomena, accurate and robust methods of identifying jets containing a bottom quark, or *b-jets*, have been developed. Multiple calibration schemes are used to ensure the application of these algorithms in real data is predictable in MC simulation. This chapter will discuss the basic principles behind the b-jet identificaion procedures used by the ATLAS experiment and will present a calibration analysis used to correct their identification efficiencies in MC simulation to match those in real data.

The mechanisms for identifying b-jets are statistical procedures called tagging algorithms. These use properties like the b hadron energy, lifetime, and decay modes to predict properties of the tracks associated with b-jets, or of some decay products of b hadrons, to compute a statistic which discriminates between b-jets and non-b-jets. A requirement placed on this statistic imparts a particular *b-purity*, or fraction of jets passing the cut which contain b quarks, and *b-jet tagging efficiency*, or fraction of the total number of b-jets that pass this

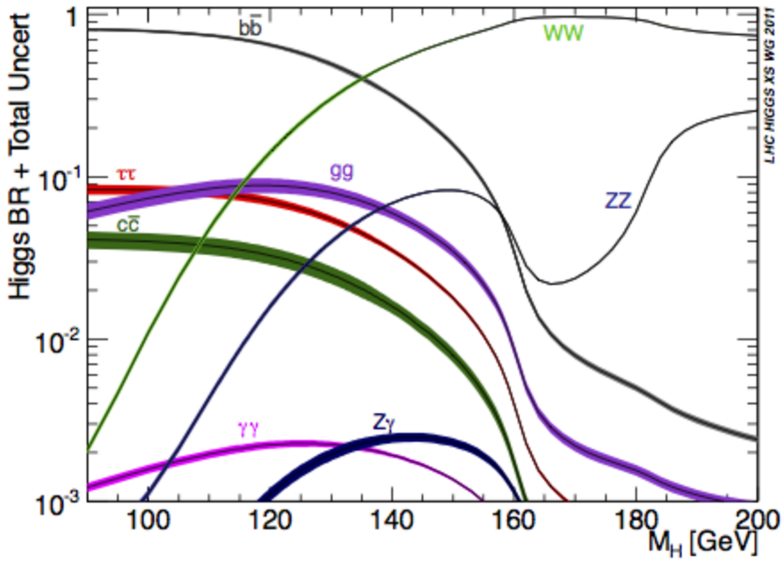

Figure V.1: Higgs branching ratios as a function of the Higgs boson mass. For $m_H = 125$ GeV as measured by the ATLAS and CMS collaborations, the $b\bar{b}$ final state constitutes 57.8% of all H decays. See Ref. [103].

requirement, to the sample. The choice of this requirement must weigh this efficiency with the probability that the tagged jet contained instead a charm quark, quantified by the *c-jet tagging efficiency*, or that the jet was a light-flavor jet (containing only the three lightest quark flavors d, u, and s), quantified by the *mistag rate*. The statistic formed by each of these algorithms, called *tagging weights*, are calibrated to ensure that their tagging efficiencies and mistag rate are comparable in MC simulation and in data with a set of scale factors varying with jet p_{T} or η. The calibration compare flavor frations in reference distributrions, identify b quarks from a high-purity sample, or cross-validate between uncorrelated tagging algorithms. Details on the latter calibration method, called *System8*, are given in some detail in Section V.C.

A. IDENTIFICATION OF B-JETS

As discussed in Section II..4, the b quark's unique location in the parameter space of the SM results in long-lived hadronic bound states with lifetimes ~ 1.5 ps [20]. For a b hadron with a typical transverse momentum of $p_{\mathrm{T}} = 50$ GeV, the average length of its flight path will be ~ 3 mm in the rest frame of the detector. This means the decay will occur within inner detector's closest sensitive region at 5 cm, but will be displaced distinguishably from the primary vertex. The resulting *secondary vertex* can be identified from detector observables by combining the impact parameter significances of tracks associated with the jet [104], or by reconstructing the vertex and considering its displacement from the primary vertex [105]. The decay modes of the b can also be leveraged to identify b-jets. One algorithm [106] reconstructs displaced vertices for the decay of the b hadron and the charmed hadron to which it decays weakly in most cases. The production of muons in some b quark decay chains [105] can be used to identify that subset of events without recourse to the full tracking information for the jet, and provides an independent verification of other tagging weights computed for those events. As many of these individual algorithms have complementary properties, combined algorithms are often used which are each defined as a combination of the output statistics of other taggers varied with kinematic and flavor properties.

The lifetime-based algorithms applied to 2011 data at $\sqrt{s} = 7$ TeV by ATLAS are `IP3D` which uses track impact parameters, `SV1` which reconstructs a secondary vertex, `JetFitter` which reconstructs the $b \to c \to X$ decay chain. All of these algorithms are sensitive to the choice of primary vertex, and to the measurement resolution of reconstructed tracks used in the algorithm. Stringent requirements are thus placed on track and vertex definitions. Tracks for `IP3D` must have at least 7 hits in the Pixel or SCT detectors, with at least 2 in the Pixel layer and 1 in the innermost layer; $p_{\mathrm{T}} > 1$ GeV; transverse and longitudinal impact parameters $|d_0| < 1$ mm and $|z_0| \sin\theta < 1.5$ mm, where the $\sin\theta$ term reduces the tracks' dependence on their polar angle. Vertex-fitting algorithms have looser selections, requiring only 1 hit in the Pixel detector. `SV1` also requires $p_{\mathrm{T}} > 400$ MeV and $|d_0| < 3.5$ mm, and `JetFitter` also requires $p_{\mathrm{T}} > 500$ MeV, $|d_0| < 7$ mm and $|z_0| \sin\theta < 10$ mm. As the pile-up conditions during the collection of 2011 data resulted in numerous primary vertices being

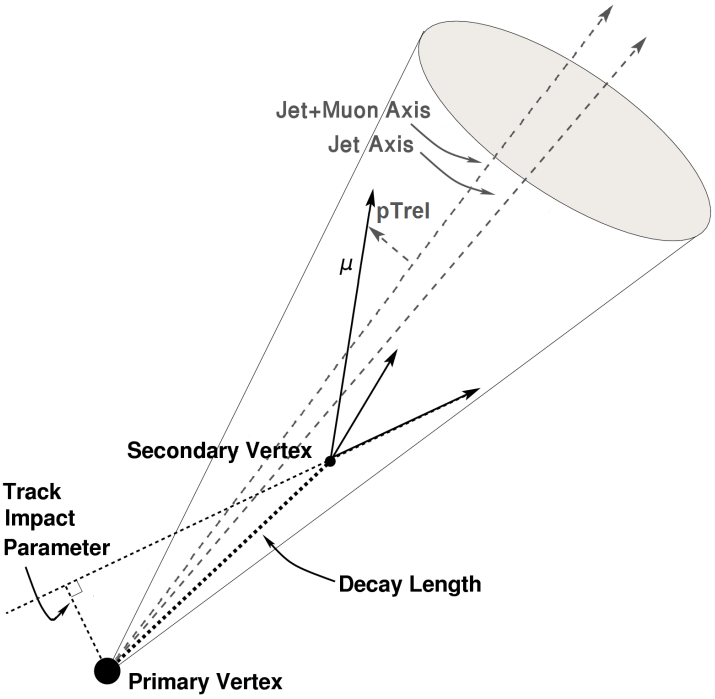

Figure V.2: Observable properties of b-jets which distinguish them from jets containing no b quarks. The impact parameter, d_0, is used by lifetime-based tagging algorithms. If the muon meets certain requirements, it could be used to compute a tagging weight from a soft-muon algorithm. The $p_{\mathrm{T}}^{\mathrm{rel}}$ variable describes the momentum of the muon perpendicular to the jet direction, and is used in calibrations described in Section V.B.

reconstructed, one is selected which maximizes the p_{T}^2 of the tracks associated to the jet.

Soft-muon tagging is an alternative method which doesn't use any lifetime information, and instead looks for muons near a jet which may come from b decays. For a muon to be considered by this tagging method, it must be a combined muon according to the definitions in Section IV.D. It must also satisfy the requirements $p_{\mathrm{T}} > 4$ GeV, $|d_0| < 3$ mm and $|z_0| \sin\theta < 3$ mm, ensuring that it can be loosely associated with the primary vertex. It is considered to be associated with a jet j if $\Delta R\,(j, \mu) < 5$; if multiple jets fit this criteria, only the closest one is considered. Since only $\approx 20\%$ of all b-quark decay chains produce muons, the general applicability of this algorithm is limited. It is applied primarily in calibration

analysis, where its its use of information independent of that used by lifetime-based tagging algorithms is an advantage for cross-calibration.

Multiple combined algorithms were defined for 2011 data. The `IP3D` and `SV1` weights are defined such that they can simply be summed to form the `IP3D+SV1` algorithm. Artificial neural networks are used to combine other tagging weights, so more detailed information can be incorporated. The `IP3D` and `JetFitter` weights are both input to a neural network, the output statistic of which is called the `IP3D+JetFitter` weight. The `MV1` algorithm, the recommended b-jet tagging algorithm for 2011 data, is such a combination of the tagging weights of the `IP3D`, `SV1` and `JetFitter` algorithms.

1. Track impact parameter tagging

The longitudinal and transverse impact parameters of the tracks associated with jets are expected to be small in most cases, as they arise from hadrons forming near the primary vertex associated with the jet which either decay very close to this vertex or live long enough to leave tracks in the inner detectors. In both cases, the impact parameters associated with these tracks will be small, and evenly distributed around the primary vertex. Hadrons formed with b quarks, however, are long-lived but decay before entering the tracking detector. This results in a distribution containing many more events with large impact parameters, most of which are above the plane through the primary vertex and perpendicular to the jet direction. The `JetProb` algorithm [107] is one of the first methods developed to take advantage of this property. It measures the significance of the signed impact parameter, $S_{d_0} = d_0/\sigma_{d_0}$, where σ_{d_0} is the uncertainty on the measurement of d_0, and its sign is positive if the track intersects the jet axis on the same side of the primary vertex as the jet and negative if on the opposite side. As tracks originating from a secondary decay vertex should have a positive impact parameter, a measurement resolution function $\mathcal{R}(S_{d_0})$ is determined from tracks in data with negative impact parameter, excluding effects from secondary decay vertices. With this function, the probability that track i in a jet originates at the associated primary vertex is

$$P_{\mathrm{trk},i} = \int_{-\inf}^{-|S^i_{d_0}|} \mathcal{R}(x)dx. \tag{V.1}$$

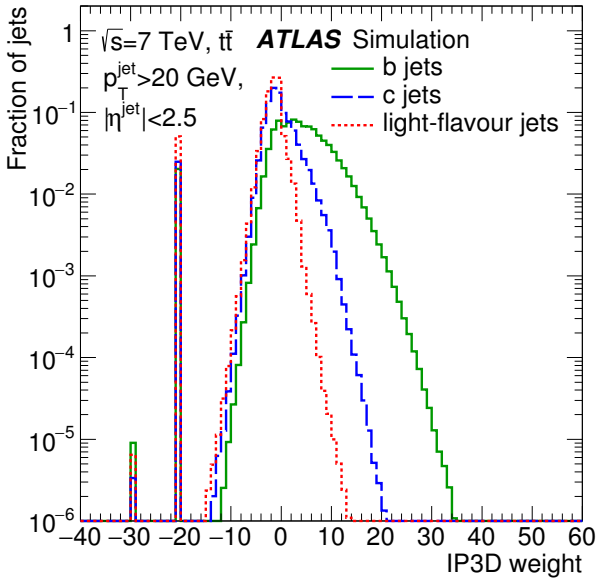

Figure V.3: The distribution of the `IP3D` tagging weight for b-jets (green), c-jets, (blue), and light-flavor jets (red). Pathological cases at $w_{\text{IP3D}} \approx -20$ and $w_{\text{IP3D}} \approx -30$ occur when the weight cannot be calculated.

The individual probabilities for each track in a jet containing N total tracks are combined into what will become the output statistic for `JetProb`,

$$P_{\text{jet}} = P_0 \sum_{j=0}^{N-1} \frac{(-\ln P_0)^j}{j!}, \text{ for } P_0 = \prod_{i=1}^{N} P_{\text{trk},i}. \tag{V.2}$$

The `IP3D` algorithm improves on `JetProb` by using both the longitudinal and transverse impact parameter significances, $S_{d_0} = d_0/\sigma_{d_0}$ and $S_{z_0} = z_0/\sigma_{z_0}$, and their correlation. Instead of a resolution function, two-dimensional probability densities for the b-jet and light-flavor jet hypotheses are determined from MC simulation as histograms. For each track associated to the jet, the likelihood ratio with respect to these distributions is calculated, and the ratio of the resulting probabilities defines the track weight, $w_{\text{trk},i}$. The total weight for a jet is then the sum of the logarithms of the track weights, as

$$P_{\text{jet}} = \sum_{i=0}^{N-1} \ln w_{\text{trk},i}. \tag{V.3}$$

By defining this weight as a log-likelihood ratio, it can be combined with other tagging weights defined in the same way by simply summing them. This is useful in forming the combined algorithms discussed in Section V.A.4.

2. Secondary-vertex tagging

Instead of using the probabilities for individual tracks to arise from a secondary vertex, the vertex itself can be reconstructed and its properties compared to those expected for b hadron decays in jets. This was first taken advantage of in ATLAS with the SV0 algorithm [108]. To find the vertex, a list of tracks associated with a jet which pass the quality criteria described previously are first combined into two-track vertices. Only tracks with a 3-dimensional impact parameter significance $S_{\vec{d}} = |\vec{d}|/\sigma_{|\vec{d}|} > 2.3$ and with a track $\chi^2 > 4.5$ are considered. Two-track vertices must have $\sum S_{\vec{d}} > 6.6$, and are not considered if their masses are consistent with known decays. The tracks in the remaining two-track vertices are collected into a single secondary vertex, then iteratively removed by those with the largest χ^2 relative to this vertex. The removal procedure continues until the fit probability is greater than 0.001, the largest track $\chi^2 < 7$, and the invariant mass of the sum of all tracks associated with the vertex, or *vertex mass*, $m_{\text{vtx}} < 6$ GeV. The signed decay length significance L/σ_L of this vertex projected onto the jet axis then forms the tagging weight for the SV0 algorithm. This algorithm's main drawback is its limited vertex-finding efficiency, of around 70%.

The SV1 algorithm is constructed using the log-likelihood ratio formalism introduced in IP3D. It improves on SV0 by exploiting in the likelihood the vertex mass m_{vtx}, the ratio of the sum of energies of the tracks in the vertex to that of all the tracks in the jet, the number of two-track vertices, and the ΔR value between the jet and the line connecting the primary and secondary vertex. They are incorporated as a two-dimensional distribution in the first two variables and one-dimensional distributions in the second two. The resulting algorithm can be easily combined with other log-likelihood ratio algorithms.

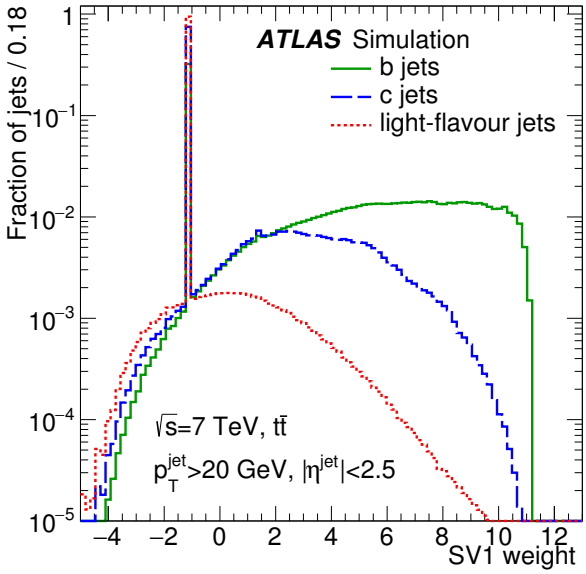

Figure V.4: `SV1` tagging weight distributions for b-jets (green), c-jets, (blue), and light-flavor jets (red). The pathological case near $w_{\mathrm{SV1}} \approx -1$ is where no secondary vertex could be found. Here, discrete probabilities for a b-jet and light-flavor jet not to have a vertex are assigned.

3. Reconstructing the b decay chain

Secondary vertex-finding algorithms can be designed to take advantage of the topology of b hadron decays within jets. As $|V_{cb}| \gg |V_{ub}|$, most b-jets will have two secondary vertices: one where the b hadron decays to a charmed hadron, and another where the charmed hadron decays into lighter particles. In the `SV1` algorithm, either only one of these vertices is found, or the two are merged. The `JetFitter` algorithm [106] is designed to identify both vertices. It first defines the flight path of the b and c hadrons along a common line, then constructs vertices with the points of intersection between tracks and the flight path. A Kalman filter is defined to reconstruct this decay chain; the parameters chosen for updating are the primary vertex location, the direction of the b hadron flight path, and the distances of the fitted vertices from the primary vertex along that flight path. The fit proceeds by adding a vertex

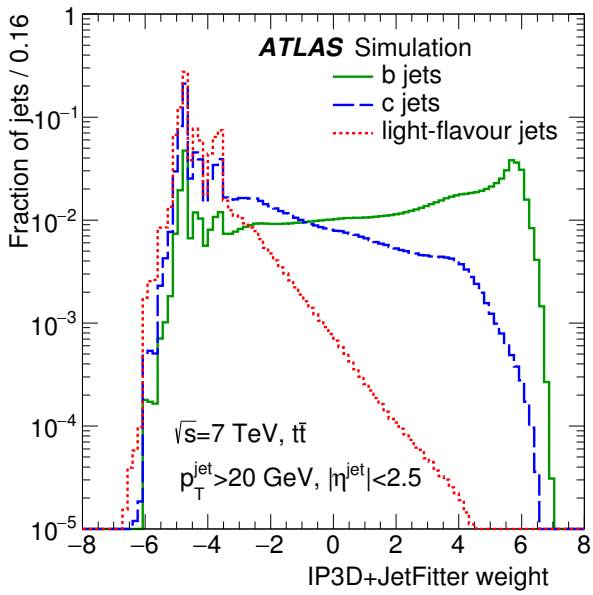

Figure V.5: The distribution of the `IP3D+JetFitter` algorithm tagging weight, for b-jets (green), c-jets, (blue), and light-flavor jets (red).

for each track intersection on the b hadron flight path, then iteratively clustering vertices until those remaining are below a χ^2 threshold.

The reconstructed b decay chain determined from this algorithm is adapted to separate b-jets from c- and light-flavor jets with a likelihood dependent on several variables affecting the decay topology and vertex information. The number of vertices with at least two tracks, the total number of tracks at these vertices, and the number of additional vertices with only one track along the b hadron flight path describe the decay topology. These variables form discrete categories in which each jet flavor (b, c, and light) has a unique probability. The invariant mass of all tracks attached to the decay chain, the energy fraction of these tracks compared to the energy of all tracks associated to the jet, and the flight length significance L/σ_L of the weighted average position of all vertices on the b hadron flight path characterize the vertex information. They are described by mutually independent, but category-dependent, probability densities. The likelihoods for b-, c-, and light-flavor jets are determined from an artificial neural network with these six parameters as input variables.

The p_{T} and $|\eta|$ of the jet affect these variables, and must also be included in the neural network. To avoid jet flavor being affected by these kinematic variables, the training sample is reweighted to form distributions flat in these variables for all three flavors. The outputs of the neural network are the probabilities P_b, P_c, and P_l of a jet matching the b-jet, c-jet, or light-flavor jet hypotheses. Finally, a tagging weight can be chosen to distinguish b-jets from light-flavor jets, $w_{\mathrm{JetFitter}} = P_b/P_l$, or from c-jets, $w^c_{\mathrm{JetFitter}} = P_b/P_c$.

4. Multivariate techniques and the `MV1` algorithm

Each of the three primary lifetime-based tagging algorithms used by ATLAS with 2011 data described in Sections V.A.1 - V.A.3 have different strengths. In particular, the vertex-finding algorithms `SV1` and `JetFitter` have better rejection of light-flavor jets (and thus a lower mistag rate) than the `IP3D` algorithm, but are limited by the vertex reconstruction efficiency. Since their tagging weights are log-likelihood ratios, a linear combination of these weights produces a tagging weight with some benefit from all taggers involved. The `IP3D+SV1` tagger is a simple sum of these two tagging weights. The `IP3D+JetFitter` weight is defined by augmenting the `JetFitter` neural network with the `IP3D` weight as an input variable. Weights rejecting light-flavor jets and c-jets can be defined in the same way.

The `MV1` algorithm uses three different tagging weights (w_{IP3D}, w_{SV1}, and $w_{\mathrm{IP3D+JetFitter}}$) as inputs to a neural network with a single output discriminant. The neural network is trained on jets in $t\bar{t}$ events, with an average p_{T} around 60 GeV. Dijet events in the range 200 GeV $< p_{\mathrm{T}}^{\mathrm{jet}} <$ 500 GeV are included to ensure a broader range of jet p_{T} is incorporated. As in the `JetFitter` algorithm, the training samples are weighted to give flat jet p_{T} and $|\eta|$ distributions to avoid spurious correlation of jet flavor with these variables. The `IP3D+JetFitter` and `MV1` algorithms can also be tuned to improve c-jet rejection.

5. Soft-lepton tagging

Soft-lepton taggers are often applied as a metric complementary to the lifetime-tagging algorithms. The leptons from b decays arise from a secondary vertex, giving them a displacement and reduced energy relative to those originating from the primary vertex. They will be close

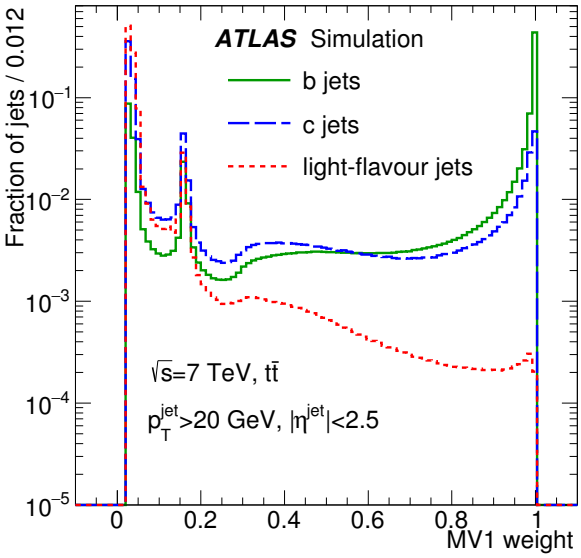

Figure V.6: The distribution of the tagging weight for the `MV1` algorithm for b-jets (green), c-jets, (blue), and light-flavor jets (red).

to the jet in which they arose in ΔR, and have lower energy on average ("soft") and larger impact parameters than prompt leptons. To make sure these properties don't result in the rejection of such soft leptons, these tagging algorithms must be defined with looser selections on p_{T}, d_0, and z_0 than those described previously, and with relaxed isolation criteria. Though soft-electron tagging has been used in some contexts [109], the challenge of distinguishing electromagnetic showers produced by electrons from showers reconstructed as jets make this difficult to implement. Only a soft-muon tagger (SMT) was used with 2011 data, and is described here.

As light charged mesons also frequently decay into muons, this is a significant background to b-jet identification that needs to be reduced by some discriminating statistic. The long lifetimes of these mesons means that some will decay within the inner detector, and part of the track will be associated to the meson itself. When the muon spectrometer and inner detector tracks are combined, the χ^2_{match} between them, defined by

$$\chi^2_{\mathrm{match}} = \frac{1}{5}(\mathbf{p}_{\mathrm{ID}} - \mathbf{p}_{\mathrm{MS}})^{\mathbf{T}}(\mathbf{V}_{\mathrm{ID}} + \mathbf{V}_{\mathrm{MS}})^{-1}(\mathbf{p}_{\mathrm{ID}} - \mathbf{p}_{\mathrm{MS}}), \tag{V.4}$$

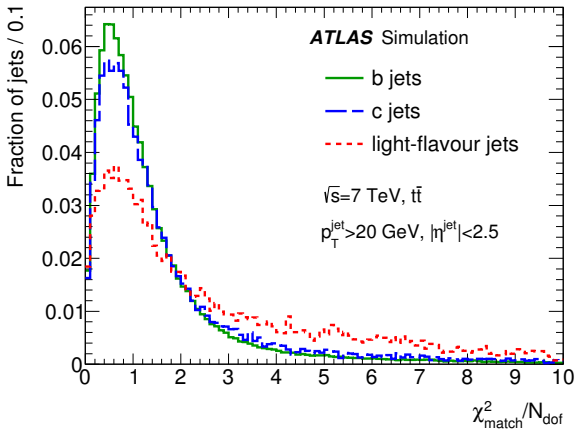

Figure V.7: The distribution of the χ^2-match statistic between inner detector and muon spectrometer tracks for muons associated with b-jets (green), c-jets, (blue), and light-flavor jets (red).

will be reduced by the resulting kink. The discriminating power of this statistic is shown in Figure V.7, from which a cut on this variable of $\chi^2_{\text{match}} < 3.2$ was chosen for inclusion in the definition of the SMT. The b-tagging efficiency of this method is significantly lower than for the lifetime algorithms, especially due to the low branching ratios of the decays $b \to \mu$ and $b \to c \to \mu$; in a simulated sample of $t\bar{t}$ events, it was measured to be 11.1%, or $\approx 50\%$ efficient in the subsample of b-jets containing muons from b hadron decay. Choosing jets containing muons can provide a simple way to define a sample enriched in b-jets, and in this sample the SMT can be compared to the lifetime-based tagging methods to calibrate these more inclusive algorithms.

B. CALIBRATING B-TAGGING ALGORITHMS

The tagging algorithms described in Section V.A all provide one or more variables which can be adjusted to the needs of analyses for b-jet efficiency or c- and light-flavor jet rejection. To be sure that a particular cut on one of these variables provides the same efficiencies

in MC simulation samples and in data, the taggers are calibrated to bring their output weights from data and MC samples into agreement. Tagging weights are calibrated at a discrete set of tagging efficiency values, called *working points*. This approach provides a range of options to analyzers, while reducing the number of independent calibration analysis tasks. Where a dependence of the b-jet tagging efficiency, ϵ_b, on the jet p_{T} and $|\eta|$ is found, calibrations are performed in multiple separate ranges over one or both these variables. Each calibration produces a set of scale factors to be applied to the tagging weight distributions in MC simulation. These calibration methods can be grouped into two categories, representing two different ways of choosing samples enriched in b-jets: $t\bar{t}$-based methods, and muon-based methods. The details of all calibration methods used in 2011 data can be found in Ref. [110].

Top quarks almost always decay to a b quark and a W boson; studying tagging weights in events containing $t\bar{t}$ pairs thus selects a sample of b-jets by the properties of their production mode, and provides information about their efficacy in an inclusive decay sample. Top pair events are selected with requirements on the leptons, jets, and $E_{\mathrm{T}}^{\mathrm{miss}}$, avoiding any requirements which affect the b-jet multiplicity or properties used by the tagging algorithms. Calibrations in this sample include counting tagged jets in events with only one lepton from a W-boson decay, called the *single-lepton channel*, and a set of analyses requiring knowledge of the jet flavor composition (b-, c-, and light-flavor jets) and backgrounds of the sample, determined from MC simulation or data-driven methods and applied to both single-lepton channel events and events with two leptons from W decay, called the *dilepton channel*. The first such method extracts the jet-flavor fractions and tagging efficiencies from MC simulation events passing either the single-lepton or dilepton selections, and background events are measured in a data control region. Another such method, used only in the single-lepton channel, performs a χ^2 fit to determine a mapping from the reconstructed lepton, jets, and missing transverse momentum onto the true b-jets and the leptonic and hadronic final states of the W-boson decays. A third method uses a likelihood fit applied to dilepton channel events to extend the previous fit-based method, taking correlations in jet p_{T} among b-jets and each of the other jet flavors into account.

A pair of alternative methods use an orthogonal sample of events containing two jets, produced via QCD interactions, which contain jets with an associated muon. As the b hadron

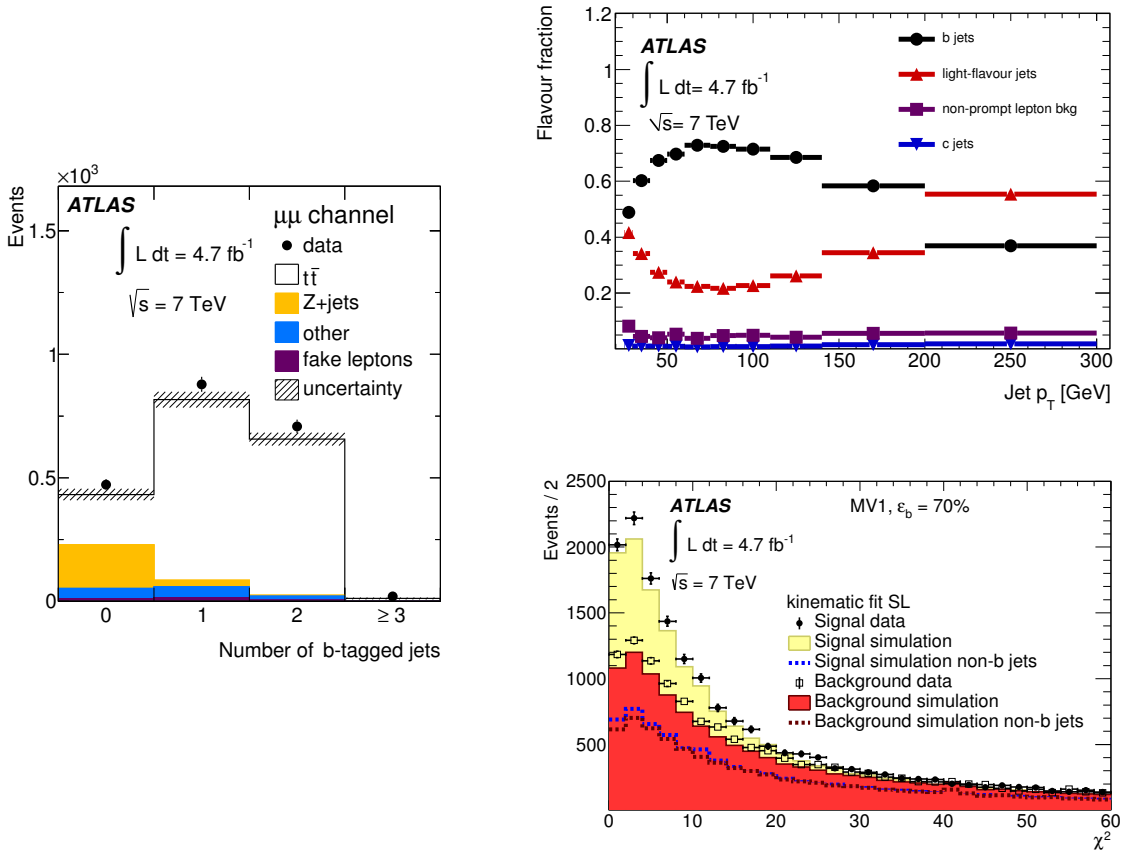

Figure V.8: Three distributions used to extract measurements for ϵ_b from $t\bar{t}$ samples: the tag counting method for a two-muon dilepton sample (left); the kinematic selection method, showing flavor fractions as a function of jet p_{T} (top); and the kinematic fit method, comparing the χ^2 distribution for the signal and the combined backgrounds in MC simulation to those in data (bottom).

in a jet is likely to contain a large fraction of that jet's energy, a muon arising from its decay is more likely to have a greater momentum component perpendicular to the jet axis, denoted $p_{\mathrm{T}}^{\mathrm{rel}} = \vec{p}_{\mu} \times \vec{p}_{\mathrm{jet}}/|\vec{p}_{\mathrm{jet}}|$, than for c-jets or light jets. This can be seen in the $p_{\mathrm{T}}^{\mathrm{rel}}$ spectra for each flavor shown in Figure V.9. This variable also has the benefit of being invariant with boosts along the jet axis, or overall rescaling of the jet energy. The corresponding $p_{\mathrm{T}}^{\mathrm{rel}}$ method fits MC-derived templates of this variable for b-jets, c-jets, and light-flavor jets in bins of jet p_{T}

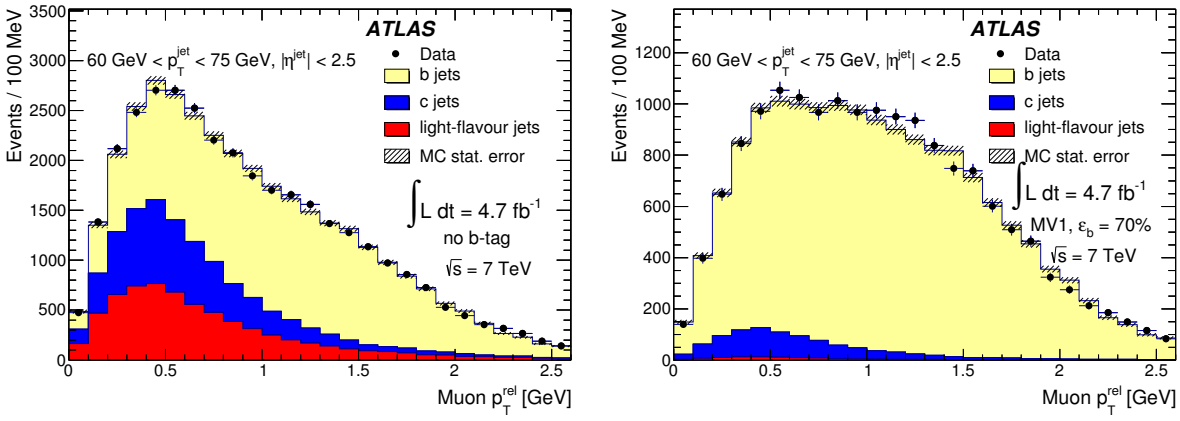

Figure V.9: Distributions of muon $p_{\mathrm{T}}^{\mathrm{rel}}$, used by tagging weight calibrations performed in dijet samples with a muon associated to a jet. For the 60 GeV $< p_{\mathrm{T}}^{\mathrm{jet}} <$ 75 GeV bin, (a) shows this distribution before a cut on the b-tagging weight is applied, and (b) shows the same distribution after placing a cut on the `MV1` tagging weight at 70% b-tagging efficiency.

and $|\eta|$ to obtain ϵ_b for the data, and the scale factors to correct the efficiency in MC to this value. The *System8* method, originally developed by the DØ experiment [111], is designed to have minimal input from simulation to reduce the associated systematic uncertainties. This thesis will describe an analysis using this calibration method performed on 2011 data in detail in the following section.

C. THE *SYSTEM8* CALIBRATION ANALYSIS

The *System8* b-tagging efficiency calibration method is designed as a simultaneous calibration of a lifetime-based and a soft-lepton tagging algorithm. In ATLAS, the soft-muon tagger is used to calibrate each of the lifetime-based taggers of interest, in particular `SV0`, `IP3D+SV1`, `IP3D+JetFitter`, and `MV1`. The analysis was designed to rely minimally on simulations by ensuring that the only information taken from MC simulation entered as multiplicative

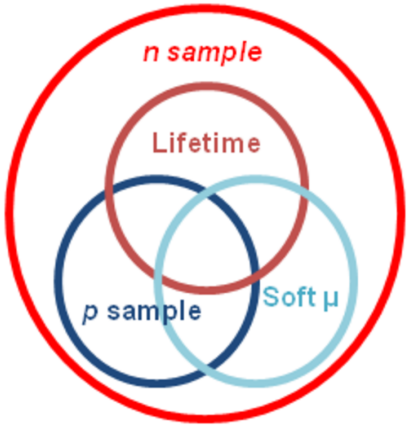

Figure V.10: Pictoral representation of *System8* sample selection as a circle diagram. The three selection criteria create overlapping regions, dividing the full sample into 8 independent groups which each contain all events fulfilling a subset of these criteria.

factors close to 1. It was first applied to the full 2010 ATLAS dataset with 35pb^{-1} at $\sqrt{s}$ = 7TeV [112]. The present analysis will apply this calibration method to 4.6fb^{-1} of data collected in 2011 with center-of-mass energy $\sqrt{s}$ = 7 TeV to derive ϵ_b^{data} for the four lifetime-based tagging algorithms described in data, and a set of scale factors $\kappa_b^{\text{data/sim}}$ to correct MC samples' efficiencies to match those in data. The scale factors derived in the *System8* calibration analysis will be combined with those determined via the $p_{\text{T}}^{\text{rel}}$ method and with the $t\bar{t}$ methods [110], to determine the full set of b-tagging scale factors used in analyses performed with 2011 data.

1. The *System8* procedure

The principle behind the design of the *System8* calibration method is that N uncorrelated sets of selections performed on the same sample of events separates those events into 2^N statistically-independent samples in which the b-tagging efficiency can be measured. The *System8* method measures abundances of b-, c-, and light-flavor jets passing cuts on lifetime-based and soft-muon tagging weights in all combinations, and uses this to discern each flavor's tagging efficiency. A third, uncorrelated selection is added to produce a sample of higher

b purity as a reference, in which the efficiency can be measured for each tagger from data. This replaces what is typically a sample derived from MC simulation, reducing the impact of associated systematic uncertainties. In this $N = 3$ scenario, these correlated subsamples are derived from a pre-selected sample which requires at least one jet with an associated muon, called the n sample. Events passing the lifetime-tagger selection fall in the LT sample, events passing the muon-tagger selection fall in the MT sample, and events passing the purifying selection fall in the p sample. Eight independent observable samples result from the overlaps between these categories; each represent events passing different exclusive combinations of these criteria. This selection structure is shown pictorially in Figure V.10.

The observable samples are related to eight unknown variables which *System8* is designed to measure. This relationship is expressed in a system of eight equations, expressed in Equation V.5, which has a unique solution. Eight variables are determined simultaneously by this solution: the selection efficiency of b-jet events for each tagger, the selection efficiency of c- and light-flavor jet events for each tagger, and the number of events containing b-jets or c- and light-flavor jet events in the n and p samples. The selections in this analysis are designed to measure the efficiency of b-jet identification, and they lack the discriminating power to distinguish jets arising from gluons, or from c, s, u, or d quarks. All of these jets are combined into the category of cl-jets, where the charm quark is specifically referenced due to its increased impact on b-jet discrimination.

$$
\begin{aligned}
n &= n_b + n_{cl} \\
p &= p_b + p_{cl} \\
n^{LT} &= \epsilon_b^{LT} n_b + \epsilon_{cl}^{LT} n_{cl} \\
p^{LT} &= \alpha_6 \epsilon_b^{LT} p_b + \alpha_4 \epsilon_{cl}^{LT} p_{cl} \\
n^{MT} &= \epsilon_b^{MT} n_b + \epsilon_{cl}^{MT} n_{cl} \\
p^{MT} &= \alpha_5 \epsilon_b^{MT} p_b + \alpha_3 \epsilon_{cl}^{MT} p_{cl} \\
n^{LT,MT} &= \alpha_1 \epsilon_b^{LT} \epsilon_b^{MT} n_b + \alpha_2 \epsilon_{cl}^{LT} \epsilon_{cl}^{MT} n_{cl} \\
p^{LT,MT} &= \alpha_7 \alpha_6 \alpha_5 \epsilon_b^{LT} \epsilon_b^{MT} p_b + \alpha_8 \alpha_4 \alpha_3 \epsilon_{cl}^{LT} \epsilon_{cl}^{MT} p_{cl}
\end{aligned}
\tag{V.5}
$$

In the *System8* equations, the n and p observable samples correspond to the number of events in the full and purified samples, respectively, not passing either the lifetime or muon

tagging weight selections. The n^X and p^X samples correspond to those passing the selections from one or more taggers X which either fail or pass the purifying selection, respectively. These observable numbers of events are mapped to the numbers of events containing b- and c- or light-flavor jets in the full and purified samples, n_b, n_{cl}, p_b, and p_{cl}, and their tagging efficiencies ϵ_b^{LT}, ϵ_b^{MT}, ϵ_{cl}^{LT}, and ϵ_{cl}^{MT}. The parameters α_i describe correlations between the samples' selection efficiencies, and are the only components of these equations relying on MC simulation. They are defined in Equation V.6:

$$\begin{aligned}
\alpha_1 &= \epsilon_b^{LT,MT,n}/(\epsilon_b^{LT,n}\epsilon_b^{MT,n}) & \alpha_2 &= \epsilon_{cl}^{LT,MT,n}/(\epsilon_{cl}^{LT,n}\epsilon_{cl}^{MT,n}) \\
\alpha_5 &= \epsilon_b^{MT,p}/\epsilon_b^{MT,n} & \alpha_3 &= \epsilon_{cl}^{MT,p}/\epsilon_{cl}^{MT,n} \\
\alpha_6 &= \epsilon_b^{LT,p}/\epsilon_b^{LT,n} & \alpha_4 &= \epsilon_{cl}^{LT,p}/\epsilon_{cl}^{LT,n} \\
\alpha_7 &= \epsilon_b^{LT,MT,p}/(\epsilon_b^{LT,p}\epsilon_b^{MT,p}) & \alpha_8 &= \epsilon_{cl}^{LT,MT,p}/(\epsilon_{cl}^{LT,p}\epsilon_{cl}^{MT,p})
\end{aligned} \tag{V.6}$$

A lack of correlation between the efficiencies of two different selection criteria would imply that the related correlation factor $\alpha_i = 1$. All α factors are expected to be $\mathcal{O}(1)$, and extreme values approaching 2 or 0 would likely indicate significant mismodeling in simulation.

The n sample used in this implementation of the *System8* method requires that an event contain at least one jet with an associated combined muon. The three *System8* subsamples are further defined as follows:

- The p sample is formed by all events in which the jet in the event with the highest value of the `SV0` tagging weight, excluding the jet under study, is above some threshhold. This requirement increases the fraction of events in the sample coming from $b\bar{b}$ pair production without introducing a bias with respect to the n sample. In this analysis, the threshold chosen is $w_{\mathrm{SV0}} > 1.0$.
- The LT sample is formed by all events passing a minimum-value cut on the tagging weight of the lifetime-based tagging algorithm under study. It is determined by a preliminary measure of the b-tagging efficiency used to label the working point; for example, `MV170` refers to a value of the `MV1` tagging weight above which $\epsilon_b = 70\%$. Calibration should not affect this efficiency significantly.

- The MT sample is formed by all events passing a cut on the soft-muon tagging weight under study, which translates to a cut on the $p_{\mathrm{T}}^{\mathrm{rel}}$ variable in the current implementation. The default cut performed in in the final analysis of 2011 data is $p_{\mathrm{T}}^{\mathrm{rel}} > 700$ MeV, with ± 100 MeV on this cut value used as systematic variations.

The choice of these three selections is motivated by their lack of correlation, and by the fact that using different types of tagging algorithms leaves open the option to calibrate both. The analysis performed on 2011 data focuses on the calibration of the efficiencies for the lifetime taggers, but providing a simultaneous calibration of a soft-lepton tagger is straightforward. The p sample definition must produce a set of events with a sufficiently different b purity from the n sample, but it is not necessary that it be higher purity. The choice used here is convenient to the mechanics of the analysis, and is equivalent to a b-purifying selection made in the related $p_{\mathrm{T}}^{\mathrm{rel}}$ calibration method. This simplifies the combination of the two methods' results, performed via the method described in Ref. [113].

The *System8* method is applied to both real data and data taken from MC simulation, the latter being used to construct the correlations factors α_i and validate the method. The b and cl components are extracted from samples of true flavor-identified jets. The first sample thus is b-pure, selecting only events in which the jet under study is initiated by a generated b quark. The second is then constructed from two different samples; a c-pure sample is derived similarly to the b sample, and a light-flavor jet sample, with jets initiated by u, d, s, g, approximated from a sample dominated by jets with no associated muons by transforming a track in a jet in each event into a muon. The construction of this sample is described in Section V.C.2.

The system of equations comprising the *System8* method is nonlinear, but a general analytic solution is known [111]. This solution is equivalent to that determined from a χ^2 minimization procedure applied to the separated system, which also returns the covariance matrix for the correlated samples and efficiencies, and does not take significantly more computation time. This solution is attained by minimizing the differences in the observed numbers of events in data from those computed in Equation V.5, varying the efficiencies ϵ_b, ϵ_{cl} and sample fractions $f_n = n_b/(n_b + n_{cl})$, $f_p = p_b/(p_b + p_{cl})$, for each of the eight categories. The minimized χ^2 is defined as a sum of the χ^2 values for each category, with measured

numbers of events n_i, Poisson uncertainties σ_i, and minimization functions $\mu_i(\epsilon, \ldots, f_b, \ldots)$:

$$\chi^2 = \sum_{i=1}^{8} \frac{\left(n_i - \mu_i(\epsilon_b^{LT}, \epsilon_b^{MT}, \epsilon_{cl}^{LT}, \epsilon_{cl}^{MT}, f_{b,n}, f_{b,p})\right)^2}{\sigma_i^2}, \ \sigma_i = \sqrt{n_i}. \tag{V.7}$$

The fit starts with the measured numbers of events in eight statistically independent, or *disjoint*, samples and recombines them into the observable categories in Equation V.5. The efficiencies and sample fractions are constrained to their physical region (between 0 and 1), and the χ^2 minimization is performed by MINUIT [114]. Because the system has eight degrees of freedom and eight constraining equations, we expect the solution to satisfy $\chi^2 \approx 0$. This is therefore imposed as a requirement on the convergence of the fit. The equations are symmetric under interchange of the n and p sample definitions, so multiple solutions exist. The solution chosen is that for which the efficiency of any b-tagging algorithm is higher for b-jets than for c- or light-flavor jets. The statistical uncertainty on each fit parameter is taken from the covariance matrix determined in the fit.

The fit as described above contains only information on the uncertainties associated with the input data. However, the α_i correlation parameters taken from MC simulation also have some statistical uncertainty related to the size of the MC samples from which they are derived. The fit is expanded to account for this uncertainty by adding eight gaussian constraints centered on the α_i central values, $\vec{\alpha_0}$, with the width set as the covariance matrix V containing these statistical uncertainties and correlations. These constraints enter as additive terms in the χ^2:

$$\chi^2 \to \chi'^2 = (\vec{\alpha} - \vec{\alpha_0})^T V^{-1} (\vec{\alpha} - \vec{\alpha_0}). \tag{V.8}$$

The same minimum χ^2 is expected from this fit, as all introduced parameters are paired with a constraining equation. The possibility of improving the fit is greater in the case when correlation factors are drawn from a low-statistics MC simulation sample, but in all cases the increased uncertainty will accurately reflect the statistical uncertainty introduced through the correlation factors.

2. *System8* sample selection and construction

The *System8* calibration analysis was performed on the full data sample collected by the ATLAS experiment during 7 TeV proton-proton collisions in 2011, including data periods B through M, with a total integrated luminosity of $4.6\,\text{fb}^{-1}$. MC simulation samples used to derive the correlation factors are taken from a sample of jets arising from QCD processes, generated with the ATLAS `AUET2B LO**` tune [115] of `PYTHIA 6` [116]. Samples with and without a muon filter are used, where the muon filter is a requirement that a $\mu^{\pm}$ with $p_{\text{T}} > 3$ GeV appears in the generated event. About $25.5 \cdot 10^6$ events were generated across four bins in $\hat{p}_{\perp}$, the momentum of the primary-vertex scattering process perpendicular to the beamline, beginning at $\hat{p}_{\perp} = 17\text{GeV}$. The generator-level final state particles are then processed by the ATLAS simulation, described in Section III..3.

Muons are required to be reconstructed with the combined-muon method implemented within the STACO algorithm chain (see Section IV.D). Jets are reconstructed from calorimeter clusters via the anti-k_t algorithm (see Section IV.E), applying the distance requirement $\Delta R < 0.4$ [49]. The analysis is divided into a series of bins in b-jet p_{T}, defined in the analysis as the p_{T} of the jet with the muon included, and corrected for the missing energy carried by the neutrino with the definition

$$p_{\text{T}}^{b-\text{jet}} = C_{\nu}(\vec{p}_{\text{jet}} - \vec{p}_{\mu}^{\,\text{calo}} + \vec{p}_{\mu}) \cdot \hat{z}. \tag{V.9}$$

In this definition, $\vec{p}_{\mu}^{\,\text{calo}}$ is modeled by setting the expected energy loss of a muon in the calorimeter, typically $\sim$ 3 GeV, as the energy of a massless 4-vector directed along the muon trajectory. The neutrino-energy correction factor, C_{ν}, is determined from a separate analysis which rescales the energies of jets containing b quarks which decay semileptonically ($b \to \ell X$), to account for the jet energy lost to the lepton and neutrino as a function of the jet and muon momenta. The b-jet contains most of the information used to determine the value of the b-jet tagging weights, so the analysis is performed in bins of $p_{\text{T}}^{b-\text{jet}}$, shown in Table V.1. Further details are available in Ref. [90].

The events selected for this analysis at the L1 trigger level must have calorimeter clusters with energies above certain thresholds, and hits in the muon spectrometer spatially matched

to a track in the inner detector. Matching is also required between the muon and the jet at the EF trigger level. The calorimeter E_T required for the jet to be accepted at the L1 trigger level, and the p_{T} required for the muon in the analysis, varies based on which bins fall into the highest-efficiency jet selection regions above different trigger energy thresholds. Table V.1 indicates which triggers and selections were used for each bin in the analysis. A set of "cleaning" selections are implemented to remove poorly-reconstructed jets [117], and similar selections reject poor-quality or incorrectly-associated muons. All b-jets and muons are required to have $|\eta| < 2.5$, and the muon and b-jet must have $\Delta R(\text{jet}, \mu) < 0.4$. All events used in the analysis should have their associated jets originating at the primary vertex. To ensure this, events are selected only if their *jet vertex fraction*[1], or JVF, satisfies $\epsilon_{\mathrm{JVF}} > 0.75$.

As the simulated samples contain information about the true abundances of jets with individual flavors (b, c, and light), they are separated according to a generator-level flavor assignment. A jet is labeled a b-jet if a b quark is found within $\Delta R < 0.3$ of the jet, then the procedure is repeated for c-jets and jets coming from hadronic decays of τ leptons, and the remaining jets are labeled as light-flavor. The *System8* categories require a b-jet sample and a combined c-jet and light-flavor jet sample to specify the correlation factors, so the latter is constructed from a combination of the non-b-jet samples. The combination is weighted by relative fractions for the c-jet and light-flavor jet samples taken from events simulated without the muon filter applied. The c-jet sample is taken from muon-filtered simulation events, while the light-flavor jet sample is constructed with a dedicated procedure.

The *System8* framework limits input from MC simulation to ratios of tagging efficiencies, which are allowed to vary in the fit within their statistical errors, but these ratios are still sensitive to the statistics of the samples used. For the muon-filtered b- and c-jet simulation samples, each flavor makes up a large fraction of the sample. Sufficient numbers of events are available to these samples to keep their statistical uncertainties low. However, the requirement that a muon exists at the generator level excludes events, common for real light-flavor jets, in which the muon is a product of light-hadron decays in the jet (such as $\pi \to \mu\nu$ or $K \to \mu\nu$). As a result, a much smaller fraction of the light-flavor jets which might appear

[1] The jet vertex fraction is defined as the ratio of the scalar sum of the transverse momentum of tracks associated to the primary vertex to that of all tracks matched to a jet.

to have a muon from a secondary decay vertex at the level of the reconstructed event are included in the muon-filtered sample. The unfiltered sample is inherently statistically limited, and would be further reduced in size when only considering jets with associated muons.

A larger sample of light-flavor jets with associated muons is constructed for this analysis following a procedure which treats individual tracks in light-flavor jets from the unfiltered sample as *mock muons*. These mock muons are created by randomly choosing a charged particle track associated to the jet, passing the requirements placed on inner-detector tracks used in the definition of combined muons, and treating it as a muon. Weights are applied to the resulting p_{T} and $|\eta|$ spectrum of these mock b-jets to ensure their kinematic distributions conform to those expected from simulated light-flavor jets containing real muons. This weight is derived from the binned p_{T} and $|\eta|$ distributions of muons and tracks. The total numbers of events in these samples are reweighted by the probability that a reconstructed track in the inner detector corresponds to a muon in the muon chambers, and by a model of the muon trigger activation efficiency for muons near the trigger's threshhold ($\sim$ 4GeV). The mock b-jet object also has its trigger E_T altered, and the trigger decision is recalculated accordingly. The triggers used in this sample do not contain a muon requirement, but the energy of the jet as seen at the trigger level is higher than if one track had been a muon. This is taken into account by removing the transverse energy of the mock muon track from the trigger energy and replacing it with the average muon energy deposition in the calorimeter, then re-applying the trigger decision. Following this prescription, the semileptonic correction, b-jet composition, and all further required cuts are performed as for the b- and c-jet samples.

3. *System8* systematic uncertainties

An important benefit of the *System8* efficiency calibration method is its suppression of systematic errors. Systematic shifts not dependent on the selection category are significantly reduced, or sometimes eliminated, as information taken from MC simulation enters only as ratios between selection efficiencies. The size of the real data sample recorded during the 2011 data-taking period is the largest contribution to the uncertainty, entering through the p, LT, and MT subsamples. The total uncertainties on the efficiencies

Table V.1: Selection placed on *System8* analysis by b-Jet p_{T} bin, designed to maximize availability of useful events in the given ranges.

b-Jet p_{T} (GeV)	p_{T}^{μ} cut (GeV)	Trigger (data)	Trigger (light-flavor)
$20 \leq p_{\mathrm{T}} < 30$	4.0	EF_mu4_j10_a4tc_EFFS_matched	EF_j10(j15)_a4tc_EFFS
$30 \leq p_{\mathrm{T}} < 40$	4.0	EF_mu4_j10_a4tc_EFFS_matched	EF_j10(j15)_a4tc_EFFS
$40 \leq p_{\mathrm{T}} < 50$	4.0	EF_mu4_j10_a4tc_EFFS_matched	EF_j10(j15)_a4tc_EFFS
$50 \leq p_{\mathrm{T}} < 60$	4.0	EF_mu4_j10_a4tc_EFFS_matched	EF_j10(j15)_a4tc_EFFS
$60 \leq p_{\mathrm{T}} < 75$	6.0	EF_mu4_L1J10_matched	EF_j30_a4tc_EFFS_l2cleanph
$75 \leq p_{\mathrm{T}} < 90$	6.0	EF_mu4_L1J10_matched	EF_j30_a4tc_EFFS_l2cleanph
$90 \leq p_{\mathrm{T}} < 110$	8.0	EF_mu4_L1J10_matched	EF_j30_a4tc_EFFS_l2cleanph
$110 \leq p_{\mathrm{T}} < 140$	8.0	EF_mu4_L1J30_matched	EF_j55_a4tc_EFFS
$140 \leq p_{\mathrm{T}} < 200$	8.0	EF_mu4_L1J30_matched	EF_j55_a4tc_EFFS

are calculated from data and from MC simulation by performing the procedures as described, symmetrizing the results for "up" and "down" systematic shifts via the formula $\kappa_b^{\mathrm{data/sim}}(\mathrm{sym}) = \frac{1}{2}(\kappa_b^{\mathrm{data/sim}}(\mathrm{up}) - \kappa_b^{\mathrm{data/sim}}(down))$ if two such variations are calculated, and keeping the sign of the symmetrization to indicate the dominant shift direction. These uncertainties are then propagated from each efficiency to the scale factors, $\kappa_b^{\mathrm{data/sim}}$. Table V.2 presents the resulting fractional uncertainties on the scale factors from both statistical and systematic sources, measured for the MV170 working point.

a. Simulation statistical uncertainties The statistical uncertainty associated with the tagging efficiencies for b- and cl-jet events calculated from MC simulation impart some uncertainty to the correlation coefficients, α_i. The fit solving the *System8* equations allows the α_i to vary according to a Gaussian constraint with a covariance matrix constructed from these uncertainties, as described in Section V.C.1. The resulting variances are compared to those attained without these constraints, and the difference in quadrature is applied as a systematic uncertainty. These statistical unceratinties also affect the tagging efficiencies measured in MC simulation, and appear in the denominator of the scale factors, $\kappa_b^{\mathrm{data/sim}} = \frac{\epsilon_b^{data}}{\epsilon_b^{sim}}$. The simulation statistical uncertainties are thus included directly as a source of systematic uncertainty.

b. Modeling of b- and c-quark production Production of b and c quarks can occur either directly from a pp collision, or from gluon splitting. The latter production mechanism can result in two such quarks being in the same jet, resulting in different jet kinematic spectra and event topologies for the two production mechanisms which affect all categorical selections. A systematic uncertainty is assigned to cover this variation by reweighting jets in MC simulation containing two b or c quarks by either 2 or 0, then performing the analysis with the resulting correlation factors and taking the deviation from the central-value scale factors and the uncertainty.

c. b-quark fragmentation Two sources of systematic uncertainty address the modeling of b-quark behavior during fragmentation. First, the model of the relative abundances of different b hadron flavors used by the generator agrees with measurements made at LEP, but similar measurements at the Tevatron were consistent with the LEP results only at 2σ [118]. Using the wrong b hadron fragmentation fractions can skew jet and muon momenta. The discrepancy is accounted for by reweighting the b hadron fractions to match those measured at the Tevatron, then symmetrizing to get a systematic uncertainty. Additionally, this fragmentation model determines the directions and energies of the b hadrons produced, and thus variance in this model affects which muons pass selection and alters their $p_{\mathrm{T}}^{\mathrm{rel}}$ spectra. The distribution of the momentum fraction of simulated b-jets which ends up in the b hadron is calculated, then reweighted to modify the central value of the momentum fraction distribution by $\pm 5\%$. The symmetrized deviation of the resulting scale factors from the central value is taken as the systematic uncertainty.

d. Modeling of the b-hadron direction Using the $p_{\mathrm{T}}^{\mathrm{rel}}$ variable to identify b-jets requires that the μ +jet axis is a good model of the direction of the b hadron. A different jet resolution would result in an incorrect determination of the shape of the b-jet p_{T} distribution. Two alternate $p_{\mathrm{T}}^{\mathrm{rel}}$ values are generated by applying a random angular smearing to the b-jet, chosen from a normal distribution with widths 0.004 in ϕ and 0.008 in η. The systematic uncertainty on the scale factor is determined from the average deviation of these variations from the central value.

e. *b*-quark decay modeling Two sources of systematic uncertainty describe variance in models of b-quark decay. First, a semileptonically-decaying b-quark is most likely to either decay directly, $\mathcal{B}(b \to \ell X) = (10.69 \pm 0.22)\%$, or through a $b \to c$ cascade, $\mathcal{B}(b \to c/\bar{c} \to \mu X) = (9.62 \pm 0.53)\%$. Varying the ratio of these decays can affect the muon p_{T}, and thus $p_{\mathrm{T}}^{\mathrm{rel}}$, spectrum. Thus, this ratio is varied up and down by its uncertainty, $\mathcal{B}(b \to \mu X)/\mathcal{B}(b \to c/\bar{c} \to \mu X) = 1.11 \pm 0.07$ [20], and the symmetrized deviation is taken as a systematic uncertainty. The distribution of the muon momentum in the b hadron rest frame, p^*, is also directly linked to the muon p_{T} spectrum. The distribution of p^* in simulated samples agrees with that measured by the BaBar collaboration [119], but differs from a similar measurement performed by the DELPHI collaboration [120]. A systematic uncertainty is assigned in which the p^* spectrum is reweighted to match the second measurement, and the deviation of the resulting scale factors from the central value is taken as the systematic uncertainty.

f. Charm-to-light ratio The c- and light-flavor jet fractions used in the analysis are fixed to those in the unfiltered MC simulation (see Section V.C.2). These fractions are thus susceptible to the statistical and systematic uncertainties inherent in these samples. In the *System8* equations, this enters through the correlation factors α_2, α_3, α_4, and α_8. To account for these uncertainties, the ratio of these jet flavors is varied up and down by a factor of 2, and the symmetrized deviation of the results from the central value is taken as the systematic uncertainty.

g. Muon momentum uncertainties The effect of variation in the muon momentum spectrum on the categorical selections is addressed in two sources of systematic uncertainty. First, the shape of the muon p_{T} spectrum is crucial to the selection of events for the n sample, and in the definition of $p_{\mathrm{T}}^{\mathrm{rel}}$. It was found that this spectrum in MC simulation is softer in general than in data for this jet sample. To quantify the effect of this on sample selection, the MC simulation spectrum is reweighted to match that measured in data, and the deviation from the central value is taken as the systematic uncertainty. In this analysis, the soft-muon tagging algorithm is represented as a cut on the $p_{\mathrm{T}}^{\mathrm{rel}}$ variable. The *System8* procedure described in Section V.C.1 uses a requirement that $p_{\mathrm{T}}^{\mathrm{rel}} > 700$ MeV, but this

value is not calibrated independently. Since variations in this cut will affect the size and b-purity of the MT sample, a systematic uncertainty is determined by varying the cut value by $\pm$100 MeV. Scale factors are derived for each value, and the symmetrized deviation from the central value is taken as the systematic uncertainty.

h. Fake muons in b- or c-jets As the sample of light-flavor jets is constructed from unfiltered MC simulation, muons not arising directly from b- or c-decay, called *fake muons*, can be separated into jet flavor categories. Scale factors are derived using only light-flavor jets from the unfiltered sample and only b- and c-jets from the muon-filtered sample, but in data, b-tagging algorithms cannot discern real muons from fake muons in b- or c-jets. The *System8* analysis acknowledges this limitation by combining the fake b- and c-jet samples, derived in the same way as the light-flavor sample from the unfiltered simulation, with the real b- and c-jet samples derived from muon-filtered MC simulation and calculating the resulting scale factors. The deviation of the resulting scale factors from the central value is taken as the systematic uncertainty.

i. Jet energy corrections Jet energy measurements contain inherent uncertainty, which result in two systematic sources. A difference in the jet energy resolution in MC simulation from that in data affects our knowlege of jet p_{T} and $|\eta|$ distributions, and a difference in the jet energy scale can bias those distributions. A resolution uncertainty is defined as a gaussian smearing to the energy of the jet with a width parameter set to the uncertainty on the measured energy resolution. The deviation of the resulting scale factors from the central value is taken as the systematic uncertainty. An uncertainty covering the jet energy scale is applied by rescaling jet energies according to the uncertainty in their measurement. An additional uncertainty arises from the asymmetric energy profiles of b-jets, which augments this measurement uncertainty. The systematic uncertainty is defined by varying jet energies by this total uncertainty comparing the results to the central value.

j. Semileptonic correction The jet energy transferred to the lepton and neutrino in $b \to \ell\nu_\ell X$ decays results in a different hadronic jet energy spectrum than in an inclusive

sample of b-jets. To account for this, a set of corrections are derived to bring the semileptonic-decay spectrum into agreement with that from the inclusive sample. The uncertainty on this correction factor comes from generator and simulation modeling uncertainty, correlation with b-tagging weights, and the agreement between the resulting spectrum in data and MC simulation. These variations are applied in total as a fractional correction to the jet energy for uncertainties not related to simulation modeling, and the deviation from the central value is taken as the systematic uncertainty. For simulation modeling uncertainties such as variations in the fragmentation model, the systematics are derived under the same conditions as modeling systematics applied in this analysis. The resulting variance in the semileptonic correction is applied simultaneously with those systematic variations, and is included in those systematic uncertainties.

k. Pileup reweighting Increases in the average number of pileup events, or $\langle\mu\rangle$ in 2011 data have been shown to have a small impact on the precision of the *System8* calibration in Ref. [113]. To be sure that the impact of these conditions is minimal, the $\langle\mu\rangle$ distribution in MC simulation is reweighted to match that in data. A systematic uncertainty is determined by varying $\langle\mu\rangle$ in MC simulation by $\pm 9\%$ before reweighting, and the deviation of the symmetrized scale factors from the central value is assigned as the systematic uncertainty.

l. Extrapolation to inclusive b-jets The requirement of a leptonically-decaying b hadron and a well-measured muon in the sample of b-jets analyzed by the *System8* method limits the direct applicability of its results to samples with the same efficiencies as a function of p_{T} and $|\eta|$. However, if the assumption is correct that the MC simulation provides a good model of the differences between hadronic and semileptonic b-jets, these scale factors $\kappa_b^{\mathrm{data/sim}}$ should be applicable to an inclusive sample of b-jets as well. To ensure that this assumption is correct, a b-tagging calibration analysis was performed on an inclusive, high-purity sample of b-jets in $t\bar{t}$ events, discussed in Ref. [113]. The resulting scale factors for separate semileptonically-decaying and hadronically-decaying jets were compared, and found to be consistent with 1 for all tagging algorithms and working points. An uncertainty of 4% determined from this analysis is assigned as a systematic uncertainty on the scale factors in

Table V.2: Table of systematic errors for the MV1 tagging algorithm at the `MV170` working point, corresponding to $w_{\mathrm{MV1}} = 0.6017130$.

	b-Jet p_{T} Bin [GeV]								
Source	20–30	30–40	40–50	50–60	60–75	75–90	90–110	110–140	140–200
Simulation statistics	2.1	1.5	0.6	0.8	1.2	1.3	2.1	3.6	2.9
Simulation tagging efficiency	< 0.1	< 0.1	< 0.1	< 0.1	< 0.1	0.2	0.2	0.4	0.5
$g \to b\bar{b}$ modeling	< 0.1	< 0.1	< 0.1	< 0.1	< 0.1	-0.1	< 0.1	< 0.1	0.2
$g \to c\bar{c}$ modeling	< 0.1	< 0.1	< 0.1	< 0.1	< 0.1	< 0.1	-0.2	< 0.1	0.2
b-hadron direction modeling	0.5	< 0.1	< 0.1	-0.3	-0.1	0.2	< 0.1	-0.4	1.2
b-fragmentation fraction	2.1	1.8	1.8	2.1	1.2	1.8	2.5	-0.9	0.8
b-fragmentation function	< 0.1	-0.2	< 0.1	< 0.1	< 0.1	0.3	-0.4	0.5	-0.8
b-decay branching fractions	< 0.1	< 0.1	< 0.1	< 0.1	< 0.1	< 0.1	< 0.1	-0.1	< 0.1
b-decay p^* spectrum	-0.2	0.3	< 0.1	0.1	-0.3	-0.1	-0.3	0.1	-0.1
Charm-light ratio	-0.2	< 0.1	< 0.1	-0.1	-0.1	-0.2	< 0.1	-0.3	< 0.1
$p_{\mathrm{T}}^{\mathrm{rel}}$ cut variation	0.7	1.3	-1.0	1.4	< 0.1	-0.2	2.7	2.1	-1.8
Muon p_{T} spectrum	-3.1	-2.0	-1.4	-0.9	-0.4	0.4	0.2	0.6	2.7
Fake muons in b- and c-jets	0.3	0.1	< 0.1	0.2	0.1	0.4	0.2	0.5	0.3
Jet energy resolution	1.7	-0.9	2.8	< 0.1	< 0.1	0.2	-0.8	2.3	-1.3
Jet energy scale	0.1	-0.2	0.6	< 0.1	< 0.1	0.6	-0.4	1.0	0.4
Semileptonic correction	0.4	0.4	1.1	0.5	-0.7	1.3	0.2	-2.1	0.6
Pileup $< \mu >$ reweighting	< 0.1	-0.1	< 0.1	< 0.1	0.1	< 0.1	-0.4	-0.4	< 0.1
Extrapolation to inclusive b-jets	4.0	4.0	4.0	4.0	4.0	4.0	4.0	4.0	4.0
Total Systematic	6.2	5.3	5.7	4.9	4.4	4.9	5.9	6.8	6.4
Statistical	2.0	1.4	1.8	2.6	1.5	2.2	3.4	2.7	4.1
Total	6.5	5.9	6.0	5.5	4.6	5.4	6.8	7.3	7.6

all p_{T} bins determined by the *System8* calibration method.

4. Scale factor measurement with *System8*, and combinations with other measurements

The *System8* b-tagging efficiency calibration method was performed on four lifetime-tagging algorithms at a total of 12 working points, deriving both efficiencies in data $\epsilon_b^{\mathrm{data}}$ and the corresponding scale factors $\kappa_b^{\mathrm{data/sim}}$ in 9 bins of b-jet p_{T}. The results of these measurements are presented in Figure V.11 for the `MV170` working point, which retains 70% of b-jets. The black error bars shown represent data statistical uncertainty, while the green boxes represent total statistical and systematic uncertainty.

The majority of the $\kappa_b^{\mathrm{data/sim}}$ are $\lesssim 1$, between 0.9 and 1 for loose cuts on the b-tagging

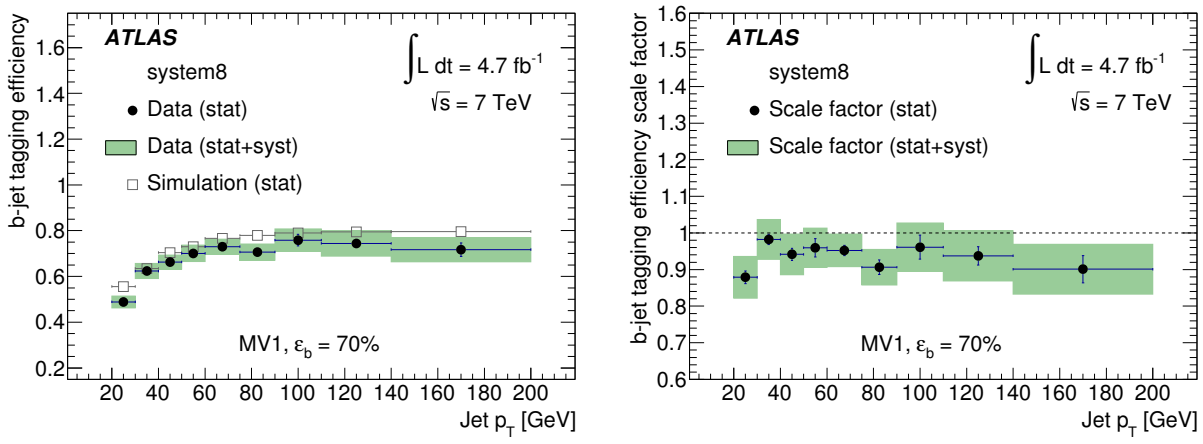

Figure V.11: Results of the *System8* calibration analysis, for the `MV170` working point ($w_{\mathrm{MV1}} = 0.6017130$): (a) b-tagging efficiency, $\epsilon_b^{\mathrm{data}}$, and (b) simulation-to-data scale factors, $\kappa_b^{\mathrm{data/sim}}$.

discriminant and consistent with 1 for tighter cuts. The decrease in efficiency at low and high b-jet p_T can indicate where the tools used in the method become less accurate, or where available MC simulation and measured data is sparse or subject to large systematic uncertainties. The measurements are characterized by a mix of statistical and systematic uncertainties, and the overall uncertainty is small. The dominant systematic as seen in Table V.2 is from the extrapolation of the scale factors to inclusive b-jets, derived from an independent measurement. The next-largest uncertainty comes from the size of the MC simulation samples. Comparison of these results with those from the $p_{\mathrm{T}}^{\mathrm{rel}}$ method, shown in Ref. [110], are consistent within uncertainties. The *System8* analysis also does not have significant increases in uncertainty at high b-jet p_{T}, and its range of sensitivity can likely be extended to b-jets in a boosted regime.

The statistical combination of the scale factors determined from the $p_{\mathrm{T}}^{\mathrm{rel}}$ and *System8* calibration analyses was performed, resulting in an overall measurement for muon-based methods on dijet samples with increased precision. A subsequent full combination of muon-based scale factors with $t\bar{t}$-based scale factors produced the final versions of the $\kappa_b^{\mathrm{data/sim}}$

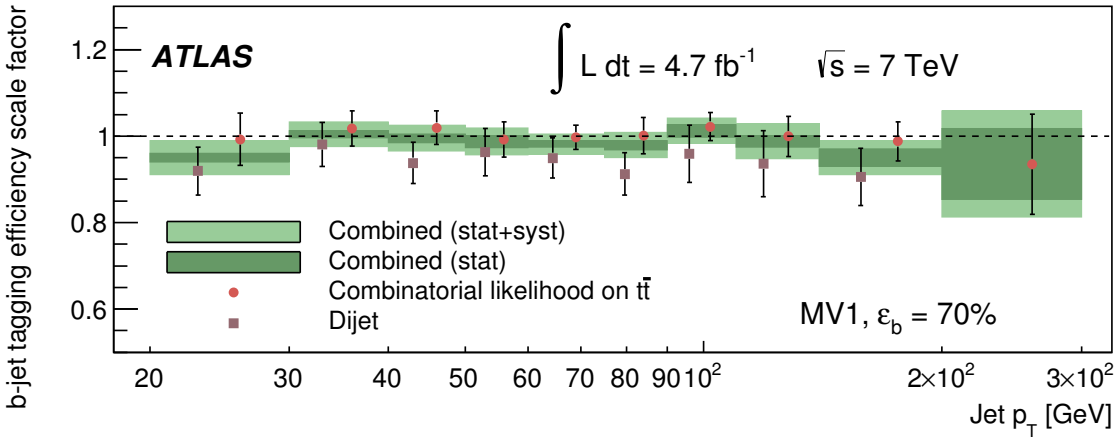

Figure V.12: Combined simulation-to-data scale factors, $\kappa_b^{\text{data/sim}}$, for the muon-based (purple squares) and $t\bar{t}$-based (red circles) methods, and for the full combination (green error bands) at the `MV170` working point ($w_{\text{MV1}} = 0.6017130$).

used in analyses of 2011 data. Since the $p_{\text{T}}^{\text{rel}}$ and *System8* measurements are performed with many of the same MC simulation samples, their statistical and systematic errors are partly correlated within each bin. Systematic correlations are handled by allowing their contribution to the true central value of $\kappa_b^{\text{data/sim}}$ in each analysis to vary with a Gaussian with a mean of 0 and width parameter $\sigma_{\text{syst},i}$ for each systematic source i. Statistical correlations are handled by dividing the combination likelihood into fully correlated and fully uncorrelated components added in ratio. Including the $t\bar{t}$-based scale factors in the combination does not affect intercalibration correlations, but does introduce correlations between bins. These are included in the covariance matrix used in the full combination. The results of the $t\bar{t}$-based and muon-based calibrations is shown together with the full combination in Figure V.12 for the `MV170` working point.

VI. SEARCH FOR ANOMALOUS COUPLINGS IN THE TOP-QUARK DECAY VERTEX WITH SINGLE TOP-QUARK EVENTS

This chapter presents a measurement of effective contributions to the interaction vertex between a top and bottom quark mediated by a W boson, called alternately effective couplings or, in the case of those couplings which do not exist at leading order in the SM, anomalous couplings. It is performed using single top events selected from data collected in 2011 at $\sqrt{s} = 7$ TeV. These events are selected to have one jet in the forward region, an isolated lepton and missing energy representing the leptonic decay of the W coming from top-quark decay, and a b-jet. A novel technique was developed for performing the *folding* step of the analysis, in which the measured quantities of interest are related to the underlying couplings, which uses spherical harmonics ($Y_l^m(\theta^*, \phi^*)$) as the basis functions for this procedure and for modeling background processes. This method is presented in some detail here, and in Refs. [121, 122]. Further mathematical details on the use of spherical harmonics in describing the statistical properties of a distribution are given in Appendix A. The results of the analysis, presented also in Ref. [122], set limits simultaneously on two effective coupling parameters. Some extensions to the analysis are envisioned, and some are being implemented on an updated version to be performed on 8 TeV data; some details will be given in Chapter VII.

A. SINGLE TOP QUARK PHYSICS AT HADRON COLLIDERS

The top quark was first observed at the Tevatron at the Fermi National Accelerator Laboratory, or Fermilab, in 1995 by the CDF [123] and DØ [124] experiments. The initial production

mode observed was top-quark pair production through gluon splitting, $g \to t\bar{t}$, from which measurements of properties such as the top mass m_t have been performed. Top quarks produced singly through the Wtb vertex are much less common, and required a larger dataset for observation. In 2009, both CDF [125] and DØ [126] observed single top quarks produced in a combination of the s-channel and t-channel production modes. In the s-channel production process, a W boson produced in the hard interaction decays to a top quark and a b quark, while in the t-channel production process, a virtual W boson is exchanged between a b quark and a lighter quark, typically producing a top quark and another light quark. A third production process first observed at ATLAS and CMS is called associated production, in which an excited b-quark radiates a W boson and transforms into a top quark. Both ATLAS and CMS have either observed and measured or set limits on the cross-sections of these top pair and single-top production modes for data collected at 7 TeV and 8 TeV.

Of the three SM modes of production of single top quarks, the t-channel exchange of a virtual W boson between a light quark and a b quark is the dominant production process in proton-proton (pp) collisions at $\sqrt{s} = 7$ TeV at the LHC. Its cross-section has been measured precisely by both experiments at 7 TeV [127, 128], using the largest sample of such events collected up to that point. The size of this sample makes precision measurements of properties of the top quark and its couplings feasible from top quarks produced in the t-channel, and the CKM matrix element $|V_{tb}|$, differential cross-sections, and other decay topology properties [129, 130] have all been measured in these events with the 2011 dataset.

Its theoretical cross-section is calculated in the SM with all contributions from next-to-leading order (NLO) QCD diagrams with re-summed next-to-next-to-leading logarithmic (NNLL) accuracy, or approximate next-to-next-to-leading order (NNLO), a top quark mass of $m_t = 172.5$ GeV and using MSTW2008NNLO [8] PDF sets, to be $64.6^{+2.6}_{-1.7}$ pb [131]. The uncertainties correspond to the sum in quadrature of the error obtained from the MSTW PDF set at the 90% confidence level (C.L.) and the uncertainties associated with the factorization and renormalization scales in the parton shower simulation. Properties of the top quark have also been calculated at high precision, such as the fractions of W bosons in top quark decays with helicities of ± 1 or 0, called *helicity fractions*. These have been calculated with all NNLO diagrams involving QCD interactions to get $F_L = 0.687 \pm 0.005$, $F_+ = 0.0017 \pm 0.0001$, and

$F_- = 0.311 \pm 0.005$ [132]. The uncertainties in F_L and F_- arise largely from the experimental uncertainty in the top mass, while the uncertainty on F_+ comes largely from α_s and m_b. The precision of these calculations invites experimental tests of their consistency with the SM, and searches for new physics phenomena.

1. Effective couplings in the Wtb vertex

Measuring properties of the top quark and its electroweak coupling, Wtb, in samples of single top quarks produced in the t-channel provides some advantages with respect to measurements using $t\bar{t}$ pairs. One such benefit is that t-channel events isolate all top interaction vertices to the Wtb vertex. Top pairs are produced through a gluon coupling, then each top quark decays through the Wtb vertex, meaning that different physics processes can affect the production and decay of the top quarks independently. In the t-channel, single top quarks are both produced and decay through the Wtb vertex, meaning that at leading order, the same physics processes which modify the production will modify the decay in the same manner. Another benefit arises from the fact that top quarks produced in the t-channel are polarized along a measurable axis. Though there are correlations between the spins of the t and $\bar{t}$ in top pair production events, the spins of the individual top quarks are not constrained. In t-channel production events, as described in Section II..4, the top quark is produced with its spin direction aligned with the direction of the outgoing light quark. This correlation is reduced somewhat at the level of the reconstructed objects, but it remains large enough to significantly constrain the kinematics of the top quark's decay products.

The form and magnitude of the coupling between the top and bottom quarks and the W boson can serve as a probe of new physics phenomena. In the SM at leading order, only a left-handed vector coupling exists, with a coupling coefficient $V_{\mathrm{L}} = V_{tb} \sim 1$. Fields with higher masses can contribute corrections to this vertex which are not present in the SM, potentially modifying this effective coupling strength or contributing new effective leading-order terms with different lorentz transformation properties. Of particular interest are modifications which generate a $\mathcal{CP}$-violating correction, which modify the relative phase between two such terms by allowing complex values for these new coupling strengths. These modifications are

parameterized by adding the effective couplings to the interaction lagrangian as in Equation II.36. Only the parameter V_{L} is present in the SM, but it is allowed to vary in this framework beyond its SM value. Three entirely new couplings are added: a right-handed vector coupling V_{R}, and left- and right-handed tensor couplings $g_{\mathrm{L,R}}$. This extended description of the Wtb vertex is its the most general Lorentz-covariant form, and each term can also be mapped one-to-one onto a standard dimension-6 coupling from the complete set defined in Ref. [28] (see Equation II.35). These couplings can then be translated into modifications of a normalized differential decay rate, with respect to the angular variables θ^* and ϕ^* which parameterize the decay distribution of the W boson to a lepton and neutrino in the inertial rest frame of the top quark. More theoretical details on this description are presented in Sections II..4 - II..5.

The differential decay rate presented in Equation II.31 is dependent on the helicity amplitudes $A_{1,\frac{1}{2}}$, $A_{0,\frac{1}{2}}$, $A_{0,-\frac{1}{2}}$, and $A_{-1,-\frac{1}{2}}$. The SM forms of these amplitudes, or their probability, are given by the expressions in Equations II.37 - II.42. When the effective couplings are introduced through the couplings $V_{\mathrm{L,R}}$ and $g_{\mathrm{L,R}}$, the probability associated with each amplitude is modified to include their effect. In the analysis presented, a further parameterization of the helicity amplitudes is introduced, defining the observable parameters

- $f_1 \in [0,1]$, the fraction of decays containing transversely polarized W bosons;

$$\begin{aligned} f_1 &= \frac{\left|A_{-1,-\frac{1}{2}}\right|^2 + \left|A_{1,\frac{1}{2}}\right|^2}{\left|A_{-1,-\frac{1}{2}}\right|^2 + \left|A_{0,-\frac{1}{2}}\right|^2 + \left|A_{0,\frac{1}{2}}\right|^2 + \left|A_{1,\frac{1}{2}}\right|^2} \\ &= \frac{2\left(|x_W V_{\mathrm{L}} - g_{\mathrm{R}}|^2 + |x_W V_{\mathrm{R}} - g_{\mathrm{L}}|^2\right) + \mathcal{O}(x_b)}{2\left(|x_W V_{\mathrm{L}} - g_{\mathrm{R}}|^2 + |x_W V_{\mathrm{R}} - g_{\mathrm{L}}|^2\right) + |V_{\mathrm{L}} - x_W g_{\mathrm{R}}|^2 + |V_{\mathrm{R}} - x_W g_{\mathrm{L}}|^2 + \mathcal{O}(x_b)} \end{aligned} \tag{VI.1}$$

- $f_1^+ \in [0,1]$, the fraction of transversely polarized W boson decays that are right-handed;

$$f_1^+ = \frac{\left|A_{1,\frac{1}{2}}\right|^2}{\left|A_{-1,-\frac{1}{2}}\right|^2 + \left|A_{1,\frac{1}{2}}\right|^2} = \frac{|x_W V_{\mathrm{R}} - g_{\mathrm{L}}|^2 + \mathcal{O}(x_b)}{|x_W V_{\mathrm{L}} - g_{\mathrm{R}}|^2 + |x_W V_{\mathrm{R}} - g_{\mathrm{L}}|^2 + \mathcal{O}(x_b)} \tag{VI.2}$$

- $f_0^+ \in [0,1]$, in events with longitudinally polarized W bosons, the fraction of b-quarks that are right-handed;

$$f_0^+ = \frac{\left|A_{0,\frac{1}{2}}\right|^2}{\left|A_{0,-\frac{1}{2}}\right|^2 + \left|A_{0,\frac{1}{2}}\right|^2} = \frac{|V_\mathrm{R} - x_W g_\mathrm{L}|^2 + \mathcal{O}(x_b)}{|V_\mathrm{R} - x_W g_\mathrm{L}|^2 + |V_\mathrm{L} - x_W g_\mathrm{R}|^2 + \mathcal{O}(x_b)} \tag{VI.3}$$

- $\delta_+ \in [-\pi, \pi]$, the phase between the amplitudes for longitudinally polarized and transversely polarized W bosons recoiling against right-handed b-quarks;

$$\delta_+ = \arg A_{1,\frac{1}{2}} A^*_{0,\frac{1}{2}} = \arg\left((x_W V_\mathrm{R} - g_\mathrm{L})(V_\mathrm{R} - x_W g_\mathrm{L})^* + \mathcal{O}(x_b)\right) \tag{VI.4}$$

- $\delta_- \in [-\pi, \pi]$, the phase between the amplitudes for longitudinally polarized and transversely polarized W bosons recoiling against left-handed b-quarks;

$$\delta_- = \arg A_{-1,-\frac{1}{2}} A^*_{0,-\frac{1}{2}} = \arg\left((x_W V_\mathrm{L} - g_\mathrm{R})(V_\mathrm{L} - x_W g_\mathrm{R})^* + \mathcal{O}(x_b)\right), \tag{VI.5}$$

- and $P \in [-1, 1]$, which is considered separately from $\vec{\alpha}$ because it depends on the production of the top quark, rather than the decay. There is no analytical expression for P in terms of anomalous couplings, but a parameterization is determined in Ref. [133] by fitting simulated samples produced with the leading-order (LO) Protos [134] generator[1] with different values for the various couplings.

Note that the fraction f_1 is also directly related to the W-boson helicity fractions, $f_1 = F_R + F_L$, where $F_R = f_1 f_1^+$ and $F_L = f_1(1 - f_1^+)$.

The present analysis only measures the angles θ^* and ϕ^*, so Equation II.31 must be integrated over θ and ϕ; this eliminates all terms with $P_1^0(\cos\theta)$ and introduces a multiplicative factor of 4π. After this integration and reparameterization, only spherical harmonic terms

[1] Protos (PROgram for TOp Simulations) is a generator for studying new physics processes involving the top quark. It has generators for single top-quark and top-quark pair production with anomalous Wtb couplings.

remain with contributions up to a *degree* of $l = 2$ and an *order* of $m = \pm 1$. Identifying $\rho(\theta^*, \phi^* |\ \vec{\alpha}, P)$ as the angular probability density representing this decay distribution,

$$\rho(\theta^*, \phi^* |\ \vec{\alpha}, P) \equiv \frac{1}{N}\frac{dN}{d\Omega^*} = \sum_{l=0,m=-1}^{l=2,m=1} a_l^m(\vec{\alpha}, P)\, Y_l^m\,(\theta^*, \phi^*)\,, \text{ where} \tag{VI.6}$$

$$\vec{\alpha} = \left(f_1, f_1^+, f_0^+, \delta_+, \delta_-\right) \text{ and} \tag{VI.7}$$

$$\begin{aligned}
a_0^0 &= \frac{1}{\sqrt{4\pi}}, \qquad a_1^0 = \frac{\sqrt{3}}{\sqrt{4\pi}} f_1 \left(f_1^+ - \frac{1}{2}\right), \qquad a_2^0 = \frac{1}{\sqrt{20\pi}}\left(\frac{3}{2}f_1 - 1\right), \\
a_1^1 &= -a_1^{1*} = P\frac{\sqrt{3\pi}}{16}\sqrt{f_1(1-f_1)}\left\{\sqrt{f_1^+ f_0^+}\, e^{i\delta_+} + \sqrt{(1-f_1^+)(1-f_0^+)}\, e^{-i\delta_-}\right\}, \\
a_2^1 &= -a_2^{1*} = P\frac{\sqrt{3\pi}}{16\sqrt{5}}\sqrt{f_1(1-f_1)}\left\{\sqrt{f_1^+ f_0^+}\, e^{i\delta_+} - \sqrt{(1-f_1^+)(1-f_0^+)}\, e^{-i\delta_-}\right\}.
\end{aligned} \tag{VI.8}$$

Measurements of points in the angular space (θ^*, ϕ^*) set limits on the possible values of the parameterization variables, $(\vec{\alpha}, P)$, and correspondingly on the values of the couplings $V_{\mathrm{L,R}}$ and $g_{\mathrm{L,R}}$.

Three parameters in $\vec{\alpha}$ are limited by their dependence on the production of right-handed b-quarks, a rare event if the values of the couplings are near the SM values of $V_{\mathrm{L}} = 1$, $V_{\mathrm{R}} = g_{\mathrm{L,R}} = 0$. The fractions f_1^+ and f_0^+ in the SM are nearly 0, near the edge of their physical parameter space, where they can be constrained but not well-measured. If these fractions are 0, the amplitude associated with the phase δ_+ is also nearly 0, leaving little resolultion. Thus, the parameters to which this analysis is most sensitive and which can be reliably measured near the SM are the fraction f_1 and the phase δ_-.

The dependence of the phase δ_- on V_{R} and g_{L} is suppressed by a factor of the ratio of the b-quark mass to the top-quark mass, x_b, while both f_1 and δ_- are dependent on V_{L} and g_{R} directly or through the mass ratio x_W. Thus, to simplify the analysis, only variations in V_{L} and g_{R} are considered, while V_{R} and g_{L} are assumed to be zero. This assumption results in small values being assigned to f_1^+ and f_0^+, which agrees with the expectations established by the descriptions of parameter sensitivities. The value of P is also determined from the values of V_{L} and g_{R}. The highest-order dependence of f_1 and δ_- on the couplings V_{L} and g_{R} appear as the ratio $\frac{g_{\mathrm{R}}}{V_{\mathrm{L}}}$, where the real and imaginary parts of this ratio are measured separately. This motivates quoting the results in the reduced parameter space (f_1, δ_-) and the coupling space $(\mathrm{Re}[\frac{g_{\mathrm{R}}}{V_{\mathrm{L}}}], \mathrm{Im}[\frac{g_{\mathrm{R}}}{V_{\mathrm{L}}}])$.

Figure VI.1 shows the shape of the model in these two variables for the SM values of $fu \approx 0.30$ and $\delta_- = 0.00$, as well as two non-SM variations, generated with PROTOS. Further details on the characterization of this space, supporting the descriptions above, are presented in Appendix B.

2. Current constraints on anomalous couplings

Indirect constraints on V_{R}, g_{L}, and g_{R} have been obtained [135] from precision measurements of B-meson decay. These result in tight constraints on V_{R} and g_{L}, but much looser constraints on g_{R}. A recent update of this calculation [136] yields $\mathrm{Re}[V_{\mathrm{R}}] \in [-0.0008, 0.0021]$, $\mathrm{Re}[g_{\mathrm{L}}] \in [-0.0011, 0.0004]$, $\mathrm{Re}[g_{\mathrm{R}}] \in [-0.19, 0.48]$. Calculations of the anomalous couplings in specific models expect a much larger contribution to g_{R} than to V_{R} or g_{L} [137]. The precision achieved from the first two indirect constraints, and the need for stronger constraints on g_{R}, motivates further the choice to focus on V_{L} and g_{R}.

Limits on deviations from the SM values of $V_{\mathrm{L,R}}$ and $g_{\mathrm{L,R}}$ have been set previously at ATLAS. By measuring W-boson helicity fractions in $t\bar{t}$ events in Ref. [138], ATLAS sets limits on $\mathrm{Re}[V_{\mathrm{R}}] \in [-0.20, 0.23]$, $\mathrm{Re}[g_{\mathrm{L}}] \in [-0.14, 0.11]$, and $\mathrm{Re}[g_{\mathrm{R}}] \in [-0.08, 0.04]$ at the 95% confidence level (CL). These measurements have been combined with CMS results [139], and the resulting LHC combination [140] is less constraining, with $\mathrm{Re}[g_{\mathrm{R}}] = -0.10 \pm 0.06(\mathrm{stat.})^{+0.07}_{0.08}(\mathrm{syst.})$. This analysis is sensitive through its measurement of θ^* to the couplings $\mathrm{Re}[V_{\mathrm{R}}]$ and $\mathrm{Re}[g_{\mathrm{L,R}}]$. An angular asymmetry measured in Ref. [130] sets a limit on $\mathrm{Im}[\frac{g_{\mathrm{R}}}{V_{\mathrm{L}}}] \in [-0.2, 0.3]$, the first ATLAS analysis to directly probe this potentially $\mathcal{CP}$-violating coupling. The asymmetry A_{FB}^{N} is defined as the asymmetry in the number of events with positive or negative values of $\cos\theta^{\mathrm{N}}$, the angle between the lepton and the direction perpendicular to the plane formed by the W boson direction in the top rest frame and the top spin direction. Both analyses average over a subset of the (θ^*, ϕ^*) space, and the present analysis increases the size of this subspace to include the underlying physics of both analyses, removing the assumptions used in the evalutation of the previous limits.

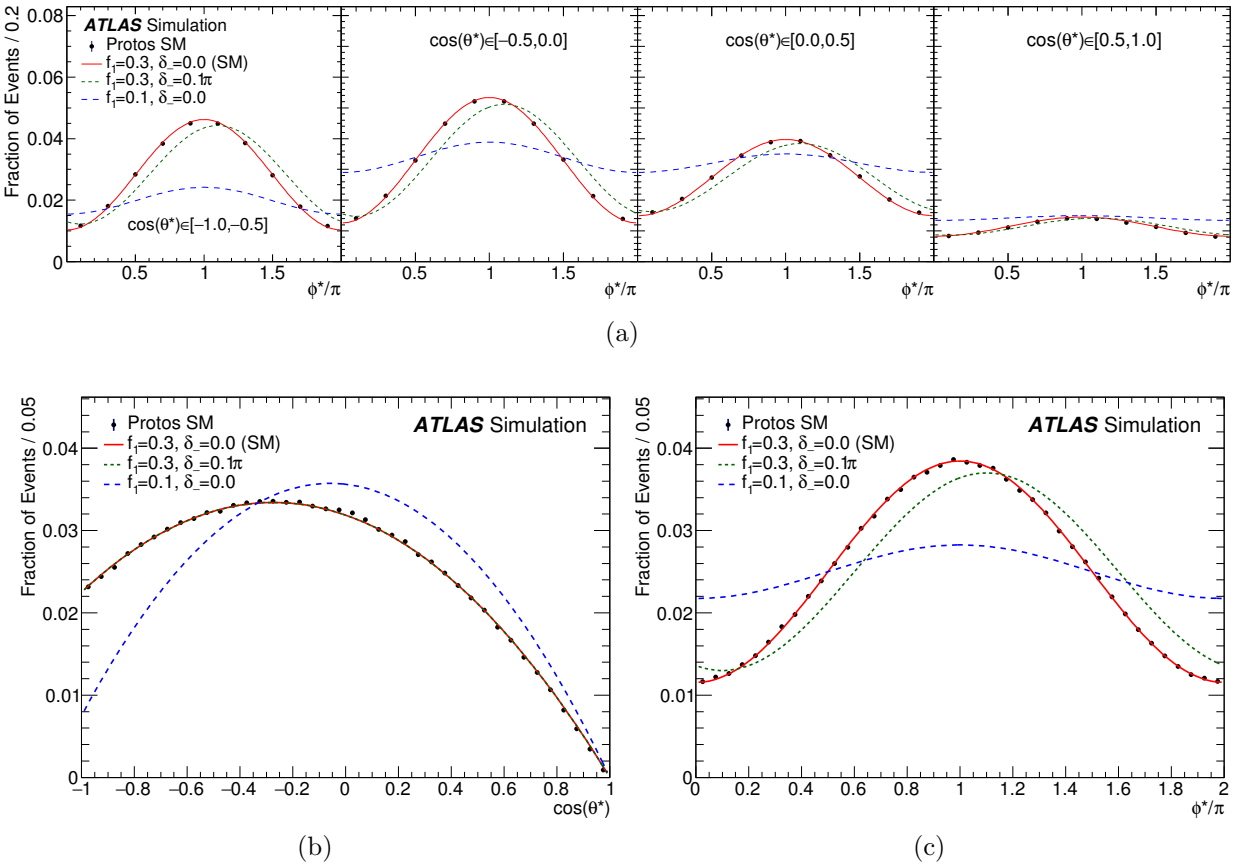

Figure VI.1: Projections into (a) ϕ^* in bins of $\cos\theta^*$, (b) $\cos\theta^*$, and (c) ϕ^* in Equation VI.8, for different values of f_1 and δ_-. The black points represent the PROTOS t-channel signal generated with SM parameters, and the curves shown represent the signal model. For the three curves shown, the parameters f_1 and δ_- are set to their values in the SM, $f_1 = 0.3$, $\delta_- = 0$ (solid red), and to two sets of beyond-the-SM values, $f_1 = 0.1$, $\delta_- = 0$ (dashed blue) and $f_1 = 0.3$, $\delta_- = 0.1\pi$ (dotted green).

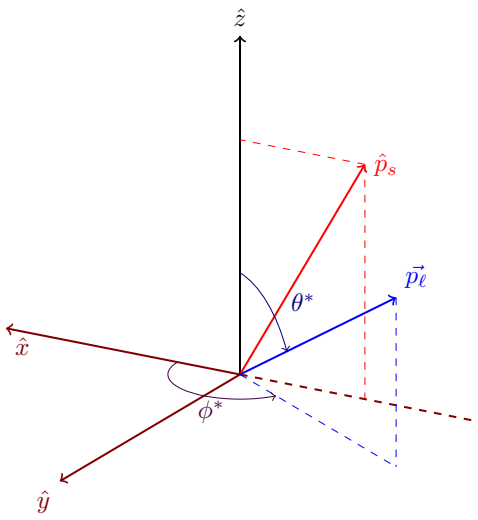

Figure VI.2: Definition of the coordinate system. $\hat{x}$, $\hat{y}$, and $\hat{z}$ are defined as shown from the momentum directions of the W boson, $\hat{q} \equiv \hat{z}$, and the spectator jet, $\hat{p}_s$, in the top-quark rest frame. The angles θ^* and ϕ^* indicate the lepton direction $\hat{p}_\ell$ in this coordinate system.

3. Definition of coordinate system

As was shown in Section II..4, the spin of the top quark in its rest frame, $\vec{s}_t$, is nearly 100% polarized along the direction of the light-quark jet produced in t-channel production, called the *spectator jet*, with momentum direction $\hat{p}_s = \frac{\vec{p}_s}{|\vec{p}_s|}$. As information about the spin is not directly accessible from the decay kinematics, $\hat{p}_s$ provides a proxy with some inherent uncertainty, called the *spin-analyzing direction*. The *degree of polarization* for this axis is shown in Refs. [141, 142], for SM values of the couplings, to be $P \equiv \hat{p}_s \cdot \vec{s}_t/|\vec{s}_t| \approx 0.9$ in pp collisions at $\sqrt{s} = 7$ TeV in the LHC. The z-axis is chosen along the direction of the W boson boosted into the top-quark rest frame, $\hat{z} \equiv \hat{q} = \vec{q}/|\vec{q}|$. The angle θ^* between $\vec{q}$ and the momentum of the lepton in the W boson rest frame, $\vec{p}_\ell$, is the same angle used to measure the W boson helicity fractions in top-quark decays [143, 144, 145, 146]. The three-dimensional coordinate system in Figure VI.2 is defined from the $\hat{q}$–$\hat{p}_s$ plane and the perpendicular direction $\hat{y} = \hat{p}_s \times \hat{q}$, so $\hat{x} = \hat{y} \times \hat{q}$. In this coordinate system, the direction of

the lepton in the W boson rest frame, $\hat{p}_\ell$, is given by θ^* and the complementary azimuthal angle ϕ^*.

These angles θ^* and ϕ^* describe a spherical coordinate system parameterizing the angular distribution of the $W \to \ell\nu_\ell$ decay with respect to the W-boson momentum and spectator-jet direction in the top-quark rest frame. This event-specific coordinate system is constructed in MC simulation using the true kinematics of these particles to develop the distributions shown in Figure VI.1. In real data, these momenta must be reconstructed from the detector signals, resulting in some deviation from the true distributions of interest. The directions of the jets, lepton, and $E_{\mathrm{T}}^{\mathrm{miss}}$ in the event are used to describe the observable angular coordinates (θ^*, ϕ^*), which are then *unfolded* to a set of distributions in the true coordinates, (θ_t^*, ϕ_t^*), using models of these detector effects derived from MC simulation. The details of this unfolding procedure are explained in Section VI.D.1.

B. DATA AND SIMULATED SAMPLES

This analysis is performed using the full sample of high-quality pp collision data delivered by the LHC in 2011 at $\sqrt{s} = 7$ TeV and recorded by the ATLAS experiment. Data quality is ensured by a set of stringent detector and data quality requirements; the sample of events meeting these requirements corresponds to a total integrated luminosity of 4.59 ± 0.08 fb^{-1} [147]. The events used in the analysis are selected by single-lepton triggers [148], which require a minimum E_{T} of 20 GeV or 22 GeV for electrons and a minimum transverse momentum of 18 GeV for muons, depending on the data-taking conditions.

Samples of events generated using Monte Carlo (MC) simulations are produced for t-channel signal and the background processes. They are used to evaluate models of efficiency and resolution, and to estimate systematic uncertainties. Simulated t-channel single top-quark events are produced with the AcerMC multi-leg LO generator [149] (version 3.8) using the LO `CTEQ6L1` [150] PDF sets. The AcerMC samples incorporate both the $2 \to 2$ process, in which the b quark needed to product the top quark is taken directly from the proton's parton distribution function, and the $2 \to 3$ process, in which this b quark is one of

two arising from gluon splitting $g \to b\bar{b}$ in the event simulation. It also features an automated procedure to remove the overlap in phase space between them [151]. The factorization and renormalization scales are set to $\mu_{\mathrm{F}} = \mu_{\mathrm{R}} = 172.5$ GeV. These samples are used to evaluate systematic uncertainties related to the reconstruction of the final-state objects and generator modeling. Additional t-channel samples with varied anomalous couplings are produced with PROTOS, version 2.2, using the four-flavor scheme[2], with the `CTEQ6L1` PDF sets. These samples only incorporate the $2 \to 3$ process, and anomalous couplings are enabled in both the production and the decay vertices. For the purposes of this analysis, $\mathrm{Re}[V_{\mathrm{R}}]$, $\mathrm{Re}[g_{\mathrm{R}}]$, and $\mathrm{Im}[g_{\mathrm{R}}]$ are varied simultaneously to keep the total top-quark width invariant. The factorization scale is set to $\mu_{\mathrm{F}}^2 = -p_W^2$ for the light quark and $\mu_{\mathrm{F}}^2 = p_b^2 + m_b^2$ for the gluon. These samples are used to derive folding models with non-SM values of the couplings for validation tests in MC simulation and measurements in real data, and to evaluate systematic uncertainties related to the t-channel generator modeling and the folding model determination. The parton showering (PS), hadronization, and underlying-event (UE) modeling in these samples are simulated with PYTHIA [152], version 6.426, applying the Perugia 2011C (`P2011C`) parameter tunings [153], and using the `CTEQ6L1` PDF sets.

Some additional samples are created to evaluate uncertainties related to the generator, PS, hadronization, and UE models. Samples generated with ACERMC and showered with HERWIG [154] version 6.5.20 are compared to those showered with PYTHIA to estimate variance in the results related to the PS, hadronization, and UE models. The POWHEG-BOX [155] NLO generator version 1.0, with the `CT10` [9] NLO PDF sets, is used to estimate the systematic uncertainty related to the differences between the LO and NLO processes. This generator is also used to estimate variances resulting from the choice of factorization and renormalization scales, in which μ_{F} and μ_{R} are varied independently by factors of 0.5 and 2.0 while the scale of the parton shower varies consistently with the renormalization scale.

Samples of $t\bar{t}$ events, s-channel single top-quark events, and associated production of a W boson and top quark (Wt) are generated with POWHEG-BOX, coupled with the `CT10` PDF

[2] In the four-flavour scheme, the PDFs only contain those quarks lighter than the b-quark — that is, d, u, s, and c.

sets and showered with PYTHIA using the P2011C tune and the CTEQ6L1 PDF sets. Additional $t\bar{t}$ samples are produced with PROTOS using the CTEQ6L1 PDF sets, which are used to evaluate the background model with non-SM values of the couplings. The PS, hadronization, and UE in these samples are simulated with PYTHIA using the AUET2B tune [156] with the MRST LO** [157] PDF sets. All processes involving top quarks are produced assuming $m_t = 172.5$ GeV.

Vector-boson ($W^{\pm}$ or Z^0) production in association with jets (V+jets) is simulated using the multi-leg LO ALPGEN generator [158], version 2.13, using the CTEQ6L1 PDF sets and interfaced to HERWIG with the JIMMY UE model [159], version 4.31. The contributions of W+light-jets and W+heavy-jets ($W+b\bar{b}, W+c\bar{c}, W+c$) are simulated separately. To remove overlaps between the n-parton and $(n+1)$-parton samples, the MLM matching scheme [160] is used. Double counting between the inclusive $W + n$-parton samples and samples with associated heavy-quark pair production is removed using an overlap-removal algorithm based on parton-jet ΔR matching [161]. Diboson processes (WW, WZ and ZZ) are produced using the HERWIG generator with the MRST LO** PDF sets.

After the event-generation step, the ACERMC samples are passed through the full ATLAS detector simulation described in Section III..3. The PROTOS samples are passed through the ATLFAST2 simulation [162] of the ATLAS detector, which uses a simplified geometry and parameterizations of particle showers and their corresponding calorimeter response, including both primary and pile-up interactions. They are then reconstructed using the same procedure as for data. The events are weighted such that the distribution of the average number of collisions per bunch crossing is the same as in data.

C. SAMPLE CONSTRUCTION

The samples mentioned are produced from the detector, or its simulation, and processed to convert the recorded hits and energy depositions into the variables used in the measurement. The first step is to define the objects needed in the analysis: muons, jets, b-jets, and missing transverse momentum describe this final state. The definitions for these objects are discussed

in Chapter IV, which concerns definitions of kinematics and specific thresholds used in identifying them, while further requirements given here are analysis-specific. Next, the largest backgrounds to this process are modeled, so they can be subtracted from the signal region in the final analysis. Most backgrounds are modeled with MC simulation events, exceptional background models which require more complex procedures are described here. Finally, two stages of event selection criteria are applied to enhance the ratio of the contributions of the signal to that of the background. The definitions of objects used in the analysis and the criteria constituting the first stage of event selection are chosen to be identical to those used for the t-channel cross-section measurements in Ref. [127], and the background construction method is similar.

1. Object definitions

The definition of all physics objects is dependent on the reconstructed position of the hard interaction. Primary interaction vertices are computed from reconstructed tracks that are compatible with originating in the luminous interaction region. The hard-interaction primary vertex is chosen as the vertex featuring the highest $\sum p_{\mathrm{T}}^2$, where the sum runs over all tracks with $p_{\mathrm{T}} > 0.4$ GeV associated with the vertex.

Electron candidates are selected from clusters in the LAr electromagnetic calorimeter associated with a well-measured track fulfilling the quality requirements described in Ref. [80]. Candidate clusters must pass a modified transverse energy requirement, $E_{\mathrm{cluster}}/\cosh(\eta_{\mathrm{track}}) > 25$ GeV, and pseudorapidity requirement $|\eta_{\mathrm{cluster}}| < 2.47$. Clusters falling in the calorimeter barrel-endcap transition region, $1.37 < |\eta_{\mathrm{cluster}}| < 1.52$, are rejected. Since electrons from the W boson decay are typically isolated from hadronic jet activity, backgrounds are suppressed by *isolation criteria*, requiring minimal calorimeter activity and only allowing low p_{T} tracks in a $\Delta\eta$-$\Delta\phi$ cone around the electron candidate. These criteria are optimized in MC simulation to achieve a uniform cut efficiency of 90% as a function of η_{cluster} and E_{T}. The direction of the electron candidate is taken from its associated track. For the calorimeter isolation, a cone size of $\Delta R = 0.2$ is used. The scalar sum of all track transverse momenta within a cone of size $\Delta R = 0.3$ around the electron direction is required to produce an isolation efficiency

in simulation of 90%. The track belonging to the electron candidate is excluded from this requirement.

Muon candidates are reconstructed from combined muons passing tight identification requirements. They must have transverse momentum $p_{\mathrm{T}} > 25$ GeV and fall within the pseudorapidity range of the inner detectors, $|\eta| < 2.5$. Muons tracks are required to have at least two hits in the pixel detector, and six or more hits in the SCT. Tracks are rejected if they have more than two missing hits in the SCT and pixels detectors, or an excessive number of outlier hits in the TRT. The longitudinal impact parameter of the muon track with respect to the primary vertex, z_0, is required to be smaller than 2 mm. Isolation criteria are applied to reduce contamination from events in which a muon is produced from a quark decay (e.g. b and c quarks that decay leptonically and produce a muon inside a jet), requiring that the energy in a cone of $\Delta R = 0.2$ be $\sum E_{\mathrm{T}}^{\mathrm{calo}} < 4.0$ GeV, and the momentum in a cone of $\Delta R = 0.3$ be $\sum p_{\mathrm{T}}^{\mathrm{track}} < 2.5$ GeV. The efficiency of this combined isolation requirement varies between 95% and 97%, depending on the data-taking period.

Jets are reconstructed from topological calorimeter clusters using the anti-k_t algorithm [88] with $R = 0.4$. The clusters are calibrated with the local cluster weighting method described in Ref. [90]. They are required to have $p_{\mathrm{T}} > 30$ GeV and $|\eta| < 4.5$. Jets overlapping with identified electron candidates within a cone of $\Delta R = 0.2$ are not considered, as the jet and the electron are very likely to correspond the same object. To reduce the effect of pile-up, the jet vertex fraction, defined as in Section V.C.2, must satisfy $\epsilon_{\mathrm{JVF}} > 0.75$. Jets containing b hadrons satisfying $|\eta| < 2.5$ and $p_{\mathrm{T}} > 30$ GeV are identified from a selection on the tagging weight of the `IP3D+JetFitter` algorithm, introduced in Section V.A.4, with a tuning which improves rejection of c-jets. The chosen requirement on $w_{\mathrm{IP3D+JetFitter}}$ is calibrated to have a b-jet tagging efficiency of 55% in $t\bar{t}$ events, and results in a c-tagging efficiency of 4.8% and a mistag rate of 0.48%.

The missing transverse momentum, $\vec{E}_{\mathrm{T}}^{\mathrm{miss}}$, defined in Section IV.F, is considered to be a measure of the momentum imbalance due to the neutrino produced in the decay of the W. It is calculated as the vector sum over the energy of all clusters of adjacent calorimeter cells reconstructed in the event projected onto the transverse plane and is corrected for the presence of electrons, muons, and jets, and its magnitude must satisfy $E_{\mathrm{T}}^{\mathrm{miss}} > 30$ GeV.

The W boson coming from the decay of the top quark can be reconstructed from the momenta of the lepton and the neutrino using four-momentum conservation. The $\vec{E}_{\mathrm{T}}^{\mathrm{miss}}$ represents the transverse component of the neutrino momentum and the longitudinal component p_{ν}^{z} is chosen such that the resulting W boson is on its mass shell. This yields a quadratic expression for p_{ν}^{z}, generally with two solutions. If there are two possible real values, the value closer to zero is taken. Complex solutions can arise through variance in the resolution of the $E_{\mathrm{T}}^{\mathrm{miss}}$ measurement. In this case, the $E_{\mathrm{T}}^{\mathrm{miss}}$ is rescaled to produce physically-allowed solutions for p_{ν}^{z}. If two solutions are found, the one resulting in the smaller value of $|p_{\nu}^{z}|$ is taken. The top-quark momentum is reconstructed from the W boson momentum and the momentum of the b-tagged jet. The momenta of the W boson and spectator jet are boosted into its rest frame to obtain the directions $\vec{q}$ and $\vec{p}_{s}$ used to generate the coordinate system in Figure VI.2. The lepton is boosted into the W boson rest frame to obtain $\vec{p}_{\ell}$.

2. Background Estimation

The largest background contributions to single top-quark t-channel production in the signal region are events from $t\bar{t}$ production and from W boson production in association with jets (called W+jets). Events containing $t\bar{t}$ production are difficult to distinguish from single top-quark events, as they also have real top quarks in the final state. The production of a W boson with two jets, where one is identified as containing a b-hadron, can mimic the t-channel final state. The high rate of multiple-jet production via QCD (called multijets) can result in a few such events to appear like the signal as well, and data-driven techniques are required to accurately model them. Other backgrounds originate from Wt-channel and s-channel single top-quark, diboson (WW, WZ, and ZZ) and Z+jets production. Most of these background models are derived directly from MC simulation, but specialized procedures are implemented for W+jets and multijet production.

The $t\bar{t}$ cross-section is calculated at NNLO in QCD including resummation of next-to-next-to-leading logarithm (NNLL) soft-gluon terms with the Top++ 2.0 [163, 164, 165, 166, 167, 168, 169] program, and are found to be 177^{+10}_{-11} pb. The uncertainties on the PDFs at 68% C.L. and the strong coupling constant α_{s} are calculated following the PDF4LHC [170]

prescription for the MSTW2008NNLO, CT10, and NNPDF2.3 [10] error PDF sets, and are added in quadrature to the scale uncertainty to yield a total uncertainty of 6%. Single top-quark production cross-sections for s-channel and Wt associated production are calculated with approximate NNLO precision and are found to be 15.7±1.2 pb [171] and $4.63^{+0.20}_{-0.18}$ pb [172], respectively. The uncertainties correspond to the sum in quadrature of the uncertainty derived from the MSTW2008NNLO error PDF sets at 90% C.L. and the scale uncertainties, yielding a final uncertainty of about 8% for Wt-channel and about 4% for s-channel production. The Z+jets inclusive production cross-section is estimated with NNLO precision using the FEWZ program [173]. Diboson events (WW, WZ, and ZZ) are normalized to the NLO cross-section prediction calculated with MCFM [174]. The uncertainty on the combined Z+jets and diboson background is estimated to be 60% as in Ref. [127].

For the production of a W boson in association with jets, the shapes of the relevant kinematic distributions are predicted from the ALPGEN sample. They are initially normalized to make the inclusive W cross-section correspond to the NNLO prediction using FEWZ, with the same scaling factor being applied to the ALPGEN prediction for the $W+b\bar{b}$, $W+c\bar{c}$, and W+light-jets samples. The ALPGEN prediction for the $W+c$ process is scaled by a factor that is obtained from a study based on NLO calculations using MCFM. Data-driven techniques are then used to estimate the flavor composition and the overall normalization as described in Ref. [175]. An uncertainty of 18% (15%) for electron (muon) selections is applied.

Multijet background events pass the signal region selection if a jet is mis-identified as an isolated lepton, or if the event has a non-prompt lepton from the isolated decay of a hadron. Since it is neither possible to simulate a sufficient number of those events, nor to calculate the rate precisely, special techniques employing both collision data and simulated events are used to model multijet events and estimate their production rate. In the electron channel, mis-identified jets are the main source of this background. This is modeled by the jet-lepton method [127], in which a jet producing an electromagnetic shower resembling that of an electron is selected in PYTHIA dijet MC samples and redefined as a lepton. In the muon channel, a data-driven matrix method [176, 127] based on the muon impact

parameter significance is used. An uncertainty of 50% is assigned to the estimated yield based on comparisons of the rates obtained by using alternative methods [127], i.e. the matrix method in the electron channel and the jet-lepton method in the muon channel, and using an alternative variable, i.e. $m_{\mathrm{T}}(\ell, E_{\mathrm{T}}^{\mathrm{miss}})$ instead of $E_{\mathrm{T}}^{\mathrm{miss}}$.

3. Event selection and validation

This analysis requires exactly one isolated charged light lepton, either an electron, a muon, or a tau decaying leptonically, exactly one b-tagged jet, and exactly one untagged jet, with each object satisfying the given requirements. Two additional selection criteria are applied to reduce multijet backgrounds. The transverse mass of the lepton–$E_{\mathrm{T}}^{\mathrm{miss}}$ system,

$$m_{\mathrm{T}}(\ell, E_{\mathrm{T}}^{\mathrm{miss}}) = \sqrt{2p_{\mathrm{T}}(\ell) \cdot E_{\mathrm{T}}^{\mathrm{miss}} \left[1 - \cos\left(\Delta\phi(\ell, E_{\mathrm{T}}^{\mathrm{miss}})\right)\right]}, \tag{VI.9}$$

is required to be larger than 30 GeV. A more stringent cut on the lepton p_{T} is applied to events in which the lepton and leading jet, j_1, are back-to-back,

$$p_{\mathrm{T}}(\ell) > \max\left(25, 40\left(1 - \frac{\pi - |\Delta\phi(j_1, \ell)|}{\pi - 1}\right)\right) \text{ GeV}, \tag{VI.10}$$

where $\Delta\phi(j_1, \ell)$ is the difference in azimuthal angle between the lepton momentum and the leading jet. The distributions of the angles $\cos\theta^*$ and ϕ^* after these definitional and background-rejecting criteria are applied are shown in Figure VI.3.

After this basic event selection, further discrimination between t-channel single top-quark events and background events is achieved by applying additional criteria:

- The pseudorapidity of the untagged jet must satisfy $|\eta| > 2$, since the spectator jet tends to be forward in the t-channel signature.
- The sum of the p_{T} of all final-state objects, H_{T}, must be larger than 210 GeV, since the H_{T} distributions of the backgrounds have their peaks just below this value.
- The mass of the top quark reconstructed from its decay products is required to be within 150–190 GeV, to reject background events from processes not involving top quarks.
- The distance in η between the untagged jet and the b-tagged jet must be larger than 1, to further reduce $t\bar{t}$ contributions.

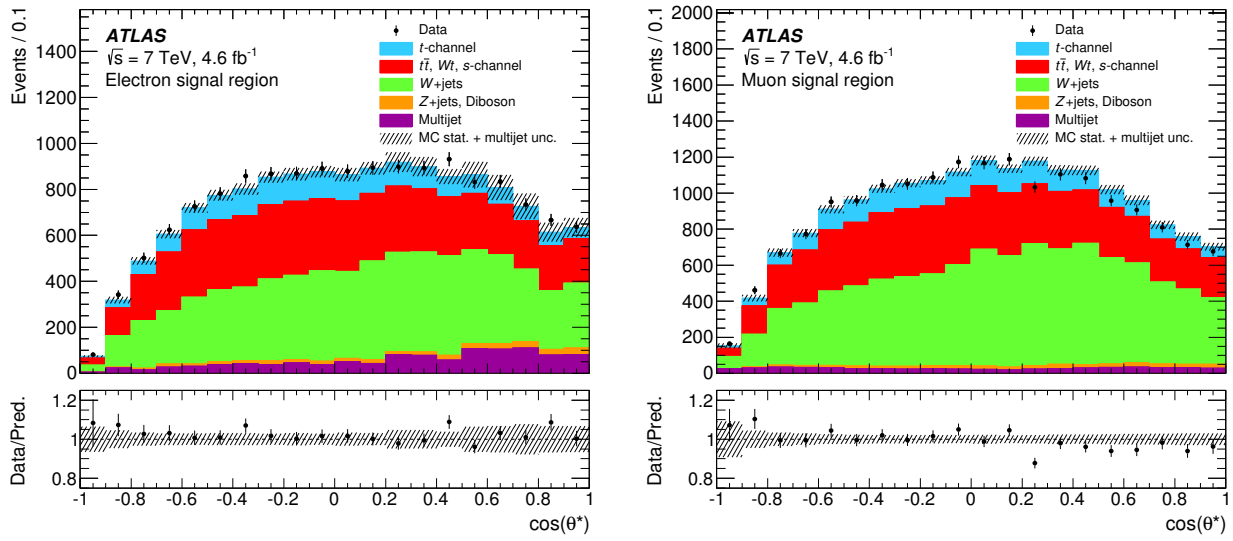

(a)

(b)

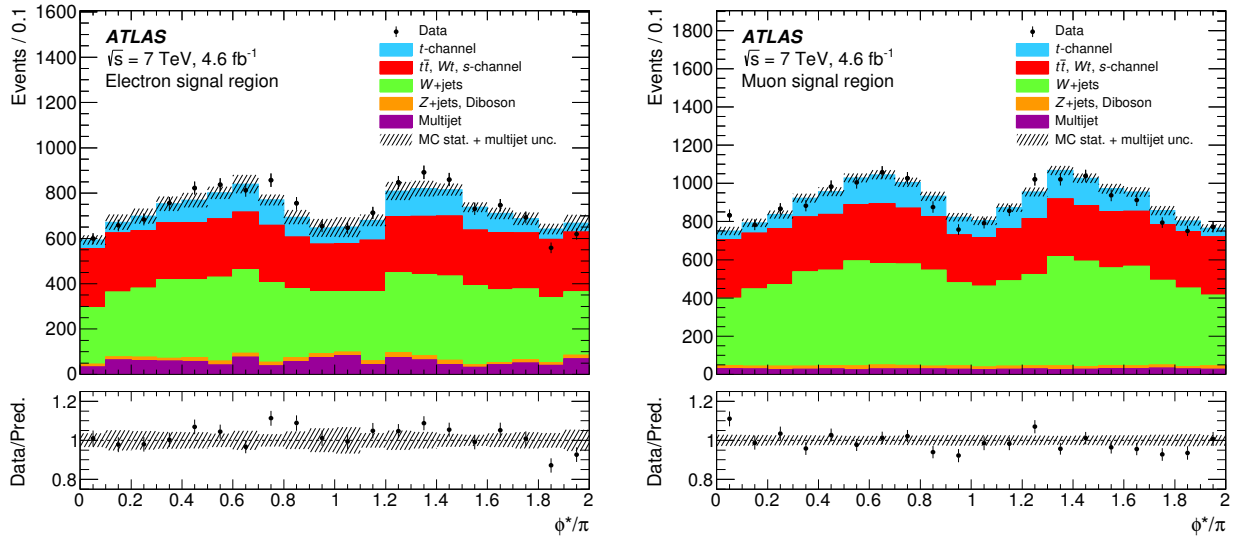

(c)

(d)

Figure VI.3: Angular distributions $\cos\theta^*$ (upper row) and ϕ^* (lower row) after the basic selection for electrons (left) and muons (right), comparing data (black points with statistical uncertainties) to SM signal and background predictions. The uncertainties shown on the prediction include MC statistics and the 50% systematic uncertainty on the normalization of the multijet background. The lower plot shows the ratio of data to prediction in each bin.

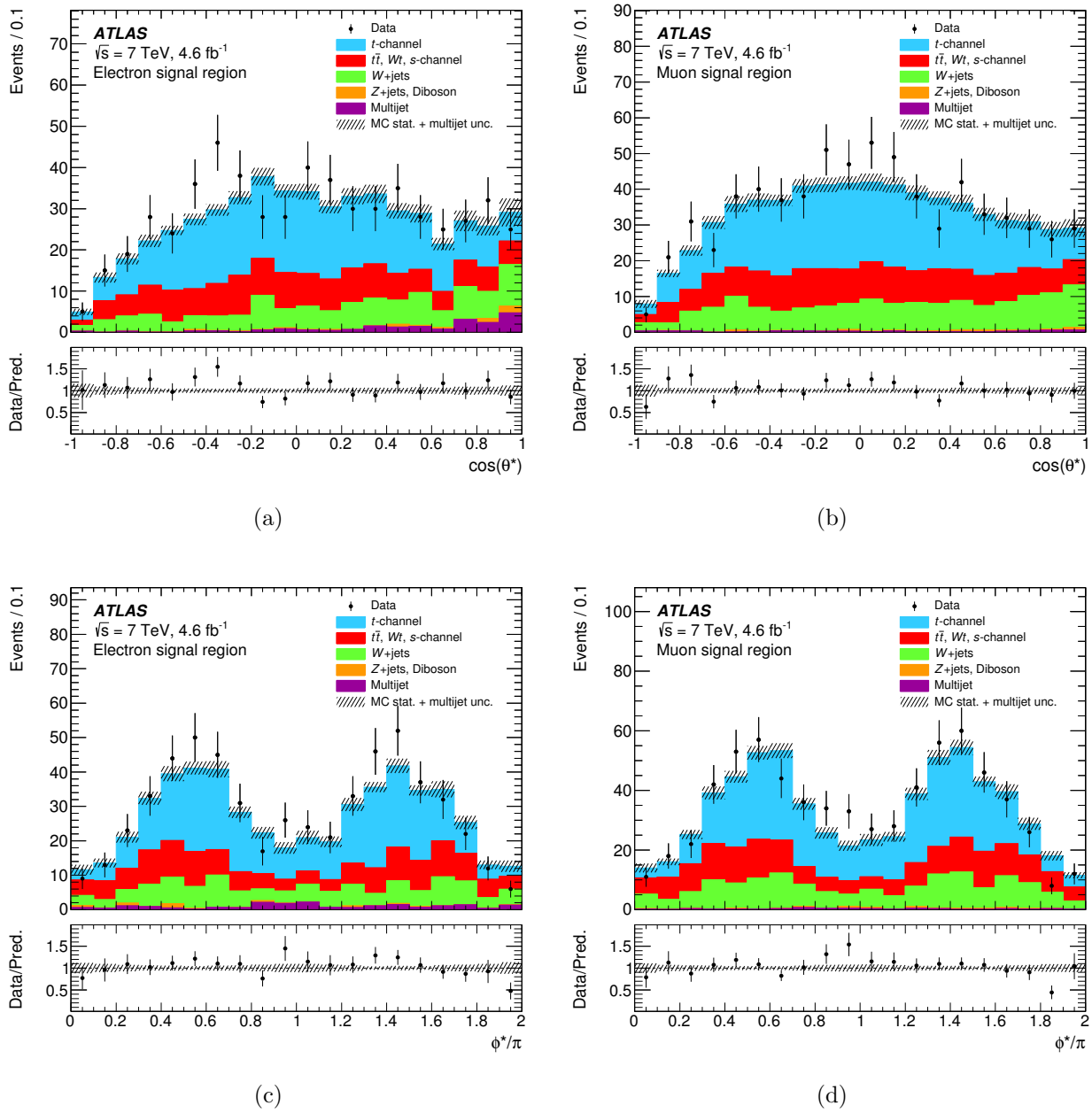

Figure VI.4: Angular distributions $\cos\theta^*$ (upper row) and ϕ^* (lower row) in the signal region for electrons (left) and muons (right), comparing data (black points with statistical uncertainties) to SM signal and background predictions. The uncertainties shown on the prediction include MC statistics and the 50% systematic uncertainty on the normalization of the multijet background. The lower plots show the ratio of data to prediction in each bin.

These criteria and the basic event selection together define the *signal region* of the analysis. The distributions of the angles $\cos\theta^*$ and ϕ^* in the signal region are shown in Figure VI.4.

Table VI.1: Event yields for the electron and muon channels in the signal region. The uncertainties shown are statistical only. Uncertainties of less than 0.5 events appear as zero.

	Electrons	Muons
t-channel	274 ± 2	336 ± 2
s-channel	4 ± 0	5 ± 0
Wt-channel	13 ± 1	16 ± 1
$t\bar{t}$	119 ± 2	147 ± 3
W+heavy-jets	92 ± 7	128 ± 8
W+light-jets	13 ± 4	18 ± 3
Z+light-jets	4 ± 1	3 ± 1
Diboson	1 ± 0	2 ± 0
Multijet	20 ± 7	6 ± 1
Total expected	538 ± 11	660 ± 10
Data	576	691

Table VI.1 provides the event yields for the electron and muon channels after the event selection. Since the number of events in W+light-jets and multijet samples are low, statistical fluctuations and events with large generator weights affect the sample shapes. Therefore, shape templates from events selected without the b-tagging requirement are used for these two backgrounds to smooth the simulated models. The hardest jet in each of these events is chosen to take the place of the b-tagged jet for the purposes of the event selection and reconstruction. Overall, good agreement between the observed and expected distributions is found.

Two *control regions* are also defined, enhanced in each of the two dominant backgrounds, $t\bar{t}$ and W+jets, to validate their modeling in MC simulation. In the control region where the $t\bar{t}$ background is enriched, events are selected which have exactly four jets, exactly one of which is b-tagged, passing the basic event selection, the top-quark mass requirement, and the H_{T} requirement. In the control region where W+jets backgrounds are enriched, events with exactly two jets passing the basic event selection and an inversion of the top-quark

mass criterion are required. The distributions of the angles $\cos\theta^*$ and ϕ^* in the four-jet and anti-selection control regions are shown in Figures VI.5 - VI.6.

Distributions of control variables play an important role in validating the sample construction. Appendix C contains many distributions of variables important to the selection and reconstruction of these events in the signal region and the two control regions, which demonstrate the level of agreement in the model.

D. ANALYSIS METHOD

The model describing the t-channel signal in Equation VI.8 is related to the angles measured in reconstructed events in the signal region via an analytic folding procedure, using some of the statistical properties described in Appendix A. Models of the selection efficiency and detector resolution are derived from simulated t-channel signal events, and a model of the reconstructed background is derived from the sum of the combined background processes described in Section VI.B. Both the t-channel signal and the $t\bar{t}$ background are sensitive to the values of f_1 and δ_- through top-quark decay, as they parameterize the form of the Wtb coupling.

Only the angular distributions for the leptonic decay of the W boson are measured, but the efficiency and resolution may also depend on other unmeasured variables, such as those associated with the η distribution of the top or spectator quark in the center-of-mass inertial frame. The efficiency, resolution, and background models are constructed such that they incorporate a functional dependence on the values of f_1 and δ_-, which removes such biases affecting the values of these parameters. A probability density is derived for all events in the signal region, as a function of the reconstructed angles $\cos\theta^*$ and ϕ^*, and conditional on the parameters $(\vec{\alpha}, P)$. This density is then used to construct a likelihood, from which f_1 and δ_- are measured in simulated events as validation and in real data.

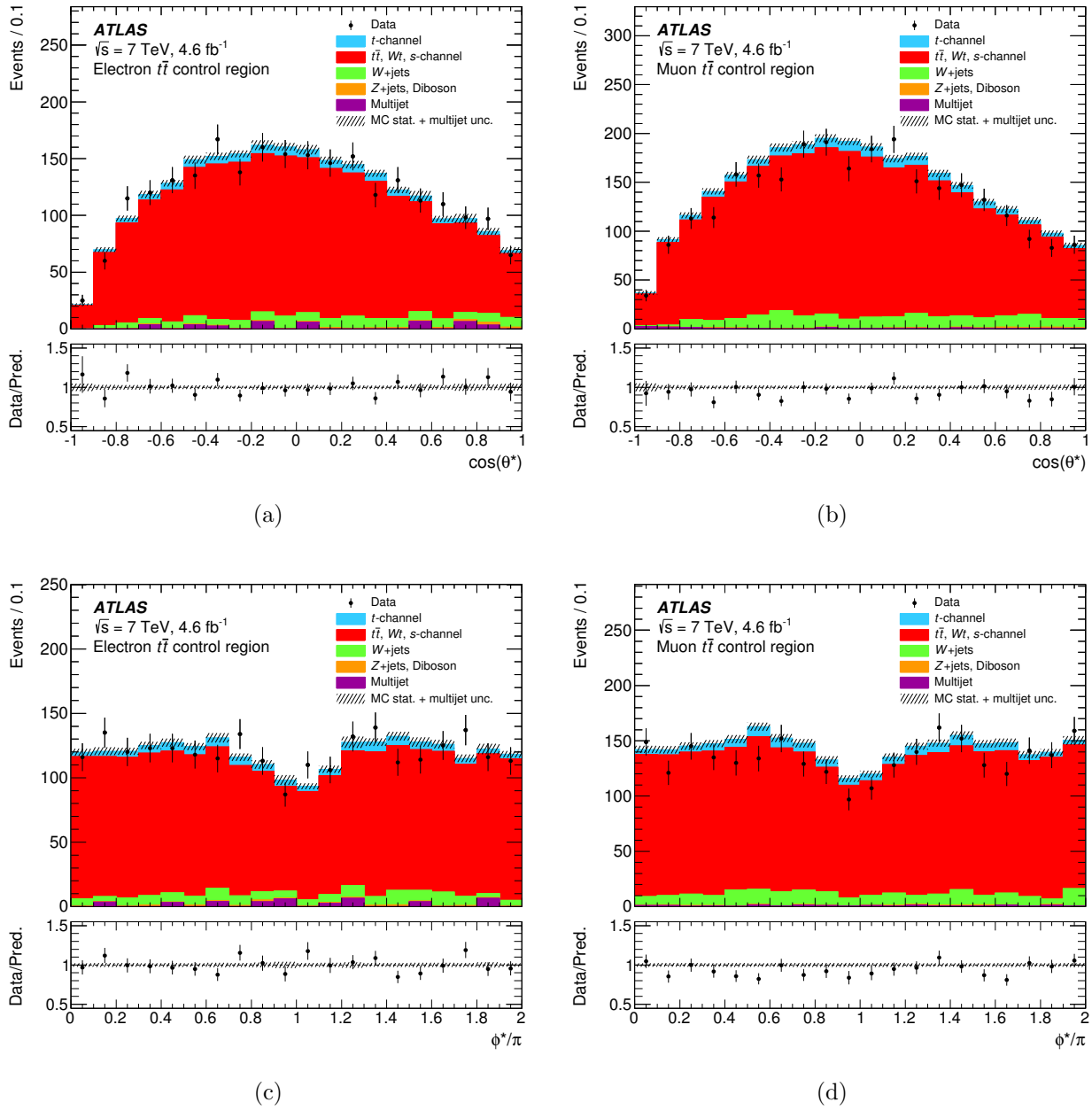

Figure VI.5: Angular distributions $\cos\theta^*$ (upper row) and ϕ^* (lower row) in the $t\bar{t}$ control region for electrons (left) and muons (right), comparing data (black points with statistical uncertainties) to SM signal and background predictions. The uncertainties shown on the prediction include MC statistics and the 50% systematic uncertainty on the normalization of the multijet background. The lower plot shows the ratio of data to prediction in each bin.

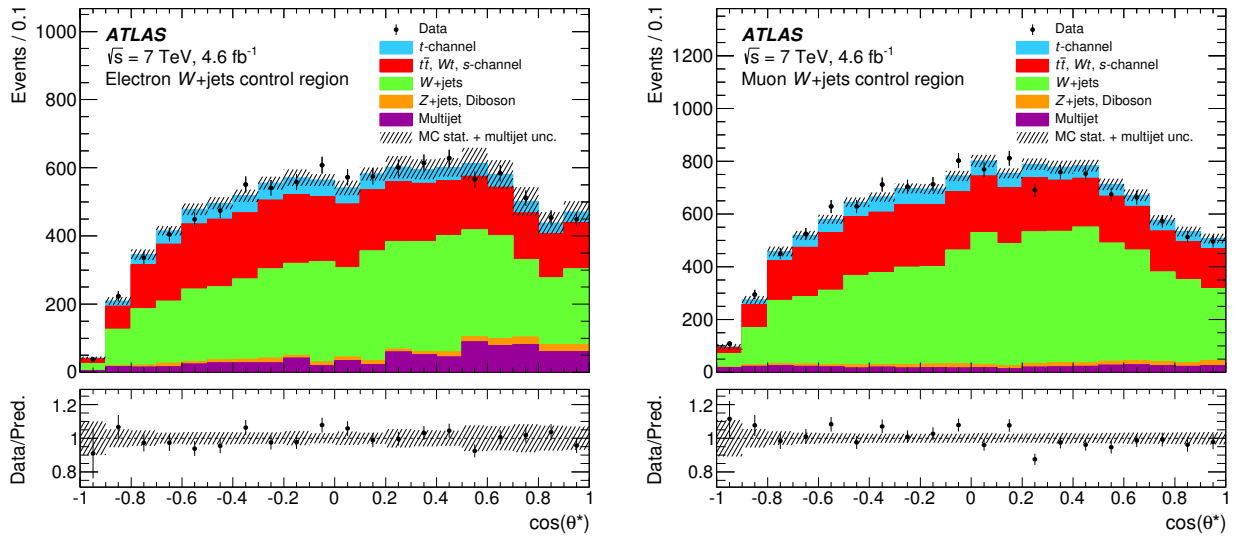

(a)

(b)

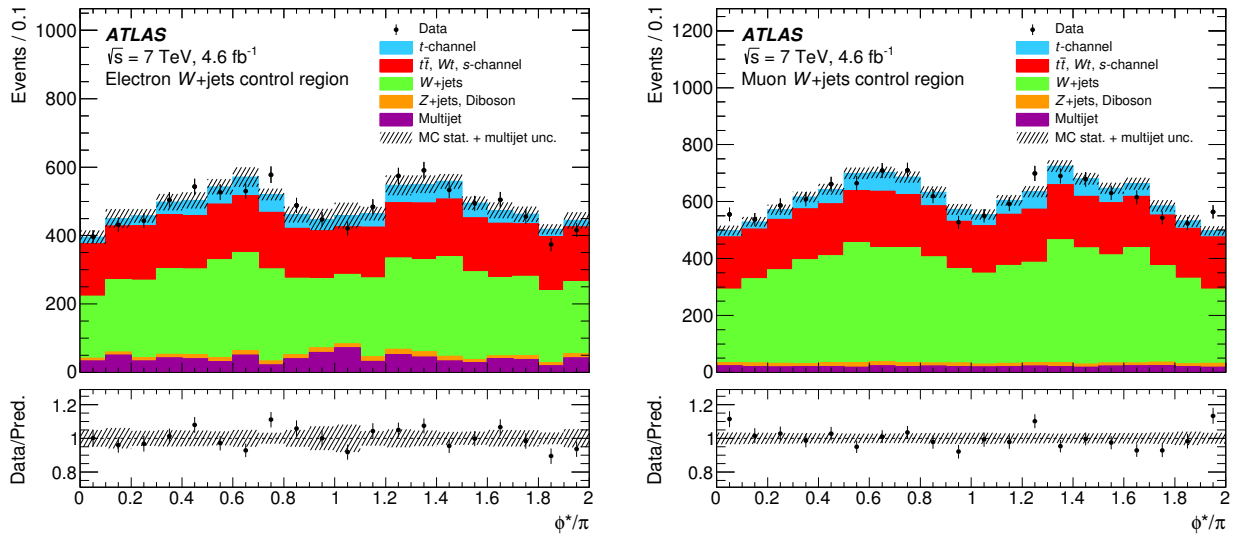

(c)

(d)

Figure VI.6: Angular distributions $\cos\theta^*$ (upper row) and ϕ^* (lower row) in the W+jets control region for electrons (left) and muons (right), comparing data (black points with statistical uncertainties) to SM signal and background predictions. The uncertainties shown on the prediction include MC statistics and the 50% systematic uncertainty on the normalization of the multijet background. The lower plot shows the ratio of data to prediction in each bin.

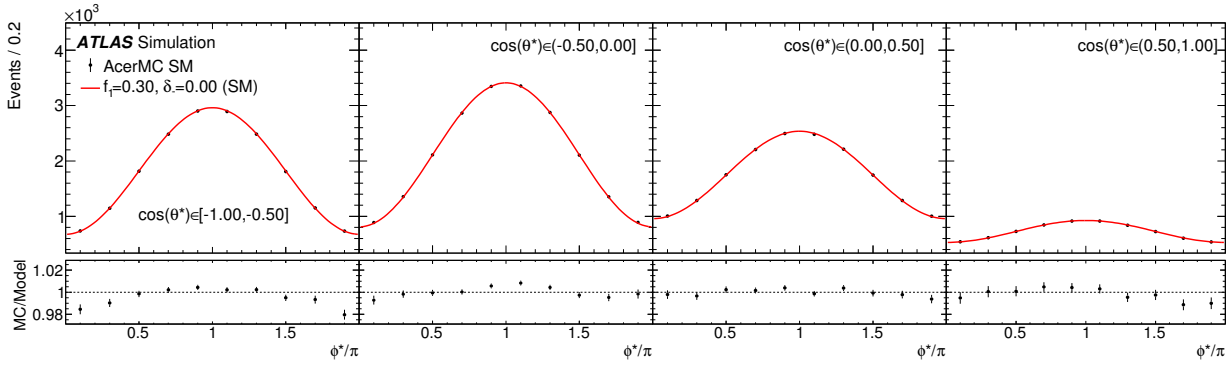

(a)

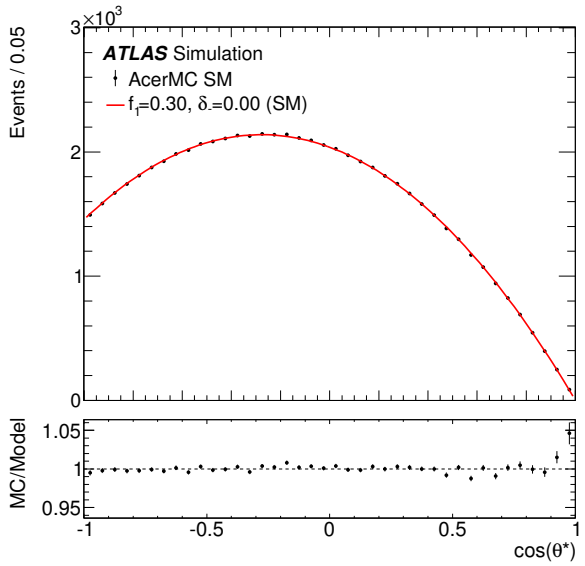

(b)

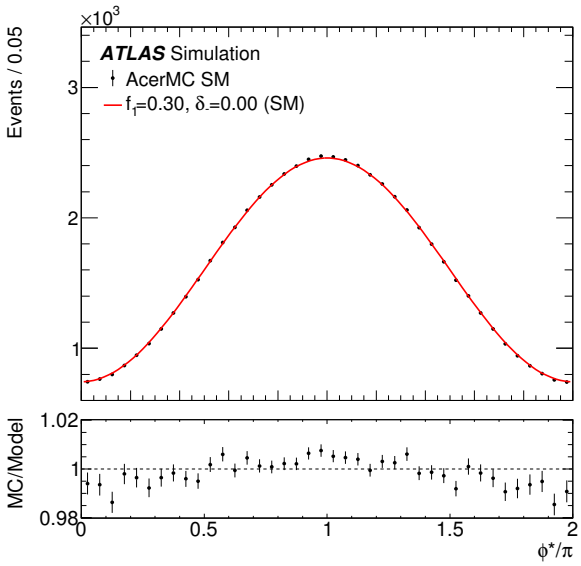

(c)

Figure VI.7: Projections into (a) ϕ^* in bins of $\cos\theta^*$, (b) $\cos\theta^*$, and (c) ϕ^* of the probability density representing the true decay distribution at leading order, $\rho(\theta^*, \phi^* | \vec{\alpha}, P)$, with SM values for the parameters. The histogram shows t-channel events generated with SM couplings by AcerMC and showered with Pythia. The lower plots show the ratio of the histogram ("MC") to the density curve ("Model").

1. Folding and background models

The signal model described by Equation VI.8 is a series in spherical harmonics, only containing terms up to a maximum value of l, $l^{\text{sig}}_{\text{max}} = 2$. This model is shown in Figure VI.7 compared to events simulated with the AcerMC generator and showered with Pythia to illustrate the accuracy of the parameterization. Describing the efficiency and resolution models similarly allows the use of the orthogonality properties of spherical harmonics to construct analytically-folded distributions [121]. An efficiency function, given by

$$\epsilon(\theta_t^*, \phi_t^*;\ \vec{\alpha}, P) = \sum_{l',m'}^{l^{\text{eff}}_{\text{max}}} e_{l'}^{m'}(\vec{\alpha}, P)\, Y_{l'}^{m'}\,(\theta_{\text{t}}^*, \phi_{\text{t}}^*)\,, \tag{VI.11}$$

describes the probability that a t-channel signal event with the given true angles θ_t^* and ϕ_t^* will be reconstructed in the signal region. The series contains all allowed values of l' and m' up to a maximum spherical harmonic degree, $l^{\text{eff}}_{\text{max}}$. The selected signal density, ρ_{s}, is then defined as the product of the efficiency function and the signal model, ρ, normalized to the overall rate,

$$\begin{aligned}
\rho_{\text{s}}(\theta_t^*, \phi_t^*;\ \vec{\alpha}, P) &= \frac{\epsilon(\theta_t^*, \phi_t^*;\ \vec{\alpha}, P)\rho(\theta_t^*, \phi_t^*;\ \vec{\alpha}, P)}{\int \epsilon(\theta_t^*, \phi_t^*;\ \vec{\alpha}, P)\rho(\theta_t^*, \phi_t^*;\ \vec{\alpha}, P)\mathrm{d}\Omega_{\text{T}}^*} = \sum_{L,M} c_L^M(\vec{\alpha}, P)\, Y_L^M\,(\theta_{\text{t}}^*, \phi_{\text{t}}^*)\,, \\
\text{for}\quad c_L^M(\vec{\alpha}, P) &= \frac{\sum_{l,l',m,m'} e_{l'}^{m'}(\vec{\alpha}, P)\, a_l^m(\vec{\alpha}, P)\, G_{l\ l'\ L}^{m\,m'\,M}}{\sum_{l,m}(-1)^m e_l^{-m}(\vec{\alpha}, P)\, a_l^m(\vec{\alpha}, P)}.
\end{aligned} \tag{VI.12}$$

The Gaunt coefficients G are defined in terms of Clebsch-Gordan coefficients, $C_{l_1\ l_2\ L}^{m_1 m_2 M}$, as

$$G_{l\ l'\ L}^{m\,m'\,M} = \sqrt{\frac{(2l+1)(2l'+1)}{4\pi(2L+1)}} C_{l\,l'\,L}^{0\,0\,0} C_{l\ l'\ L}^{m\,m'\,M}.$$

The efficiency function is determined from a likelihood fit to simulated t-channel events. A value is chosen for $l^{\text{eff}}_{\text{max}}$ by comparing the associated values of the corrected Akaike Information Criteria, AICc [177, 178], a likelihood-ratio test with an additional penalty term which increases with the number of parameters. From this test, $l^{\text{eff}}_{\text{max}} = 6$ is chosen.

In Figure VI.8, the selected signal density derived for AcerMC simulated events is compared to the selected events from which it is derived. The variations in the results from the selection of efficiency models with maximum degree $l^{\text{eff}}_{\text{max}} \pm 2$ are included as systematic

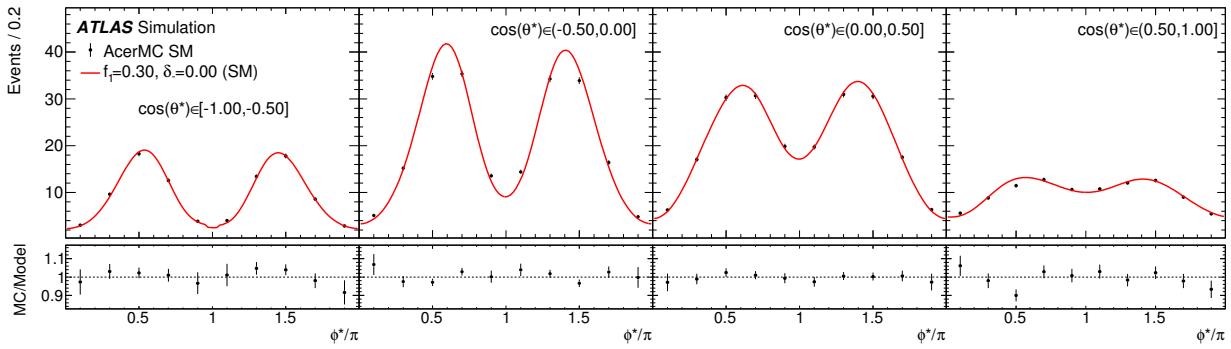

(a)

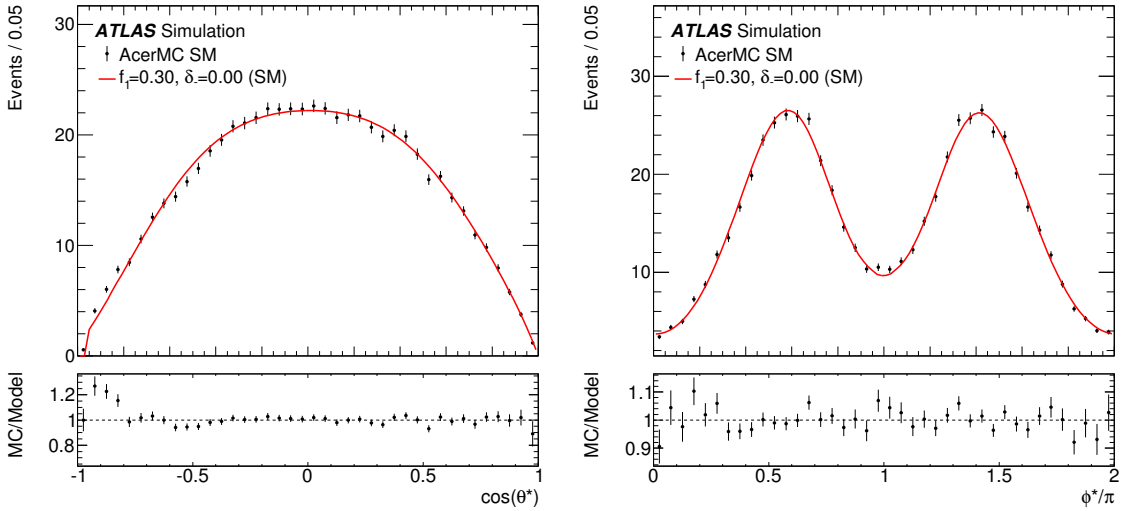

(b) (c)

Figure VI.8: Projections into (a) ϕ^* in bins of $\cos\theta^*$, (b) $\cos\theta^*$, and (c) ϕ^* of the probability density representing the true signal distribution for electrons and muons after selection, $\rho_s(\theta_t^*, \phi_t^* | \vec{\alpha}, P)$, with SM values for the parameters and an efficiency model obtained from a fit to MC simulation. The histogram shows t-channel events generated with AcerMC which pass all selection criteria. The lower plots show the ratio of the histogram ("MC") to the density curve ("Model").

uncertainties. Other criteria, such as the Schwarz Criteria [179], select values of $l_{\rm max}^{\rm eff}$ within the range chosen for this uncertainty.

When reconstructing events in the signal region, the finite resolution of the detector results in a migration from the true angles to measured angles θ^* and ϕ^*. This migration is modeled by the resolution function,

$$\mathcal{R}(\theta^*,\phi^*|\theta_t^*,\phi_t^*;\ \vec{\alpha},P) = \sum_{\lambda,\mu}^{l_{\rm max}^{\rm reco}} \sum_{L',M'}^{l_{\rm max}^{\rm true}} r_{\lambda L'}^{\mu M'}(\vec{\alpha},P)\, Y_\lambda^\mu\,(\theta^*,\phi^*)\, Y_{L'}^{M'}\,(\theta_{\rm t}^*,\phi_{\rm t}^*)\,. \tag{VI.13}$$

This series contains all terms with allowed values of λ, μ, L', and M' up to the maximum degree parameters $l_{\rm max}^{\rm true}$, associated with the dependence on θ_t^* and ϕ_t^*, and $l_{\rm max}^{\rm reco}$, associated with the dependence on θ^* and ϕ^*. The reconstructed signal density, $\rho_{\rm r}$, is defined as the convolution of this function with the selected signal density,

$$\begin{aligned}
\rho_{\rm r}(\theta^*,\phi^*;\ \vec{\alpha},P) &= \int \mathcal{R}(\theta^*,\phi^*|\theta_t^*,\phi_t^*;\ \vec{\alpha},P)\rho_s(\theta_t^*,\phi_t^*;\ \vec{\alpha},P){\rm d}\Omega_{\rm T}^* \\
&\equiv \int \left(r_{\lambda L'}^{\mu M'}(\vec{\alpha},P)\, Y_\lambda^\mu\,(\theta^*,\phi^*)\, Y_{L'}^{M'}\,(\theta_{\rm t}^*,\phi_{\rm t}^*)\right)\left(c_L^M(\vec{\alpha},P)\, Y_L^M\,(\theta_{\rm t}^*,\phi_{\rm t}^*)\right) d\Omega_T^* \\
&= \sum_{\lambda,\mu} d_\lambda^\mu(\vec{\alpha},P)\, Y_\lambda^\mu\,(\theta^*,\phi^*)\,,\ \text{for}\ \ d_\lambda^\mu(\vec{\alpha},P) = \sum_{L,M}(-1)^M c_L^M(\vec{\alpha},P)\, r_{\lambda L}^{\mu -M}(\vec{\alpha},P)\,.
\end{aligned}$$

The resolution function is determined using a spherical Fourier technique [180], with a finite maximum degree $l_{\rm max}^{\rm true} = 8$ defined by the sum $l_{\rm max}^{\rm sig} + l_{\rm max}^{\rm eff} = 2 + 6$. The parameter $l_{\rm max}^{\rm reco}$ is determined using the mean integrated squared error,

$$\text{MISE} = \text{E}\left[\int \left(\rho\left(\theta^*,\phi^*\right) - \hat{\rho}\left(\theta^*,\phi^*\right)\right)^2 d\Omega^*\right], \tag{VI.14}$$

where $\rho\left(\theta^*,\phi^*\right)$ is the true probability density and $\hat{\rho}\left(\theta^*,\phi^*\right)$ is a distribution estimating that density. Calculating the MISE with $\rho_{\rm r}$ yields a broad minimum for $l_{\rm max}^{\rm reco} > 4$, and for this analysis $l_{\rm max}^{\rm reco} = 6$ is chosen. In Figure VI.9, the reconstructed signal density derived for AcerMC simulated events is compared to the reconstructed events in the signal region from which it is derived. The variations in the results arising from using resolution models with $l_{\rm max}^{\rm reco} \pm 2$ are included as systematic uncertainties.

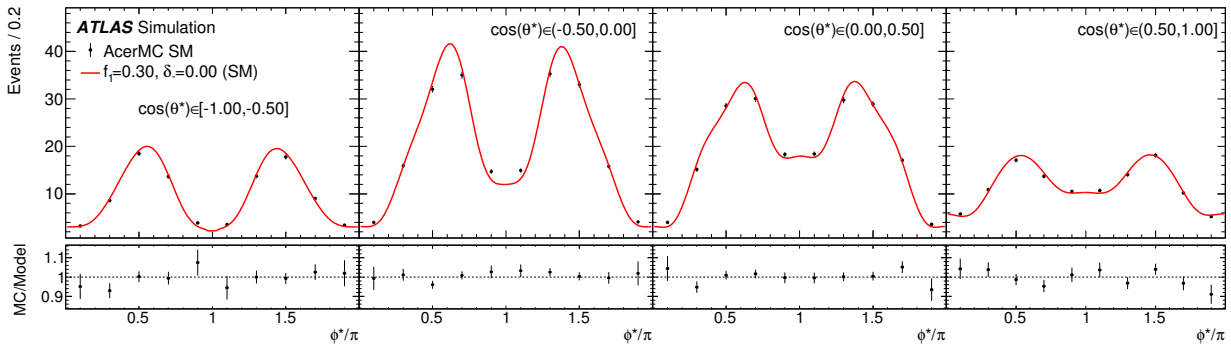

(a)

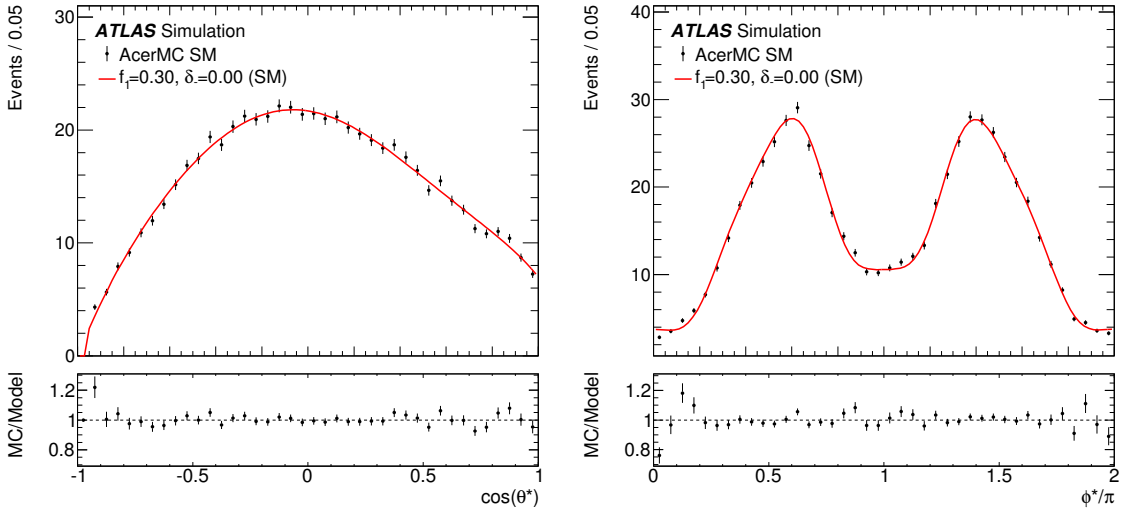

(b) (c)

Figure VI.9: Projections into (a) ϕ^* in bins of $\cos\theta^*$, (b) $\cos\theta^*$, and (c) ϕ^* of the probability density representing the reconstructed signal distribution for electrons and muons, $\rho_r(\theta^*, \phi^* |\ \vec{\alpha}, P)$, with SM values for the parameters and efficiency and resolution models obtained from a fit to MC simulation. The histogram shows reconstructed t-channel events generated with AcerMC which pass all selection criteria. The lower plots show the ratio of the histogram ("MC") to the density curve ("Model").

This density of reconstructed t-channel signal events is a series in spherical harmonics, with coefficients which are functions of the physics parameters describing the production (P) and decay ($\vec{\alpha}$) of the top quark. A background model,

$$\beta(\theta^*, \phi^*;\ \vec{\alpha}, P) = \sum_{\lambda,\mu}^{l_{\max}^{\text{bkg}}} b_\lambda^\mu(\vec{\alpha}, P)\, Y_\lambda^\mu\,(\theta^*, \phi^*)\,, \tag{VI.15}$$

is derived which is also a series in spherical harmonics, and is added to the reconstructed signal density via the signal fraction, f_s. This background function is determined from a likelihood fit to all simulated background events in the signal region, and contains all terms with allowed values of λ and μ up to the maximum degree parameter $l_{\max}^{\text{bkg}}$. This parameter is determined like the equivalent parameter in the efficiency function, using the AICc, to be $l_{\max}^{\text{bkg}} = 6$. The variations in the results from the selection of background models with $l_{\max}^{\text{bkg}} \pm 2$ are included as systematic uncertainties.

The probability density of all events in the signal region, ρ_{t}, is the sum of the reconstructed signal and background densities with signal fraction f_s,

$$\begin{aligned}
\rho_{\text{t}}(\theta^*, \phi^*;\ \vec{\alpha}, P, f_s) &= \sum_{\lambda,\mu}^{\max\left(l_{\max}^{\text{reco}}, l_{\max}^{\text{bkg}}\right)} \mathcal{A}_\lambda^\mu(\vec{\alpha}, P, f_s)\, Y_\lambda^\mu\,(\theta^*, \phi^*) \ \text{ for} \\
\mathcal{A}_\lambda^\mu(\vec{\alpha}, P, f_s) &= f_s d_\lambda^\mu(\vec{\alpha}, P) + (1 - f_s) b_\lambda^\mu(\vec{\alpha}, P) \\
&= f_s \frac{\sum_{l,l',L,m,m',M} (-1)^M e_{l'}^{m'}(\vec{\alpha}, P)\, a_l^m(\vec{\alpha}, P)\, G_{l\ l'\ L}^{m m' M}\, r_{\lambda L}^{\mu -M}(\vec{\alpha}, P)}{\sum_{l,m} (-1)^m e_l^{-m}(\vec{\alpha}, P)\, a_l^m(\vec{\alpha}, P)} + (1 - f_s) b_\lambda^\mu(\vec{\alpha}, P)\,.
\end{aligned} \tag{VI.16}$$

In Figure VI.10, the total reconstructed signal and background density in the signal region, for AcerMC simulated t-channel events and combined backgrounds including Powheg simulated $t\bar{t}$ events, is compared to all reconstructed events in the signal region from which it is derived.

An unbinned likelihood function is constructed from the probability density in Equation VI.16 and from a set of events $\mathcal{D} = \{\theta_i^*, \phi_i^*, w_i\}$, $i = 1, 2, \ldots, N$,

$$\mathcal{L}(\vec{\alpha}) = \prod_{i=1}^{N} \exp\left(w_i \rho_{\text{t}}\left(\theta_i^*, \phi_i^* |\ \vec{\alpha}, P, f_s\right)\right), \tag{VI.17}$$

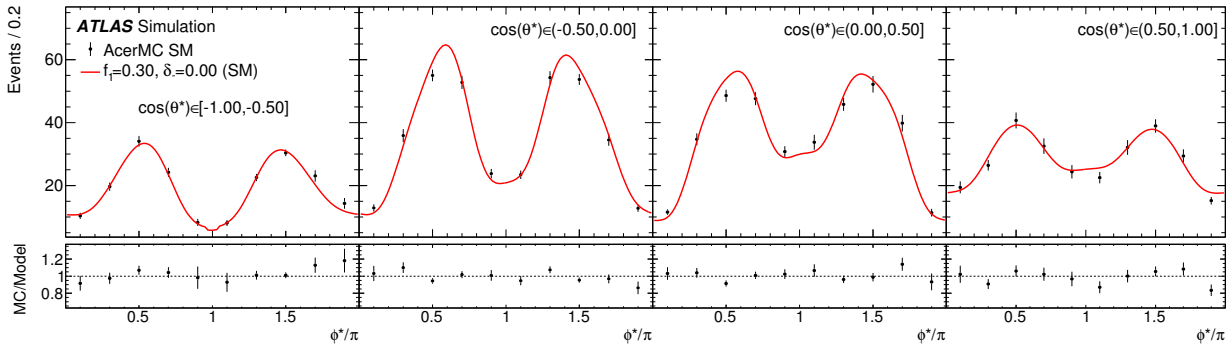

(a)

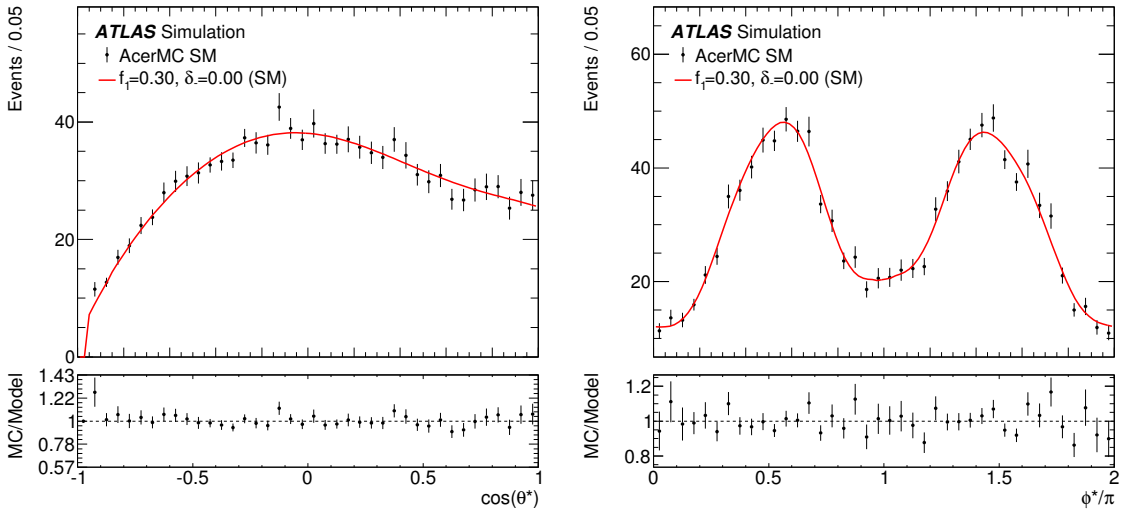

(b) (c)

Figure VI.10: Projections into (a) ϕ^* in bins of $\cos\theta^*$, (b) $\cos\theta^*$, and (c) ϕ^* of the probability density representing the reconstructed t-channel signal and combined background distribution for electrons and muons, $\rho_t(\theta^*, \phi^* | \vec{\alpha}, P)$, with SM values for the parameters, an efficiency model with $l_{\max}^{\text{eff}} = 3$, a resolution model with $l_{\max}^{\text{true}} = 8$ and $l_{\max}^{\text{reco}} = 8$, and a background model with $l_{\max}^{\text{bkg}} = 6$. The histogram shows reconstructed AcerMC t-channel signal and combined background events which pass all selection criteria. The lower plots show the ratio of the histogram ("MC") to the density curve ("Model").

where θ_i^* and ϕ_i^* can be taken either from data or MC simulation, and the event weights w_i are 1 for measured data. The likelihood is evaluated on a grid[3] with spacing 0.01 in f_1 and 0.01π in δ_-. The efficiency and resolution models at each point are derived from PROTOS t-channel simulated events, and the background model uses PROTOS $t\bar{t}$ simulated events. Interpreting these parameters as varying the coupling ratio g_R/V_L, the polarization P is varied simultaneously according to the parameterization in Ref. [133].

A central value is measured at the maximum value of $\mathcal{L}$ on this grid, determined from a Gaussian fit to the points at which $\mathcal{L}$ is evaluated. The 68% and 95% confidence limits are defined by the region where the likelihood ratio, $\mathcal{L}/\mathcal{L}_{\max}$, is larger than the value that would yield the same likelihood for a two-dimensional Gaussian distribution. They are refined to increase the accessible precision by interpolating between points on either side of the contours determined from these evaluated points. The statistical uncertainty is estimated from the symmetrized 68% C.L. interval of each parameter.

The model is checked for closure both with MC samples, and by defining toy-MC samples based on Equation VI.16 with the same number of events as in data. These samples were generated at multiple points in (f_1, δ_-) space, and in all cases they are found to reproduce the expected values of these parameters. These toy-MC samples were also used to derive pull distributions for f_1 and δ_- to check the statistical uncertainties returned by the fit. This full closure-testing procedure is also used to investigate the possibility of parameter dependences in the efficiency, resolution, and background models.

2. Incorporating parameter dependence

The derivation of the efficiency, resolution, and background models is based on the true form of these distributions in the MC simulation used to derive them. As the coordinates (θ^*, ϕ^*) do not fullly capture the degrees of freedom in the system, other variables which can be affected by the values of the couplings have been implicitly integrated over their full

[3] In addition to evaluating the likelihood at a discrete set of grid points, a method allowing continuous variation in the parameter space was developed for finding the maximum likelihood using a *Markov chain Monte Carlo* technique. This method is also very useful for characterizing the space of the model in detail, so a brief explanation of the technique and some demonstrations of the characterization of the space are shown in Appendix B.

range, instilling a dependence on these parameters into the folding and background models. Variations in the values of $\mathrm{Re}[\frac{g_\mathrm{R}}{V_\mathrm{L}}]$ and $\mathrm{Im}[\frac{g_\mathrm{R}}{V_\mathrm{L}}]$ affect the background model through events containing top quarks, which primarily arise in $t\bar{t}$ production. The efficiency and resolution models are affected by the variation induced by changing V_L and g_R in these unmeasured variables. For instance, t-channel single top-quark production depends on anomalous coupling in both the top-quark production and decay vertices, so varying the couplings alters production-side distributions, such as the p_T and η distributions of the top or spectator quark.

To test how these potential sources of dependence affect the models, they should be derived from MC events simulated with values of the coupling at a variety of different points in the $(\mathrm{Re}[\frac{g_\mathrm{R}}{V_\mathrm{L}}], \mathrm{Im}[\frac{g_\mathrm{R}}{V_\mathrm{L}}])$ space; however, only a limited set of these samples existed, with only $\mathrm{Im}[\frac{g_\mathrm{R}}{V_\mathrm{L}}]$ varied. Instead, a reweighting technique was used to estimate how the angular distributions for the existing samples would change for different values of these couplings. The LO matrix element used in the production of the events by the Protos generator, with built-in dependence on the couplings, was evaluated given the full kinematics of each event at the point where the event was generated (SM values of $V_\mathrm{L} = 1$ and $g_\mathrm{R} = 0$ in this case) and at the desired point in parameter space. Then, the events have a weight

$$w_i = \frac{|\mathcal{M}(x_i; \vec{\alpha}_g)|^2}{|\mathcal{M}(x_i; \vec{\alpha}_d)|^2}.$$

applied, and the resulting distributions in θ^* and ϕ^* approximate those which would arise from events generated at the new point in $(\mathrm{Re}[\frac{g_\mathrm{R}}{V_\mathrm{L}}], \mathrm{Im}[\frac{g_\mathrm{R}}{V_\mathrm{L}}])$ space. Figure VI.11 shows a validation test of the reweighting procedure — distributions of $\cos\theta^*$ and ϕ^* are compared between events generated at or reweighted to the values of V_L and $\mathrm{Im}[g_\mathrm{R}]$ given.

The form and size of the effect of this parameter dependence is *a priori* unknown, and the reweighting technique can increase uncertainty in some regions where few events are reconstructed. Thus, closure tests are performed with input MC events generated at a variety of values of the parameters f_1 and δ_- using efficiency, resolution, and background models derived from MC events generated with SM parameter values. These tests produce an ensemble of individual toy-MC samples the same size as the data, each contributing an event in the (f_1, δ_-) space at it maximum likelihood, from which a value and statistical

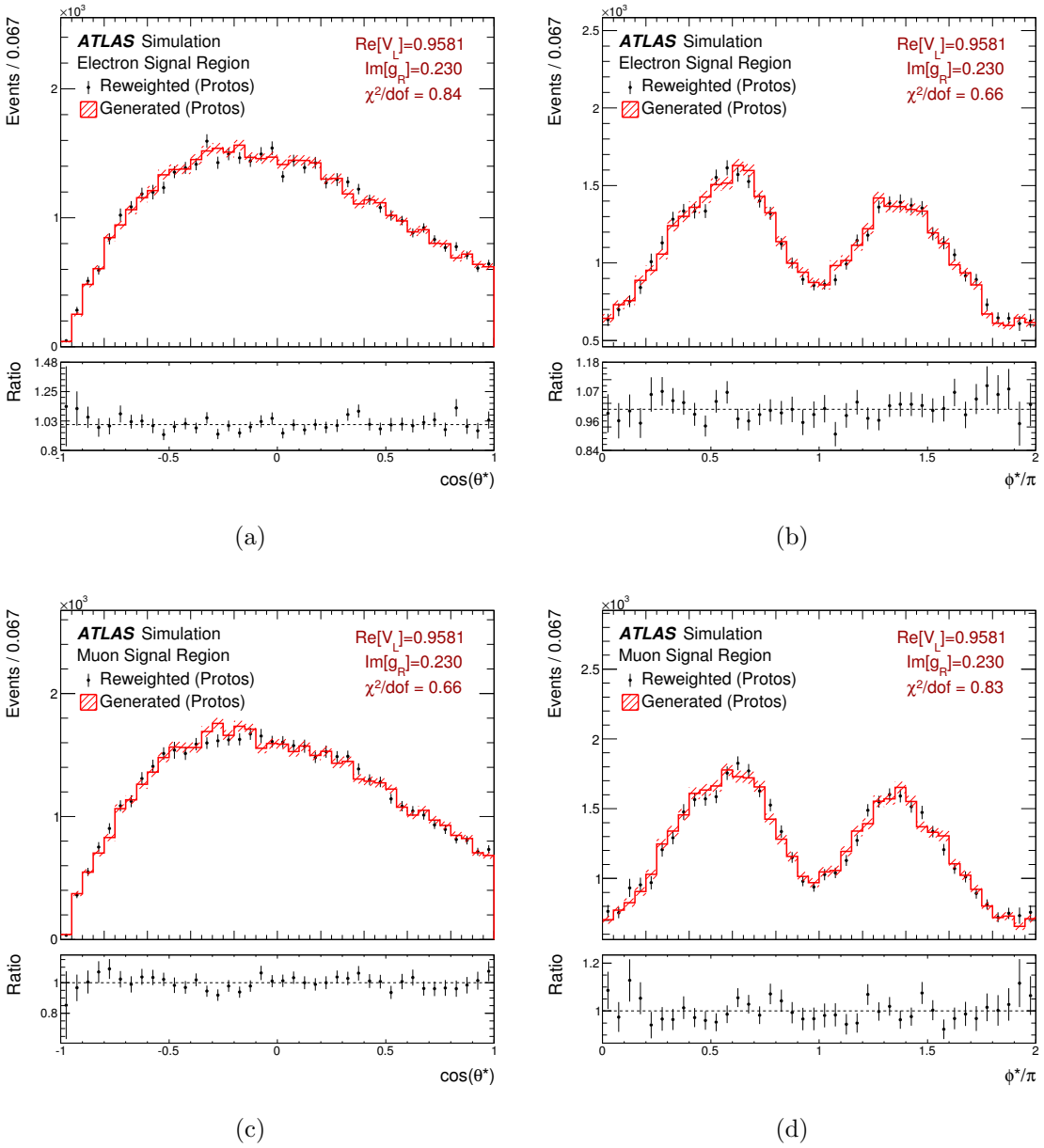

Figure VI.11: Projections into $\cos\theta^*$ (left column) and ϕ^* (right column) of PROTOS signal events with $\mathrm{Re}[V_\mathrm{R}] = 0.9581, \mathrm{Im}[g_\mathrm{R}] = 0.230$, for electrons (top row) and muons (bottom row). The red histogram and hatched red band represents events generated with these values of the couplings and the statistical uncertainties on each bin, while the black histogram and bars are obtained by reweighting a PROTOS sample generated at the SM to this point. The lower plot shows the ratio of the reweighted event histogram to the generated event histogram. A χ^2/dof figure is provided to quantify the comparison.

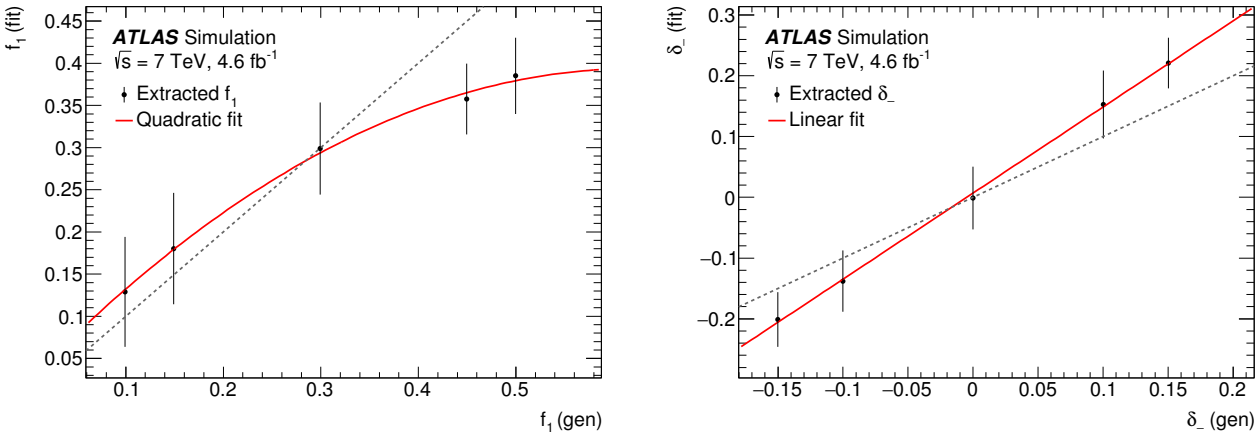

(a) (b)

Figure VI.12: Biases in the estimation of the values of the parameters (a) f_1 and (b) δ_- which arise when the folding and background models are determined from SM simulated events, ($f_1 = 0.3$, $\delta_- = 0$). The plotted points are obtained from likelihood fits, shown with the expected statistical uncertainty in $4.6\,\text{fb}^{-1}$ of data at $\sqrt{s} = 7$ TeV. The dashed line represents no bias in the measurement. The non-negligible biases are represented by a linear fit for δ_- and a quadratic fit for f_1.

uncertainty are extracted. The t-channel signal and $t\bar{t}$ background events are based on models derived from with PROTOS events for the input MC events. The results of these closure tests are compared to the values with which the input events were generated; any statistically-significant trend connecting them other than a line with a slope of one and an intercept of zero indicates a dependence which could bias the measurement.

The biases in the extracted parameters are illustrated by Figure VI.12. If they are due to the mismatch between the values of f_1 and δ_- in the folding and background models with the values in the signal model, using versions of these models derived from events reweighted to the appropriate values should remove the biases. This is tested by deriving these models from t-channel signal MC events representing each point in (f_1, δ_-), and performing the same procedure described for calculating the likelihood and extracting the values of f_1 and δ_-.

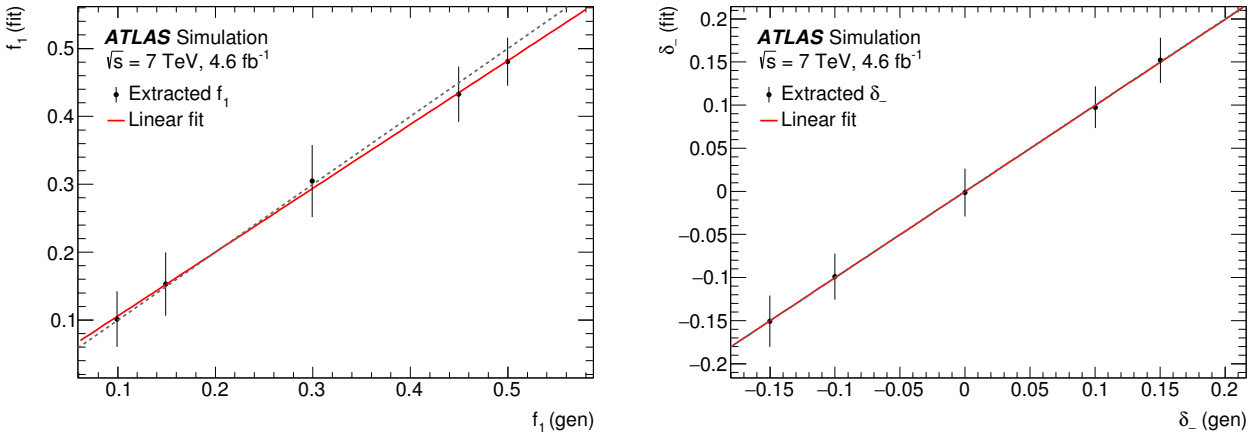

(a) (b)

Figure VI.13: Comparison of the estimated values of the parameters (a) f_1 and (b) δ_-, derived by varying their values in the folding and background models to match the signal model. The plotted points are obtained from likelihood fits, shown with their expected statistical uncertainty in $4.6\,\text{fb}^{-1}$ of data at $\sqrt{s} = 7$ TeV. The dashed line represents no bias in the measurement. All estimates are consistent with this line; linear fits produce a slope consistent with one and an intercept consistent with zero.

The results, shown in Figure VI.13, indicate that this procedure eliminates the biases shown in Figure VI.12. Therefore, this procedure for deriving the efficiency, resolution, and background models is used for performing the measurement in data. The full models used the likelihood, with this procedure applied, is shown in Figure VI.14 compared to real data, summed over the electron and muon channels in the signal region. Three representative models are also shown: one for the SM expectation, one near the expected 95% C.L. sensitivity in f_1, and one near the expected sensitivity in δ_-. These f_1 and δ_- values are the same as those used in Figure VI.1, now including the effects of efficiency, resolution and background functions derived at each point independently. The main differences between the two figures are due to the isolation requirements placed on the leptons. For $\cos\theta^* = -1$, the lepton overlaps the b-tagged jet, while for $\phi^* = \pi$, the lepton may overlap the spectator jet.

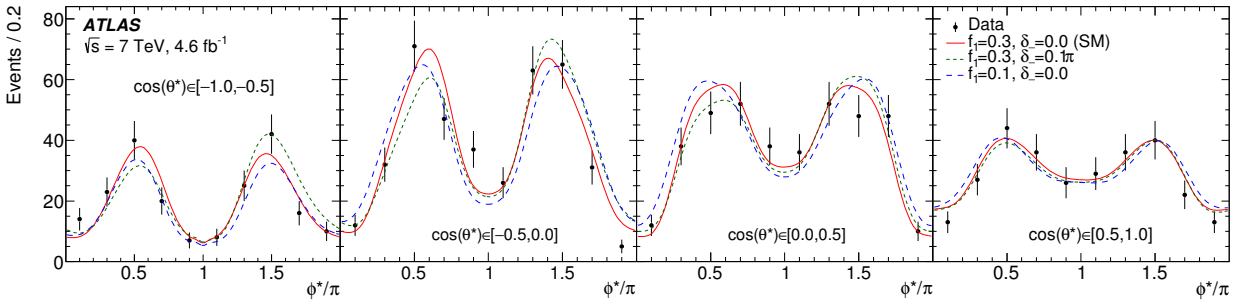

(a)

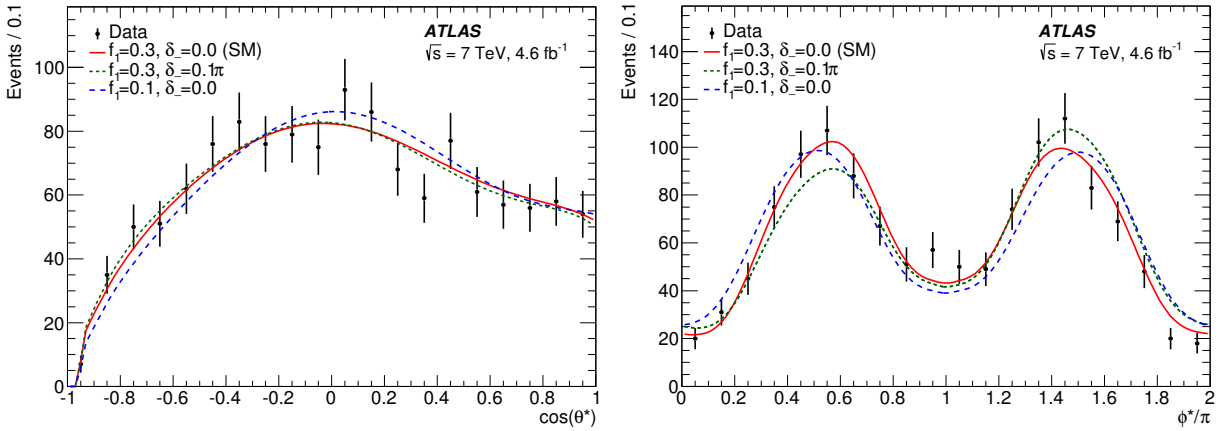

(b) (c)

Figure VI.14: Projections into (a) ϕ^* in bins of $\cos\theta^*$, (b) $\cos\theta^*$, and (c) ϕ^* of the function described in Equation VI.16, for different values of f_1 and δ_-. The black points shown are for the selected data events with statistical uncertainties. The curves shown represent the model at the SM point $f_1 = 0.3$, $\delta_- = 0$ (solid red), and two sets of beyond-the-SM values, $f_1 = 0.1$, $\delta_- = 0$ (dashed blue) and $f_1 = 0.3$, $\delta_- = 0.1\pi$ (dotted green).

E. SOURCES OF UNCERTAINTY

Uncertainties on the measured central value can be either statistical, arising from the limited number of events in the sample, and systematic, arising from inherent uncertainty in some input to the procedure. The statistical unceratinty in the measurement is determined as described in Section VI.D.1, from the 68% C.L. contour determined in the measurement. The systematic uncertainties must be evaluated individually for each source in the full (f_1, δ_-) parameter space. Efficiency, resolution, and background models are determined from MC samples with a parameter varied by its uncertainty, or a subset where appropriate. Likelihoods are constructed from the resulting model, using events generated with nominal values of the varied parameters. The difference between the central values estimated at the nominal value of a parameter and at the value varied by its uncertainty, or half the difference between central values estimated with the parameter varied up and down symmetrically by its uncertainty, determines the elements of a covariance matrix in (f_1, δ_-) space for each source. The total covariance matrix for the systematic uncertainties and its correlation matrix are found from the sum of the covariance matrices determined for individual uncertainties. Table VI.2 presents the statistical uncertainty, individual systematic uncertainties, and the combined uncertainty on the measurement.

1. Object modeling

The uncertainties in the reconstruction of jets, leptons, and $E_{\mathrm{T}}^{\mathrm{miss}}$ are propagated to the analysis, following the same procedures as described in Ref. [127]. The main source of uncertainty from these physics objects is the jet energy scale (JES) [181], which is the largest systematic uncertainty on the measurement of f_1. To estimate the impact of the JES uncertainty on the result, the jet energy is scaled up and down by its uncertainty, which ranges from 2.5% in the central region with high-p_{T} jets to 14% in the far forward region with low-p_{T} jets. Uncertainties are also estimated for jet energy resolution and reconstruction efficiency; the impact of varying the jet-vertex fraction requirement; $E_{\mathrm{T}}^{\mathrm{miss}}$ reconstruction and the effect of pile-up collisions on the $E_{\mathrm{T}}^{\mathrm{miss}}$; b-tagging efficiency and mistagging rate; lepton

trigger, identification, and reconstruction efficiencies; and lepton momentum, energy scale, and resolution.

2. MC generators and PDFs

Multiple MC event generators are used to model the t-channel and $t\bar{t}$ processes in this analysis, and the differences between these generators are included as systematic uncertainties. Comparing the AcerMC generator used for t-channel events and the Powheg-box generator used for $t\bar{t}$ events to the Protos generator used for both the t-channel single top-quark events and $t\bar{t}$ events yields the largest uncertainty in δ_{-}. Additional t-channel comparisons are performed between the AcerMC and Powheg-box generators and between AcerMC events with showering by Pythia and Herwig. The renormalization and factorization scales in the Powheg-box t-channel sample are also varied independently by factors of 0.5 and 2.0. Additional $t\bar{t}$ comparisons are performed between the Powheg-box generator and the mc@nlo [182] generator with showering by Herwig, and between Powheg-box events with showering by Pythia and Herwig. The variations between the NNPDF2.3, CT10, and MSTW2008nlo68cl PDF sets and within individual sets are used to estimate a systematic uncertainty following the PDF4LHC prescription.

3. Signal and background normalization

Cross-sections for background processes given in Section VI.C.2 are varied up and down by their uncertainties. The multijet normalization is varied by 50%, and the remaining backgrounds are varied simultaneously to produce a conservative estimate. The impact of object modeling and other uncertainties on the W+jets background normalization are considered in parallel with the variations made in t-channel and $t\bar{t}$ samples. A separate shape uncertainty is assigned to the W+jets samples by varying the matching and factorization scales in the Alpgen generator. The integrated luminosity is varied up and down by its uncertainty, $\pm 1.8\%$, derived as detailed in Ref. [147].

4. Detector correction and background parameterization

An uncertainty due to the limited size of the MC samples used to estimate the efficiency and resolution models is estimated from the statistical uncertainties derived from a measurement of f_1 and δ_- in the t-channel signal MC sample alone. The background statistical uncertainty is estimated by varying the background model according to the eigenvectors of its covariance matrix. The background statistical uncertainty dominates the total "MC statistics" uncertainty listed in Table VI.2. Its significance reflects the small size of some background samples in the signal region, and the resulting disparate values of the sample weights. The effect of varying the cutoff degree $l_{\max}$ in the determination of these models is also estimated, and is found to be small compared to MC statistical uncertainty.

5. Uncertainty combination

Table VI.2 shows the contribution of each source of uncertainty to the measurement of the parameters f_1 and δ_- and their correlation, $\rho(f_1, \delta_-)$. The total systematic uncertainty and correlation is obtained from the sum of the covariance matrices determined for each source. It is combined with the covariance matrix of the statistical uncertainty with a specialized method. At each point $\vec{\alpha}_i$ in the (f_1, δ_-) space, a multivariate normal distribution $\mathcal{N}_i$ is constructed with the covariance matrix representing the systematic uncertainties, $\mathbf{\Sigma}^{\text{syst}}$, and the mean, $\vec{\alpha}_i$. The resulting distribution is evaluated at a point $\vec{\alpha}_j$ and multiplied by the likelihood at this point, $\mathcal{L}_j^{\text{stat}}$. The maximum modified likelihood value, over all possible points $\vec{\alpha}_j$, is kept, and the resulting broadened likelihood distribution $\mathcal{L}_i^{\text{stat+syst}}$ represents the measurement with both statistical and systematic variation incorporated:

$$\mathcal{L}_i^{\text{stat+syst}} = \max_j \left\{ \mathcal{N}_i(\vec{\alpha}_j; \vec{\alpha}_i, \mathbf{\Sigma}^{\text{syst}}) \cdot \mathcal{L}_j^{\text{stat}} \right\}. \tag{VI.18}$$

The confidence limits arising from this modified likelihood are taken as the full uncertainty in the measurement, as given in the results shown in Figure VI.15.

Table VI.2: Sources of systematic uncertainty on the measurement of f_1 and δ_- using AcerMC t-channel single top-quark simulated events and backgrounds estimated from both MC simulation and data, including Powheg-box $t\bar{t}$ simulation. Individual sources are evaluated separately for shifts up and down, and symmetrized uncertainties $\sigma(f_1)$, $\sigma(\delta_-)$ and correlation coefficients $\rho(f_1, \delta_-)$ are given.

Source	$\sigma(f_1)$	$\sigma(\delta_-)/\pi$	$\rho(f_1, \delta_-)$
Data statistics	0.05	0.023	0.01
Jets	0.03	0.015	0.39
b-tagging	< 0.01	< 0.001	-0.70
Leptons	0.02	0.007	0.39
$E_{\mathrm{T}}^{\mathrm{miss}}$	0.01	0.004	-0.27
Generator	0.02	0.017	0.40
Parton shower	0.02	0.001	0.98
PDF variations	0.01	0.009	0.23
Cross-sections	< 0.01	< 0.001	1.00
W+jets shape	< 0.01	0.001	-0.59
Multijet normalization	< 0.01	0.002	-1.00
Luminosity	< 0.01	< 0.001	-1.00
Model $l_{\max}$ variation	0.01	0.001	-0.70
MC statistics	0.02	0.011	0.14
Combined systematic	0.05	0.028	0.27
Total	0.07	0.036	0.15

F. RESULTS

The result for (f_1, δ_-) and the coupling ratios $(\mathrm{Re}[\frac{g_\mathrm{R}}{V_\mathrm{L}}], \mathrm{Im}[\frac{g_\mathrm{R}}{V_\mathrm{L}}])$ are both shown in Figure VI.15. The 68% contour represents the total uncertainty on the measurement, after the uncertainty combination procedure is performed.

The parameters f_1 and δ_- and their uncertainties are measured to be

$$\begin{aligned} f_1 &= 0.37 \pm 0.05\ (\mathrm{stat.}) \pm 0.05\ (\mathrm{syst.}), \\ \delta_- &= -0.014\pi \pm 0.023\pi\ (\mathrm{stat.}) \pm 0.028\pi\ (\mathrm{syst.}). \end{aligned} \tag{VI.19}$$

The correlation in the measurement of these parameters is $\rho\,(f_1, \delta_-) = 0.15$. The results are compatible with the SM expectations at LO, derived from expressions in Refs. [183, 30] with $m_t = 172.5$ GeV, $m_W = 80.399$ GeV, and $m_b = 4.95$ GeV: $f_1 = 0.304$ and $\delta_- = 0$.

The dependence of the parameters f_1 and δ_- on the top-quark mass is evaluated using t-channel and $t\bar{t}$ simulation samples with a range of different top-quark masses. A linear dependence is found,resulting from changes in acceptance at different masses, with a slope of -0.019 GeV^{-1} for f_1 and a negligible slope for δ_-. The uncertainty due to the top-quark mass dependence is not included in the total systematic uncertainty since it has no significant impact on the results.

The propagation of the uncertainties to the $(\mathrm{Re}[\frac{g_\mathrm{R}}{V_\mathrm{L}}], \mathrm{Im}[\frac{g_\mathrm{R}}{V_\mathrm{L}}])$ space is shown in Figure VI.15. The 68% confidence limits in this figure are not elliptical, but an approximate covariance matrix can be defined from the maximum extent of this region in $\mathrm{Re}[\frac{g_\mathrm{R}}{V_\mathrm{L}}]$ and $\mathrm{Im}[\frac{g_\mathrm{R}}{V_\mathrm{L}}]$ by

$$\begin{aligned} \mathrm{Re}[\frac{g_\mathrm{R}}{V_\mathrm{L}}] &= -0.13 \pm 0.07\ (\mathrm{stat.}) \pm 0.10\ (\mathrm{syst.}), \\ \mathrm{Im}[\frac{g_\mathrm{R}}{V_\mathrm{L}}] &= 0.03 \pm 0.06\ (\mathrm{stat.}) \pm 0.07\ (\mathrm{syst.}). \end{aligned} \tag{VI.20}$$

The correlation in the measurement of these coupling ratios is $\rho\left(\mathrm{Re}[\frac{g_\mathrm{R}}{V_\mathrm{L}}], \mathrm{Im}[\frac{g_\mathrm{R}}{V_\mathrm{L}}]\right) = 0.11$. The effect on the propagation due to the current uncertainty in the top-quark, W boson and b-quark masses [20] is < 0.01 in $\mathrm{Re}[\frac{g_\mathrm{R}}{V_\mathrm{L}}]$, and < 0.0001 in $\mathrm{Im}[\frac{g_\mathrm{R}}{V_\mathrm{L}}]$.

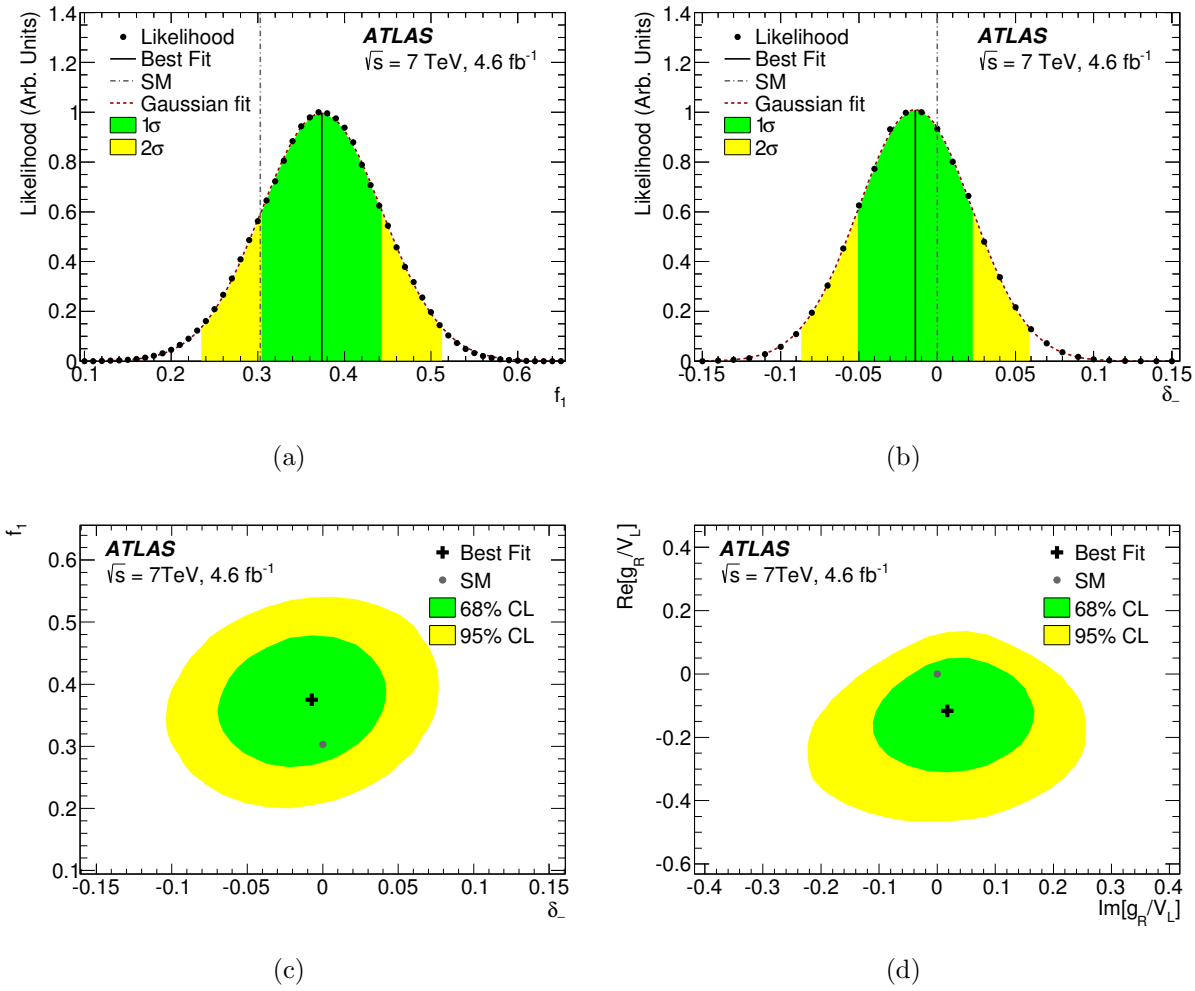

Figure VI.15: Projections of the likelihood function constructed from the signal region probability density Equation VI.16 and data events into (a) f_1, (b) δ_-, (c) f_1 vs. δ_-, and (d) $\mathrm{Re}[\frac{g_\mathrm{R}}{V_\mathrm{L}}]$ vs. $\mathrm{Im}[\frac{g_\mathrm{R}}{V_\mathrm{L}}]$, with systematic uncertainties incorporated. The black points indicate the largest evaluated likelihood in each bin of the projected variable. Gaussian fits to the one-dimensional projections were performed, displayed as the red curve. Regions shown in green and yellow represent the 68% and 95% confidence level regions, respectively. A black line or cross indicates the observed value, and the grey line or point indicates the SM expectation.

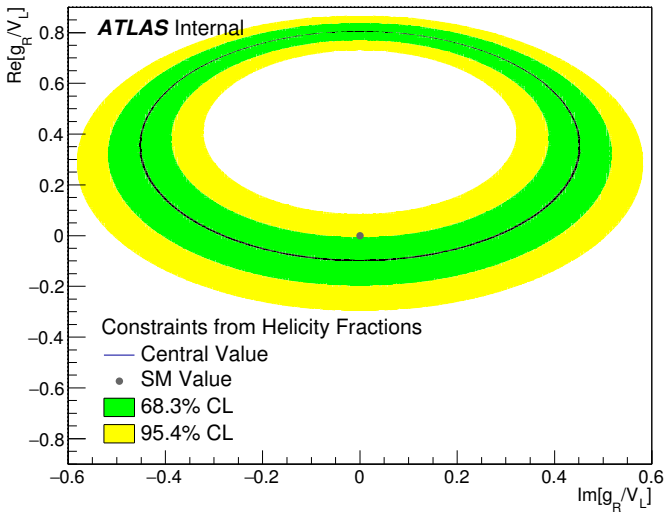

Figure VI.16: Constraints on the anomalous coupling g_{R} from the combination of ATLAS and CMS measurements of the W helicity fraction F_0. The limits reported by the analyses [140] are only measured in $\mathrm{Re}[\frac{g_{\mathrm{R}}}{V_{\mathrm{L}}}]$, with $\mathrm{Im}[\frac{g_{\mathrm{R}}}{V_{\mathrm{L}}}] = 0$. This projection relaxes that assumption.

Limits are placed simultaneously on the possible complex values of the ratio of the anomalous couplings g_{R} and V_{L} at 95% C.L.,

$$\mathrm{Re}[\frac{g_{\mathrm{R}}}{V_{\mathrm{L}}}] \in [-0.36, 0.10] \quad \text{and} \quad \mathrm{Im}[\frac{g_{\mathrm{R}}}{V_{\mathrm{L}}}] \in [-0.17, 0.23]. \tag{VI.21}$$

The best constraints on $\mathrm{Re}[g_{\mathrm{R}}]$ come from W boson helicity fractions in top-quark decays, with $\mathrm{Re}[g_{\mathrm{R}}]$ of $[-0.08, 0.04]$ and $[-0.08, 0.07]$, both at 95% C.L., from ATLAS [143] and from CMS [144], respectively. However, these limits use the measured single top-quark production cross-section [127, 128] along with the assumption that $V_{\mathrm{L}} = 1$ and $\mathrm{Im}[g_{\mathrm{R}}] = 0$. Without these assumptions, no value within the range $0.0 \lesssim \mathrm{Re}[\frac{g_{\mathrm{R}}}{V_{\mathrm{L}}}] \lesssim 0.8$ can be excluded; this is demonstrated in Figure VI.16. The limits set by this analysis remove these assumptions and extend the knowledge of g_{R} to the whole complex plane by simultaneously measuring information about $\mathrm{Re}[\frac{g_{\mathrm{R}}}{V_{\mathrm{L}}}]$ and $\mathrm{Im}[\frac{g_{\mathrm{R}}}{V_{\mathrm{L}}}]$; the latter is previously unmeasured.

The measured limits on $\mathrm{Re}[\frac{g_{\mathrm{R}}}{V_{\mathrm{L}}}]$ and $\mathrm{Im}[\frac{g_{\mathrm{R}}}{V_{\mathrm{L}}}]$ are a first step toward a unified framework for measuring anomalous couplings. The decision to focus on two parameters was strongly

motivated by the size of the sample of single top quarks produced in the t-channel accessible in 2011 dataset, and the resulting limits on the resolvability of the parameters $\vec{\alpha}$ and the polarization P (see Appendix B). However, the statistical framework described herein can be generally applied to measure statistical properties in any space defined by angular relationships (see Appendix A), and specifically the full space of $\vec{\alpha}$ and P, or by correspondence, all accessible degrees of freedom in the $V_{\mathrm{L,R}}$ and $g_{\mathrm{L,R}}$ couplings.

VII. CONCLUSIONS AND OUTLOOK

Studying heavy quarks produced by the LHC in the ATLAS detector has improved our knowledge of their properties and relationship to other quantities of interest significantly. This thesis presents two analyses which contribute to our understanding of b and t quarks, both using $4.6\,\text{fb}^{-1}$ of pp collisions at a $\sqrt{s} = 7$ TeV center-of-mass energy collected by the ATLAS detector at the LHC. The first investigates properties of the b quark used to identify its presence in a jet. Calibrating the selection efficiency of algorithms designed to identify b-jets so that this efficiency in MC simulation agrees with that measured in data is essential to measurements that rely on finding b quarks in the final state of a process. The *System8* calibration technique minimizes the contributions of MC simulation to this task, thus reducing the effect of any biases or systematic uncertainties arising from it. The second analysis uses b-jets identificed with these algorithms to study properties of top-quark decay. Top quarks produced through a virtual W boson exchange in the t-channel are characterized by properties of both their production and decay. A b-jet and a non-b-jet, an electron or muon, and missing transverse momentum identify top quarks produced in this mode, and reconstruct their subsequent decay. The angles between these final state objects are correlated with the structure of the vertex between the top quark, the W boson, and the b quark, and a detailed analysis of their distributions can reveal whether its structure is SM-like, or shows evidence of new physics phenomena. These analyses both have potential for expanding their capabilities and improving precision in the existing $\sqrt{s} = 8$ TeV and upcoming $\sqrt{s} = 13$ TeV datasets.

Techniques for identifying b-jets have significantly improved from their inception in experiments based at the LEP and Tevatron colliders. The diversification of tagging algorithms and increases in statistical precision have driven the development of multiple calibration tech-

niques. The *System8* calibration technique was developed by the DØ collaboration to be significantly less dependent on systematic effects in MC simulation. Using a set of three categories defined by simple event selection requirements, a system of eight equations is defined to relate the numbers of events in regions defined by these categories and their overlaps, and the efficiencies of selecting events in those categories, to the actual number of b-tagged events and their selection efficiency with a particular tagging algorithm. The equations are designed to only use information from MC simulation in ratios expected to be close to 1, relating efficiencies between various categories, and thus reduce the effect of systematic uncertainties on the results. The system of equations is solved by a χ^2 fit which inverts a matrix, independently in bins of b-jet p_{T} and for a discrete number of selection thresholds on each tagging algorithm weight, and the resulting b-tagging efficiency in data, $\epsilon_b^{\mathrm{data}}$, is divided by the same quantity in MC simulation to get the scale factors, $\kappa_b^{\mathrm{data/sim}}$, which are used to correct the efficiency distributions in these simulated samples. The binned scale factors are all between 0.9 and 1, meaning the corrections are relatively small.

Originally envisioned in ATLAS as a cross-check of the $p_{\mathrm{T}}^{\mathrm{rel}}$ method, its use in the 2011 dataset resulted in complementary scale factors $\kappa_b^{\mathrm{data/sim}}$ which, combined with $p_{\mathrm{T}}^{\mathrm{rel}}$ improved the overall accuracy of these corrections to the b-tagging distributions in data. Such data-driven techniques will become more of an asset as the data sample collected by ATLAS increases and the impact of systematic uncertainties is felt on the precision of the measurement, and as more data becomes available in extreme regions of parameter space (especially high-p_{T} regions). A similar implementation was used in $\sqrt{s} = 8$ TeV, resulting in comparable scale factors and uncertainties to those determined in $t\bar{t}$-based methods. Future applications of this technique should improve sample construction with more efficient and higher p_{T} jet triggers, higher simulation statistics to improve systematic errors independent of the *System8* method, and take advantage of the growing ATLAS dataset to improve accuracy and expand its applicable range.

Since the top quark was discovered 20 years ago, properties like its mass and CKM matrix element have been measured with increasing accuracy. The dataset collected by the ATLAS detector allows improvements in precision in these properties, and the size of the dataset allows a parallel increase in generality. The more recent observation of t-channel

production of single top quarks expands the potential for such insight further, and the size of this dataset has given ATLAS the opportunity for some of the first significant measurements of the properties of this production mode. The analysis presented herein measures the form of the top decay vertex, Wtb, through potential modifications known as anomalous couplings. It describes a two-dimensional measurement of a subspace of these couplings, using an analytic folding and likelihood maximization techniques to extract values for f_1 and δ_- in a parameterization of the decay of the top quark, which translate to limits on the couplings $\mathrm{Re}[\frac{g_\mathrm{R}}{V_\mathrm{L}}]$ and $\mathrm{Im}[\frac{g_\mathrm{R}}{V_\mathrm{L}}]$ assuming $V_\mathrm{R} = g_\mathrm{L} = 0$. The coupling parameterization in terms of the spherical angles θ^* and ϕ^* defines the angular distribution of the t-channel signal process through a spherical Fourier-transform space. Efficiency and resolution functions are fit in this space, which are then folded into the signal model describing the underlying physics analytically. A background function is fit and added to the signal model in ratio. The full model is used to construct a likelihood, which provides estimators of the best-fit central value, uncertainties, and correlations between f_1 and δ_-, or $\mathrm{Re}[\frac{g_\mathrm{R}}{V_\mathrm{L}}]$ and $\mathrm{Im}[\frac{g_\mathrm{R}}{V_\mathrm{L}}]$. The result is combined with estimated sources of systematic uncertainty to give the measurement of the parameters, $f_1 = 0.37 \pm 0.05$ (stat.) ± 0.05 (syst.), $\delta_- = -0.014\pi \pm 0.023\pi$ (stat.) $\pm$ 0.028π (syst.), and $\rho(f_1, \delta_-) = 0.15$, or $\mathrm{Re}[\frac{g_\mathrm{R}}{V_\mathrm{L}}] = -0.13 \pm 0.07$ (stat.) ± 0.10 (syst.), $\mathrm{Im}[\frac{g_\mathrm{R}}{V_\mathrm{L}}] =$ 0.03 ± 0.06 (stat.) ± 0.07 (syst.), and $\rho(\mathrm{Re}[\frac{g_\mathrm{R}}{V_\mathrm{L}}], \mathrm{Im}[\frac{g_\mathrm{R}}{V_\mathrm{L}}]) = 0.11$ in terms of the couplings. The measurement sets limits at the 95% confidence level on $\mathrm{Re}[\frac{g_\mathrm{R}}{V_\mathrm{L}}] \in [-0.36, 0.10]$ and $\mathrm{Im}[\frac{g_\mathrm{R}}{V_\mathrm{L}}] \in [-0.17, 0.23]$. The limits on $\mathrm{Re}[\frac{g_\mathrm{R}}{V_\mathrm{L}}]$ are complementary to limits from B-meson decay and W helicity measurements, and contain previously unmeasured information about $\mathrm{Im}[\frac{g_\mathrm{R}}{V_\mathrm{L}}]$. The measured values are in agreement with SM expectations.

The design of this analysis to work in a spherical Fourier space is novel within ATLAS analyses. It holds the potential for use across a broad range of searches and precision measurements with well-measured final states. There is also room for improvement in the implementation of the techniques developed for analysis of 7 TeV data when performing the analysis on 8 TeV and 13 TeV datasets. One such improvement is the parameterization used in the measurement; though the $(\vec{\alpha}, P)$ parameters are physically straightforward, the minimization space they form is complicated by physical limits near which measurement accuracy is limited. Another source of complexity is the construction of the folding method

as separate efficiency and resolution functions, estimated with entirely different techniques. Combining these into a single migration function estimated with the techniques used with the resolution function, which could then be used for either folding or unfolding measurements, will simplify the analysis procedure and error estimation. The dependence of the folding and the $t\bar{t}$ background samples on the measured parameters resulted in a significant expansion of the time needed to perform the analysis, and limited the accuracy available to report in the final measurement. A future version of this analysis would be more efficient if the reweighting procedure could be integrated into the estimation of these functions and the likelihood minimization procedure which results, or if MC simulation could be generated in equal amounts across the parameter space in the t-channel and $t\bar{t}$ samples and the reweighting applied for each point of interest. Other improvements include increasing MC simulation of some background samples to reduce the corresponding systematic uncertainties, and streamlining the longest processing steps to reduce the total analysis time.

Fortunately, many of these improvements are being implemented in a version of the analysis to be performed on 8 TeV data. This measurement has also increased the space of the measurement to include a third angle, between the spectator jet direction, $\hat{p}_s$, and the direction of the W boson in the rest from of the top quark, $\hat{q}$. This increases the sensitivity of the analysis to the polarization, P, opening up comparisons to a number of complementary measurements. This is achieved with the definition of a set of orthonormal functions through coupled spherical harmonics,

$$M^m_{k,l}(\theta, \theta^*, \phi^*) = \sqrt{2\pi} Y^m_k(\theta, 0)\, Y^m_l(\theta^*, \phi^*)\,,$$

which have many of the same convenient statistical properties as the spherical harmonics (see Appendix A). The analysis measures the coefficients a^m_l in data rather than the parameterization $(\vec{\alpha}, P)$, which have no physical limits, and the true values of these parameters are extracted by folding in detector effects represented by a migration matrix estimated with the spherical Fourier technique described in Section VI.D.1. The dependence of this matrix on the parameters is also achieved by performing the reweighting in concert with its extraction, calculating matrix elements with the PROTOS generator's routines during the fit.

These changes, along with increases in the amount of both MC simulation and real data compared to the 7 TeV analysis and some increase in the signal cross-section relative to its backgrounds gives this updated analysis good prospects for expanding and improving upon the existing measurements of the parameters presented here. Extension to 13 TeV should further improve the measurement, assuming further refinement of the technique and increasing total data and signal-to-background ratios. The measurement of the top quark couplings in this process is one to which the LHC has great sensitivity, and has limit-setting and discover potential for many extensions to the Standard Model, and I believe the method used here has the potential to improve many other measurements. Both should be vigorously pursued in future ATLAS and CMS measurements.

APPENDIX A

PROPERTIES OF PROJECTIVE SERIES IN SPHERICAL HARMONICS

The signal, efficiency, resolution, and background models used in the analysis presented in Chapter VI are all functions on a space described by the spherical angles (θ^*, ϕ^*), and make use of a projective series in the orthonormal spherical harmonics, defined here as

$$Y_l^m(\theta^*, \phi^*) = (-1)^m \sqrt{\frac{2l+1}{4\pi}\frac{(l-m)!}{(l+m)!}} P_l^m(\cos\theta^*)\, e^{im\phi^*}.$$

so that the orthonormality condition satisfies

$$\int Y_l^m(\theta^*, \phi^*)\, Y_{l'}^{m'}(\theta^*, \phi^*)\, d\Omega^* = \delta_{ll'}\delta_{mm'}.$$

These two properties of the spherical harmonics give it the properties of a Fourier series in a spherical space. Integrating a function multiplied by a spherical harmonic with a particular 'frequency' (quantified by an l, m pair) selects out the coefficient in a series expansion of that function. A statistical distribution defined as a series in spherical harmonics makes the moments of the distribution simple to compute, and reducible to a lower order. Combining these two properties with the reduction of the product of spherical harmonics to a series through Gaunt's formula in Section A.A, the statistical properties of individual spherical frequencies described in Section A.B become useful for determining and manipulating probability distributions as described in Section A.C. These distributions are important here only for determining the resolution function, but in the more detailed analysis described in Chapter VII, they take on a more central role in performing the folding procedure.

A. DERIVATION OF THE GAUNT COEFFICIENTS

First, the expansion of the product of two spherical harmonics in a series of spherical harmonics is crucial for the analyticity of the combination of the efficiency and resolution functions with the signal model as described in Section VI.D. The general form used to define the Gaunt coefficients described in Equation VI.D.1, $G_{l\ l'\ L}^{mm'M}$, is

$$Y_l^m\left(\theta^*,\phi^*\right)Y_{l'}^{m'}\left(\theta^*,\phi^*\right)=\sum_{L=l-l'}^{l+l'}G_{l\ l'\ L}^{mm'M}Y_L^M\left(\theta^*,\phi^*\right), \tag{A.1}$$

where the limits on the sum over L reflects the values where the Gaunt coefficients are non-zero, and similarly the requirement that $M=m+m'$ allows the removal of the sum over M. In Ref. [184], these coefficients are determined for the *Clebsch-Gordan series*, which describes the quantum-mechanical rotation of two different angular momenta by the same rotation matrix in terms of a set of independent rotations. I will present the brief derivation here for reference.

This series can be written in terms of Wigner D-matrices, $\mathcal{D}^l_{m,m'}(R)$, defining the state of a quantum mechanical system after a spatial rotation defined by the orthogonal matrix R. If these matrix elements are taken from the operator $\mathcal{D}(R)$, then the product of two such elements can be defined by the expectation value of this operator,

$$\mathcal{D}^{l_1}_{m_1,m_1'}(R)\mathcal{D}^{l_2}_{m_2,m_2'}(R)=\langle l_1m_1|\mathcal{D}(R)|l_1m_1'\rangle\langle l_2m_2|\mathcal{D}(R)|l_2m_2'\rangle\langle l_1l_2;m_1m_2|\mathcal{D}(R)|l_1l_2;m_1'm_2'\rangle. \tag{A.2}$$

The combined angular momentum space defined by the $|l_1l_2;m_1m_2\rangle$ states are related to a combined $|l_1l_2;lm\rangle$ space through the Clebsch-Gordan coefficients,

$$C_{l_1\ l_2\ l}^{m_1m_2m}=\langle l_1l_2;m_1m_2|l_1l_2;lm\rangle.$$

Thus, inserting a complete set of states $|lm\rangle$ through the identity property $\sum_{l,m}|lm\rangle\langle lm|=\mathbf{1}$,

$$\begin{aligned}\langle l_1l_2;m_1m_2|\mathcal{D}(R)|l_1l_2;m_1'm_2'\rangle&=\sum_{l,m}\sum_{l',m'}C_{l_1\ l_2\ l}^{m_1m_2m}C_{l_1\ l_2\ l'}^{m_1'm_2'm'}\langle l_1l_2;lm|\mathcal{D}(R)|l_1l_2;l'm'\rangle\\&=\sum_{l,m}\sum_{l',m'}C_{l_1\ l_2\ l}^{m_1m_2m}C_{l_1\ l_2\ l'}^{m_1'm_2'm'}\mathcal{D}^l_{m,m'}(R)\delta_{ll'}.\end{aligned} \tag{A.3}$$

This relationship can be translated to the desired one in spherical harmoncis by noting the definition of the matrix elements (note that complex conjugation is notated as an overbar),

$$\mathcal{D}^{l}_{m,0}(\phi^*,\theta^*) = \sqrt{\frac{4\pi}{2l+1}}\overline{Y^m_l}\left(\theta^*,\phi^*\right). \tag{A.4}$$

Setting $m'_1 = m'_2 = m' = 0$ in Equations A.2 - A.3 to get the equivalent expression for spherical harmonics:

$$\begin{aligned}\sqrt{\frac{4\pi}{2l_1+1}}Y^{m_1}_{l_1}\left(\theta^*,\phi^*\right)\sqrt{\frac{4\pi}{2l_2+1}}Y^{m_2}_{l_2}\left(\theta^*,\phi^*\right) &= \sum_{l,m} C^{m_1 m_2 m}_{l_1\ l_2\ l}C^{0\,0\,0}_{l_1 l_2 l}\sqrt{\frac{4\pi}{2l+1}}Y^m_l\left(\theta^*,\phi^*\right), \text{ so}\\ Y^{m_1}_{l_1}\left(\theta^*,\phi^*\right)Y^{m_2}_{l_2}\left(\theta^*,\phi^*\right) &= \sum_{l,m} C^{m_1 m_2 m}_{l_1\ l_2\ l}C^{0\,0\,0}_{l_1 l_2 l}\sqrt{\frac{(2l_1+1)(2l_2+1)}{4\pi(2l+1)}}Y^m_l\left(\theta^*,\phi^*\right)\end{aligned} \tag{A.5}$$

The coefficients in this series are those given by the definition of the Gaunt coefficients in Equation VI.D.1, so we have demonstrated the relationship in Equation A.1. This property will also be needed to derive some statistical quantities.

B. STATISTICS OF SPHERICAL HARMONICS SERIES

The dataset used in this analysis to make inferences about the parameters (f_1, δ_-) in $\vec{\alpha}$ or the couplings $(\mathrm{Re}[\frac{g_\mathrm{R}}{V_\mathrm{L}}], \mathrm{Im}[\frac{g_\mathrm{R}}{V_\mathrm{L}}])$ is a set of coupled points in the (θ^*_t, ϕ^*_t) and (θ^*, ϕ^*) spaces, and all inferred functions used take the form of series of spherical harmonics (or coupled spherical harmonics). Some statistical transformations of this data used to estimate the coefficients of these series and their uncertainty may be unfamiliar, so they are derived or presented here. Though a dependence on $\vec{\alpha}$ exists in these coefficients, it is handled as described in Section VI.D.2 by deriving these functions independently for each value of $\vec{\alpha}$, so this dependence is left implicit. In the present analysis, many of these quantities are used in the estimation of the resolution function and related distributions. Future analyses will use the same techniques more extensively.

A function of the form

$$\rho\left(\theta^*,\phi^*\right)=\sum_{l,m}c_l^m Y_l^m\left(\theta^*,\phi^*\right), \tag{A.6}$$

must satisfy a few requirements to ensure that it can be treated as a standard probability density. First, the normalization of a probability density must be 1. From the orthonormality condition,

$$\int Y_l^m\left(\theta^*,\phi^*\right)d\Omega^*=\begin{cases}\sqrt{4\pi}, & \text{if } l=0 \text{ and } m=0.\\ 0, & \text{otherwise.}\end{cases} \tag{A.7}$$

Thus the condition is satisfied if $c_0^0=\frac{1}{\sqrt{4\pi}}$. A second condition is that the return value for any point (θ_i^*,ϕ_i^*) be real. In this case, recognizing that

$$\mathrm{Re}[Y_l^m\left(\theta_{\mathrm{i}}^*,\phi_{\mathrm{i}}^*\right)]=\frac{1}{2}\left(Y_l^m\left(\theta_{\mathrm{i}}^*,\phi_{\mathrm{i}}^*\right)+\overline{Y_l^m}\left(\theta_{\mathrm{i}}^*,\phi_{\mathrm{i}}^*\right)\right)=\frac{1}{2}\left(Y_l^m\left(\theta_{\mathrm{i}}^*,\phi_{\mathrm{i}}^*\right)+(-1)^m Y_l^{-m}\left(\theta_{\mathrm{i}}^*,\phi_{\mathrm{i}}^*\right)\right),$$

the condition will be met if the relationship $c_l^m=(-1)^m\overline{c_l^{-m}}$ also holds for all coefficients of the series with $m\neq 0$, and $c_l^0=\mathrm{Re}[c_l^0]$ for coefficients with $m=0$.

Proceeding similarly to the condition in Equation A.7, the expected value of a complex-conjugate spherical harmonic is a coefficient of the series defining the probability density:

$$\mathrm{E}\left[\overline{Y_l^m}\left(\theta^*,\phi^*\right)\right]=\int\overline{Y_l^m}\left(\theta^*,\phi^*\right)\rho\left(\theta^*,\phi^*\right)d\Omega^*=(-1)^m c_l^{-m}=c_l^m, \tag{A.8}$$

In general, the expected value of a general function of the angles, $f\left(\theta^*,\phi^*\right)$, which can be expanded as a series in spherical harmonics with coefficients $a_{l,m}$, becomes the sum of products of their coefficients,

$$\mathrm{E}\left[f\left(\theta^*,\phi^*\right)\right]=\sum_{l,m}a_l^m\overline{c_l^m}. \tag{A.9}$$

The covariance between two spherical harmonic elements can be determined straightforwardly from the expected value using Equation A.1:

$$\begin{aligned}\mathrm{Cov}\left[\overline{Y_l^m}\left(\theta^*,\phi^*\right),\overline{Y_{l'}^{m'}}\left(\theta^*,\phi^*\right)\right]&=\mathrm{E}\left[\overline{Y_l^m}\left(\theta^*,\phi^*\right)\overline{Y_{l'}^{m'}}\left(\theta^*,\phi^*\right)\right]-\mathrm{E}\left[\overline{Y_l^m}\left(\theta^*,\phi^*\right)\right]\mathrm{E}\left[\overline{Y_{l'}^{m'}}\left(\theta^*,\phi^*\right)\right]\\&=\left(\sum_L G_{l\ l'\ L}^{m m' M}c_L^M\right)-c_l^m c_{l'}^{m'}.\end{aligned} \tag{A.10}$$

The principle again can be expanded to the covariance of any functions $f(\theta^*, \phi^*)$ and $g(\theta^*, \phi^*)$, with expansion coefficients $a_{l,m}$ and $b_{l',m'}$, to yield the covariance

$$\begin{aligned}\mathrm{Cov}\left[f(\theta^*,\phi^*), g(\theta^*,\phi^*)\right] &= \mathrm{E}\left[f(\theta^*,\phi^*)\, g(\theta^*,\phi^*)\right] - \mathrm{E}\left[f(\theta^*,\phi^*)\right]\mathrm{E}\left[g(\theta^*,\phi^*)\right] \\ &= \sum_{l,m,l',m'} a_l^m b_{l'}^{m'} \left(\sum_L G_{l\ l'\ L}^{mm'M} \overline{c_L^M}\right) - \left(\sum_{l,m} a_l^m \overline{c_l^m}\right)\left(\sum_{l',m'} b_{l'}^{m'} \overline{c_{l'}^{m'}}\right)\end{aligned} \tag{A.11}$$

Estimators of the expected value and covariance are used on data samples which are designed to be unbiased. For the expected value, this is the sample average, in which the integral is replaced with a sum for (θ_i^*, ϕ_i^*) points drawn from the distribution. In the general case, the data may have weights assigned to each event; these will be 1 for real data, but may be other values in simulated events. With the definition $W_1 = \sum_{i=1}^{N} w_i$, the expression becomes:

$$\hat{\mathrm{E}}\left[\overline{Y_l^m}(\theta^*,\phi^*)\right] = \hat{c}_l^m = \frac{1}{W_1}\sum_{i=1}^{N} w_i \overline{Y_{l'}^{m'}}(\theta_\mathrm{i}^*, \phi_\mathrm{i}^*). \tag{A.12}$$

A covariance estimator is defined similarly, called the sample covariance, following its definition in terms of expected values, but with a modified normalization factor designed to ensure that the estimator is unbiased. This correction is the analog of Bessel's correction factor for weighted events, and will reduce to it when all $w_i = 1$. With the additional definition $W_2 = \sum_{i=1}^{N} w_i^2$, this estimator is

$$\hat{\mathrm{Cov}}\left[\overline{Y_l^m}(\theta^*,\phi^*), \overline{Y_{l'}^{m'}}(\theta^*,\phi^*)\right] = \hat{\Sigma}_l^m l' m' = \frac{W_1^2}{W_1^2 - W_2}\left(\sum_L G_{l\ l'\ L}^{mm'M} \hat{c}_L^M - \hat{c}_l^m \hat{c}_{l'}^{m'}\right). \tag{A.13}$$

Both estimators are unbiased, which can be shown straightforwardly for the average, Equation A.12, and follows directly from the definition of the covariance estimator, Equation A.13 in terms of this average. One more important quantity is the covariance of the average; this can be shown to be

$$\mathrm{Cov}\left[\hat{c}_{l,m}, \hat{c}_{l'}^{m'}, =\right] \frac{1}{W_1}\left(\sum_L G_{l\ l'\ L}^{mm'M} \hat{c}_L^M - \hat{c}_l^m \hat{c}_{l'}^{m'}\right) = \frac{W_1^2 - W_2}{W_1} \hat{\Sigma}_{l\ l'}^{mm'}. \tag{A.14}$$

C. ESTIMATING PROBABILITY DISTRIBUTIONS

In Section VI.D.1, the resolution function is estimated using a technique called orthogonal series density estimation, or OSDE, described in Ref. [180]. This technique simply uses the estimator of the expected value of a spherical harmonic, Equation A.12, to estimate the coefficient of the probability density corresponding to that particular spherical harmonic in a series expansion. As described in Equation VI.14, a metric called the mean integrated squared error, or MISE, is used to compare versions of the resolution function with varying maximum values of $l_{\max}^{\text{reco}}$ in the expansion of the density, with coefficients determined from the OSDE method,

$$\hat{\rho}_L\left(\theta^*, \phi^*\right) = \sum_{l=0}^{l_{\max}^{\text{reco}}} \sum_{m=-l}^{l} \hat{c}_l^m Y_l^m\left(\theta^*, \phi^*\right). \tag{A.15}$$

This metric can be reduced to a simple form dependent only on the coefficients $\hat{c}_l^m$:

$$\begin{aligned} \text{MISE}\left[\hat{\rho}_{l_{\max}^{\text{reco}}}\right] &= \text{E}\left[\int \left|\rho\left(\theta^*, \phi^*\right)\right|^2 + \left|\hat{\rho}\left(\theta^*, \phi^*\right)\right|^2 - 2\text{Re}[\rho\left(\theta^*, \phi^*\right)\hat{\rho}^*\left(\theta^*, \phi^*\right)] d\Omega^*\right] \\ &= \sum_{l=0}^{l_{\max}^{\text{reco}}} \sum_{m=-l}^{l} \text{E}\left[\left|c_l^m - \hat{c}_l^m\right|^2\right] + \sum_{l=l_{\max}^{\text{reco}}+1}^{l=\infty} \sum_{m=-l}^{l} \left|c_l^m\right|^2 \\ &= \sum_{l=0}^{l_{\max}^{\text{reco}}} \sum_{m=-l}^{l} \text{Var}\left[\hat{c}_l^m\right] + \sum_{l=l_{\max}^{\text{reco}}+1}^{l=\infty} \sum_{m=-l}^{l} \left|c_l^m\right|^2. \end{aligned} \tag{A.16}$$

As only differences in the MISE are important, an overall constant term can be ignored in its definition. Here, adding the term

$$I = \int \left|\rho\left(\theta^*, \phi^*\right)\right|^2 d\Omega^* = \sum_{l=0}^{l=l_{\max}^{\text{reco}}} \sum_{m=-l}^{l} \left|c_l^m\right|^2 + \sum_{l=l_{\max}^{\text{reco}}+1}^{l=\infty} \sum_{m=-l}^{l} \left|c_l^m\right|^2$$

leaves the upper limit in the second summation finite:

$$\begin{aligned} \text{MISE}\left[\hat{\rho}_{l_{\max}^{\text{reco}}}\right] &= I + \sum_{l=0}^{l_{\max}^{\text{reco}}} \sum_{m=-l}^{l} \left(\text{Var}\left[\hat{c}_l^m\right] - \left|c_l^m\right|^2\right) \\ &= I + \sum_{l=0}^{l_{\max}^{\text{reco}}} \sum_{m=-l}^{l} \left(2\text{Var}\left[\hat{c}_l^m\right] - \left|\hat{c}_l^m\right|^2\right). \end{aligned} \tag{A.17}$$

The variance here is of the form Equation A.14, and thus can be written as a sum over estimated coefficients up to $2l_{\max}^{\text{reco}}$. The resulting variable is straightforward to compute.

Though the discussion of statistical properties has so far been in terms of a series in $Y_l^m(\theta^*, \phi^*)$ functions, the resolution function $\mathcal{R}$ actually requires coupled spherical harmonics. It describes the probability of an event true values of the angles (θ_t^*, ϕ_t^*) being reconstructed at (θ^*, ϕ^*), and thus is a conditional probability expanded in a series in coupled spherical harmonics as defined in Equation VI.13. This function cannot be directly estimated with the OSDE method, but the coefficients $j_{\lambda L'}^{\mu M'}(\vec{\alpha}, P)$ of the joint probability $\rho(\theta_t^*, \phi_t^*, \theta^*, \phi^*;\ \vec{\alpha}, P)$ can. The estimated joint probability density is then multiplied by the probability density of the true angles determined by the multiplication of the true distribution with the efficiency, $\rho(\theta_t^*, \phi_t^*;\ \vec{\alpha}, P)$ from Equation VI.12, to form the desired conditional probability density. This conversion process can also be reduced to operations on the coefficients estimated with the OSDE technique through similar transformations as the above.

The expression for the resolution function in terms of the estimated joint probability density, $\hat{\rho}_{l_{\max}^{\text{reco}}}(\theta_t^*, \phi_t^*, \theta^*, \phi^*;\ \vec{\alpha}, P)$, and true-angle probablity density, $\hat{\rho}_{l_{\max}^{\text{true}}}(\theta_t^*, \phi_t^*;\ \vec{\alpha}, P)$, can be simplified to a relationship between their coefficients. Defining the resolution function as in Equation VI.13 and expressing it in terms of the joint and true probability densities,

$$\begin{aligned}
\rho(\theta_t^*, \phi_t^*, \theta^*, \phi^*;\ \vec{\alpha}, P) &= \rho(\theta_t^*, \phi_t^* | \theta^*, \phi^*;\ \vec{\alpha}, P)\, \rho(\theta_t^*, \phi_t^*;\ \vec{\alpha}, P) \\
&= \left(\sum_{\lambda,\mu,\lambda',\mu'} r_{\lambda\lambda'}^{\mu\mu'}(\vec{\alpha}, P)\, Y_\lambda^\mu(\theta^*, \phi^*)\, Y_{\lambda'}^{\mu'}(\theta_\text{t}^*, \phi_\text{t}^*) \right) \left(\sum_{L,M} c_L^M(\vec{\alpha}, P)\, Y_L^M(\theta_\text{t}^*, \phi_\text{t}^*) \right) \\
&= \sum_{\lambda,\mu,\lambda',\mu'} r_{\lambda\lambda'}^{\mu\mu'}(\vec{\alpha}, P)\, Y_\lambda^\mu(\theta^*, \phi^*) \sum_{L,M} c_L^M(\vec{\alpha}, P) \sum_{L'=L-\lambda'}^{L+\lambda'} G_{L\ \lambda' L'}^{M \mu' M'} Y_{L'}^{M'}(\theta_\text{t}^*, \phi_\text{t}^*)\,.
\end{aligned} \tag{A.18}$$

The coefficients of the resolution function, $r_{\lambda L'}^{\mu M'}(\vec{\alpha}, P)$, are then related directly to the $j_{\lambda\lambda'}^{\mu\mu'}(\vec{\alpha}, P)$ and $c_L^M(\vec{\alpha}, P)$ coefficients through the above expression

$$j_{\lambda L'}^{\mu M'}(\vec{\alpha}, P) = \sum_{L,M,\lambda',\mu'} r_{\lambda\lambda'}^{\mu\mu'}(\vec{\alpha}, P)\, c_L^M(\vec{\alpha}, P)\, G_{L\ \lambda' L'}^{M \mu' M'}\,. \tag{A.19}$$

Computing the resolution directly from this expression then requires the expression be inverted. This is facilitated by treating Equation A.19 as a matrix equation, recognizing that each pair of coefficients l, m is unique, and a unique index can be assigned to them through the definition $i = l(l+1) + m$. After this definition, the coefficients of the true

distribution become elements of a vector, those of the joint distribution a matrix, and the Gaunt coefficients a three-tensor transforming them simultaneously. To put the equation in a form which can be computed with standard matrix inversion routines, we combine the true-coefficient vector and Gaunt coefficients into a single matrix element with a summation:

$$\begin{aligned} \mathbf{r} &= \mathbf{T}^{-1}\mathbf{j}, \quad \text{where} \\ r_{\iota\iota'} &= r^{\mu\mu'}_{\lambda\lambda'}(\vec{\alpha}, P)\,, \\ j_{\iota I'} &= j^{\mu M'}_{\lambda L'}(\vec{\alpha}, P)\,, \quad \text{and} \\ T_{\iota' I'} &= \sum_{L,M} G^{M\mu' M'}_{L\ \lambda' L'}\, c^{M}_{L}(\vec{\alpha}, P)\,. \end{aligned} \tag{A.20}$$

The inversion can now be performed numerically. For the values of $l^{\text{reco}}_{\text{max}}$ suggested by the MISE calculation in this analysis, the matrix has $\mathcal{O}(10^3)$ elements or less, so this calculation proceeds quickly.

APPENDIX B

CHARACTERIZATION OF THE PARAMETER SPACE

The method used in the analysis presented in Chapter VI for estimating the mean value and uncertainty in the f_1-δ_- parameter space was chosen as a reasonable approach for a two-dimensional space; however, the initial characterization of the likelihood which motivated this decision was based on a more general likelihood maximization technique, which is much more efficiency in high-dimensionality problems, called *Markov chain Monte Carlo* (MCMC). This method sampled the full $(\vec{\alpha}, P)$ space simultaneously, approximating the shape of the likelihood function in each of these parameters in a tunable region around their minimum values. As a tool for visualizing the shape of the full likelihood function described by the model used in this analysis, a variety of one- and two-dimensional projections of these fits are shown here.

A. MCMC METHOD DESCRIPTION

A MCMC method samples a likelihood by moving from one point in the parameter space to another according to some metric dependent on the current and proposed point, typically favoring higher $\mathcal{L}$ so that the sampled points (collectively, the Markov chain) tend toward the maximum and nearby values. Many procedural implementations exist; the present analysis applies the Metropolis-Hastings algorithm, tuned to preferentially sample a space within 3σ of $\mathcal{L}_{\max}$.

I. For a *state*, or set of parameter values with position n in the Markov chain $\vec{\alpha}_n$, a *proposal distribution* is defined.
   a. The proposal must be symmetric in $\vec{\alpha}_n$ and $\vec{\alpha}_{n+1}$, meaning the probability of selecting $\vec{\alpha}_n$ from a distribution centered at $\vec{\alpha}_{n+1}$ is equal to that of the opposite case.
   b. A multivariate Gaussian distribution is constructed with a covariance matrix estimated from the shape of the likelihood near the maximum.

II. From this proposal distribution centered at $\vec{\alpha_n}$, a possible next state is randomly drawn, $\vec{\alpha}_{n+1}$.

III. The likelihood ratio $r = \frac{\mathcal{L}(\vec{\alpha}_{n+1})}{\mathcal{L}(\vec{\alpha}_n)}$ is used to determine whether to move to state $n+1$ or remain at state n.
   a. If $r > 1$, then $\vec{\alpha}_{n+1}$ is selected as the the next state in the Markov chain.
   b. If $r < 1$, a random number between 0 and 1 is thrown; if that number is less than r, then $\vec{\alpha}_{n+1}$ is selected, otherwise $\vec{\alpha}_n$ is reentered into the chain as $\vec{\alpha}_{n+1}$.

The MCMC method is subject to potential pitfalls, and some diagnostics must be evaluated to extract a reasonable result. First, the proposal distribution must be defined such that a reasonable number of proposed points are accepted into the chain. If the covariance matrix used to define the proposal is either too broad or does not take large correlations between parameters into account, this can lead to *blocking*, where the chain remains at single states for too long to smoothly trace the shape of the likelihood. The proposal must also be defined such that it can reach the maximum after a reasonable number of steps and then have time to trace the region around the maximum. If this distribution is very narrow, then the *burn-in time*, during which it is moving toward the maximum, may be too long to get a reasonable approximation of the likelihood near its maximum.

A diagnostic plotting the value of $-2\ln(\mathcal{L})$ for multiple Markov chains as a function of the state number is shown in Figure B1 for a well-tuned covariance matrix. Blocking would be indicated by an extended plateau in a chain which does not coincide with the values in other chains, while an extended burn-in period would produce a monotonically decreasing curve. Instead, all chains move relatively quickly to plateaus in similar regions, indicating they have found a stable minimum in $-2\ln(\mathcal{L})$, and proceed to move between different values in that region.

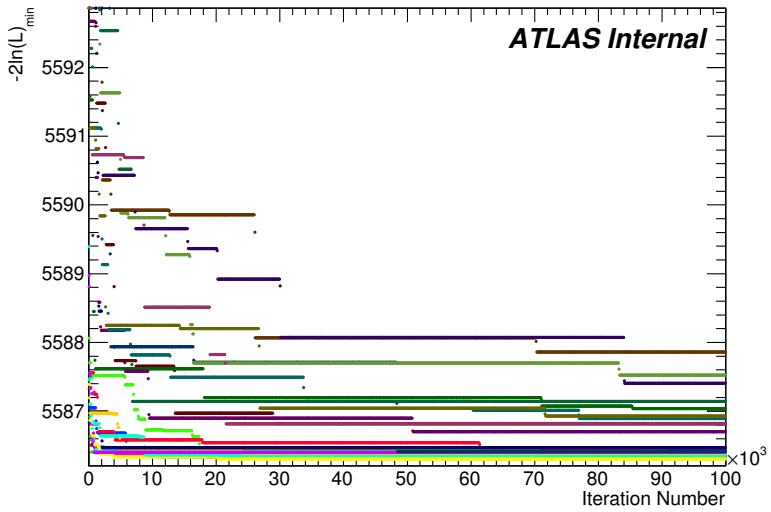

Figure B1: Example MCMC diagnostic: $-2\ln(\mathcal{L})$ vs. sequential state number in 24 markov chains. This process had different scales applied to different chains, resulting in different burn-in times. After 15000 states in this fit, all chains have reached a stable minimum region.

B. LIKELIHOOD PROJECTIONS

From the six-dimensional $(\vec{\alpha}, P)$ parameter space, a projective method can be used to visualize the shape of the likelihood in either one or two dimensions. The *joint profile* likelihood projection finds the minimum-likelihood value in the non-projected coordinates for a given value (or here, in a given bin) of the projected coordinates, tracing the maximum-value path through the remaining space in these coordinates.

The projections shown in Figures B2 - B5 represent a likelihood constructed from the full AcerMC signal sample and combined background samples. The variables f_1 and δ_- are the most well-described in this space; the likelihood is approximately gaussian in these variables, and they are far from their physical limits. This makes these variables ideal candidates for measurement. The parameter f_1^+ is correlated with f_1 and is tighly constrained, but

proximity to its physical limit makes it more complicated to measure with this technique. The parameters f_0^+ and P are highly correlated, and poorly constrained; the alternative parameter $P\sqrt{1-f_0^+}$ is better estimated, but still close to its physical limit. Finally, the parameter δ_+ is unconstrained by this data, as the amplitude associated with this phase is 0 when f_1^+ and f_0^+ are both near 0.

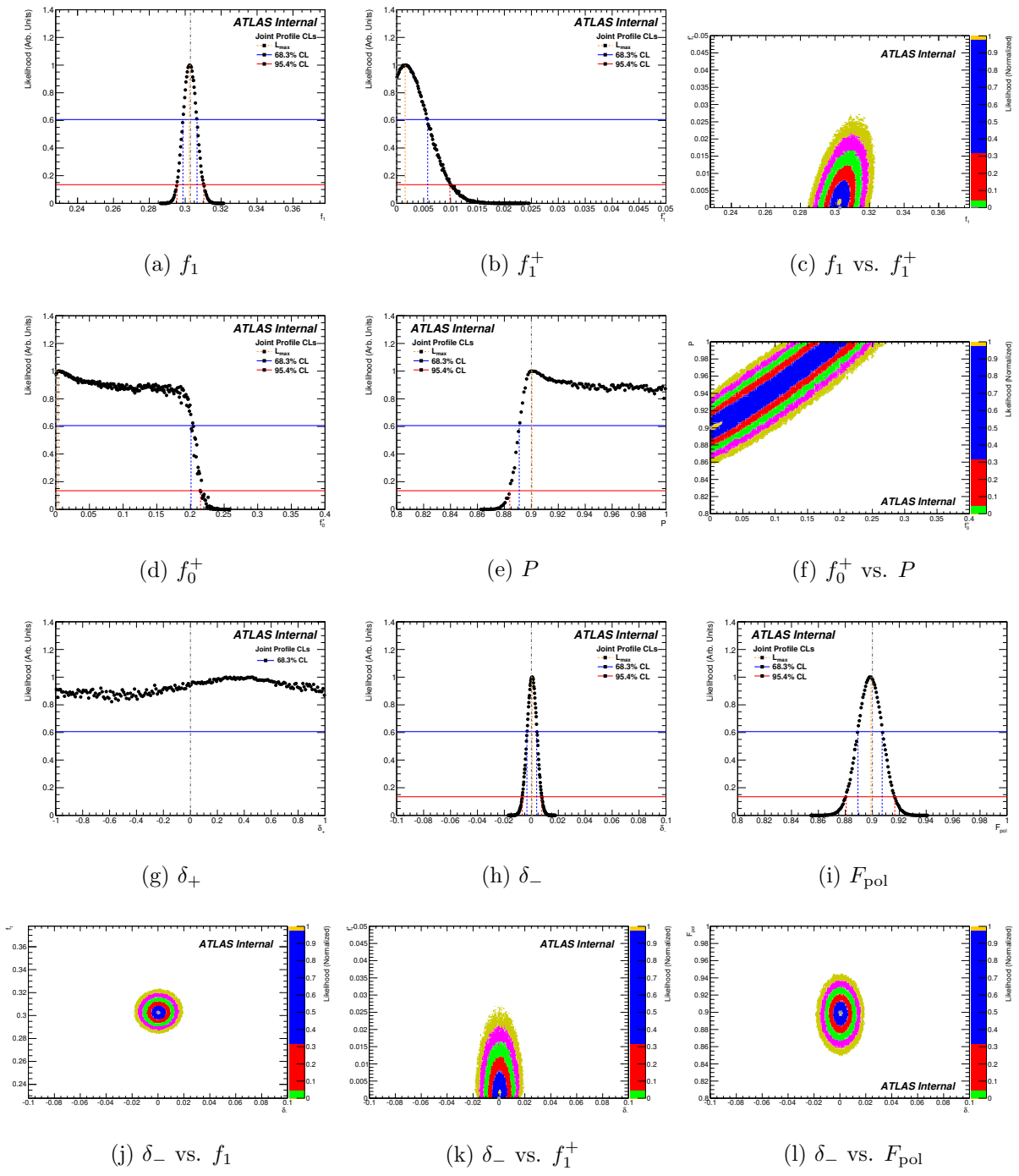

(a) f_1 (b) f_1^+ (c) f_1 vs. f_1^+

(d) f_0^+ (e) P (f) f_0^+ vs. P

(g) δ_+ (h) δ_- (i) F_{pol}

(j) δ_- vs. f_1 (k) δ_- vs. f_1^+ (l) δ_- vs. F_{pol}

Figure B2: Joint profile likelihood projections of a likelihood representing AcerMC-generated events in one- and two-dimensional projections as indicated for each plot. The blue, red, green, magenta, and yellow represent the 68%, 95%, 99.7%, 99.99%, and $> 99.99\%$ credibility regions; orange represents the minimum value or region in the projection, and the gray line or point indicates the SM expected values of the variables.

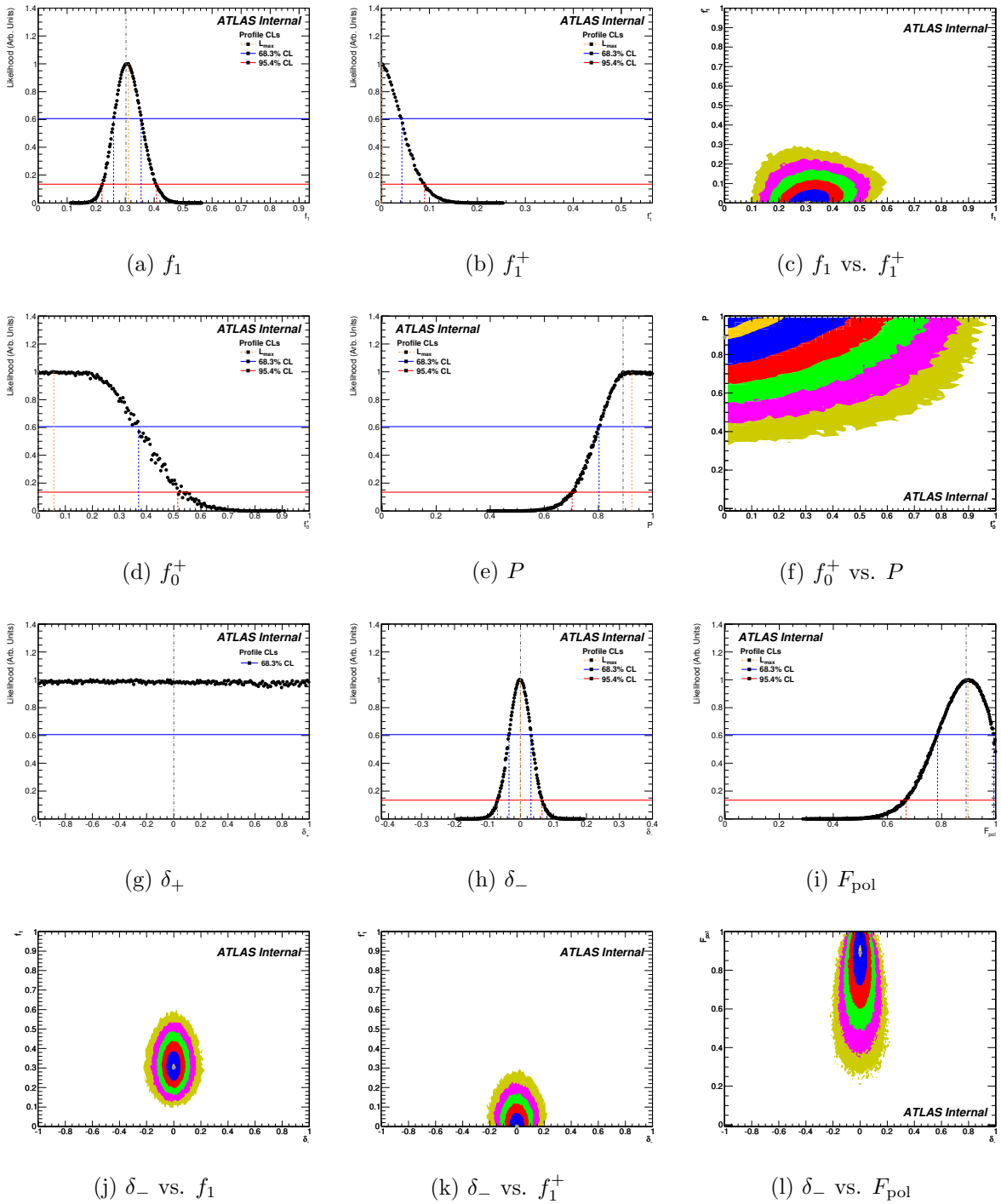

(a) f_1 (b) f_1^+ (c) f_1 vs. f_1^+

(d) f_0^+ (e) P (f) f_0^+ vs. P

(g) δ_+ (h) δ_- (i) F_{pol}

(j) δ_- vs. f_1 (k) δ_- vs. f_1^+ (l) δ_- vs. F_{pol}

Figure B3: Joint profile likelihood projections of a likelihood representing a selected signal distribution in one- and two-dimensional projections as indicated for each plot. The blue, red, green, magenta, and yellow represent the 68%, 95%, 99.7%, 99.99%, and 99.99% credibility regions; orange represents the minimum value or region in the projection, and the gray line or point indicates the SM expected values of the variables.

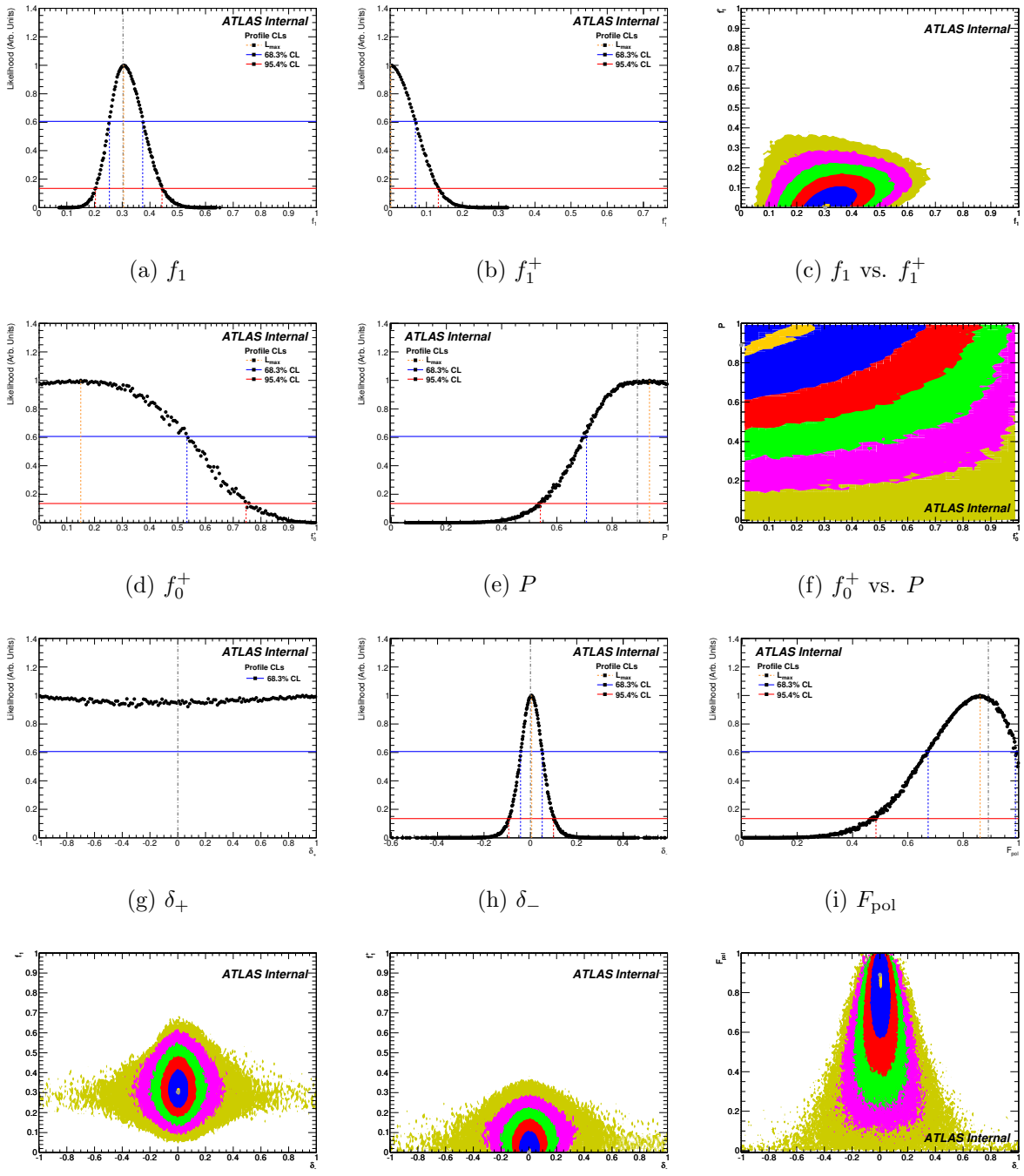

(a) f_1 (b) f_1^+ (c) f_1 vs. f_1^+

(d) f_0^+ (e) P (f) f_0^+ vs. P

(g) δ_+ (h) δ_- (i) F_{pol}

(j) δ_- vs. f_1 (k) δ_- vs. f_1^+ (l) δ_- vs. F_{pol}

Figure B4: Joint profile likelihood projections of a likelihood representing a reconstructed signal distribution in one- and two-dimensional projections as indicated for each plot. The blue, red, green, magenta, and yellow represent the 68%, 95%, 99.7%, 99.99%, and $> 99.99\%$ credibility regions; orange represents the minimum value or region in the projection, and the gray line or point indicates the SM expected values of the variables.

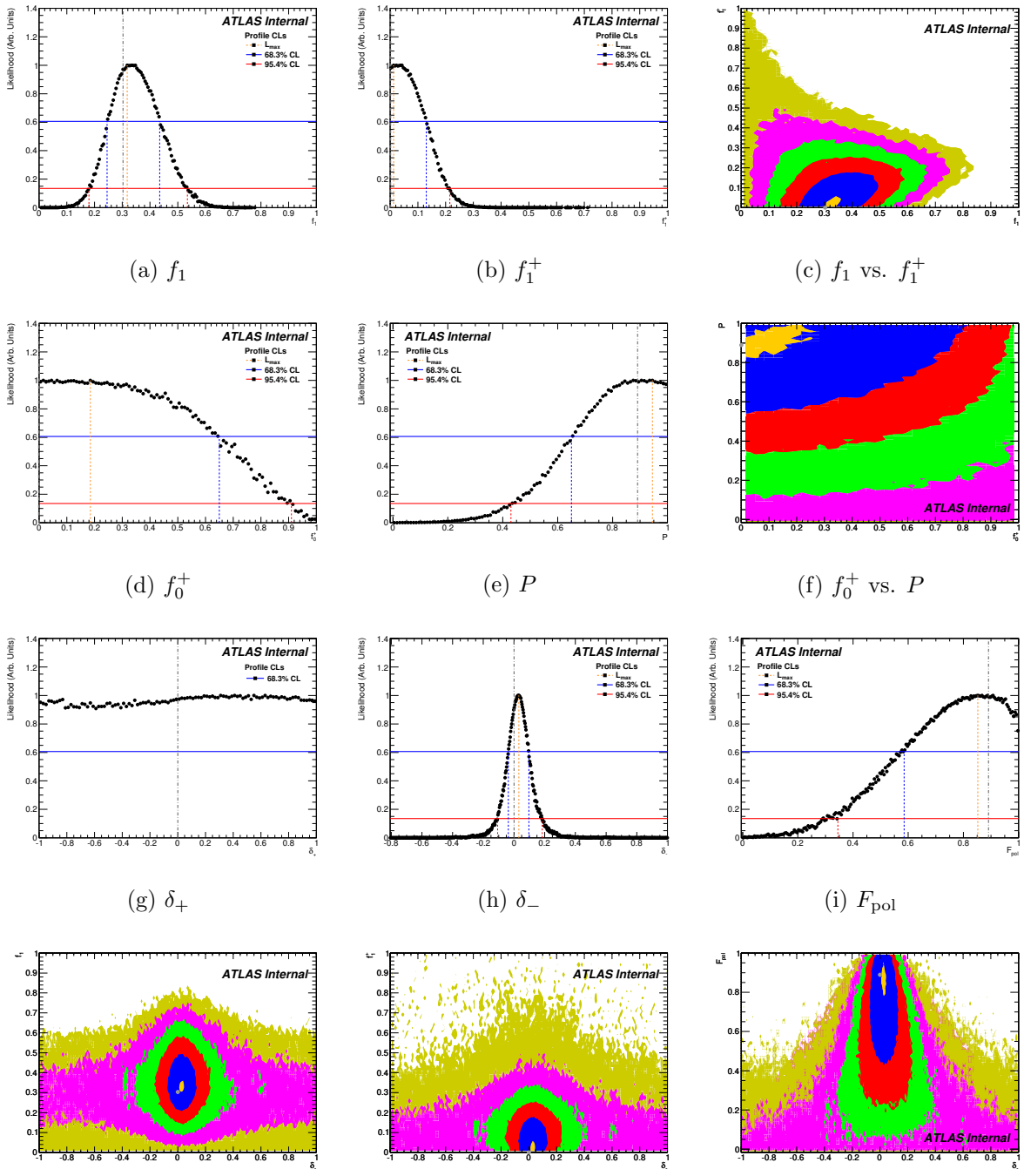

(a) f_1 (b) f_1^+ (c) f_1 vs. f_1^+

(d) f_0^+ (e) P (f) f_0^+ vs. P

(g) δ_+ (h) δ_- (i) F_{pol}

(j) δ_- vs. f_1 (k) δ_- vs. f_1^+ (l) δ_- vs. F_{pol}

Figure B5: Joint profile likelihood projections of a likelihood representing a reconstructed distribution containing signal and background processes in one- and two-dimensional projections as indicated for each plot. The blue, red, green, magenta, and yellow represent the 68%, 95%, 99.7%, 99.99%, and $>$ 99.99% credibility regions; orange represents the minimum value or region in the projection, and the gray line or point indicates the SM expected values of the variables.

APPENDIX C

CONTROL DISTRIBUTIONS

The sample construction procedures used to define the signal and control regions in Chapter VI can be validated by comparing distributions of kinematic quantities between MC simulation and data. The distributions of some of these variables are shown here in the signal region and the $t\bar{t}$ and W+jets control regions. All three regions show good agreement between these distributions in MC simulation and in data.

The comparison between data and expectation for $E_{\mathrm{T}}^{\mathrm{miss}}$, $m_{\mathrm{T}}(W)$, p_T and η of the lepton, light jet and b-jet as well as the mass of the reconstructed top quark and H_{T} is shown for the electron and muon channels in Figures C1 - C5 for the signal region, Figures C6 - C10 for the $t\bar{t}$ enriched region, and Figures C11 - C15 for the W+jets enriched region. Uncertainties on the prediction are statistical, and include the multijets normalization uncertainty.

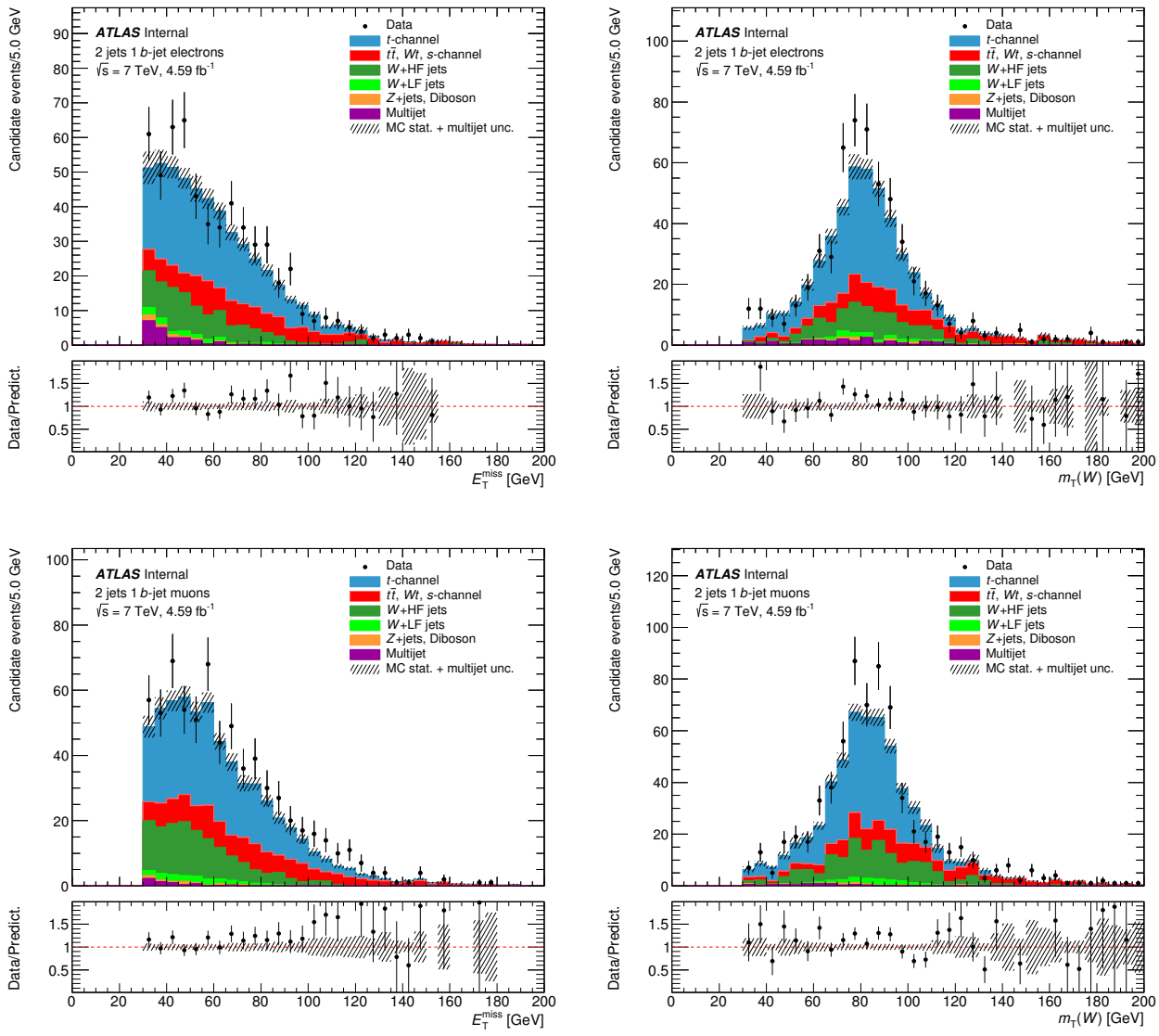

Figure C1: Comparison between data and expectation in the $E_{\mathrm{T}}^{\mathrm{miss}}$ and $m_{\mathrm{T}}(W)$ distributions in the signal region for the electron (upper row) and the muon (lower row) channels. The uncertainties shown on the prediction take into account MC statistics and the 50% systematic uncertainty on the multijets background normalization.

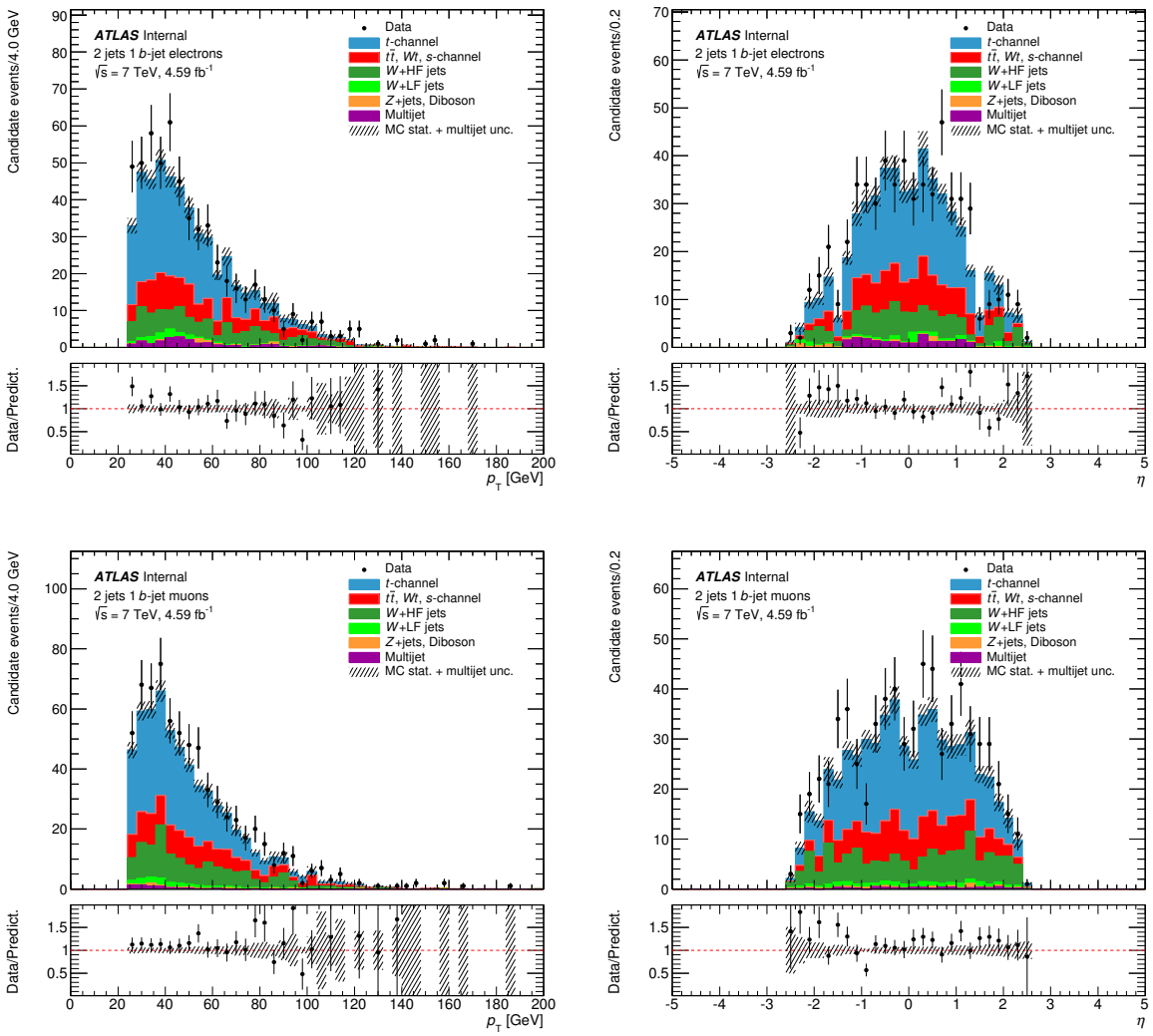

Figure C2: Comparison between data and expectation in the p_T and η distributions for the lepton from W decay in the signal region for the electron (top row) and muon (bottom row) channels. The uncertainties shown on the prediction take into account MC statistics and the 50% systematic uncertainty on the multijets background normalization.

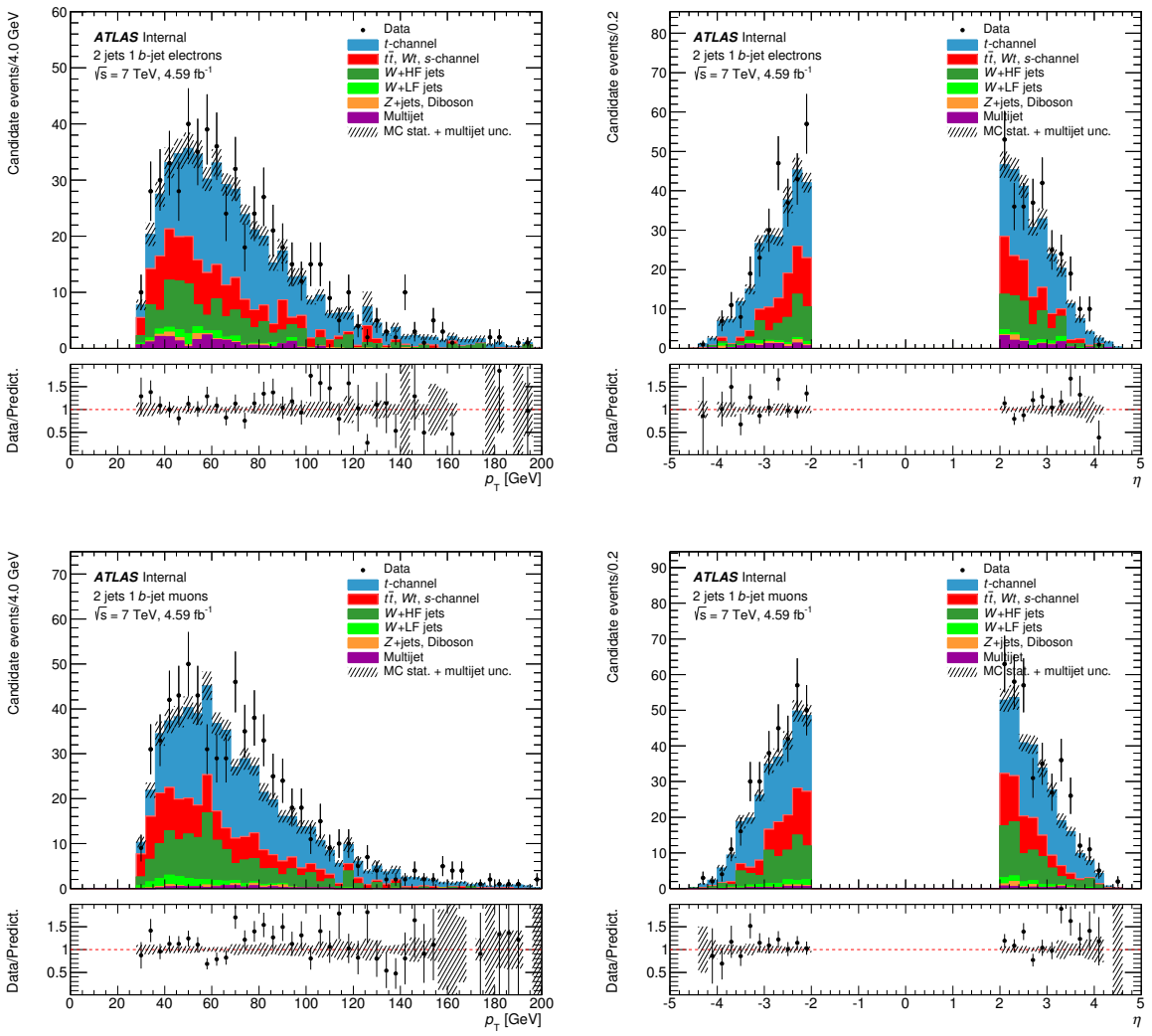

Figure C3: Comparison between data and expectation in the p_T and η distributions for the light jet in the signal region for the electron (top row) and muon (bottom row) channels. The uncertainties shown on the prediction take into account MC statistics and the 50% systematic uncertainty on the multijets background normalization.

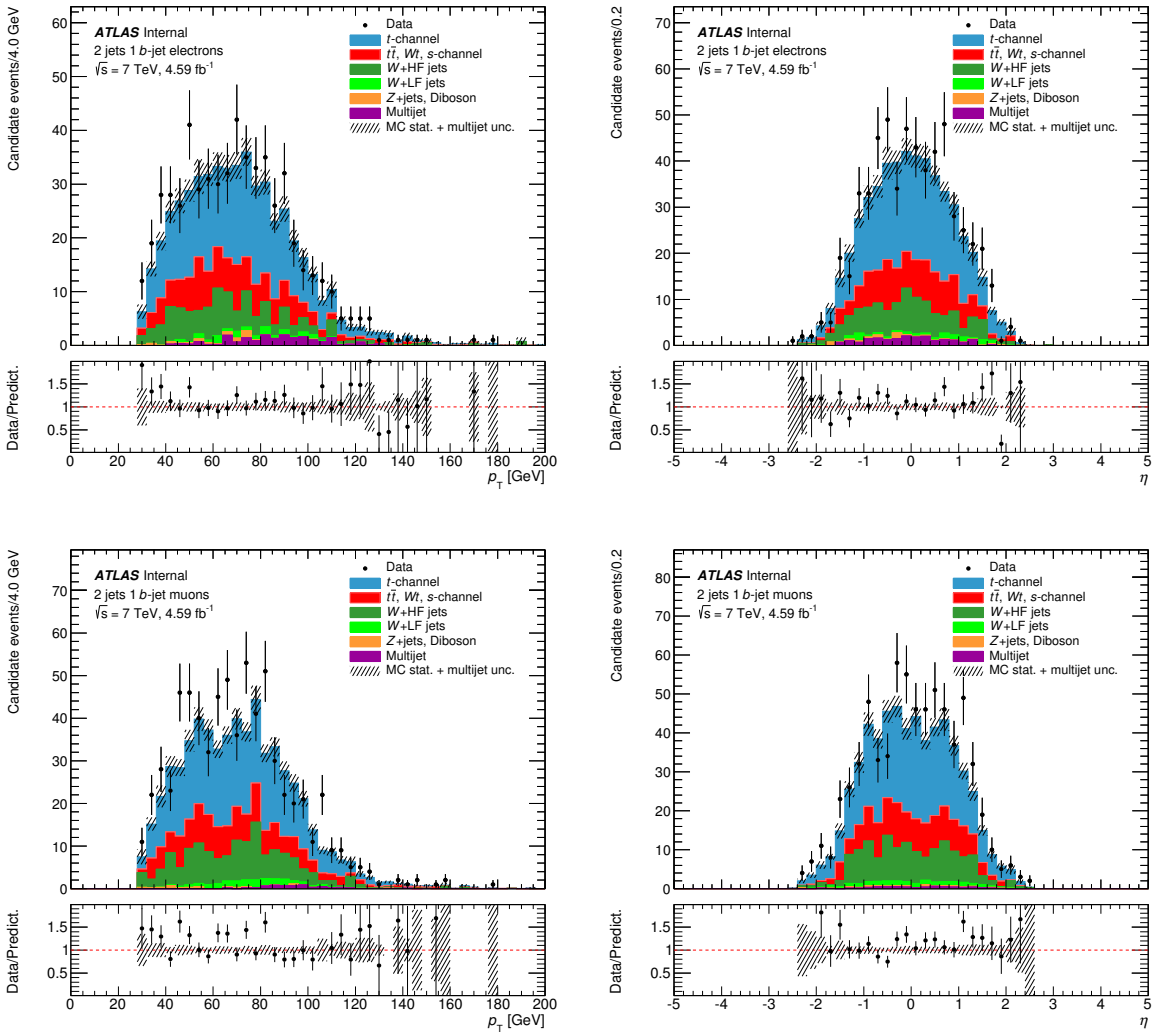

Figure C4: Comparison between data and expectation in the p_T and η distributions for the b-jet from top decay in the signal region for the electron (top row) and muon (bottom row) channels. The uncertainties shown on the prediction take into account MC statistics and the 50% systematic uncertainty on the multijets background normalization.

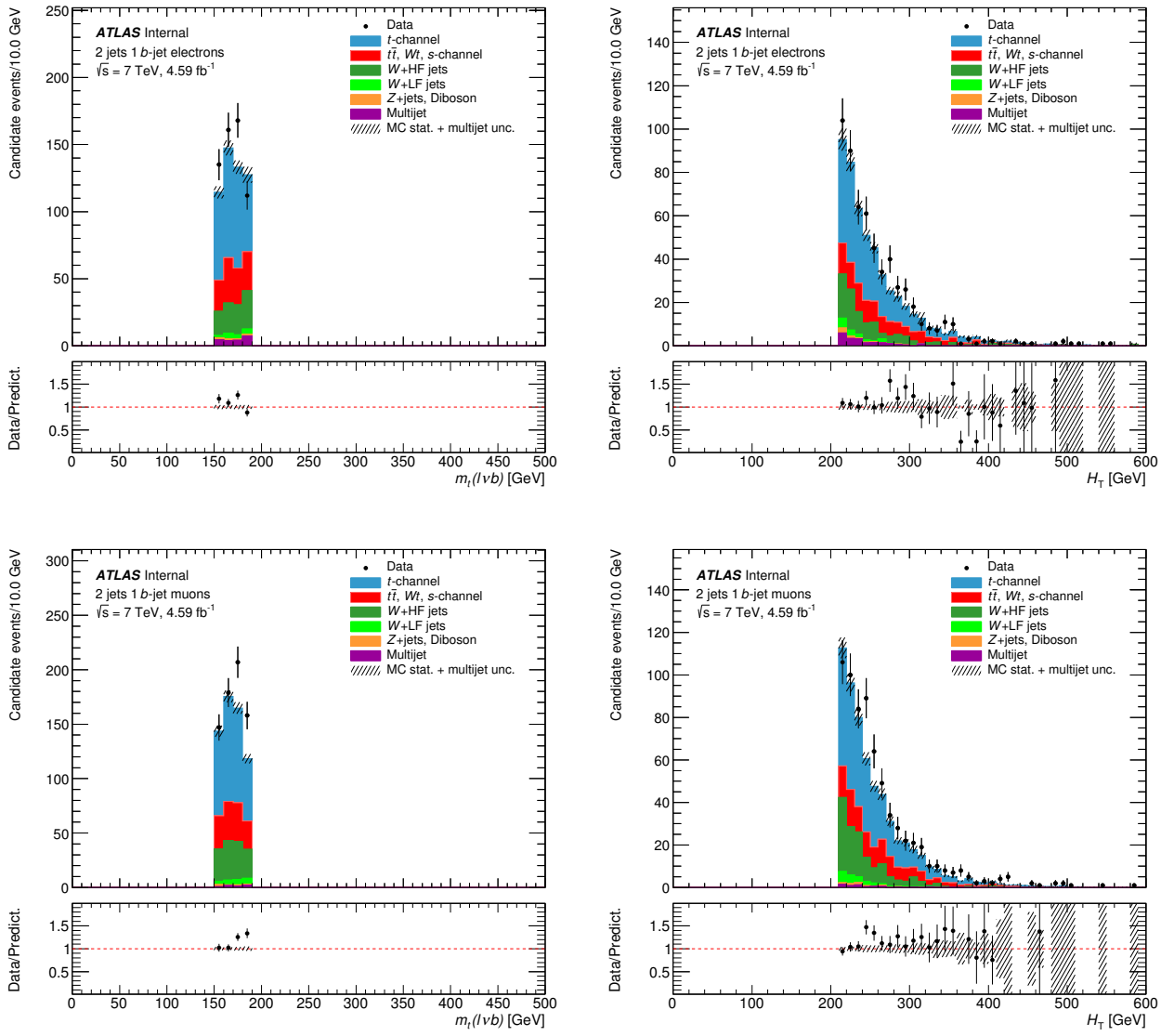

Figure C5: Comparison between data and expectation in the top quark mass and H_{T} distributions in the signal region for the electron (upper row) and the muon (lower row) channels. The uncertainties shown on the prediction take into account MC statistics and the 50% systematic uncertainty on the multijets background normalization.

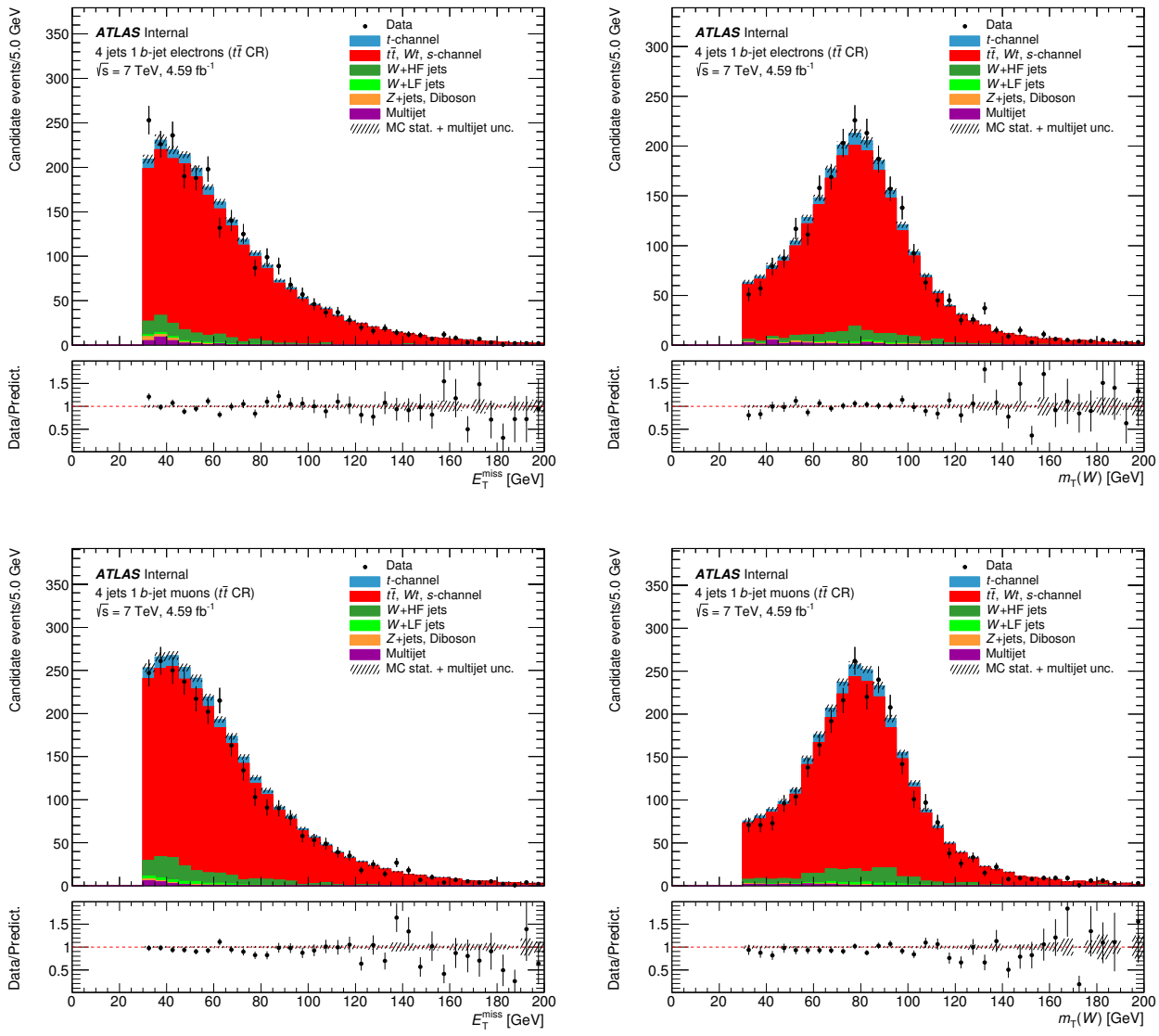

Figure C6: Comparison between data and expectation in the $E_{\mathrm{T}}^{\mathrm{miss}}$ and $m_{\mathrm{T}}(W)$ distributions in the $t\bar{t}$ enriched region for the electron (upper row) and the muon (lower row) channels. The uncertainties shown on the prediction take into account MC statistics and the 50% systematic uncertainty on the multijets background normalization.

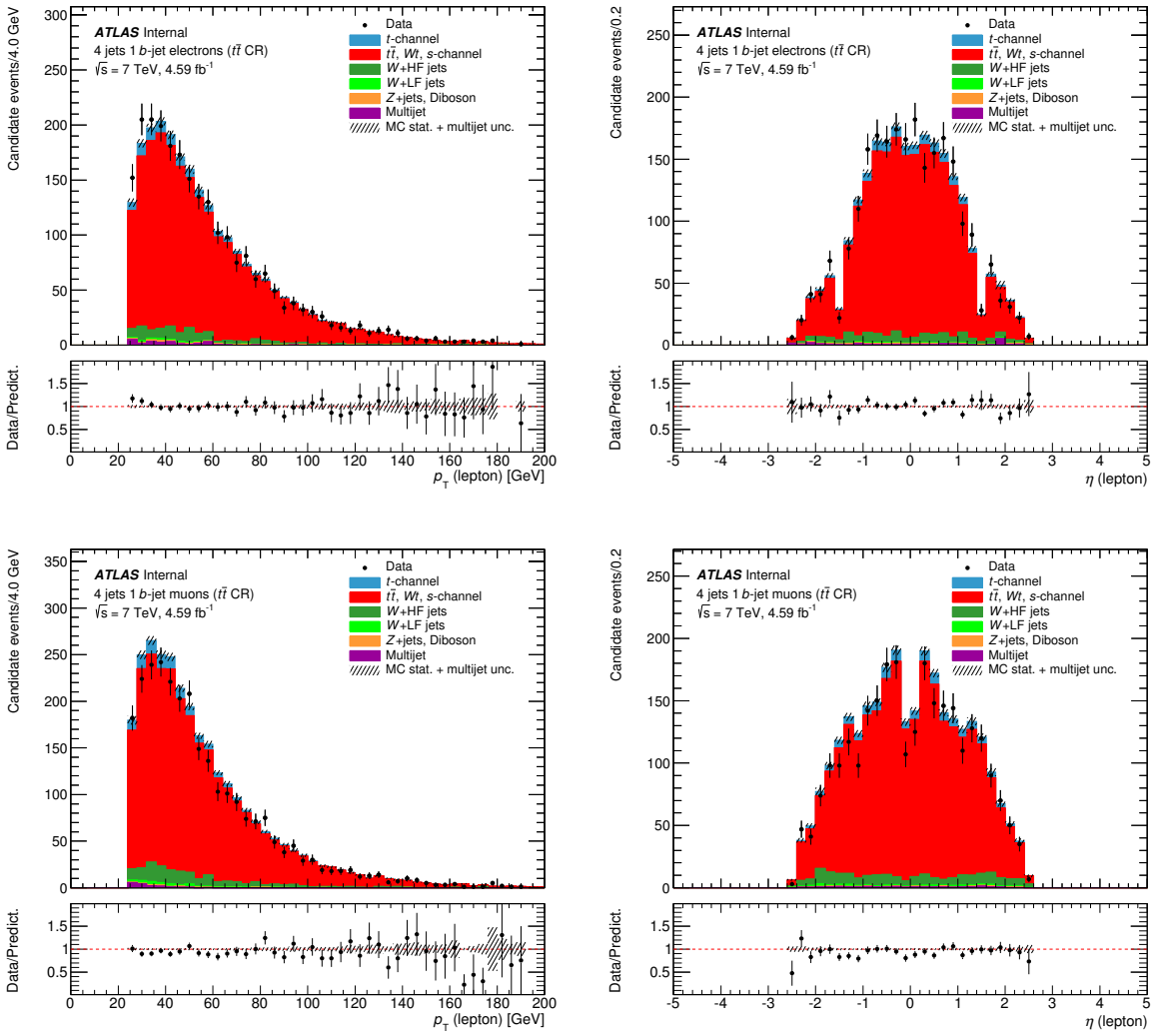

Figure C7: Comparison between data and expectation in the p_T and η distributions for the lepton from W decay in the $t\bar{t}$ enriched region for the electron (top row) and muon (bottom row) channels. The uncertainties shown on the prediction take into account MC statistics and the 50% systematic uncertainty on the multijets background normalization.

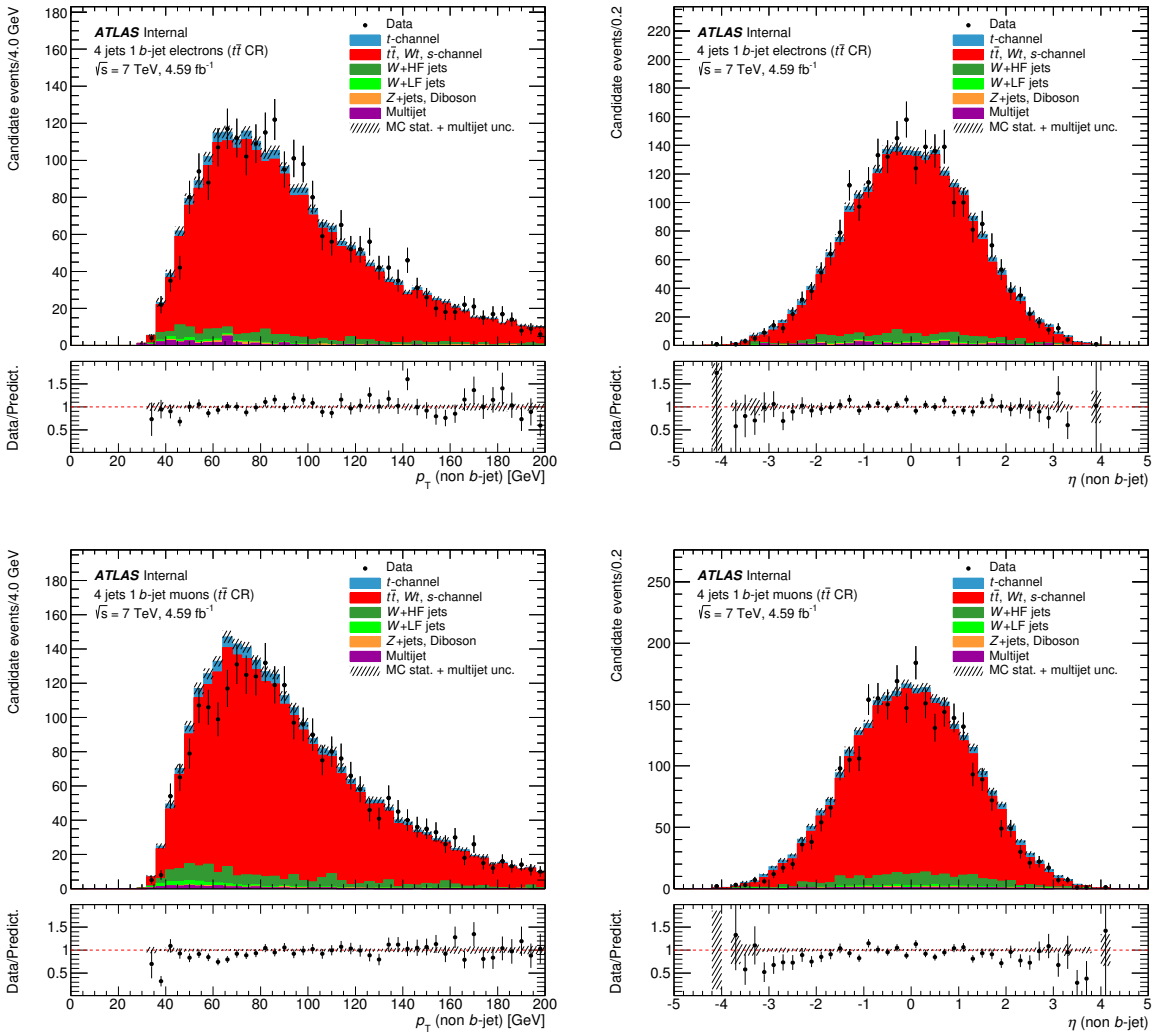

Figure C8: Comparison between data and expectation in the p_T and η distributions for the light jet in the $t\bar{t}$ enriched region for the electron (top row) and muon (bottom row) channels. The uncertainties shown on the prediction take into account MC statistics and the 50% systematic uncertainty on the multijets background normalization.

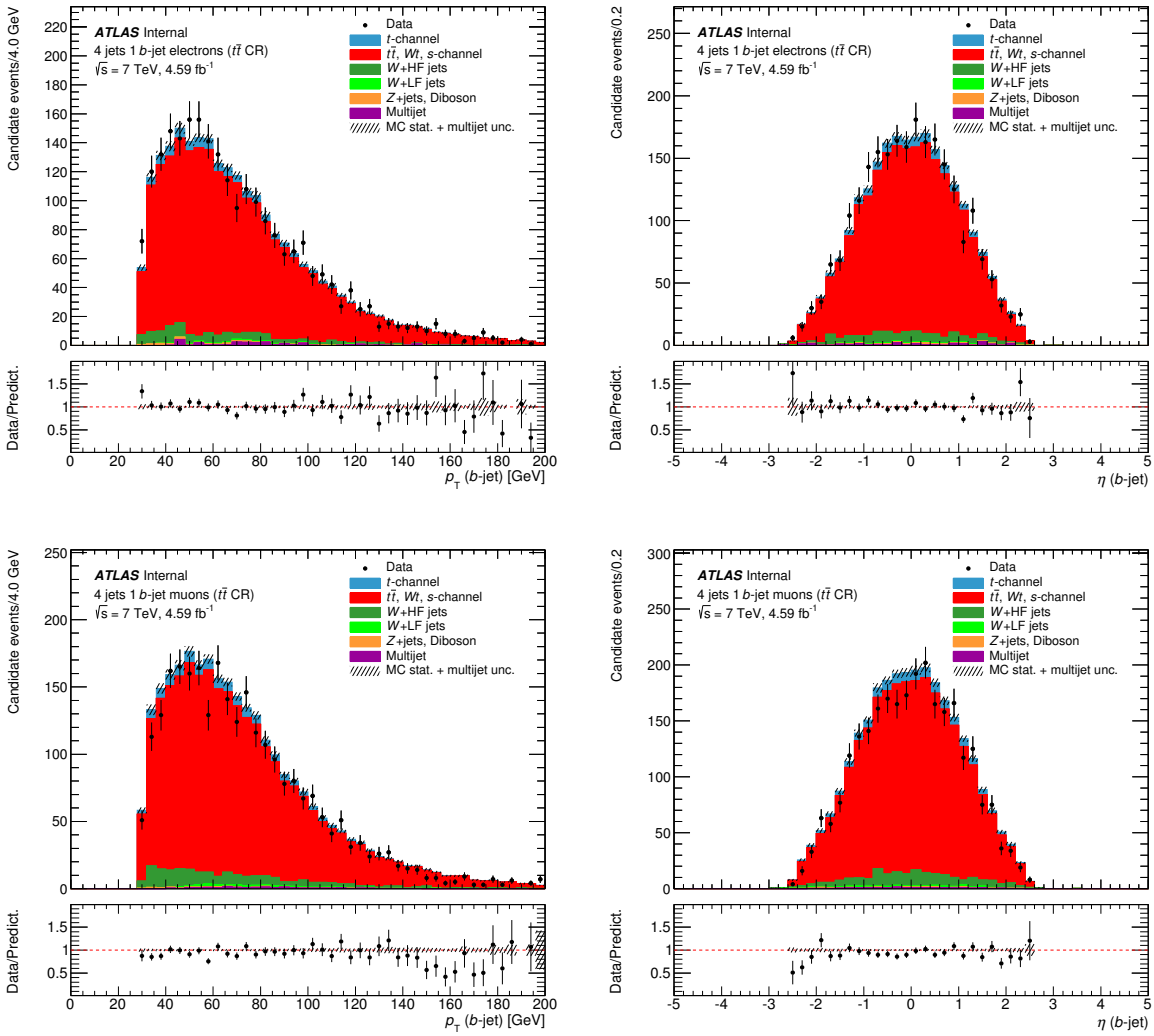

Figure C9: Comparison between data and expectation in the p_T and η distributions for the b-jet from top decay in the $t\bar{t}$ enriched region for the electron (top row) and muon (bottom row) channels. The uncertainties shown on the prediction take into account MC statistics and the 50% systematic uncertainty on the multijets background normalization.

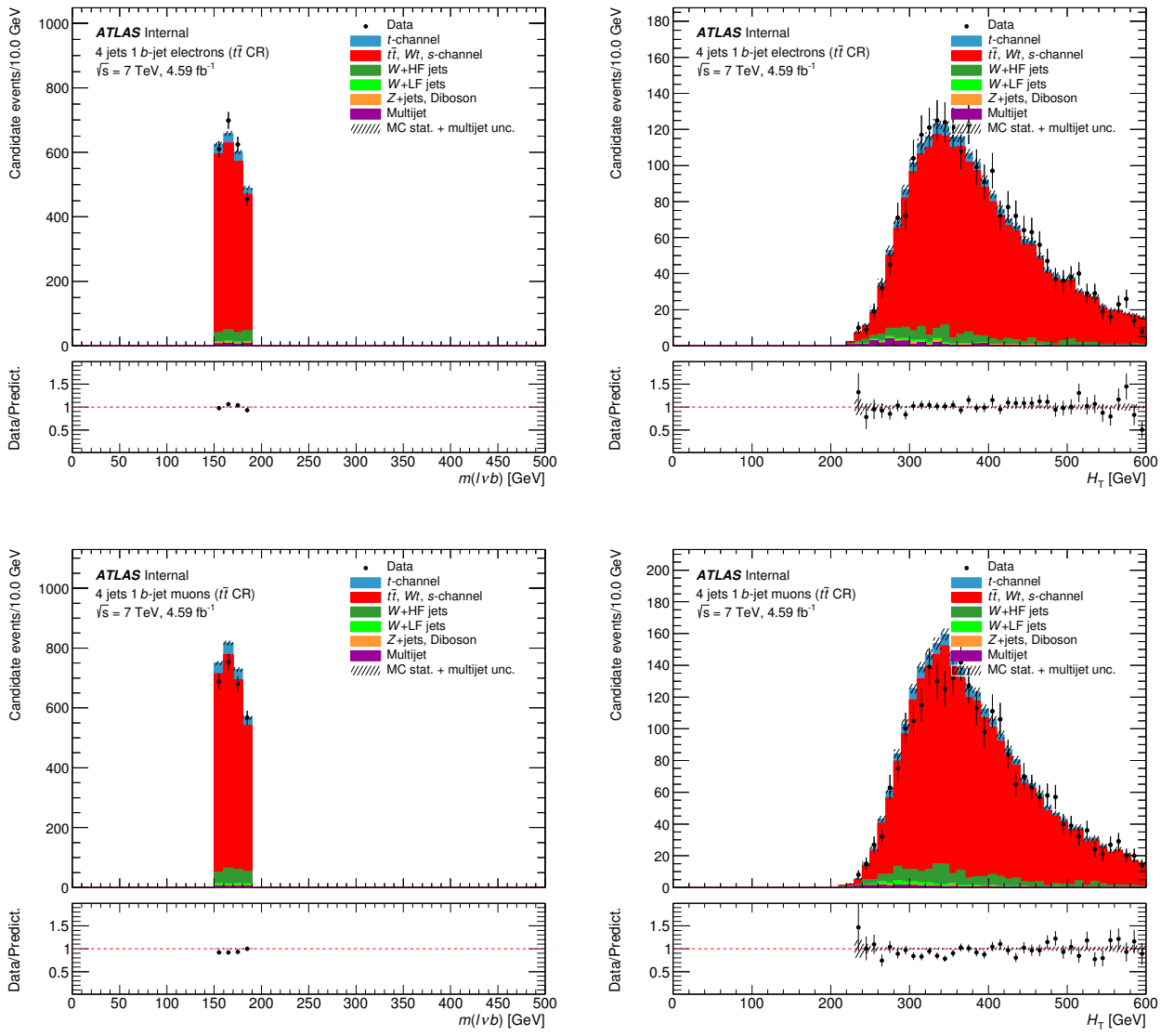

Figure C10: Comparison between data and expectation in the top quark mass and H_{T} distributions in the $t\bar{t}$ enriched region for the electron (upper row) and the muon (lower row) channels. The uncertainties shown on the prediction take into account MC statistics and the 50% systematic uncertainty on the multijets background normalization.

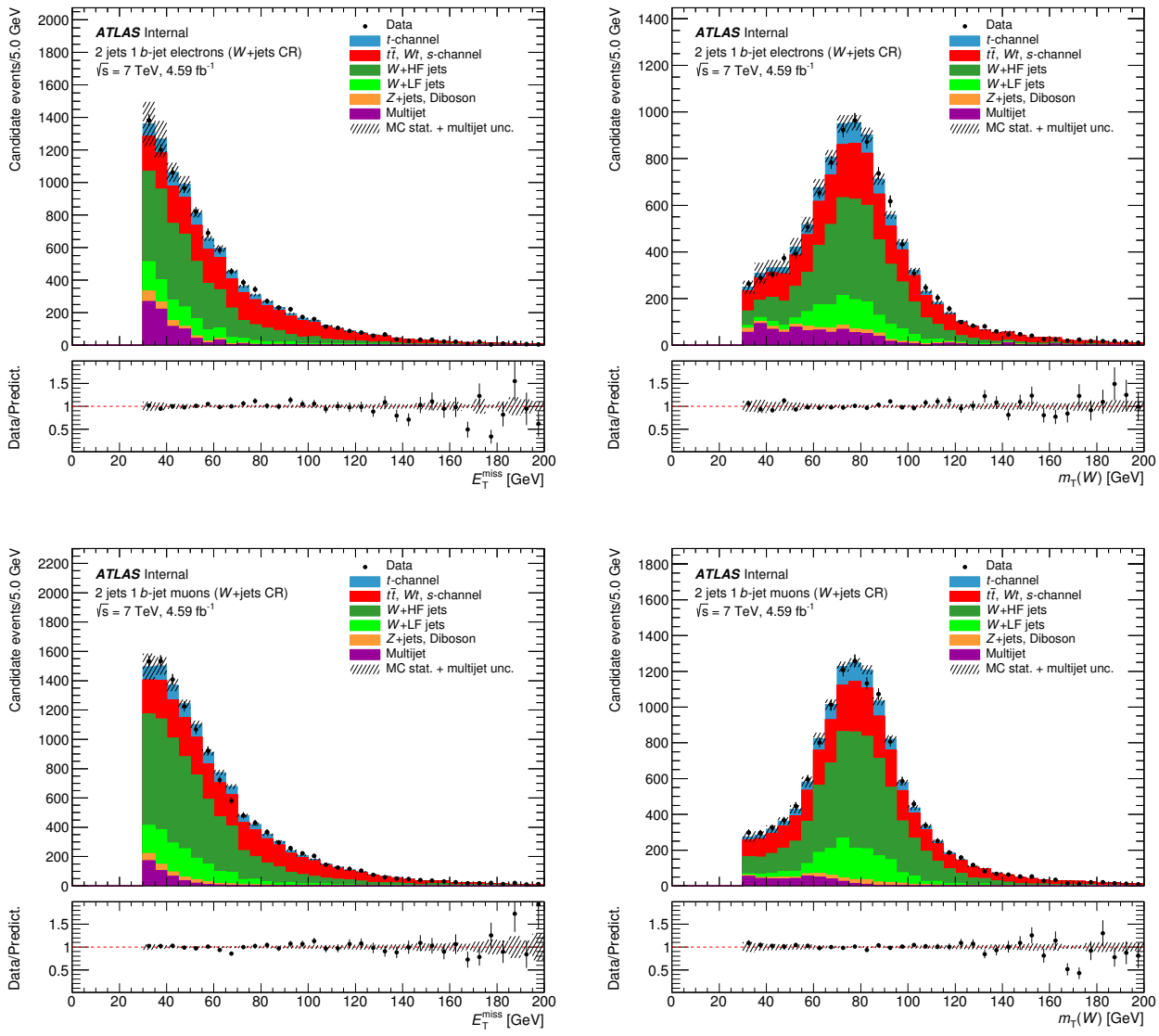

Figure C11: Comparison between data and expectation in the $E_{\mathrm{T}}^{\mathrm{miss}}$ and $m_{\mathrm{T}}(W)$ distributions in the W+jets enriched region for the electron (upper row) and the muon (lower row) channels. The uncertainties shown on the prediction take into account MC statistics and the 50% systematic uncertainty on the multijets background normalization.

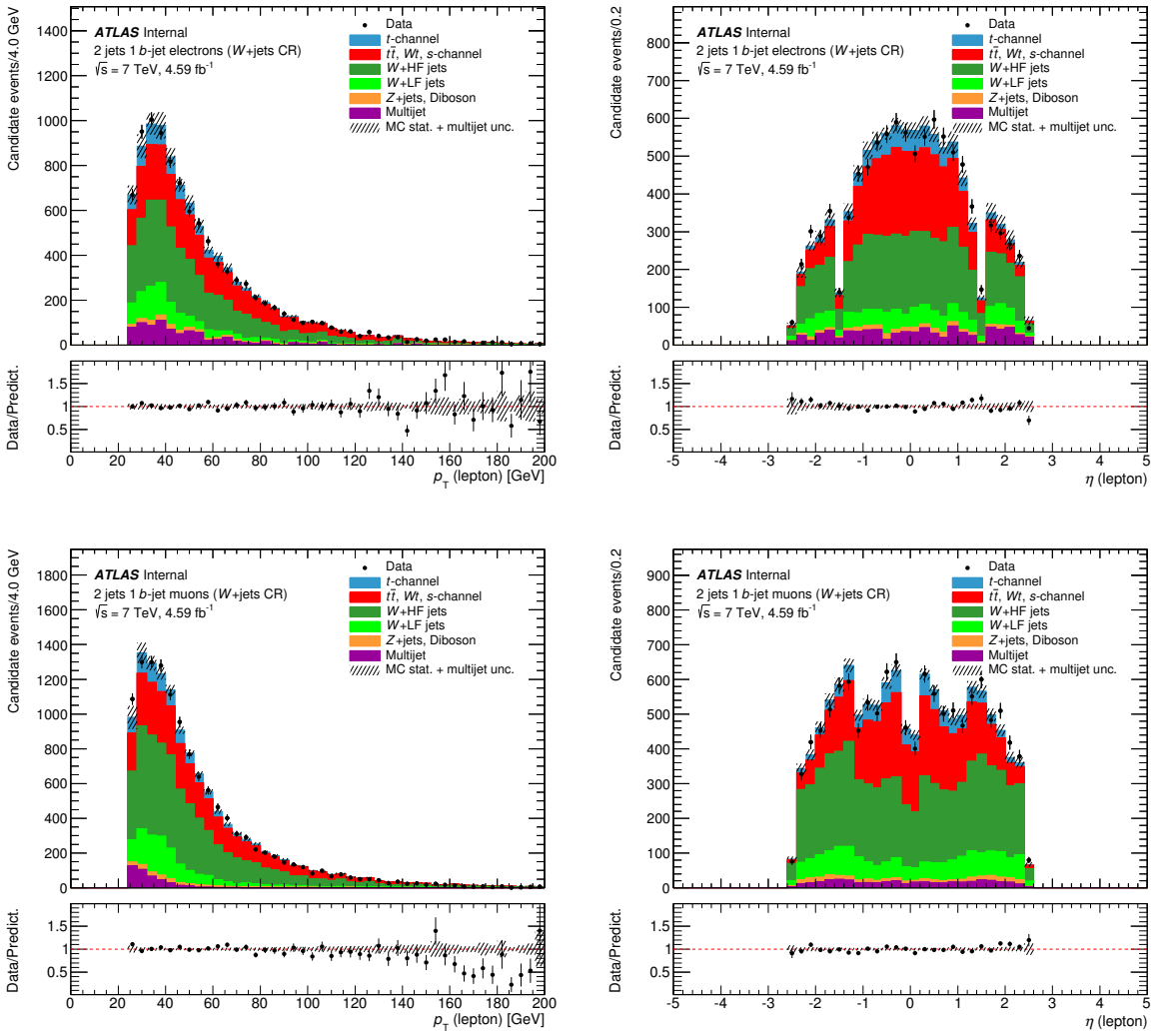

Figure C12: Comparison between data and expectation in the p_T and η distributions for the lepton from W decay in the W+jets enriched region for the electron (top row) and muon (bottom row) channels. The uncertainties shown on the prediction take into account MC statistics and the 50% systematic uncertainty on the multijets background normalization.

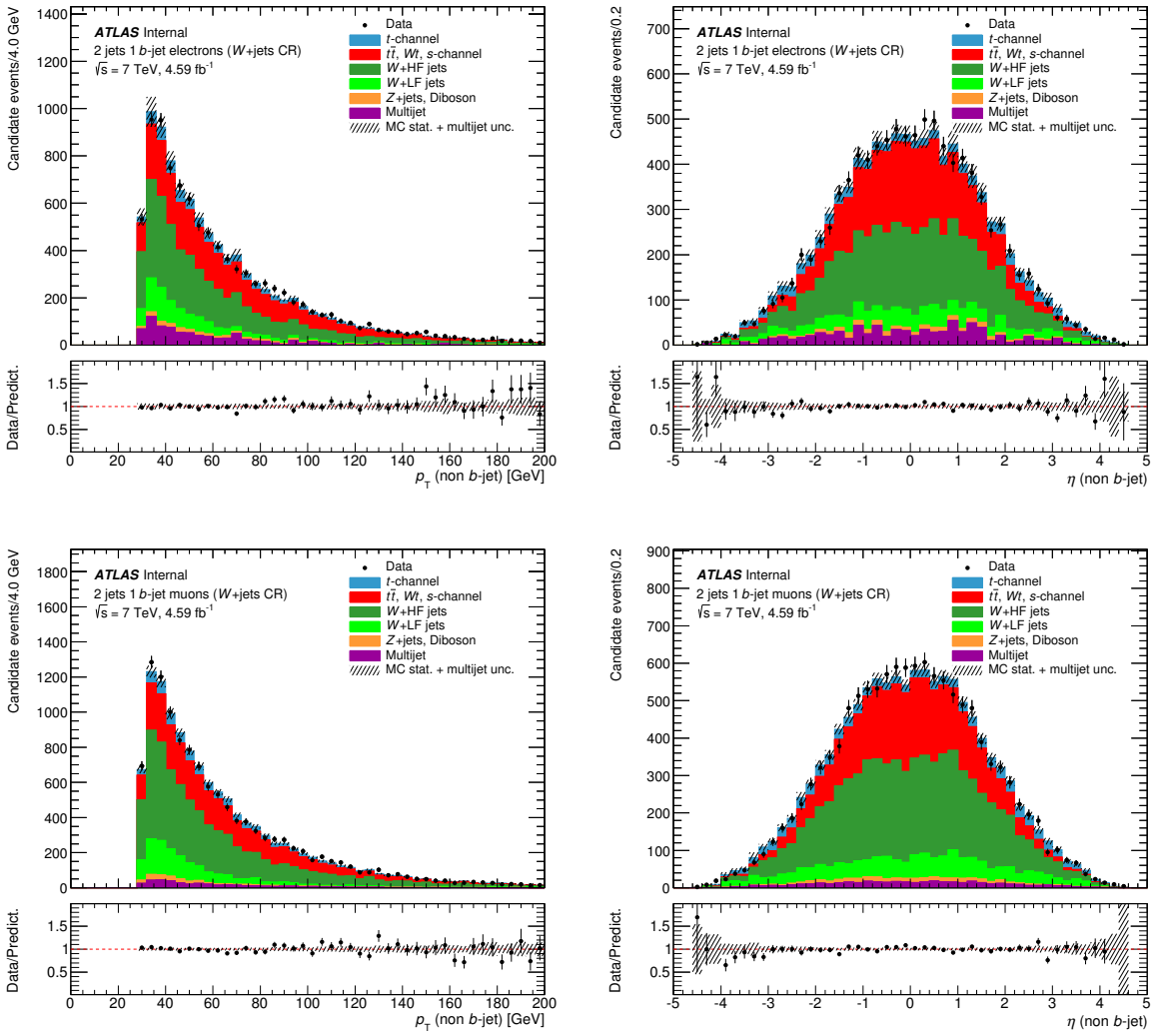

Figure C13: Comparison between data and expectation in the p_T and η distributions for the light jet in the W+jets enriched region for the electron (top row) and muon (bottom row) channels. The uncertainties shown on the prediction take into account MC statistics and the 50% systematic uncertainty on the multijets background normalization.

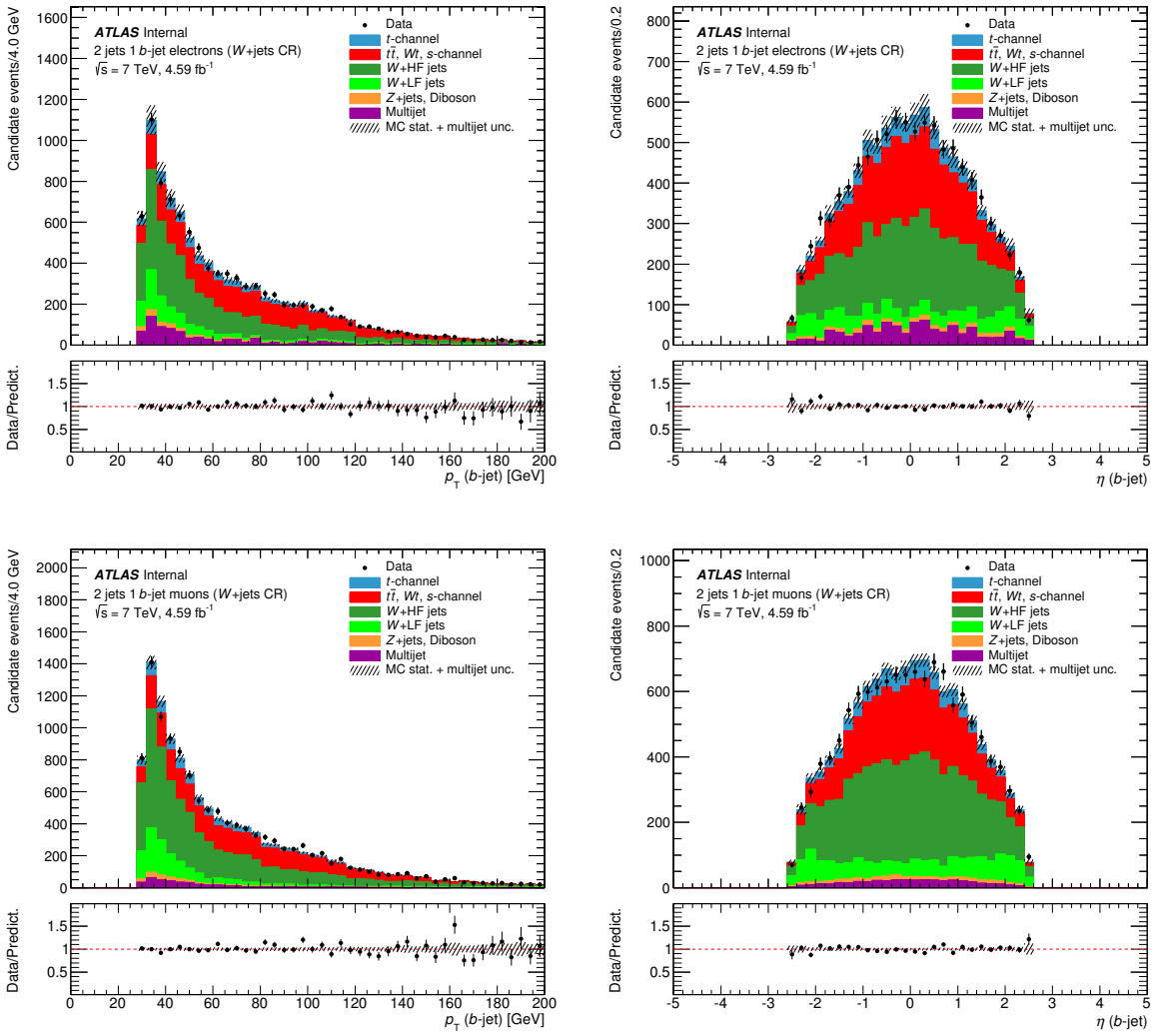

Figure C14: Comparison between data and expectation in the p_T and η distributions for the b-jet from top decay in the W+jets enriched region for the electron (top row) and muon (bottom row) channels. The uncertainties shown on the prediction take into account MC statistics and the 50% systematic uncertainty on the multijets background normalization.

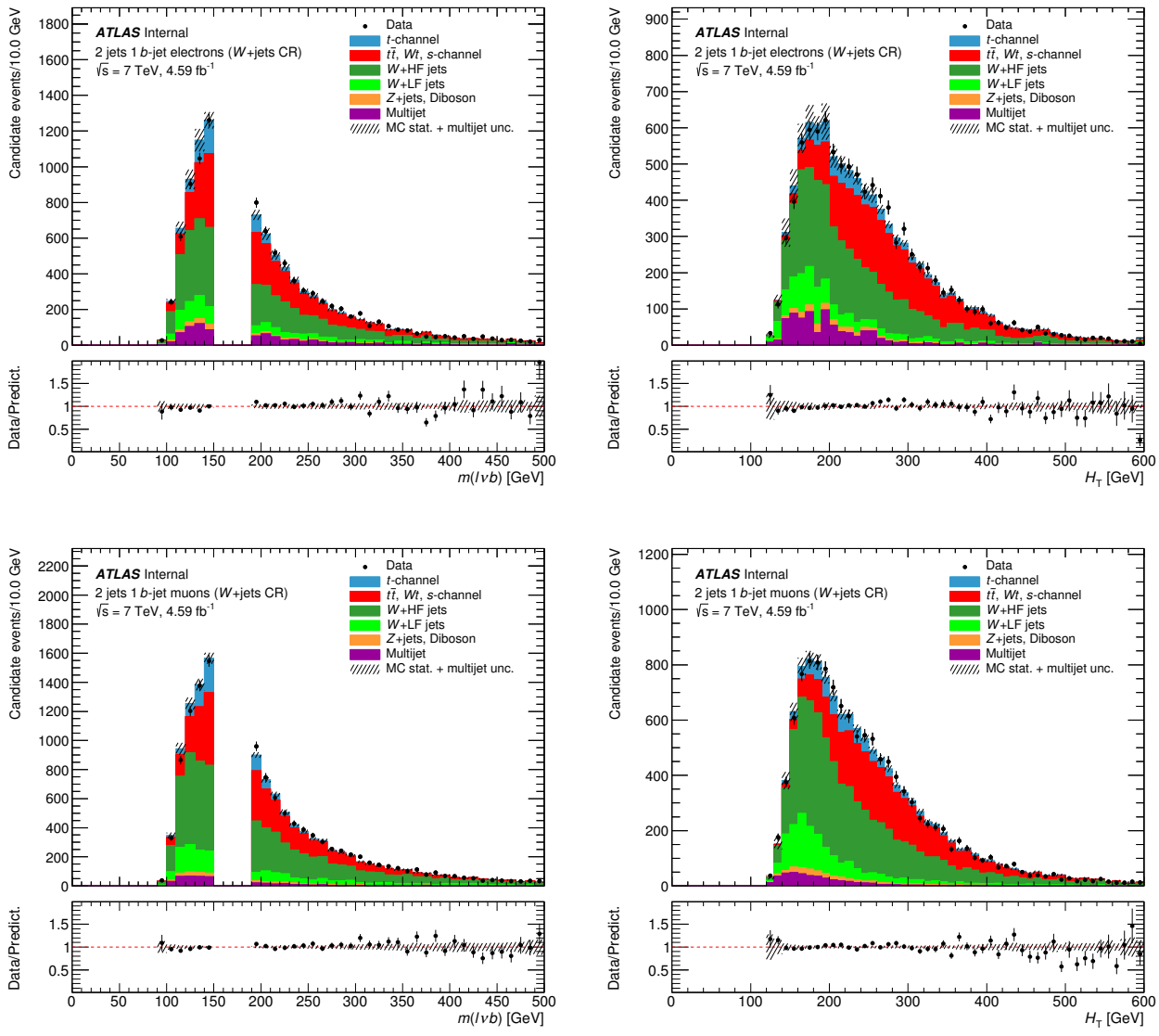

Figure C15: Comparison between data and expectation in the top quark mass and H_{T} distributions in the W+jets enriched region for the electron (upper row) and the muon (lower row) channels. The uncertainties shown on the prediction take into account MC statistics and the 50% systematic uncertainty on the multijets background normalization.

BIBLIOGRAPHY

[1] L. Boltzmann and F. Hasenöhrl, *Wissenschaftliche Abhandlungen*. Cambridge Library Collection - Physical Sciences. Cambridge University Press, 2012. https://books.google.com/books?id=sdd2Vu3g0UwC.

[2] R. Feynman, R. Leighton, and M. Sands, *The Feynman Lectures on Physics*. No. v. 3 in Addison-Wesley world student series. Addison-Wesley, 1977. https://books.google.com/books?id=86kvngEACAAJ.

[3] A. Duncan, *The Conceptual Framework of Quantum Field Theory*. OUP Oxford, 2012. https://books.google.com/books?id=MuH0TQvpY5sC.

[4] E. O. Lawrence, *Method and apparatus for the acceleration of ions*, Feb. 20, 1934. https://google.com/patents/US1948384. US Patent 1,948,384.

[5] O. S. Brning, P. Collier, P. Lebrun, S. Myers, R. Ostojic, J. Poole, and P. Proudlock, *LHC Design Report*. CERN, Geneva, 2004. https://cds.cern.ch/record/782076.

[6] Super-Kamiokande Collaboration, Y. Fukuda et al., *Evidence for oscillation of atmospheric neutrinos*, Phys. Rev. Lett. **81** (1998) 1562–1567, arXiv:hep-ex/9807003 [hep-ex].

[7] W. Buchmuller and D. Wyler, *Effective Lagrangian Analysis of New Interactions and Flavor Conservation*, Nucl. Phys. **B268** (1986) 621–653.

[8] A. D. Martin, W. J. Stirling, R. S. Thorne, and G. Watt, *Parton distributions for the LHC*, Eur. Phys. J. **C63** (2009) 189–285, arXiv:0901.0002 [hep-ph].

[9] H.-L. Lai, M. Guzzi, J. Huston, Z. Li, P. M. Nadolsky, J. Pumplin, and C.-P. Yuan, *New parton distributions for collider physics*, Phys. Rev. **D82** (2010) 074024, arXiv:1007.2241 [hep-ph].

[10] R. D. Ball, L. Del Debbio, S. Forte, A. Guffanti, J. I. Latorre, J. Rojo, and M. Ubiali, *A first unbiased global NLO determination of parton distributions and their uncertainties*, Nucl. Phys. **B838** (2010) 136–206, arXiv:1002.4407 [hep-ph].

[11] B. Andersson, G. Gustafson, G. Ingelman, and T. Sjostrand, *Parton Fragmentation and String Dynamics*, Phys. Rept. **97** (1983) 31–145.

[12] B. R. Webber, *Fragmentation and hadronization*, Int. J. Mod. Phys. **A15S1** (2000) 577–606, arXiv:hep-ph/9912292 [hep-ph], [,577(1999)].

[13] ZEUS, H1 Collaboration, M. Wlasenko, *Measurement of the Structure of the Proton at HERA*, Nucl. Phys. **A827** (2009) 276C–278C, arXiv:0902.0563 [hep-ex].

[14] Y. L. Dokshitzer, *Calculation of the Structure Functions for Deep Inelastic Scattering and e+ e- Annihilation by Perturbation Theory in Quantum Chromodynamics.*, Sov. Phys. JETP **46** (1977) 641–653, [Zh. Eksp. Teor. Fiz.73,1216(1977)].

[15] V. N. Gribov and L. N. Lipatov, *Deep inelastic e p scattering in perturbation theory*, Sov. J. Nucl. Phys. **15** (1972) 438–450, [Yad. Fiz.15,781(1972)].

[16] G. Altarelli and G. Parisi, *Asymptotic Freedom in Parton Language*, Nucl. Phys. **B126** (1977) 298.

[17] J. C. Collins, D. E. Soper, and G. F. Sterman, *Factorization of Hard Processes in QCD*, Adv. Ser. Direct. High Energy Phys. **5** (1989) 1–91, arXiv:hep-ph/0409313 [hep-ph].

[18] H. U. Bengtsson, *The Lund Monte Carlo for High p_T Physics*, Comput. Phys. Commun. **31** (1984) 323.

[19] G. Marchesini, B. R. Webber, G. Abbiendi, I. G. Knowles, M. H. Seymour, and L. Stanco, *HERWIG: A Monte Carlo event generator for simulating hadron emission reactions with interfering gluons. Version 5.1 - April 1991*, Comput. Phys. Commun. **67** (1992) 465–508.

[20] Particle Data Group Collaboration, K. A. Olive et al., *Review of Particle Physics*, Chin. Phys. **C38** (2014) 090001.

[21] M. Jezabek and Y. Sumino, *Neutrino mixing and seesaw mechanism*, Phys. Lett. **B440** (1998) 327–331, arXiv:hep-ph/9807310 [hep-ph].

[22] ATLAS Collaboration, G. Aad et al., *Observation of a new particle in the search for the Standard Model Higgs boson with the ATLAS detector at the LHC*, Phys. Lett. **B716** (2012) 1–29, arXiv:1207.7214 [hep-ex].

[23] CMS Collaboration, S. Chatrchyan et al., *Observation of a new boson at a mass of 125 GeV with the CMS experiment at the LHC*, Phys. Lett. **B716** (2012) 30–61, arXiv:1207.7235 [hep-ex].

[24] G. Mahlon and S. J. Parke, *Single top quark production at the LHC: Understanding spin*, Phys. Lett. **B476** (2000) 323–330, arXiv:hep-ph/9912458 [hep-ph].

[25] Q.-H. Cao, R. Schwienhorst, J. A. Benitez, R. Brock, and C. P. Yuan, *Next-to-leading order corrections to single top quark production and decay at the Tevatron: 2. t^- channel process*, Phys. Rev. **D72** (2005) 094027, arXiv:hep-ph/0504230 [hep-ph].

[26] J. D. Richman, *An Experimenter's Guide to the Helicity Formalism*,.

[27] C. Degrande, N. Greiner, W. Kilian, O. Mattelaer, H. Mebane, T. Stelzer, S. Willenbrock, and C. Zhang, *Effective Field Theory: A Modern Approach to Anomalous Couplings*, Annals Phys. **335** (2013) 21–32, arXiv:1205.4231 [hep-ph].

[28] J. A. Aguilar-Saavedra, *A Minimal set of top anomalous couplings*, Nucl. Phys. **B812** (2009) 181–204, arXiv:0811.3842 [hep-ph].

[29] M. Fischer, S. Groote, J. G. Korner, and M. C. Mauser, *Complete angular analysis of polarized top decay at O(alpha(s))*, Phys. Rev. **D65** (2002) 054036, arXiv:hep-ph/0101322 [hep-ph].

[30] J. A. Aguilar-Saavedra and J. Bernabeu, *W polarisation beyond helicity fractions in top quark decays*, Nucl. Phys. **B840** (2010) 349–378, arXiv:1005.5382 [hep-ph].

[31] LHC Study Group Collaboration, T. S. Pettersson and P. Lefvre, *The Large Hadron Collider: conceptual design*, Tech. Rep. CERN-AC-95-05-LHC, CERN, Geneva, Oct, 1995. https://cds.cern.ch/record/291782.

[32] L. Evans and P. Bryant, *LHC Machine*, Journal of Instrumentation **3** no. 08, (2008) S08001, http://stacks.iop.org/1748-0221/3/i=08/a=S08001.

[33] T. Linnecar, M. E. Angoletta, L. Arnaudon, P. Baudrenghien, T. Bohl, O. Brunner, A. Butterworth, E. Ciapala, F. Dubouchet, J. Ferreira-Bento, D. Glenat, G. Hagmann, W. Hfle, C. Julie, F. Killing, G. Kotzian, D. Landre, R. Louwerse, P. Maesen, P. Martinez-Yanez, J. Molendijk, E. Montesinos, C. Nicou, J. Noirjean, G. Papotti, A. Pashnin, G. Pechaud, J. Pradier, V. Rossi, J. Sanchez-Quesada, M. Schokker, E. Shaposhnikova, R. Sorokoletev, D. Stellfeld, J. Tckmantel, D. Valuch, U. Wehrle, and F. Weierud, *Hardware and Initial Beam Commissioning of the LHC RF Systems*, Tech. Rep. LHC-PROJECT-Report-1172. CERN-LHC-PROJECT-Report-1172, CERN, Geneva, Oct, 2008. https://cds.cern.ch/record/1176380.

[34] ATLAS Collaboration, A. Airapetian et al., *ATLAS: Detector and physics performance technical design report. Volume 1*, tech. rep., CERN, 1999.

[35] ATLAS Collaboration, A. Airapetian et al., *ATLAS: Detector and physics performance technical design report. Volume 2*, tech. rep., CERN, 1999.

[36] ATLAS Collaboration, G. Aad et al., *The ATLAS Experiment at the CERN Large Hadron Collider*, Journal of Instrumentation **3** no. 08, (2008) S08003, http://stacks.iop.org/1748-0221/3/i=08/a=S08003.

[37] *LEP design report*. CERN, Geneva, 1984. https://cds.cern.ch/record/102083. Copies shelved as reports in LEP, PS and SPS libraries.

[38] D. A. Finley, *Calculation of Integrated Luminosity for Beams Stored in the Tevatron Collider*, Conf. Proc. **C8903201** (1989) 1834.

[39] B. Muratori, *Luminosity and luminous region calculations for the LHC*, Tech. Rep. LHC-PROJECT-NOTE-301, CERN, Geneva, Sep, 2002. https://cds.cern.ch/record/691967.

[40] CMS Collaboration Collaboration, S. e. a. Chatrchyan, *The CMS experiment at the CERN LHC. The Compact Muon Solenoid experiment*, J. Instrum. **3** (2008) S08004. 361 p, https://cds.cern.ch/record/1129810, Also published by CERN Geneva in 2010.

[41] ALICE Collaboration Collaboration, K. e. a. Aamodt, *The ALICE experiment at the CERN LHC*, Journal of Instrumentation **3** no. 08, (2008) S08002, http://stacks.iop.org/1748-0221/3/i=08/a=S08002.

[42] LHCb Collaboration Collaboration, A. J. e. a. Augusto Alves, *The LHCb Detector at the LHC*, Journal of Instrumentation **3** no. 08, (2008) S08005, http://stacks.iop.org/1748-0221/3/i=08/a=S08005.

[43] TOTEM Collaboration Collaboration, V. Berardi, M. G. Catanesi, E. Radicioni, R. Herzog, R. Rudischer, E. Wobst, M. Deile, K. Eggert, F. Haug, P. Jarron, D. Macina, H. Niewiadomski, E. Noschis, M. Oriunno, A. L. Perrot, G. Ruggiero, W. Snoeys, A. Verdier, V. Boccone, M. Bozzo, A. Buzzo, F. Capurro, S. Cuneo, F. Ferro, M. Macri, S. Minutoli, A. Morelli, P. Musico, M. Negri, A. Santroni, G. Sette, A. Sobol, V. Avati, E. Goussev, M. Jrvinen, J. Kalliopuska, K. Kurvinen, R. Lauhakangas, F. Oljemark, R. Orava, K. sterberg, V. G. Palmieri, H. Saarikko, A. Toppinen, V. Kundrt, M. Lokajcek, C. Da Vi, J. Hasi, A. Kok, and S. Watts, *Total cross-section, elastic scattering and diffraction dissociation at the Large Hadron Collider at CERN: TOTEM Technical Design Report*. Technical Design Report TOTEM. CERN, Geneva, 2004. https://cds.cern.ch/record/704349.

[44] LHCf Collaboration Collaboration, O. Adriani, L. Bonechi, M. Bongi, R. D'ALessandro, D. A. Faus, M. Haguenauer, Y. Itow, K. Kasahara, K. Masuda, Y. Matsubara, H. Menjo, Y. Muraki, P. Papini, T. Sako, T. Tamura, S. Torii, A. Tricomi, W. C. Turner, J. Velasco, and K. Yoshida, *LHCf experiment: Technical Design Report*. Technical Design Report LHCf. CERN, Geneva, 2006. http://cds.cern.ch/record/926196.

[45] MoEDAL Collaboration Collaboration, J. Pinfold, R. Soluk, Y. Yao, S. Cecchini, G. Giacomelli, M. Giorgini, L. Patrizii, G. Sirri, D. H. Lacarrre, K. Kinoshita, J. Jakubek, M. Platkevic, S. Pospsil, Z. Vykydal, T. Hott, A. Houdayer, C. Leroy, J. Swain, D. Felea, D. Hasegan, G. E. Pavalas, and V. Popa, *Technical Design Report of the MoEDAL Experiment*, Tech. Rep. CERN-LHCC-2009-006. MoEDAL-TDR-001, CERN, Geneva, Jun, 2009. http://cds.cern.ch/record/1181486.

[46] ATLAS Collaboration, G. Aad et al., *Improved luminosity determination in pp collisions at sqrt(s) = 7 TeV using the ATLAS detector at the LHC*, Eur. Phys. J. **C73** no. 8, (2013) 2518, arXiv:1302.4393 [hep-ex].

[47] CMS Collaboration Collaboration, S. Chatrchyan et al., *CMS Luminosity Based on Pixel Cluster Counting - Summer 2012 Update*, Tech. Rep. CMS-PAS-LUM-12-001, CERN, Geneva, 2012. http://cds.cern.ch/record/1482193.

[48] D. Fournier, *Performance of the LHC, ATLAS and CMS in 2011*, EPJ Web Conf. **28** (2012) 01003, arXiv:1201.4681 [hep-ex].

[49] ATLAS Collaboration, G. Aad et al., *Expected Performance of the ATLAS Experiment - Detector, Trigger and Physics*, arXiv:0901.0512 [hep-ex].

[50] ATLAS Collaboration, The ATLAS Collaboration, *ATLAS central solenoid: Technical design report*, tech. rep., CERN, 1997.

[51] ATLAS Collaboration, The ATLAS Collaboration, *ATLAS barrel toroid: Technical design report*, tech. rep., CERN, 1997.

[52] ATLAS Collaboration, The ATLAS Collaboration, *ATLAS endcap toroids: Technical design report*, tech. rep., CERN, 1997.

[53] ATLAS Collaboration, The ATLAS Collaboration, *ATLAS inner detector: Technical design report. Vol. 1*, tech. rep., CERN, 1997.

[54] ATLAS Collaboration, The ATLAS Collaboration, *ATLAS inner detector: Technical design report. Vol. 2*, tech. rep., CERN, 1997.

[55] ATLAS Collaboration, M. S. Alam et al., *ATLAS pixel detector: Technical design report*, tech. rep., CERN, 1998.

[56] A. Abdesselam et al., *The barrel modules of the ATLAS semiconductor tracker*, Nucl. Instrum. Meth. **A568** (2006) 642–671.

[57] ATLAS Collaboration, A. Abdesselam et al., *The ATLAS semiconductor tracker end-cap module*, Nucl. Instrum. Meth. **A575** (2007) 353–389.

[58] D. Attree et al., *The evaporative cooling system for the ATLAS inner detector*, JINST **3** (2008) P07003.

[59] ATLAS TRT Collaboration, E. Abat et al., *The ATLAS TRT barrel detector*, JINST **3** (2008) P02014.

[60] E. Abat et al., *The ATLAS TRT end-cap detectors*, JINST **3** (2008) P10003.

[61] E. Abat et al., *The ATLAS TRT electronics*, JINST **3** (2008) P06007.

[62] ATLAS Collaboration, The ATLAS Collaboration, *ATLAS liquid argon calorimeter: Technical design report*, tech. rep., CERN, 1996.

[63] ATLAS Collaboration, The ATLAS Collaboration, *ATLAS tile calorimeter: Technical design report*, tech. rep., CERN, 1996.

[64] A. Artamonov et al., *The ATLAS forward calorimeters*, JINST **3** (2008) P02010.

[65] ATLAS Collaboration, The ATLAS Collaboration, *ATLAS muon spectrometer: Technical design report*, tech. rep., CERN, 1997.

[66] J. Goodson, *Search for Supersymmetry in States with Large Missing Transverse Momentum and Three Leptons including a Z-Boson*. PhD thesis, Stony Brook University, May, 2012. Presented 17 Apr 2012.

[67] ATLAS Collaboration, The ATLAS Collaboration, *ATLAS first level trigger: Technical design report*, tech. rep., CERN, 1998.

[68] ATLAS Collaboration, The ATLAS Collaboration, *ATLAS high-level trigger, data acquisition and controls: Technical design report*, tech. rep., CERN, 2003.

[69] ATLAS Collaboration Collaboration, The ATLAS Collaboration, *ATLAS Computing: technical design report*. Technical Design Report ATLAS. CERN, Geneva, 2005. http://cds.cern.ch/record/837738.

[70] ATLAS Collaboration Collaboration, G. e. a. Aad, *The ATLAS Simulation Infrastructure*, The European Physical Journal C **70** no. 3, (2010) 823–874, http://dx.doi.org/10.1140/epjc/s10052-010-1429-9.

[71] *The GeoModel toolkit for detector description*. 2005. http://doc.cern.ch/yellowrep/2005/2005-002/p353.pdf.

[72] GEANT4 Collaboration, S. Agostinelli et al., *GEANT4: A Simulation toolkit*, Nucl. Instrum. Meth. **A506** (2003) 250–303.

[73] E. Barberio, J. Boudreau, B. Butler, S. L. Cheung, A. Dell'Acqua, A. D. Simone, E. Ehrenfeld, M. V. Gallas, A. Glazov, Z. Marshall, J. Mueller, R. Plaakyte, A. Rimoldi, P. Savard, V. Tsulaia, A. Waugh, and C. C. Young, *Fast simulation of electromagnetic showers in the ATLAS calorimeter: Frozen showers*, Journal of Physics: Conference Series **160** no. 1, (2009) 012082, http://stacks.iop.org/1742-6596/160/i=1/a=012082.

[74] T. Cornelissen, M. Elsing, S. Fleischmann, W. Liebig, E. Moyse, and A. Salzburger, *Concepts, Design and Implementation of the ATLAS New Tracking (NEWT)*, Tech. Rep. ATL-SOFT-PUB-2007-007. ATL-COM-SOFT-2007-002, CERN, Geneva, Mar, 2007. https://cds.cern.ch/record/1020106.

[75] Kalman, Rudolph, and Emil, *A New Approach to Linear Filtering and Prediction Problems*, Transactions of the ASME–Journal of Basic Engineering **82** no. Series D, (1960) 35–45.

[76] ATLAS Collaboration Collaboration, The ATLAS Collaboration, *CSC Note - Photon Conversions in ATLAS*, Tech. Rep. SMU-HEP-08-13, CERN, Geneva, August, 2008. http://www.physics.smu.edu/web/research/preprints/SMU-HEP-08-13.pdf.

[77] A. Wildauer, K. Prokofiev, and S. Pagan Griso, *Update of primary vertex plots on 7 TeV data from 2011*, Tech. Rep. ATL-COM-PHYS-2011-571, CERN, Geneva, May, 2011. https://cds.cern.ch/record/1353244.

[78] W. Waltenberger, R. Frhwirth, and P. Vanlaer, *Adaptive vertex fitting*, Journal of Physics G: Nuclear and Particle Physics **34** no. 12, (2007) N343, http://stacks.iop.org/0954-3899/34/i=12/a=N01.

[79] W. Lampl, S. Laplace, D. Lelas, P. Loch, H. Ma, S. Menke, S. Rajagopalan, D. Rousseau, S. Snyder, and G. Unal, *Calorimeter clustering algorithms: Description and performance*,.

[80] ATLAS Collaboration, G. Aad et al., *Electron performance measurements with the ATLAS detector using the 2010 LHC proton-proton collision data*, Eur. Phys. J. **C72** (2012) 1909, arXiv:1110.3174 [hep-ex].

[81] ATLAS Collaboration, G. Aad et al., *Electron reconstruction and identification efficiency measurements with the ATLAS detector using the 2011 LHC proton-proton collision data*, Eur. Phys. J. **C74** no. 7, (2014) 2941, arXiv:1404.2240 [hep-ex].

[82] ATLAS Collaboration, The ATLAS Collaboration, *Expected electron performance in the ATLAS experiment*, tech. rep., CERN, 2011.

[83] ATLAS Collaboration, G. Aad et al., *Electron and photon energy calibration with the ATLAS detector using LHC Run 1 data*, Eur. Phys. J. **C74** no. 10, (2014) 3071, arXiv:1407.5063 [hep-ex].

[84] A. Hoecker et al., *TMVA - Toolkit for Multivariate Data Analysis*, PoS **ACAT** (2007) 040, arXiv:physics/0703039 [PHYSICS].

[85] ATLAS Collaboration Collaboration, The ATLAS Collaboration, *Muon Performance in Minimum Bias pp Collision Data at $s = 7$ TeV with ATLAS*, Tech. Rep. ATLAS-CONF-2010-036, CERN, Geneva, Jul, 2010. https://cds.cern.ch/record/1277675.

[86] ATLAS Collaboration, G. Aad et al., *Measurement of the muon reconstruction performance of the ATLAS detector using 2011 and 2012 LHC protonproton collision data*, Eur. Phys. J. **C74** no. 11, (2014) 3130, arXiv:1407.3935 [hep-ex].

[87] ATLAS Collaboration Collaboration, G. Aad et al., *Muons, Expected performance of the ATLAS experiment: detector, trigger and physics*. CERN, Geneva, 2009. https://cds.cern.ch/record/1125884.

[88] M. Cacciari, G. P. Salam, and G. Soyez, *The anti-k_t jet clustering algorithm*, JHEP **04** (2008) 063, arXiv:0802.1189 [hep-ph].

[89] M. Cacciari and G. P. Salam, *Dispelling the N^3 myth for the k_t jet-finder*, Phys. Lett. **B641** (2006) 57–61, arXiv:hep-ph/0512210.

[90] ATLAS Collaboration, G. Aad et al., *Jet energy measurement and its systematic uncertainty in proton-proton collisions at $\sqrt{s} = 7$ TeV with the ATLAS detector*, Eur. Phys. J. **C75** (2015) 17, arXiv:1406.0076 [hep-ex].

[91] ATLAS Collaboration, G. Aad et al., *Jet energy measurement with the ATLAS detector in proton-proton collisions at $\sqrt{s} = 7$ TeV*, Eur. Phys. J. **C73** no. 3, (2013) 2304, arXiv:1112.6426 [hep-ex].

[92] ATLAS Collaboration, G. Aad et al., *Performance of Missing Transverse Momentum Reconstruction in Proton-Proton Collisions at 7 TeV with ATLAS*, Eur. Phys. J. **C72** (2012) 1844, arXiv:1108.5602 [hep-ex].

[93] ATLAS Collaboration, *Identification and energy calibration of hadronically decaying tau leptons with the ATLAS experiment in pp collisions at $\sqrt{s} = 8$* TeV, Eur. Phys. J. **C75** (2015) 303, arXiv:1412.7086 [hep-ex].

[94] CDF Collaboration, T. Aaltonen et al., *Observation of Single Top Quark Production and Measurement of —Vtb— with CDF*, Phys. Rev. **D82** (2010) 112005, arXiv:1004.1181 [hep-ex].

[95] D/0 Collaboration, V. M. Abazov et al., *Evidence for production of single top quarks and first direct measurement of —Vtb—*, Phys. Rev. Lett. **98** (2007) 181802, arXiv:hep-ex/0612052 [hep-ex].

[96] CDF Collaboration, T. Aaltonen et al., *Search for the standard model Higgs boson decaying to a bb pair in events with two oppositely-charged leptons using the full CDF data set*, Phys. Rev. Lett. **109** (2012) 111803, arXiv:1207.1704 [hep-ex].

[97] ATLAS Collaboration, G. Aad et al., *Search for the $b\bar{b}$ decay of the Standard Model Higgs boson in associated $(W/Z)H$ production with the ATLAS detector*, JHEP **01** (2015) 069, arXiv:1409.6212 [hep-ex].

[98] CMS Collaboration, S. Chatrchyan et al., *Search for the standard model Higgs boson produced in association with a W or a Z boson and decaying to bottom quarks*, Phys. Rev. **D89** no. 1, (2014) 012003, arXiv:1310.3687 [hep-ex].

[99] CMS Collaboration, V. Khachatryan et al., *Search for W' to tb in proton-proton collisions at sqrt(s) = 8 TeV*, arXiv:1509.06051 [hep-ex].

[100] ATLAS Collaboration, G. Aad et al., *Search for tb resonances in proton-proton collisions at $\sqrt{s} = 7$ TeV with the ATLAS detector*, Phys. Rev. Lett. **109** (2012) 081801, arXiv:1205.1016 [hep-ex].

[101] ATLAS Collaboration, G. Aad et al., *ATLAS Run 1 searches for direct pair production of third-generation squarks at the Large Hadron Collider*, arXiv:1506.08616 [hep-ex].

[102] CMS Collaboration, V. Khachatryan et al., *Searches for third-generation squark production in fully hadronic final states in proton-proton collisions at $\sqrt{s} = 8$ TeV*, JHEP **06** (2015) 116, arXiv:1503.08037 [hep-ex].

[103] LHC Higgs Cross Section Working Group Collaboration, S. Dittmaier et al., *Handbook of LHC Higgs Cross Sections: 1. Inclusive Observables*, arXiv:1101.0593 [hep-ph].

[104] ALEPH Collaboration, D. Buskulic et al., *Measurement of the ratio Gamma (b anti-b) / Gamma (hadron) using event shape variables*, Phys. Lett. **B313** (1993) 549–563.

[105] CDF Collaboration, F. Abe et al., *Evidence for top quark production in $\overline{p}p$ collisions at $\sqrt{s} = 1.8$ TeV*, Phys. Rev. **D50** (1994) 2966–3026.

[106] G. Piacquadio and C. Weiser, *A new inclusive secondary vertex algorithm for b-jet tagging in ATLAS*, Journal of Physics Conference Series **119** no. 3, (2008) 032032.

[107] ATLAS Collaboration, The ATLAS Collaboration, *First look at the JetProb b-tagging algorithm in the 900 GeV collision data with the ATLAS detector*, tech. rep., CERN, 2010.

[108] ATLAS Collaboration, The ATLAS Collaboration, *Performance of the ATLAS Secondary Vertex b-tagging Algorithm in 7 TeV Collision Data*, tech. rep., CERN, 2010.

[109] CDF Collaboration, T. Aaltonen et al., *Measurement of the $t\bar{t}$ Production Cross Section in $p\bar{p}$ Collisions at sqrt(s)=1.96 TeV using Soft Electron b-Tagging*, Phys. Rev. **D81** (2010) 092002, arXiv:1002.3783 [hep-ex].

[110] ATLAS Collaboration, G. Aad et al., *Performance of b-Jet Identification in the ATLAS Experiment*, arXiv:1512.01094 [hep-ex].

[111] D/0 Collaboration, V. M. Abazov et al., *b-Jet Identification in the D/0 Experiment*, Nucl. Instrum. Meth. **A620** (2010) 490–517, arXiv:1002.4224 [hep-ex].

[112] ATLAS Collaboration Collaboration, The ATLAS Collaboration, *b-Jet Tagging Efficiency Calibration using the System8 Method*, Tech. Rep. ATLAS-CONF-2011-143, CERN, Geneva, Oct, 2011. https://cds.cern.ch/record/1386703.

[113] ATLAS Collaboration, The ATLAS Collaboration, *Measurement of the b-tag Efficiency in a Sample of Jets Containing Muons with 5 fb1 of Data from the ATLAS Detector*, Tech. Rep. ATLAS-CONF-2012-043, CERN, Geneva, Mar, 2012. https://cds.cern.ch/record/1435197.

[114] F. James and M. Roos, *Minuit - a system for function minimization and analysis of the parameter errors and correlations*, Comput. Phys. Commun. **10** no. 6, (1975) 343–367, http://inspirehep.net/record/101965.

[115] The ATLAS Collaboration, *Further ATLAS tunes of PYTHIA6 and Pythia 8*, Tech. Rep. ATL-PHYS-PUB-2011-014, CERN, Geneva, Nov, 2011. https://cds.cern.ch/record/1400677.

[116] T. Sjostrand, S. Mrenna, and P. Z. Skands, *PYTHIA 6.4 Physics and Manual*, JHEP **05** (2006) 026, arXiv:hep-ph/0603175 [hep-ph].

[117] ATLAS Collaboration, The ATLAS Collaboration, *Measurement of dijet production with a jet veto in pp collisions at sqrt(s) = 7 TeV using the ATLAS detector*, Tech. Rep. ATLAS-CONF-2011-038, CERN, Geneva, Mar, 2011. https://cds.cern.ch/record/1337788.

[118] CDF Collaboration, T. Aaltonen et al., *Measurement of Ratios of Fragmentation Fractions for Bottom Hadrons in $p\bar{p}$ Collisions at $\sqrt{s}$ = 1.96-TeV*, Phys. Rev. **D77** (2008) 072003, arXiv:0801.4375 [hep-ex].

[119] BaBar Collaboration, B. Aubert et al., *Measurement of the electron energy spectrum and its moments in inclusive $B \to Xe\nu$ decays*, Phys. Rev. **D69** (2004) 111104, arXiv:hep-ex/0403030 [hep-ex].

[120] DELPHI Collaboration, J. Abdallah et al., *Determination of heavy quark non-perturbative parameters from spectral moments in semileptonic B decays*, Eur. Phys. J. **C45** (2006) 35–59, arXiv:hep-ex/0510024 [hep-ex].

[121] J. Boudreau, C. Escobar, J. Mueller, K. Sapp, and J. Su, *Single top quark differential decay rate formulae including detector effects*, arXiv:1304.5639 [hep-ex].

[122] ATLAS Collaboration, ATLAS Collaboration, *Search for anomalous couplings in the Wtb vertex from the measurement of double differential angular decay rates of single top quarks produced in the t-channel with the ATLAS detector*, arXiv:1510.03764 [hep-ex].

[123] CDF Collaboration, F. Abe et al., *Observation of top quark production in $\overline{p}p$ collisions*, Phys. Rev. Lett. **74** (1995) 2626–2631, arXiv:hep-ex/9503002 [hep-ex].

[124] D/0 Collaboration, S. Abachi et al., *Observation of the top quark*, Phys. Rev. Lett. **74** (1995) 2632–2637, arXiv:hep-ex/9503003 [hep-ex].

[125] CDF Collaboration, J. Lueck, *Observation of electroweak single top-quark production with the CDF experiment*, PoS **HCP2009** (2009) 083.

[126] D/0 Collaboration, V. M. Abazov et al., *Observation of Single Top Quark Production*, Phys. Rev. Lett. **103** (2009) 092001, arXiv:0903.0850 [hep-ex].

[127] ATLAS Collaboration, ATLAS Collaboration, *Comprehensive measurements of t-channel single top-quark production cross sections at $\sqrt{s} = 7$ TeV with the ATLAS detector*, Phys. Rev. **D90** no. 11, (2014) 112006, arXiv:1406.7844 [hep-ex].

[128] CMS Collaboration, The CMS Collaboration, *Measurement of the single-top-quark t-channel cross section in pp collisions at $\sqrt{s} = 7$ TeV*, JHEP **12** (2012) 035, arXiv:1209.4533 [hep-ex].

[129] CMS Collaboration, The CMS Collaboration, *Measurement of W-helicity fractions in single top events topology*, Tech. Rep. CMS-PAS-TOP-12-020, CERN, Geneva, 2013. https://cds.cern.ch/record/1523619.

[130] ATLAS Collaboration, The ATLAS Collaboration, *Search for $\mathcal{CP}$ violation in single top quark events in pp collisions at $\sqrt{s} = 7$ TeV with the ATLAS detector*, Tech. Rep. ATLAS-CONF-2013-032, CERN, Geneva, Mar, 2013. https://cds.cern.ch/record/1527128.

[131] N. Kidonakis, *Next-to-next-to-leading-order collinear and soft gluon corrections for t-channel single top quark production*, Phys. Rev. **D83** (2011) 091503, arXiv:1103.2792 [hep-ph].

[132] A. Czarnecki, J. G. Korner, and J. H. Piclum, *Helicity fractions of W bosons from top quark decays at NNLO in QCD*, Phys. Rev. **D81** (2010) 111503, arXiv:1005.2625 [hep-ph].

[133] J. A. Aguilar-Saavedra and S. A. dos Santos, *New directions for top quark polarization in the t-channel process*, Phys. Rev. **D89** no. 11, (2014) 114009, arXiv:1404.1585 [hep-ph].

[134] J. A. Aguilar-Saavedra, *Single top quark production at LHC with anomalous Wtb couplings*, Nucl. Phys. **B804** (2008) 160–192, arXiv:0803.3810 [hep-ph].

[135] B. Grzadkowski and M. Misiak, *Anomalous Wtb coupling effects in the weak radiative B-meson decay*, Phys. Rev. **D78** (2008) 077501, arXiv:0802.1413 [hep-ph], [Erratum: Phys. Rev.D84,059903(2011)].

[136] Q.-H. Cao, B. Yan, J.-H. Yu, and C. Zhang, *A General Analysis of Wtb anomalous Couplings*, arXiv:1504.03785 [hep-ph].

[137] W. Bernreuther, P. Gonzalez, and M. Wiebusch, *The Top Quark Decay Vertex in Standard Model Extensions*, Eur. Phys. J. **C60** (2009) 197–211, arXiv:0812.1643 [hep-ph].

[138] ATLAS Collaboration, The ATLAS Collaboration, *Measurement of the W boson polarization in top quark decays with the ATLAS detector*, JHEP **1206** (2012) 088, arXiv:1205.2484.

[139] CMS Collaboration, The CMS Collaboration, *Measurement of the W boson polarization in semileptonic top pair decays with the CMS detector at the LHC*, tech. rep., CERN, 2011. CMS-PAS-TOP-11-020.

[140] ATLAS Collaboration, The ATLAS Collaboration, *Combination of the ATLAS and CMS measurements of the W-boson polarization in top-quark decays*, tech. rep., CERN, 2013. ATLAS-CONF-2013-033.

[141] G. Mahlon and S. J. Parke, *Single top quark production at the LHC: Understanding spin*, Phys. Lett. **B476** (2000) 323–330, arXiv:hep-ph/9912458 [hep-ph].

[142] R. Schwienhorst, C. P. Yuan, C. Mueller, and Q.-H. Cao, *Single top quark production and decay in the t-channel at next-to-leading order at the LHC*, Phys. Rev. **D83** (2011) 034019, arXiv:1012.5132 [hep-ph].

[143] ATLAS Collaboration, ATLAS Collaboration, *Measurement of the W boson polarization in top quark decays with the ATLAS detector*, JHEP **06** (2012) 088, arXiv:1205.2484 [hep-ex].

[144] CMS Collaboration, The CMS Collaboration, *Measurement of the W-boson helicity in top-quark decays from $t\bar{t}$ production in lepton+jets events in pp collisions at $\sqrt{s} =$ 7 TeV*, JHEP **10** (2013) 167, arXiv:1308.3879 [hep-ex].

[145] CMS Collaboration, CMS Collaboration, *Measurement of the W boson helicity in events with a single reconstructed top quark in pp collisions at $\sqrt{s} = 8$ TeV*, JHEP **01** (2015) 053, arXiv:1410.1154 [hep-ex].

[146] CDF, DØ Collaboration, CDF and DØ Collaborations, T. Aaltonen, et al., *Combination of CDF and DØ measurements of the W boson helicity in top quark decays*, Phys. Rev. **D85** (2012) 071106, arXiv:1202.5272 [hep-ex].

[147] ATLAS Collaboration, The ATLAS Collaboration, *Improved luminosity determination in pp collisions at sqrt(s) = 7 TeV using the ATLAS detector at the LHC*, Eur. Phys. J. **C73** no. 8, (2013) 2518, arXiv:1302.4393 [hep-ex].

[148] ATLAS Collaboration, The ATLAS Collaboration, *Performance of the ATLAS Trigger System in 2010*, Eur. Phys. J. **C72** (2012) 1849, arXiv:1110.1530 [hep-ex].

[149] B. P. Kersevan and E. Richter-Was, *The Monte Carlo event generator AcerMC versions 2.0 to 3.8 with interfaces to PYTHIA 6.4, HERWIG 6.5 and ARIADNE 4.1*, Comput. Phys. Commun. **184** (2013) 919–985, arXiv:hep-ph/0405247 [hep-ph].

[150] J. Pumplin, D. R. Stump, J. Huston, H. L. Lai, P. M. Nadolsky, and W. K. Tung, *New generation of parton distributions with uncertainties from global QCD analysis*, JHEP **07** (2002) 012, arXiv:hep-ph/0201195 [hep-ph].

[151] B. P. Kersevan and I. Hinchliffe, *A consistent prescription for the production involving massive quarks in hadron collisions*, JHEP **09** (2006) 033, arXiv:hep-ph/0603068 [hep-ph].

[152] T. Sjostrand, S. Mrenna, and P. Z. Skands, *PYTHIA 6.4 Physics and Manual*, JHEP **05** (2006) 026, arXiv:hep-ph/0603175 [hep-ph].

[153] P. Z. Skands, *Tuning Monte Carlo Generators: The Perugia Tunes*, Phys. Rev. **D82** (2010) 074018, arXiv:1005.3457 [hep-ph].

[154] G. Corcella, I. G. Knowles, G. Marchesini, S. Moretti, K. Odagiri, P. Richardson, M. H. Seymour, and B. R. Webber, *HERWIG 6: An Event generator for hadron emission reactions with interfering gluons (including supersymmetric processes)*, JHEP **01** (2001) 010, arXiv:hep-ph/0011363 [hep-ph].

[155] P. Nason, *A New method for combining NLO QCD with shower Monte Carlo algorithms*, JHEP **11** (2004) 040, arXiv:hep-ph/0409146 [hep-ph].

[156] ATLAS Collaboration, The ATLAS Collaboration, *ATLAS tunes of PYTHIA 6 and Pythia 8 for MC11*, tech. rep., CERN, 2011.

[157] A. Sherstnev and R. S. Thorne, *Parton Distributions for LO Generators*, Eur. Phys. J. **C55** (2008) 553–575, arXiv:0711.2473 [hep-ph].

[158] M. L. Mangano, M. Moretti, F. Piccinini, R. Pittau, and A. D. Polosa, *ALPGEN, a generator for hard multiparton processes in hadronic collisions*, JHEP **07** (2003) 001, arXiv:hep-ph/0206293 [hep-ph].

[159] J. M. Butterworth, J. R. Forshaw, and M. H. Seymour, *Multiparton interactions in photoproduction at HERA*, Z. Phys. **C72** (1996) 637–646, arXiv:hep-ph/9601371 [hep-ph].

[160] M. L. Mangano, M. Moretti, F. Piccinini, R. Pittau, and A. D. Polosa, *ALPGEN, a generator for hard multiparton processes in hadronic collisions*, JHEP **07** (2003) 001, arXiv:hep-ph/0206293 [hep-ph].

[161] M. L. Mangano, M. Moretti, F. Piccinini, and M. Treccani, *Matching matrix elements and shower evolution for top-quark production in hadronic collisions*, JHEP **01** (2007) 013, arXiv:hep-ph/0611129 [hep-ph].

[162] ATLAS Collaboration, ATLAS Collaboration, *The simulation principle and performance of the ATLAS fast calorimeter simulation FastCaloSim*,.

[163] M. Beneke, P. Falgari, S. Klein, and C. Schwinn, *Hadronic top-quark pair production with NNLL threshold resummation*, Nucl. Phys. **B855** (2012) 695–741, arXiv:1109.1536 [hep-ph].

[164] M. Cacciari, M. Czakon, M. Mangano, A. Mitov, and P. Nason, *Top-pair production at hadron colliders with next-to-next-to-leading logarithmic soft-gluon resummation*, Phys. Lett. **B710** (2012) 612–622, arXiv:1111.5869 [hep-ph].

[165] P. Brnreuther, M. Czakon, and A. Mitov, *Percent Level Precision Physics at the Tevatron: First Genuine NNLO QCD Corrections to $q\overline{q} \to t\bar{t} + X$*, Phys. Rev. Lett. **109** (2012) 132001, arXiv:1204.5201 [hep-ph].

[166] M. Czakon and A. Mitov, *NNLO corrections to top-pair production at hadron colliders: the all-fermionic scattering channels*, JHEP **12** (2012) 054, arXiv:1207.0236 [hep-ph].

[167] M. Czakon and A. Mitov, *NNLO corrections to top pair production at hadron colliders: the quark-gluon reaction*, JHEP **01** (2013) 080, arXiv:1210.6832 [hep-ph].

[168] M. Czakon, P. Fiedler, and A. Mitov, *Total Top-Quark Pair-Production Cross Section at Hadron Colliders Through $\mathcal{O}(\alpha_S^4)$*, Phys. Rev. Lett. **110** (2013) 252004, arXiv:1303.6254 [hep-ph].

[169] M. Czakon and A. Mitov, *Top++: A Program for the Calculation of the Top-Pair Cross-Section at Hadron Colliders*, Comput. Phys. Commun. **185** (2014) 2930, arXiv:1112.5675 [hep-ph].

[170] M. Botje et al., *The PDF4LHC Working Group Interim Recommendations*, arXiv:1101.0538 [hep-ph].

[171] N. Kidonakis, *Two-loop soft anomalous dimensions for single top quark associated production with a W^- or H^-*, Phys. Rev. **D82** (2010) 054018, arXiv:1005.4451.

[172] N. Kidonakis, *NNLL resummation for s-channel single top quark production*, Phys. Rev. **D81** (2010) 054028, arXiv:1001.5034.

[173] C. Anastasiou, L. J. Dixon, K. Melnikov, and F. Petriello, *High precision QCD at hadron colliders: Electroweak gauge boson rapidity distributions at NNLO*, Phys. Rev. **D69** (2004) 094008, arXiv:hep-ph/0312266 [hep-ph].

[174] J. M. Campbell and R. K. Ellis, *MCFM for the Tevatron and the LHC*, Nucl. Phys. Proc. Suppl. **205-206** (2010) 10–15, arXiv:1007.3492 [hep-ph].

[175] ATLAS Collaboration, The ATLAS Collaboration, *Measurements of top quark pair relative differential cross-sections with ATLAS in pp collisions at $\sqrt{s} = 7$ TeV*, Eur. Phys. J. **C73** (2013) 2261, arXiv:1207.5644 [hep-ex].

[176] ATLAS Collaboration, The ATLAS Collaboration, *Measurement of the top quark pair production cross-section with ATLAS in the single lepton channel*, Phys. Lett. **B711** (2012) 244–263, arXiv:1201.1889 [hep-ex].

[177] J. E. Cavanaugh, *Unifying the derivations for the Akaike and corrected Akaike information criteria*, Statistics & Probability Letters **33** no. 2, (1997) 201.

[178] A. R. Liddle, *Information criteria for astrophysical model selection*, Mon. Not. Roy. Astron. Soc. **377** (2007) L74–L78, arXiv:astro-ph/0701113 [astro-ph].

[179] G. E. Schwarz, *Estimating the dimension of a model*, Annals of Statistics **6** no. 2, (1978) 461–464.

[180] S. Efromovich, *Orthogonal series density estimation*, Wiley Interdisciplinary Reviews: Computational Statistics **2** no. 4, (2010) 467–476.

[181] ATLAS Collaboration, The ATLAS Collaboration, *Jet energy measurement and its systematic uncertainty in proton-proton collisions at $\sqrt{s} = 7$ TeV with the ATLAS detector*, Eur. Phys. J. **C75** (2015) 17, arXiv:1406.0076 [hep-ex].

[182] S. Frixione and B. R. Webber, *Matching NLO QCD computations and parton shower simulations*, JHEP **06** (2002) 029, arXiv:hep-ph/0204244 [hep-ph].

[183] M. Fischer, S. Groote, J. G. Korner, and M. C. Mauser, *Complete angular analysis of polarized top decay at $O(\alpha_s)$*, Phys. Rev. **D65** (2002) 054036, arXiv:hep-ph/0101322 [hep-ph].

[184] J. J. Sakurai and J. Napolitano, *Modern quantum physics*. Pearson Education Limited, 2011.